Fundamental Physics of Ferroelectrics and Related Materials 2016

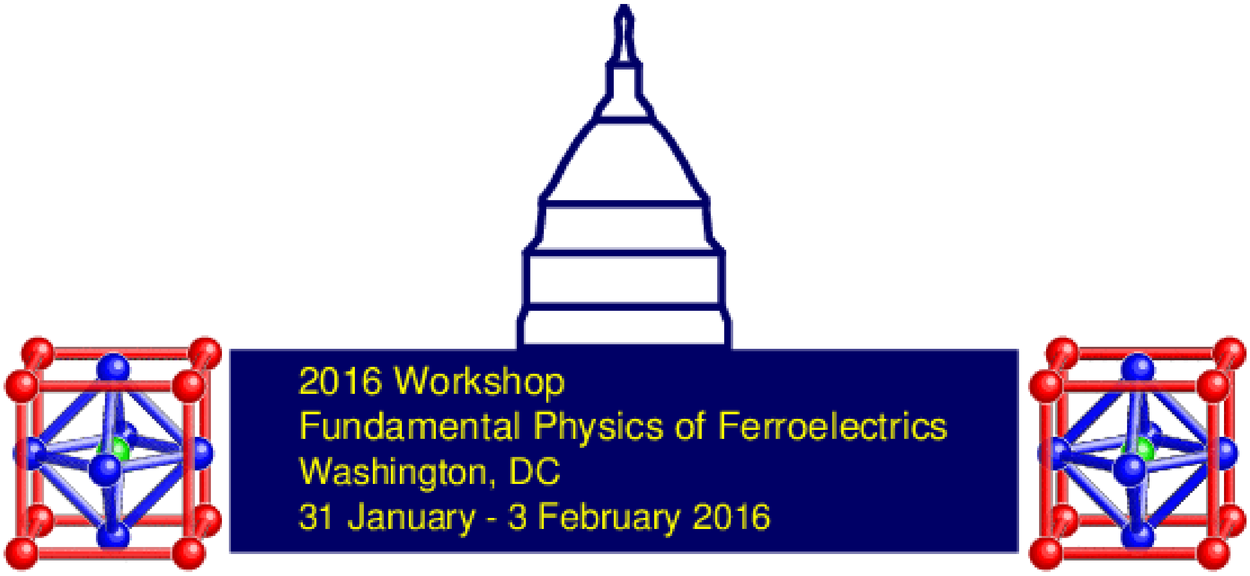

Carnegie Institution for Science
Washington, DC
January 31 – February 3, 2016

<u>Organizers</u>:
Ronald Cohen, Carnegie Institution for Science
Peter Gehring, National Institute of Standards and Technology
Zuo-Guang Ye, Simon Fraser University

Sponsors:

Carnegie Institution for Science
National Institute of Standards and Technology
Taylor & Francis Group

CARNEGIE INSTITUTION OF WASHINGTON
1902

CARNEGIE
INSTITUTION FOR
SCIENCE

NIST
National Institute of
Standards and Technology
U.S. Department of Commerce

Taylor & Francis
Taylor & Francis Group

Lunches will not be served at the Ferro2016 workshop

Attendees are encouraged to stretch their legs, get some fresh air, and sample the local food during the two 1.5-hour lunch breaks. We list below some restaurants that are within easy walking distance of the conference site. These are marked by number on the map shown on the opposite page. Many other restaurants are also located along streets shaded blue on the map.

<u>**NOTE**</u>: While this information has been obtained from current online sources, it has not been verified by the conference organizers. It is also possible that some of these restaurants may not be open for lunch.

R1	(**$$**) Distrikt Bistro	1529 16th St	Mediterranean; Kosher
R2	(**$$**) Hank's Oyster Bar	1624 Q St	Seafood
R3	(**$**) Trio	1537 17th St	American (Traditional)
R4	(**$$**) Agora	1527 17th St	Mediterranean
R5	(**$$$**) Little Serow	1511 17th St	Thai
R6	(**$$$$**) Komi	1509 17th St	Greek; Modern American
R7	(**$$$**) Sushi Taro	1503 17th St	Japanese
R8	(**$$**) Bua	1635 P St	Thai
R9	(**$**) Sweetgreen	1471 P St	American; Organic
R10	(**$$**) Tortilla Coast	1460 P St	Mexican
R11	(**$$**) Commissary	1443 P St	American (Traditional)
R12	(**$$**) Stoney's	1433 P St	Pub
R13*	(**$$**) Logan Tavern	1423 P St	Pub
R14	(**$$**) 15 Ria	1515 Rhode Isl Ave	American (New)
R15	(**$$**) Avenue Cafe and Lounge	1501 Rhode Isl Ave	American (New)

*There is a Starbucks Coffee shop at 1425 P St near R13 on the map.

LUNCH MAP

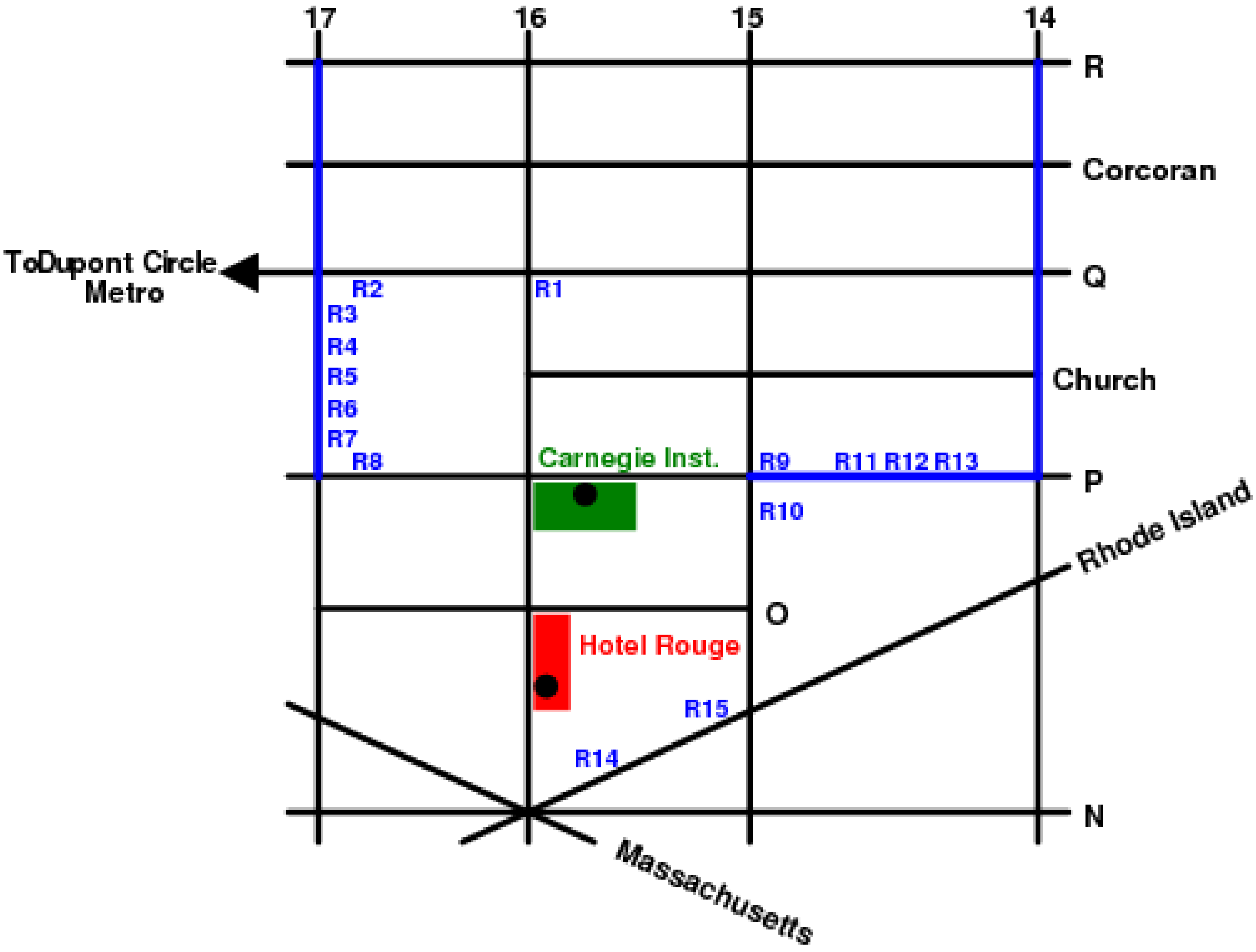
17
16
15
14
R
Corcoran
ToDupont Circle
Metro
Q
R1
R2
R3
R4
R5
R6
R7
R8
Church
Carnegie Inst.
R9
R11 R12 R13
P
R10
Rhode Island
O
Hotel Rouge
R15
R14
N
Massachusetts

CARNEGIE
INSTITUTION FOR
SCIENCE

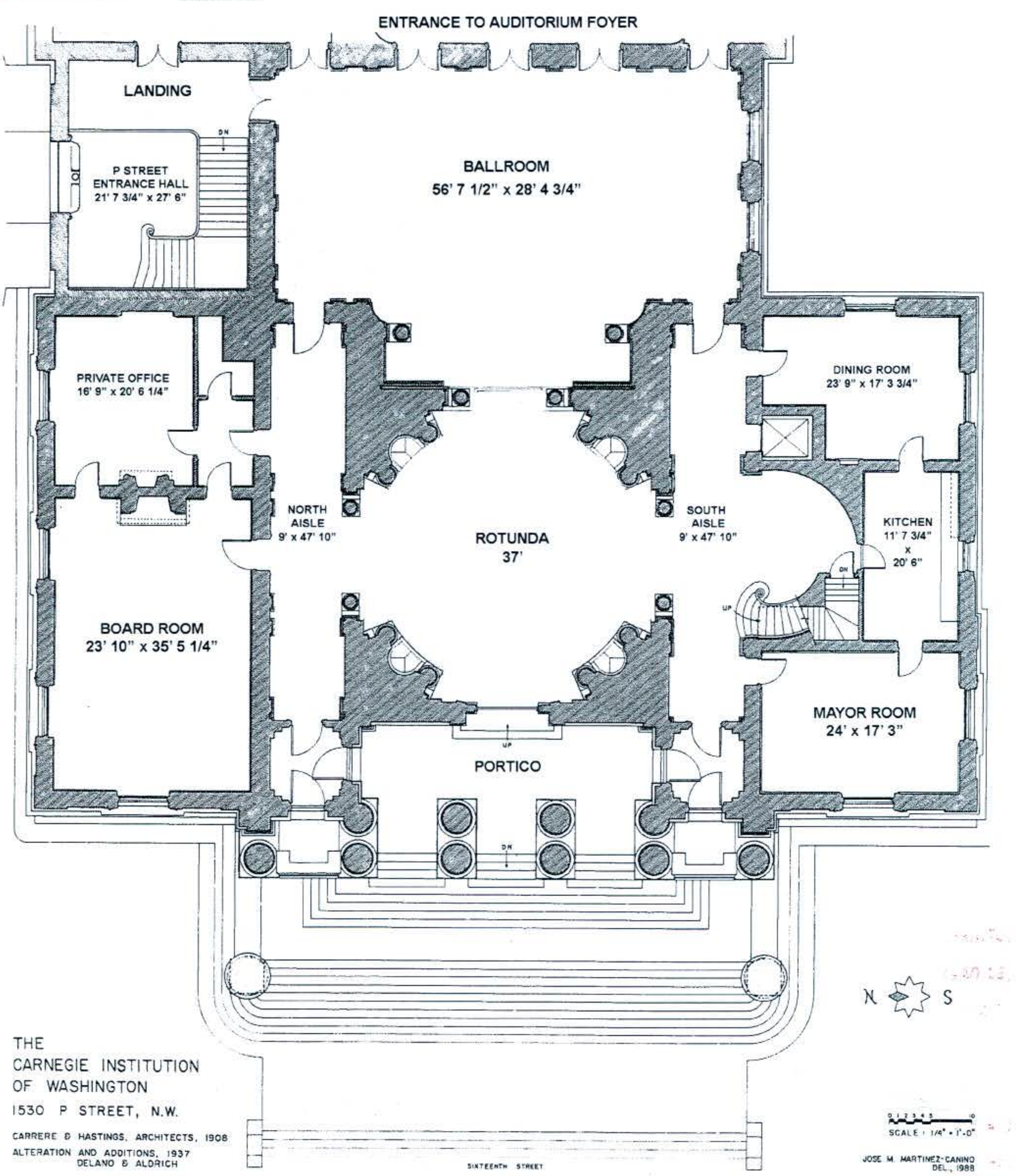

SUNDAY – 31 JANUARY, 2016

REGISTRATION AND RECEPTION – 17:00 to 19:00
(BALLROOM)

MONDAY – 1 FEBRUARY, 2016

OPENING REMARKS – 07:50 to 08:00
(AUDITORIUM)

MONDAY MORNING – 1 FEBRUARY, 2016
(AUDITORIUM)

Relaxors: 08:00 to 10:00 (Chair – A Bussmann-Holder)
08:00 S Vakhrushev – Dielectric freezing in the lead-free relaxor $Na_{1/2}Bi_{1/2}TiO_3$
08:20 S Kojima – Relaxor-like behavior of ferroelectric phase transitions in $K(Ta_{1-x}Nb)O_3$ crystals
08:40 M Manley – Complex dynamical patterns emerging from 3-phonon coupling in a relaxor ferroelectric
09:00 P Gehring – On phonon localization in relaxors
09:20 A Bosak – Diffuse scattering in $Sr_{0.6}Ba_{0.4}Nb_2\,O_6$: three faces of disorder
09:40 I Grinberg – Similarities between the structure, dynamics, and dielectric properties of perovskite oxide relaxor ferroelectrics and water

MORNING COFFEE BREAK – 10:00 to 10:30

Improper Ferroelectrics: 10:30 to 12:00 (Chair – J Rondinelli)
10:30 M Senn (INVITED) – From improper ferroelectrics to negative thermal expansion – what symmetry analysis of competing crystallographic phases can tell us about dynamics
11:00 S Kamba – High-temperature electromagnons in Z-type hexaferrite $(Ba_xSr_{1-x})_3Co_2Fe_{24}O_{41}$ and ferroelectric soft mode in improper ferroelectric 2H-$BaMnO_3$
11:20 F-T Huang – Domain topology and conducting ferroelectric walls in a hybrid improper ferroelectric
11:40 X-Z Lu – First-principles study of the layered oxides with hybrid improper ferroelectricity

LUNCH (on your own) – 12:00 to 13:30

Magnetoelectrics: 13:30 to 14:50 (Chair – P Maksymovych)
13:30 N Bristowe (INVITED) – Coupling and electrical control of structural, orbital, and magnetic orders in perovskites
14:00 A Grutter (INVITED) – Probing magnetoelectric heterostructures with polarized neutron reflectometry
14:30 A Morelli – Deterministic polarization switching in multiferroic bismuth ferrite nanoislands for magnetoelectric memories

AFTERNOON COFFEE BREAK – 14:50 to 15:20

MONDAY AFTERNOON – 1 FEBRUARY, 2016
(AUDITORIUM)

<u>Lead-Free Oxide Perovskites</u>: 15:20 to 17:00 (Chair – Z Ye)

15:20 V Cooper (INVITED) – Designing high response lead-free piezoelectrics: From first principles

15:50 O Diéguez (INVITED) – First-principles prediction of supertetragonal phases in perovskite oxide films: the case of $BiMnO_3$

16:20 H Moriwake – First-principles calculations of electric-field induced ferroelectric phase transition in $AgNbO_3$

16:40 JH Lee – Record-high ferroelectric polarization by spins and non-reciprocal directional dichroism in $BiFeO_3$

SHORT BREAK – 17:00 to 17:20

<u>High-Throughput/Efficient First Principles Calculations</u>: 17:20 to 18:20 (Chair – D Vanderbilt)

17:20 K Garrity – High-throughput first-principles search for new ferroelectrics

17:40 J Bonini – Efficient computation of spontaneous polarization using Wannier center displacements

18:00 J Sun – Accurate geometric and energetic properties of ferroelectric and related materials from an efficient density functional

BANQUET (BALL ROOM) – 19:30 to 21:30

TUESDAY MORNING – 2 FEBRUARY, 2016
(AUDITORIUM)

Domains and Domain Walls: 08:00 to 10:10 (Chair – N Barrett)

08:00 S Liu (INVITED) – Understanding the dynamics of ferroelectric domain walls with MD simulations
08:30 J Chapman – Novel ferroelectric nanobubble domains in strained prototypical thin films
08:50 G Nataf – Experimental evidence of defects stabilized by neutral domain walls
09:10 V Garcia – Learning through ferroelectric domain dynamics in solid-state synapses
09:30 A Bokov – Observation of domain wall dynamics in ferroelectrics by means of x-ray photon correlation spectroscopy
09:50 B Wang – Complex nano/micro domain structure in tetragonal $PbZr_{1-x}Ti_xO_3$ single crystals

MORNING COFFEE BREAK – 10:10 to 10:40

Energy Materials and Applications: 10:40 to 12:00 (Chair – E Bousquet)

10:40 B Dkhil – Towards improved caloric responses using ferroelectrics
11:00 J Cuozzo –Piezocaloric effect in antiferroelectric $PbZrO_3$ from atomistic simulations
11:20 B Xu – Antiferroelectric RE-substituted $BiFeO_3$: A lead-free system for large energy storage density
11:40 M Kuklja – Structural (in)stability of complex perovskites for solid oxide fuel cells: First-principles calculations

LUNCH (on your own) – 12:00 to 13:30

Photovoltaics and Novel Perovskites: 13:30 to 15:10 (Chair – B Dkhil)

13:30 J Spanier (INVITED) – Semiconducting ferroelectric photovoltaics
14:00 C Stock (INVITED) – From soft harmonic phonons to fast relaxational dynamics in $CH_3NH_3PbBr_3$
14:30 L Tan – Ferroelectric domains in the presence of molecular orientational disorder in hybrid perovskites
14:50 R Cohen – Synthesis and characterization of predicted oxynitride perovskite $YSiO_2N$

AFTERNOON COFFEE BREAK – 15:10 to 15:40

TUESDAY AFTERNOON – 2 FEBRUARY, 2016
(AUDITORIUM)

Advances in Theory/Expt: 15:40 to 17:10 (Chair – H Krakauer)

15:40 L Bellaiche (INVITED) – Atomistic simulations of complex problems in ferroelectrics
16:10 P Maksymovych (INVITED) – To switch or not to switch: Another probe microscopy perspective
16:40 M Stengel (INVITED) – First-principles theory of flexoelectricity

SHORT BREAK - 17:10 to 17:30

$BaTiO_3$-Based: 17:30 to 18:20 (Chair – S Kamba)

17:30 E Cockayne – Structure of ultrathin film Ba-Ti-O
17:50 N Barrett – Evolution of surface charge and domain structure through the ferroelectric paraelectric phase transition in $BaTiO_3$ (001) using MEM-LEEM
18:10 A Everhardt – Ferroelectric domain structures in low-strain $BaTiO_3$
18:30 S Tsukada – Disorder in $BaTiO_3$ probed by angle-resolved polarized Raman scattering
18:50 A Grünebohm – *Ab initio* phase diagram of $BaTiO_3$ under epitaxial strain revisited

POSTER SESSION/BUFFET DINNER – 19:30 to 21:30

POSTER SESSION
(ROTUNDA)

Posters should not exceed 3 feet wide by 4 feet high (91 cm by 121 cm). Pins will be provided.

** **ALL posters should remain up from Monday morning through Tuesday evening.** **

1. C Ablitt – Understanding negative thermal expansion in improper ferroelectric Ruddlesen-Popper oxides from first principles
2. A Albarakati – Finite-temperature properties of PMN-25PT nanodots from first principles
3. N Barrett – Charged domain walls and polar boundaries in LiNbO3 and CaTiO3 studied by mirror electron microscopy
4. S Bin-Omran – Application of the Wang-Landau Monte-Carlo formalism applied to ferroelectric materials
5. E Bousquet – Proper and improper ferroelectricity in the *n*=3 Dion-Jacobson material $AA_2'Ti_2NbO_{10}$
6. JH Chang – Study of mixed crystals $[N(CH_3)_4]_2Zn_{1-x}Co_xCl_4$ (x=0, 0.5, 0.7, 0.9, and 1) by NMR
7. C Dreyer – Correct implementation of polarization constants in wurtzite materials and impact on III-nitrides
8. A Dziaugys – Two types of domains in $CuInP_2Se_6$ layered crystals
9. A Everhardt – Transitions between $BaTiO_3$ ca_1/ca_2 and a/c phases
10. H Fu – Mode sequence, frequency change of non-soft phonons, and LO-TO splitting in strained tetragonal $BaTiO_3$
11. O Gindele – Evolution of the local structure of $PbZr_{0.5}Ti_{0.5}O_3$ under applied electric fields
12. E Glazkova – Electrocaloric properties of ferroelectric ultrathin films in the presence of a residual depolarizing field
13. H Hamdi – First-principles re-investigation of bulk WO_3
14. C Hendriks – Mott-Hubbard gap in insulating phases of VO_2: *ab initio* calculations of the infrared and optical spectra
15. R Herchig – Electrocaloric effect in ferroelectric nanowires from atomistic simulations
16. A Honda – Theoretical study for fundamental physics of low dielectric loss perovskite $Ba(Zn_{1/3}Ta_{2/3})O_3$
17. E Iolin – Resonance damping of the THz-frequency transverse acoustic phonon in the relaxor ferroelectric $K(Ta_{1-x}Nb_x)O_3$
18. Z Jiang – Special quasirandom structures for complex perovskite alloys
19. R Kalfarisi – Investigation of local structure and cation ordering in dielectric oxide microwave ceramics using ^7Li and ^{93}Nb solid-state NMR spectroscopy
20. K Kalke – Ultra-large-scale hybrid Monte Carlo simulations of ferroelectric and relaxor materials
21. Karandeep – Exploring the properties of [100], [110], and [111]-oriented vanadate superlattices from first principles
22. E Kotomin – First-principles calculations of oxygen vacancies in the bulk and on the surface of complex perovskites for solid oxide fuel cell cathodes

POSTER SESSION
(ROTUNDA)

Posters should not exceed 3 feet wide by 4 feet high (91 cm by 121 cm). Pins will be provided.

** **ALL posters should remain up from Monday morning through Tuesday evening.** **

23. M Krogstad – Single crystal diffuse scattering study of relaxor (1-x)$PbMg_{1/3}Nb_{2/3}O_3$-x$PbTiO_3$
24. A Lim – NMR study of Ti- or Fe-doped $LiNbO_3$:Mg single crystals
25. P Maksymovych – Chemical phase-separation in ferroelectric layered transition metal thiophosphates
26. R Nakamoto – First-principles calculations of rare-earth iron garnets
27. J Ouyang – Heterophase polydomain nanostructure in epitaxial ferroelectric films
28. C Paillard – Photostriction in BiFeO3 from first principles
29. S Park – Charge-order-induced ferroelectricity in $LaVO_3/SrVO_3$ superlattices
30. K Patel – Universal energetic coupling in complex antiferroelectric and incommensurate perovskites
31. S Prokhorenko – Symmetry vs topology and dipolar fluctuations in proper ferroelectrics
32. Y Qi – Temperature-driven phase transitions in $BaTiO_3$: An atomistic scale description
33. R Qui – Ferroelectric instability in nanotubes and spherical nanoshells
34. S Reyes-Lillo – Effect of hydrostatic strain in the photocatalytic properties of $BiVO_4$ from first principles
35. H Robinson – ONR’s research program on acoustic transduction materials and devices
36. D Saldana-Greco – Improper magnetic ferroelectricity of nearly pure electronic nature in cycloidal spiral $CaMn_7O_{12}$
37. S KC – Spin-driven polarization in $BiMO_3$ (M=3d transition metals) multiferroics: From first principles
38. O Sayedaghaee – Controlling phase coexistence in mixed phase $BiFeO_3$
39. M Senn – Emergence of long-range order in $BaTiO_3$ from local symmetry-breaking distortions
40. S Skiadopoulou – Ferroelectric-like poling in paraelectric system
41. I Sluchinskaya – Structure of color centers in $BaTiO_3$ and $SrTiO_3$ doped with cobalt
42. S Svirskas – Dielectric, IR, and Raman spectroscopic studies of NBT-based solid solutions
43. H Takenaka – First-principles studies of effects of defects on reversible electro-strain coupling in $BaTiO_3$
44. N Tillack – *Ab initio* modelling of the magnetoelectric response in Cr_2O_3
45. R Vadapoo – Effect of manganese substitution in barium titanate and PIN-PMN-PT
46. R Walter – Electrical control of chiral phases in electrotoroidic nanocomposites
47. C Wang – Polarization in ferroelectrics
48. F Wang – Effects of oxide on the detonation initiation of energetic materials from first principles
49. Y Yang – Large elasto-optic effect in epitaxial $PbTiO_3$ films
50. H You – Partial glass isosymmetry transition in multiferroic hexagonal $ErMnO_3$
51. S Yuk – A first-principles study of ferroelectric $PbTiO_3$, $BaTiO_3$, and $KNbO_3$: Exchange and correlation effects
52. F Zheng – Rashba spin-orbit coupling enhanced carrier lifetime in $CH_3NH_3PbI_3$

WEDNESDAY MORNING – 3 FEBRUARY, 2016
(AUDITORIUM)

Multiferroics: 08:00 to 10:10 (Chair – L Bellaiche)

08:00 X Wu (INVITED) – Stabilization of a highly polar $BiFeO_3$-like structure: A new interface design route for enhanced ferroelectricity in artificial perovskite superlattices
08:30 A Bussmann-Holder – Transition metal oxides: Promising candidates for multifunctional applications
08:50 J Banys – Broadband dielectric studies of cobalt-ferrite-doped lead zirconium titanate multiferroic composites
09:10 F Ricci – Unveiling the room temperature magnetoelectricity of troilite FeS
09:30 F Thöle – The macroscopic magnetoelectric monopolization in diagonal magnetoelectrics
09:50 Z-G Ye – Ferroelectric and magnetic double morphotropic phase boundaries in Dy-modified $BiFeO_3$-$PbTiO_3$ multiferroics

MORNING COFFEE BREAK – 10:10 to 10:40

Advances in Ferroelectrics: 10:40 to 12:50 (Chair – R Cohen)

10:40 C Eom (INVITED) – Emergence of room-temperature ferroelectricity at reduced dimensions
11:10 D Amoroso – *Ab-initio* approach to structural, electronic, and ferroelectric properties of antimony sulpho-iodide
11:30 E Nowadnick – Ferroelectric switching pathways in $Ca_3Ti_2O_7$ from first principles
11:50 M Itoh – Shearing-mediated ferroelectricity: Polarization switching caused by the bond recombination of cations
12:10 M Ye – Ferroelectricity in corundum derivatives
12:30 Y Nahas – Underlying topological features in ferroelectrics

END OF WORKSHOP

Monday’s Abstracts

Dielectric freezing in lead-free relaxor Na1/2Bi1/2TiO3

A. Filimonov[1], E. Koroleva[1,2], A. Naberezhnov[2], T. Vergentiev[1] S. Vakhrushev[1,2]

[1] Peter the Great St. Petersburg Polytechnic University, Polytechnicheskaya 29 195251, St.-Petersburg, Russia

[2] Ioffe Institute, Polytechnicheskaya 26 194021, St.-Petersburg, Russia

$Na_{1/2}Bi_{1/2}TiO_3$ (NBT) is one of the first known lead-free relaxor ferroelectrics [1]. Recently there is clear revival of the interest to this material. It undergoes a very peculiar sequence of phase transitions including at least two transitions: from cubic phase at 813K to tetragonal, and to rhombohedral at ~470K, and shows unusual dielectric [2-4] properties. NBT demonstrates the diffuse maximum in the ε(T) dependence beak-shaped on heating. Until now, the interpretation of these data is discussed and the question of carrying out a thorough study of the NBT dielectric response on the middle and low measuring frequency and analysis of its behavior remains actual. In this report, the results of the detailed study of the dielectric properties of single crystal NBT in wide frequency and temperature ranges are presented.

The measurements were carried out on NBT single crystal. Single crystals were grown up by Chochralski' method in the Ioffe Institute. Sample had shape of the thin plate of 9x8x1 mm3. The thin plate has been cut out with the normal to its plane parallel to the (001). The dielectric response was studied at frequency range 0.1 Hz - 10 MHz and temperature region 300-1000 K using ultrabroadband dielectric spectrometer Novocontrol BDS80 with Novotherm-HT cryosystem. Platinum electrodes were deposited on the flat sides of the crystal.

Temperature dependences of real (ε') and imaginary (ε") parts of dielectric permittivity for several measuring frequencies were obtained in the heating and cooling runs. One heating three dielectric anomaly regions are observed– region below 500K with weak frequency dispersion, asymmetric diffuse maximum of ε near 610 K and peaks at low frequencies at around 850-900 K, position and the value of which strongly depend on the measuring frequency. Above 500 K there observed a sharp increase in the dielectric losses at low frequencies. In the cooling run for the same measuring frequencies noticeable difference with the behaviorin the heating regime is observed. Asymmetric peak at 610K significantly broadens and becomes more symmetric, but the position and the amplitude do nor change significantly.

To fit the experimental data for the complex dielectric permittivity in the broad frequency range, we used sum of the phenomenological Cole-Cole (CC) distribution of relaxation time for describing relaxation processes, term describing DC-conductivity contribution to dielectric response and the high frequency contribution to permittivity:

$$\varepsilon^* = \frac{i\sigma}{\varepsilon_0\omega} + \sum_i \frac{\Delta\varepsilon_i}{\left(1+(i\omega\tau_i)^{\alpha_i}\right)} + \varepsilon_\infty ,$$

where $\Delta\varepsilon_i$ is the dielectric strength of the *i*th relaxation process, ε_∞ is the high frequency contribution to permittivity, ω - is the measuring frequency, τ_i is the mean relaxation time of ith CC process, α – is the parameter of the relaxation time distribution (0<α<1) α=1 corresponds to Debye distribution, σ – DC-conductivity of the crystal and ε_0 – the free space permittivity, respectively.

We have analyzed the experimental frequency dependences of the real and imaginary parts of permittivity on cooling with this model function in order to identify the relaxation processes and the temperature dependences of the model parameters.

In our experimental frequency window, we were able to distinguish three relaxation processes The temperature dependenc es of the dielectric strength and the mean relaxation time of the processes were obtained (Fig. 1).

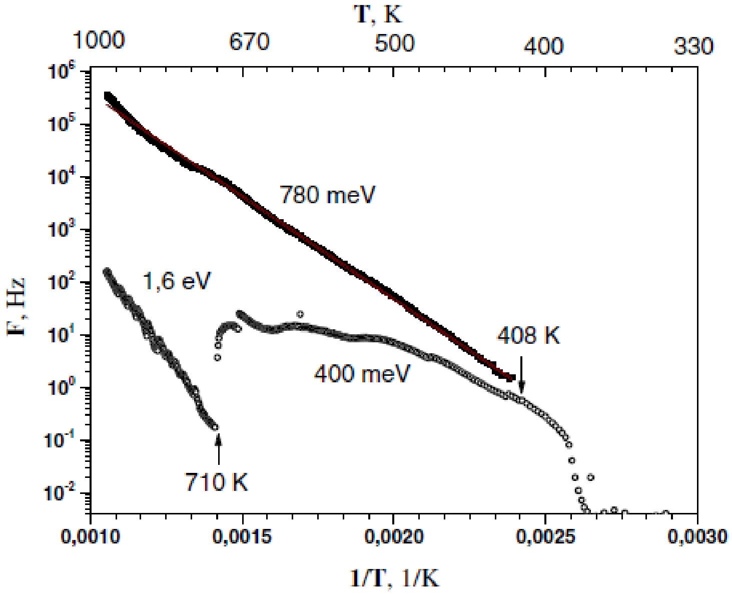

Figure 1 Temperature dependencies of the characteristic frequencies of the relaxation processes

The high frequency mode in the temperature range 1000-400 is well described by Arrhenius law with activation energy 780 meV. In the temperature range 670 - 410 K there is also another relaxation process with an activation energy of 400 meV, which merges with the high-frequency process at 410K. On further decreasing temperature characteristic relaxation frequency decreases sharply, and its behavior is no longer follows the Arrhenius law, but is well described by Vogel-Fulcher law with the freezing temperature T_f of about 370K. In our knowledge there is first direct indication of the dielectric freezing in NBT

References:

1. G. A. Smolenskii, V. A. Isupov, A. I. Agranovskaya, and N. N. Krainik, *Fiz. Tverd. Tela* (Leningrad) **2**, 2982 (1960) [*Sov. Phys. Solid State* **2**, 2651 (1960)].
2. Vakhrushev, S.B., Isupov, V.A., Kvyatkovsky, B.E., Okuneva, N.M., Pronin, I.P., Smolensky, G.A., Syrnikov, P.P.: *Ferroelectrics* **63**, 153 (1985)
3.Tu, C.-S., Siny, I.G., Schmidt, V.H.: *Phys. Rev. B* **49**, 11550 (1994)
4. J. Petzelt, D. Nuzhnyy, V. Bovtun, M. Kempa, M. Savinov, S. Kamba, J. Hlinka *Ferroelectrics* **88** (3), 320 (2015)

Relaxor like behavior of ferroelectric phase transitions in $K(Ta_{1-x}Nb_x)O_3$ crystals

S. Kojima[1], M. M. Rahaman[1], T. Imai[2], T. Sakamoto[2], and S. Tsukada[3]

[1]Graduate School of Pure and Applied Sciences, University of Tsukuba, Tsukuba, Ibaraki 305-8573, Japan

[2]NTT Corporation Device Innovation Center, Nippon Telegraph and Telephone Corporation, Atsugi, Kanagawa 243-0198, Japan

[3]Faculty of Education, University of Shimane, Matsue, Shimane 690-8504, Japan

The precursor dynamics of ferroelectric phase transitions and the relaxor like behavior were studied in $K(Ta_{1-x}Nb_x)O_3$ crystals grown by the top seeded solution growth method. The Burns temperature, T_B, and intermediate temperature, T^*, were clearly observed in a $K(Ta_{0.68}Nb_{0.32})O_3$ (KTN/0.32) crystal by the acoustic emission measurement [1]. Relaxor like behaviors were studied also by the temperature variation of longitudinal acoustic (LA) phonons and a central peak (CP) in a cubic phase using Brillouin scattering [2,3]. The anomalous behaviors of LA and CP were discussed by the polarization fluctuations of polar nanoregions (PNRs). The order-disorder nature in the vicinity of the Curie temperature, T_C, was observed by the measurement of a CP as shown in Fig. 1(a).

The relaxor nature was enhanced by 5% Li-doping, and the broadening of elastic anomaly and the extension of the temperature range between T_C and T^* were observed [4]. The origin of the increase of random fields was discussed on the basis of the occupancy of Li ions at A and B sites in the perovskite structure. The electric field effect on a first-order ferroelectric phase transition was also studied by the D-E curve and Brillouin scattering measurements, and the nonlinear response was discussed considering the bulk physical properties [5,6].

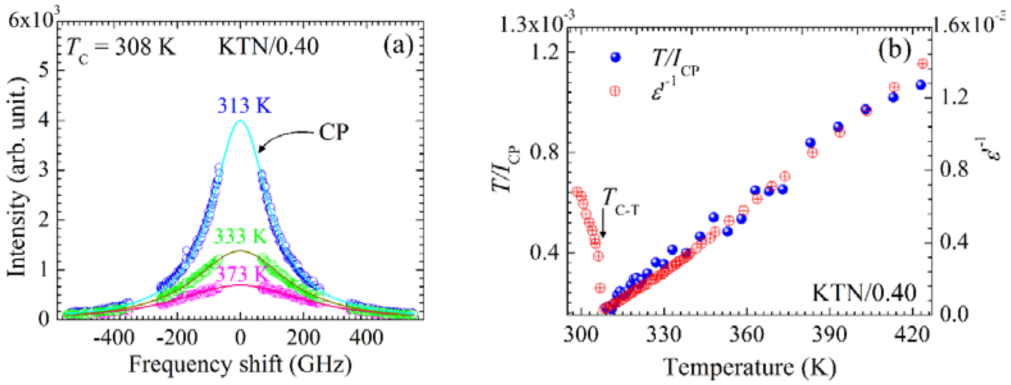

Figure 1 Temperature dependences of (a) broadband Brillouin scattering spectra and (b) the reciprocal CP intensity and the low-frequency dielectric constant measured by an impedance/gain-phase analyzer.

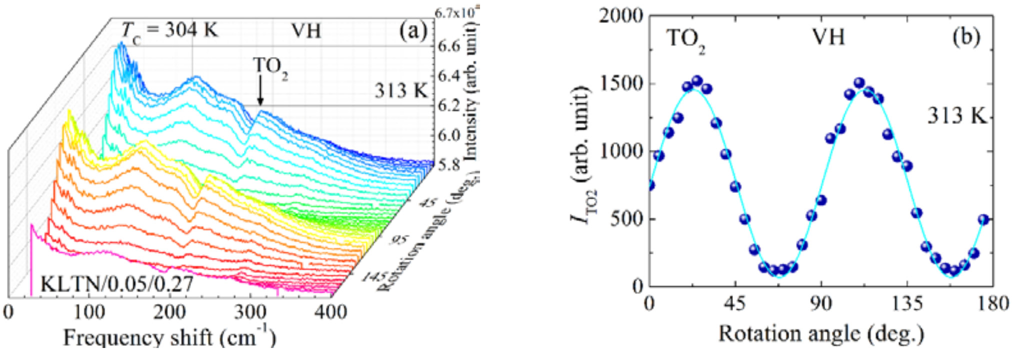

Figure 2 Angular dependences of (a) VH Raman scattering spectra of a $K_{0.95}Li_{0.05}(Ta_{0.73}Nb_{0.27})O_3$ (KLTN/0.05/0.27) crystal measured at 313 K and (b) the angular dependence of the intensity of the Fano peak in VH spectra, where closed circles and solid lines indicate the observed and calculated intensity, respectively.

The local symmetry breaking caused by the PNRs in a cubic phase was studied using the appearance of first-order Raman scattering above T_C. In KLTN/0.05/0.27, the symmetry of PNRs and Fano resonance was examined by the angular dependence of the polarization plane of the incident and scattered light of Raman scattering as shown in Fig. 2(a). In KLTN/0.05/0.27, the local symmetry breaking by the PNRs observed in a cubic phase is attributed to the E(x,y) mode of the PNRs with $R3m$ symmetry as shown in Fig. 2(b).

The origin of the Fano resonance at about 196 cm^{-1} was discussed by the temperature and electric field dependences. Its symmetry was also investigated by the angular dependence as shown in Fig. 2(b). From these experimental results, it is suggested that the origin of Fano resonance is the coupling between polarization fluctuations in PNRs and the TO$_2$ mode with the E(x,y) symmetry.

The composition gradient Li doped $K(Ta_{1-x}Nb_xO_3)$ wafer was investigated by the micro-Brillouin scattering method, and the positional variation of physical properties is discussed [7].

References

1. E. Dul’kin, S. Kojima, and M. Roth, Europhys. Lett. **97,** 57004 (2012).
2. R. Ohta, J. Zushi, T. Ariizumi, and S. Kojima, Appl. Phys. Lett. **98,** 092909 (2011).
3. M. M. Rahaman, T. Imai, J. Miyazu, J. Kobayashi, S. Tsukada, M. A. Helal, and S. Kojima, J. Appl. Phys. **116,** 074110 (2014).
4. M. M. Rahaman, T. Imai, J. Miyazu, J. Kobayashi, and S. Kojima, Jpn. J. Appl. Phys. **54,** 10NB01 (2015).
5. T. Imai, S. Toyoda, J. Miyazu, J. Kobayashi, and S. Kojima, Jpn. J. Appl. Phys. **53**, 09PB02 (2014).
6. T. Imai, S. Toyoda, J. Miyazu, J. Kobayashi, and S. Kojima, Appl. Phys. Expr. **7**, 071501 (2014).
7. M. M. Rahaman, T. Imai, J. Miyazu, J. Kobayashi, and S. Kojima, Ferroelectrics, **487**, 47, (2015).

Complex dynamical patterns emerging from 3-phonon coupling in a relaxor ferroelectric

M. E. Manley[1], D. E. Abernathy[2], R. Sahul[3], P. J. Stonaha[1], J. D. Budai[1]

[1]Materials Science and Technology Division, Oak Ridge National Laboratory, Oak Ridge, Tennessee 37831, USA
[2]Quantum Condensed Matter Division, Oak Ridge National Laboratory, Oak Ridge, Tennessee 37831, USA
[3]TRS Technologies, State College, Pennsylvania 16801, USA

A persistent controversy for relaxor ferroelectrics has been the origin of the "waterfall" effect in the phonon dispersion curves, in which low-energy transverse phonons cascade into vertical columns [1-7]. The "waterfall" effect has also been observed in other technologically important materials, including conventional ferroelectrics [8], and in a strongly anharmonic thermoelectric material [9]. Originally interpreted as phonons interacting with polar nanoregions (PNRs) [1], it was later explained as an effect of coupling damped optic and acoustic phonons, without the need for PNRs [10].

In light of a recently discovered PNR vibrational mode near the "waterfall" wavevector [11], however, we have reexamined this feature using time-of-flight inelastic neutron scattering on [100]-poled PMN-30%PT ($0.6Pb(Mg_{1/3}Nb_{2/3})O_3$ – $0.3PbTiO_3$). We make use of the fact that the PNR modes align with [100] poling to isolate the effects of the PNR mode in PMN-30%PT. Perpendicular to the poling direction no PNR mode appears, and the 2-mode coupling model proposed by Hlinka et al. [10] captures the waterfall feature. Compare the neutron experiments in Fig. 1 (a)-(c) with the related mode coupling calculations in Fig. 1 (h)-(j). Along the poling direction, on the other hand, the PNR mode appears and couples to both the TO and TA phonons, Fig. 1 (d)-(f). The 3-mode coupling results in some unexpected complex dynamical features, including intensity pockets localized in small regions of momentum-energy space (see Fig. 1(e)). A "mini-waterfall" feature also extends between the TO and PNR mode in Fig. 1(e). As with the usual "waterfall" effect this "mini-waterfall" effect depends on the structure factor of the TO phonon [10] and therefore appears different in the (300) zone, Fig. 1(g), than in the (200) zone Fig. 1(e). These features are fully explained by an expanded version of the Hlinka model [10] that includes three coupled damped harmonic oscillators representing the TO, PNR, and TA modes. The results of these calculations are shown in Fig. 1 (k)-(n). The mode coupling calculation captures the main "waterfall" effect (compare Fig. 1 (c) and (f) to Fig. 1 (j) and (m)), the "mini-waterfall" effect, and intensity pockets (compare Fig. 1 (e) and (l)). The mode coupling calculation also captures the way the "mini-waterfall" effect is diminished in going from the (200) to the (300) zone, compare Fig. 1 (g) and (n). Our results illustrate the challenges of studying the lattice dynamics of relaxor ferroelectrics; In addition to the normal phonons there are extra modes associated with the PNRs [11] and these interact with the normal phonons to produce additional complex features.

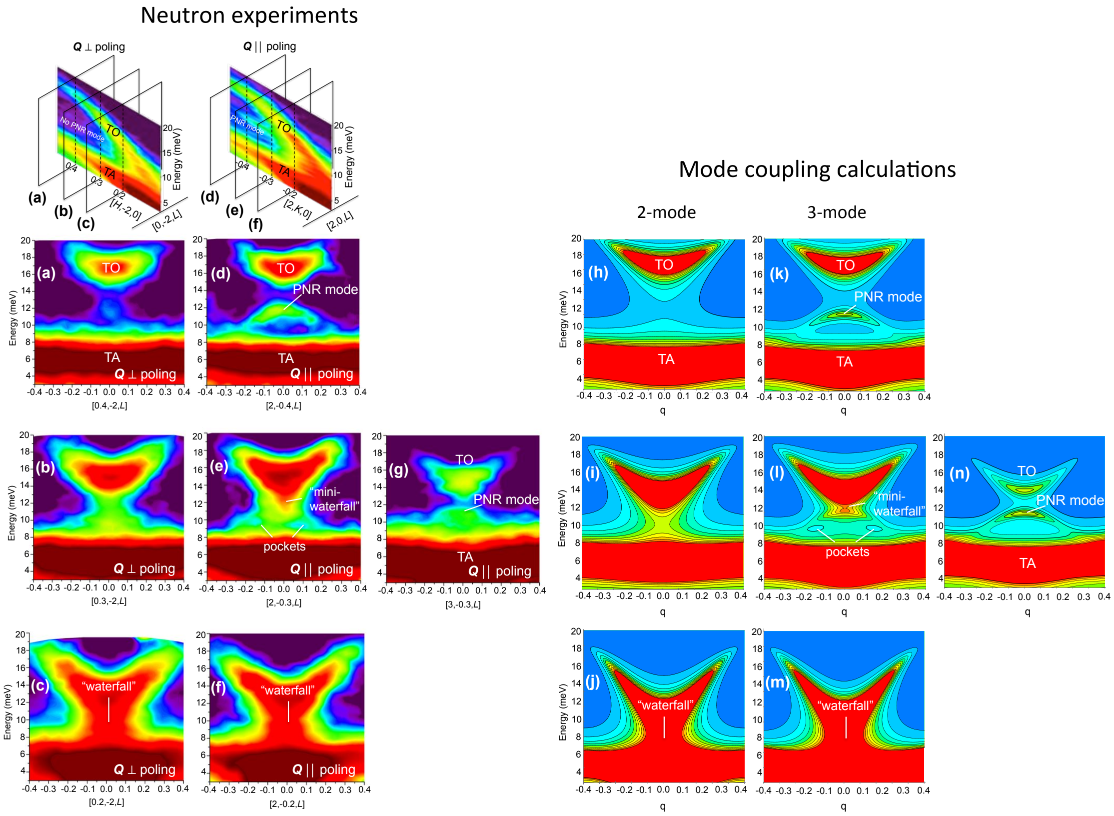

Figure 1. Inelastic neutron scattering and model calculations of the "waterfall" feature sliced into out-of-plane sections in energy-momentum space. (a)-(c) Perpendicular to the poling direction, near (0,-2,0), no PNR mode [11] is detected between the TO and TA modes and a single "waterfall" feature appears. (d)-(f) Along the poling direction, near (200), a separate PNR mode appears between the TO and TA modes. (e) A "mini-waterfall" feature appears between the TO and PNR mode. (f) TO-TA coupling dominates main "waterfall" feature. (g) "Mini-waterfall" appearance changes in (300) zone. (h)-(n) Corresponding mode coupling calculations capture the main features of the neutron experiments.

[1] P. M. Gehring, S. E. Park, and G. Shirane, Phys. Rev. Lett. **84**, 5216 (2000).
[2] P. M. Gehring, S. E. Park, and G. Shirane, Phys. Rev. B **63**, 224109 (2001).
[3] I. Tomeno, S. Shimanuki, Y. Tsunoda, and Y. Y. Ishii, J. Phys. Soc. Jpn. **70**, 1444 (2001).
[4] S. Wakimoto, C. Stock, Z.-G. Ye, W. Chen, P. M. Gehring, and G. Shirane, Phys. Rev. B **66**, 224102 (2002).
[5] P. M. Gehring, S. Wakimoto, Z.-G. Ye, and G. Shirane, Phys. Rev. Lett. **87**, 277601 (2001).
[6] D. La-Orauttapong, B. Noheda, Z.-G. Ye, P. M. Gehring, J. Toulouse, D. E. Cox, and G. Shirane, Phys. Rev. B **65**, 144101 (2002).
[7] T. Y. Koo, P. M. Gehring, G. Shirane, V. Kiryukhin, S. G. Lee, and S. W. Cheong, Phys. Rev. B **65**, 144113 (2002).
[8] G. Shirane, J. D. Axe, and J. Harada, and A. Linz, Phys. Rev. B **2**, 3651 (1970).
[9] O. Delaire, J. Ma, K. Marty, A. F. May, M. A. McGuire, M-H. Du, D. J. Singh, A. Podlesnyak, G. Ehlers, M. D. Lumsden, and B. C. Sales, Nat. Mater. **10,** 614 (2011).
[10] J. Hlinka, S. Kamba, J. Petzelt, J. Kulda, C. A. Randall, and S. J. Zhang Phys. Rev. Lett. **91**, 107602 (2003).
[11] M. E. Manley, J. W. Lynn, D. L. Abernathy, E. D. Specht, O. Delaire, A. R. Bishop, R. Sahul, and J. D. Budai, Nat. Commun. **5**, 3683 (2014).

On Phonon Localization in Relaxors

P.M. Gehring[1], D. Parshall[1], C. Stock[2], G. Xu[3], X. Li[4], and H. Luo[4]

[1]NIST Center for Neutron Research, National Institute of Standards and Technology, 100 Bureau Drive, Gaithersburg, Maryland 20899-6100, USA
[2]School of Astronomy and Physics, University of Edinburgh, Edinburgh EH9 3JZ, United Kingdom
[3]Condensed Matter Physics and Materials Science Department, Brookhaven National Laboratory, Upton, New York 11973, USA
[4]Shanghai Institute of Ceramics, Chinese Academy of Sciences, Shanghai 201800, China

In a recent lattice dynamical study of the relaxor ferroelectric $Pb[(Mg_{0.33}Nb_{0.67})_{1-x}Ti_x]O_3$ (PMN-xPT) with Ti content x = 0.30, Manley *et al.*[1] report the observation of an unexpected, weak, phonon mode located between the transverse acoustic (TA) and soft transverse optic (TO) modes. This extra mode exhibits little or no dispersion at high temperatures, which was interpreted as evidence of phonon localization. Because the extra mode is narrow in energy, it was identified as a long-lived excitation. After cooling below Tc (~405 K) to room temperature, this "localized mode" (LM) displays a dispersion similar to that of the TA and TO modes, implying that the LM has become delocalized.

In an attempt to reproduce the results and conclusions of Manley *et al.*, we performed a standard test of the LM at 297 K using a nominally identical compound and the same neutron scattering spectrometer. This was done by measuring the same energy scan performed by Manley *et al.* at two slightly different values of the scattered neutron energy Ef. These data, measured at room temperature and a scattering vector **Q** = (2,-0.35,0), are shown in Fig. 1. At Ef = 13.7 meV the LM peak is clearly visible at 11.5 meV with a linewidth of 1.2 meV (FWHM) and an energy-integrated intensity of about 3% of that of the TO mode. These values are in excellent agreement with the results of Manley *et al*;[1] so is our finding that the LM is narrower than the TA and TO modes but comparable to the elastic incoherent energy width. At Ef = 14.7 meV, however, the LM energy softens by 0.25 meV while the integrated intensity grows over 50%. By comparison, the TA and TO modes shift ≤ 0.07 meV and increase in intensity < 2%. These results demonstrate that the purported LM is spurious, as the frequency and structure factor of any intrinsic excitation must be wavelength invariant.

We propose that the LM shown in Fig. 1 results from a simple double scattering process involving a longitudinal acoustic (LA) mode. Our analysis follows that discussed by Ronnow *et al.*,[2] who described the spurious "ghoston" peaks that are generated by neutron double scattering from elastic (Bragg) and inelastic (magnon) cross sections in $CuGeO_3$. Assuming only a cubic lattice constant a = 4.02 Å, we find that Bragg scattering from the reciprocal lattice vector $\boldsymbol{\tau}$ = (2,-4,0) can generate the LM at **Q** = (2,-0.35,0) if there exists an excitation or at least some spectral intensity at **Q** - $\boldsymbol{\tau}$ = (0,3.65,0) with energy 11.5 meV. Such an excitation corresponds to a purely longitudinal mode, and in fact the neutron studies of Swainson *et al.*[3] and Tomeno *et al.*[4] on PMN and $PbTiO_3$, respectively, report LA phonon energies that closely bracket those of the LM reported for PMN-30PT. We further note that the LA phonon branch in PMN and $PbTiO_3$ exhibits little or no dispersion for wave vectors q > 0.25 rlu, just like the LM.

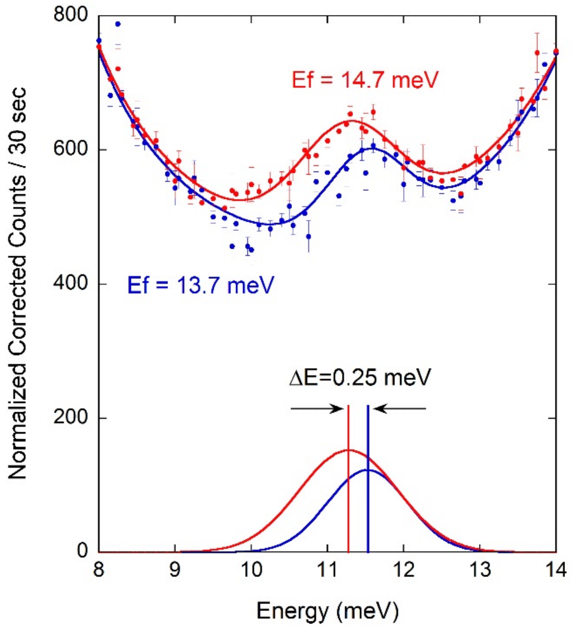

Figure 1 | LM dependence on final neutron energy Ef measured at **Q** = (2,-0.35,0) rlu and 293 K.

The Bragg + Phonon double scattering mechanism described above should exhibit a strong dependence on the out-of-plane tilt angle because the (2,-4,0) Bragg peak involved lies purely in-plane. To test this picture, the tilt dependences of the energy-integrated intensities of the LM, TA, and TO modes are plotted in Fig. 2, all of which have been normalized to one at zero tilt. These data clearly show that the LM and Bragg cross sections exhibit the same dependence on tilt, consistent with our model. By contrast the TA and TO cross sections vary much more slowly.

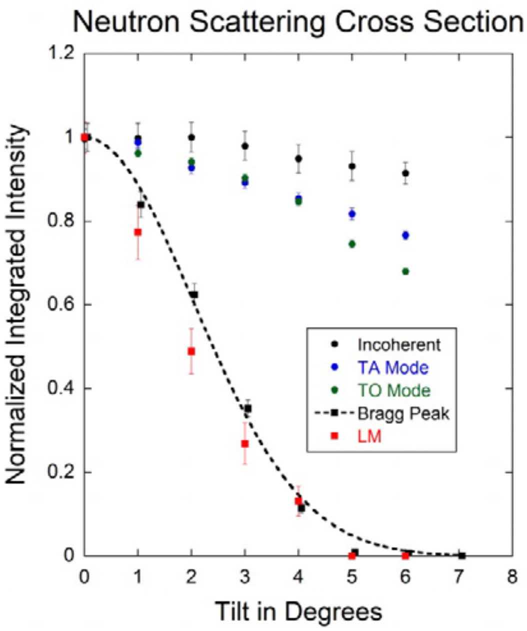

Figure 2 | Tilt dependences of the various neutron scattering cross sections

We will suggest how to extend this model to lower values of q, where the LM mode becomes dispersive below Tc.

1. Manley, M.E., Lynn, J.W., Abernathy, D.L., Specht, E.D., Delaire, O., Bishop, A.R., Sahul, R. & Budai, J.D. Phonon localization drives polar nanoregions in a relaxor ferroelectric. *Nat. Commun*. 5:3683 doi: 10.1038/ncomms4683 (2014).

2. Ronnow, H.M., Regnault, L.P. & Lorenzo, J.E. Chasing ghosts in reciprocal space – a novel inelastic neutron multiple scattering process. *Physica B* 350, 11 – 16 (2004).

3. Swainson, I.P. *et al*. Soft phonon columns on the edge of the Brillouin zone in the relaxor $PbMg_{1/3}Nb_{2/3}O_3$. *Phys. Rev. B* 79, 224301 (2009).

4. Tomeno, I., Ishii, Y., Tsunoda, Y. & Oka, K. Lattice dynamics of tetragonal $PbTiO_3$. *Phys. Rev. B* 73, 064116 (2006).

Diffuse scattering in $Sr_{0.6}Ba_{0.4}Nb_2O_6$: three faces of disorder

Alexei Bosak[1], Dmitry Chernyshov[2]

1 European Synchrotron Radiation Facility, 38043 Grenoble, France,
2 Swiss–Norwegian Beam Lines at ESRF, 38043 Grenoble, France

Solid solutions of $Sr_xBa_{1-x}Nb_2O_6$ (SBN) are uniaxial polar compounds with a tetragonal tungsten-bronze type structure, possessing relaxor properties for x≥0.6. We report the investigation of $Sr_{0.6}Ba_{0.4}Nb_2O_6$ (SBN60) single crystal by means of diffuse x-ray scattering (DS) – ID23 at ESRF, BM01A at SNBL at ESRF – complemented by the inelastic x-ray scattering (IXS) – ID28 at ESRF. The availability of data in large Q-range and in large temperature range allows us to visualize interplay between three families of diffuse objects in reciprocal space as described below.

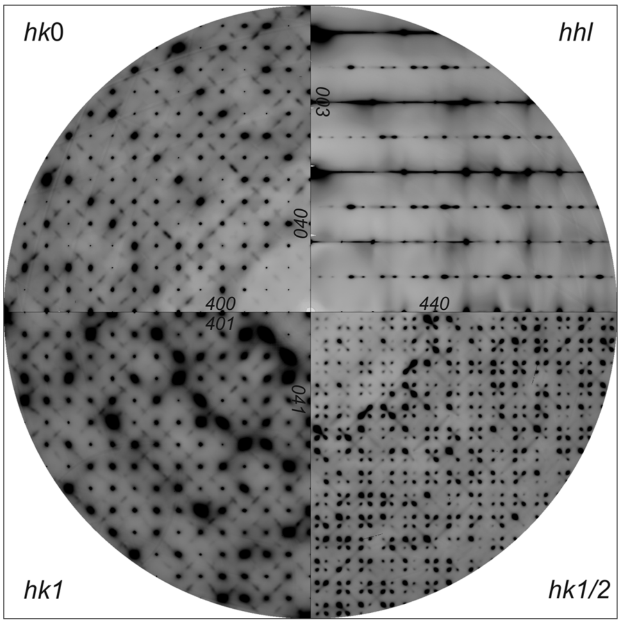

Figure 1. Reciprocal space cuts of SBN60 at 340 K. Laue symmetry applied.

As can be seen in Figure 1, diffuse scattering features with different appearance are present: **A**) compact diffuse spots with half-integer *l* previously treated as Bragg reflections due to the incommensurate modulation; **B**) pancake-like diffuse spots with integer *l*, except for *l* = 0.

In the first case the best description for the shape is found to be squared Lorentzian, while the second class of objects is better described by an anisotropic Lorentzian.

When we follow the evolution of diffuse scattering as a function of temperature, the second class appears to contain two families with very similar shape but very different temperature response. Spots like (00*l*), extensively studied with neutron scattering, and (2*h* 0 *l*) (*l* ≠ 0) acquire the maximum intensity at the temperature of the maximum of dielectric susceptibility (DS type **B1**), while the intensity around (2*h+1* 0 *l*) (*l* ≠ 0) at this temperature goes to the plateau and remains constant for nearly 100 K (DS type **B2**) before decaying together with the incommensurate modulation (DS type **A**). The most of diffuse pancakes with non-zero indices manifest mixed behavior (Figure 2).

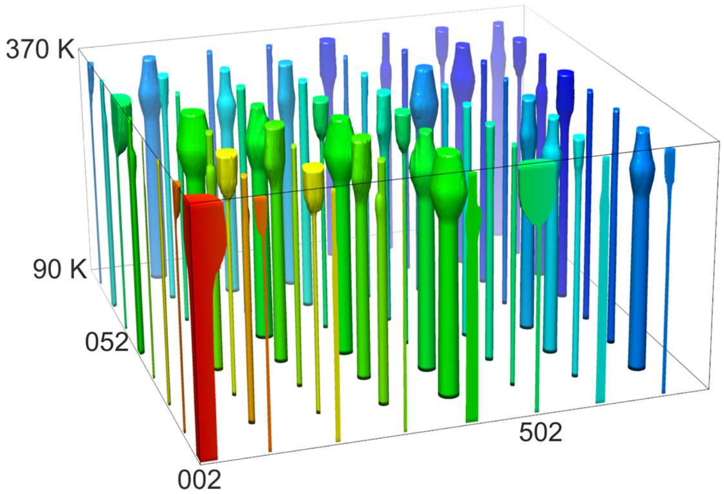

Figure 2. Temperature evolution of diffuse scattering in *hk*2 plane of SBN60. Isosurface representation, color is a function of distance to (002).

Inelastic x-ray scattering unambiguously identifies DS type **B2** as essentially elastic or quasielastic. Taking into account *hkl* selection rules, we associate **B1** component with ferroelectric-like correlated displacements of Nb, and **B2** component - with antiferroelectric-like correlated displacements of Nb, in both cases along the polar axis *c*. Temperature evolution of a number of features, when considered together, point out to the strong interplay of all three families of diffuse scattering (Figure 3). On cooling the component **A**, associated to Sr/Ba displacements, becomes visible around 800 K and then increases. For some spots this increase is rather monotonous, and for some of them step at about T_C is apparent. AFE-like component **B2** also gradually develops on cooling before being destroyed by FE-like fluctuations (**B1**) around T_C. Thus, we have observed two types of competing fluctuations, both are coupled with Sr/Ba displacements.

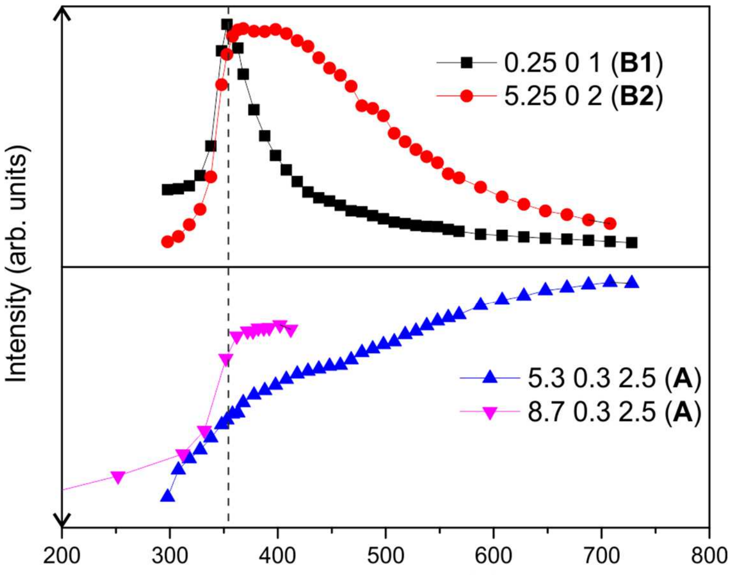

Figure 3. Temperature evolution of selected features in SBN60. Intensities are scaled for the visualization purposes.

Following questions are rising:

i) What is the structural change behind the evolution of the **A**-spots across the transition?

ii) How **B1** and **B2** components behave under DC and AC electric field?

iii) How general are our observations in SBN family?

Similarities between the structure, dynamics and dielectric properties of perovskite oxide relaxor ferroelectrics and water

Hiroyuki Takenaka[1,2], Ilya Grinberg[1,3] and Andrew M. Rappe[1]

[1]Department of Chemistry, University of Pennsylvania, Philadelphia PA, 19104
[2]Geophysical Laboratory, Carnegie Institution of Washington, Washington D.C.,
[3]Department of Chemistry, Bar-Ilan University, Ramat Gan, Israel

Relaxor ferroelectrics were first discovered in the 1960s and have been a focus of intense research due to their intriguing properties.[1] In particular the so-called butterfly shape of the diffuse scattering (DS) has been identified as the structural signature of relaxor behavior.[2] While the widely used current model of polar nanoregions (PNR) inside a non-polar matrix has been used to explain the temperature dependence of relaxor behavior observed with several experimental techniques since 1983, this model is essentially a post-hoc justification of the experimental results and has not been used predictively.

To provide a conceptual picture of the changes in the relaxor structure through the phase transitions, we have suggested an analogy between relaxors and water [3] based on the fact that the dielectric response of water shows a non-Arrhenius dispersion as well as the quadratic Lorentz dependence of the dielectric constant on temperature that are the signatures of the dielectric response of ferroelectric relaxor oxides.

The analogy between relaxors and water has become more popular recently [4-6] but has relied primarily on the similarities of the observed frequency dependence of the dielectric response. We have used molecular dynamics (MD) simulations of the classic $PbMg_{1/3}Nb_{2/3}O_3$-$PbTiO_3$ (PMN-PT) material with large supercells to elucidate the relaxor structure and dynamics. To obtain high quality DS patterns from MD, we have performed MD simulations using 64x64x64 and 72x72x72 supercells. We find that the agreement with the experimental DS is much improved for DS calculated from the trajectories of large cell simulations compared to the previous results obtained using 36x36x36 supercells, with the correct butterfly and rod shapes clearly observed for DS around the (100) and (110) spots. The good agreement with experimental DS data implies that our simulations correctly reproduce the local structure of PMN-PT.

The insights obtained from MD simulations allow us to establish the analogy between relaxors and water on a firm footing by demonstrating the similarities in the local structure and dynamics of PMN-PT and H_2O. Our MD simulations show that the relaxor transitions upon cooling from $T > T_b$ are characterized by the following features: (a) the formation of strong through-O coupling at Ti-rich sites increases the magnitude of the local Pb displacement (D_{Pb}) that serves as the local order parameter [3]; (b) a distribution of different degrees of ordering is present at all T, but shifts toward high order and slower dynamics with cooling. (c) These changes are not due to the greater extent of the correlation with cooling (growth of PNR) as thought previously. Rather, the size of the correlated region is largely unchanged from its appearance at $T=T_b$ down to low $T < T_f$, and the increased average order is due to the dramatic increase of correlations inside the region boundaries from $T > T_b$ to $T < T_f$. Examination of the literature studies of H_2O structure and dynamics shows that these features are also found in liquid water.

First, we find that the local order parameters for PMN-PT and H_2O show very similar T dependence, as shown by the comparison of $D_{Pb}(T)$ and the ^{1}H chemical shift [7] for PMN-PT and H_2O, respectively. Second, similar to PMN-PT, a correlation region of a fixed size appears in H_2O at T_b, with the correlations inside the region strengthening upon cooling. [5,8-10] Thus, for both H_2O and PMN-PT the evolution of the local structure with T can be characterized as consisting of an ordered region of a fixed size that shows increased order inside the region boundaries. This is in contrast to the picture used in previous descriptions of the evolution of PNR in relaxors where based on the classic theory of phase transition, the spatial extent of correlations was assumed to grow with cooling.

Third, despite the absence of compositional inhomogeneities on length scales larger than a few Å, both PMN-PT and H_2O contain several types of local sites that exhibit different structural and dynamic characteristics and different dynamic response properties. [8,11]

Thus, comparison of the results of our simulations with those obtained in previous studies of water shows several similarities in the local structure and dynamic response of these two seemingly very different materials. We believe that these similar features are the origin of the relaxor dielectric response observed in PMN-PT and H_2O.

References:

1) A. Bokov and Z.-G. Ye, “Recent progress in relaxor ferroelectrics with perovskite structure”, *J. Mater. Sci*. **41**, 31 (2006).
2) M. Matsuura, K. Hirota, P. M. Gehring, Z.-G. Ye, W. Chen, and G. Shirane, “Composition dependence of the diffuse scattering in the relaxor ferroelectric compound $(1-x)PbMg_{1/3}Nb_{2/3}O_3-xPbTiO_3$ $(0<x<0.40)$”, *Phys. Rev. B* **74,** 144107 (2006).
3) H. Takenaka, I. Grinberg, and A. M. Rappe, “Anisotropic Local Correlations and Dynamics in a Relaxor Ferroelectric”, *Phys. Rev. Lett*. **110**, 147602 (2013).
4) D. C. Elton and M-V. Fernández-Serra. "Polar nanoregions in water: A study of the dielectric properties of TIP4P/2005, TIP4P/2005f and TTM3F." *J. Chem. Phys.* **140,** 124504 (2014).
5) C. Zhang and G. Galli. "Dipolar correlations in liquid water." *J. Chem. Phys.* **141**, 084504 (2014)
6) D. R. Martin and D. V. Matyushov, “Dipolar Nanodomains in Protein Hydration Shells”, *J. Phys. Chem. Lett*. **6**, 407–412 (2015).
7) M. M. Hoffmann and M. S. Conradi, “Are There Hydrogen Bonds in Supercritical Water?”, *J. Am. Chem. Soc.* **119**, 3811-3817 (1997).
8) E. Guardia, I. Skarmoutsos and M. Masia, “Hydrogen Bonding and Related Properties in Liquid Water: A Car−Parrinello Molecular Dynamics Simulation Study”, *J. Phys. Chem. B* **119**, 8926−8938 (2015).
9) A. K. Soper, “The radial distribution functions of water and ice from 220 to 673 K and at pressures up to 400 MPa”, *Chem. Phys*. **258**, 121-137 (2000)
10) C. Huang, K. T. Wikfeldt, D. Nordlund, U. Bergmann, T. McQueen, J. Sellberg, L. G. M. Pettersson and A. Nilsson, “Wide-angle X-ray diffraction and molecular dynamics study of medium-range order in ambient and hot water”, *Phys. Chem. Chem. Phys*. **13**, 19997–20007 (2011).
11) P. Kumar, S. V. Buldyrev and H. E. Stanley, “A tetrahedral entropy for water”, *Proc. Nat. Acad. Sci*. **106**, 22130–22134 (2009).

From Improper Ferroelectrics to Negative Thermal Expansion – what symmetry analysis of competing crystallographic phases can tells us about dynamics

M. S. Senn,[1]

[1]*Department of Chemistry, Inorganic Chemistry Laboratory,*
University of Oxford, South Parks Road, Oxford OX1 3QR, United Kingdom

The practice of rationalising the macroscopic observable property of a material in terms of microscopic crystallographic structure is now well established. No more so than in the field of ferroelectrics where the space group alone may reveal the allowed macroscopic polarisation direction. Symmetry analysis of the ground state structure may also reveal the allowed couplings of this ferroelectricity with the magnetic and strain order parameters, and the existence of weak ferromagnetism. This approach has recently been applied to predict a new kind of ferroelectric mechanism in the Ruddlesden-Popper oxides $Ca_3B_2O_7$ (B = Mn^{4+} and Ti^{4+}) [1] leading to a renewed interest in these and related materials.

The improper ferroelectric mechanism in these materials proceeds via the coupling of two lattice instabilities (a octahedral tilt and a rotation of BO_6) to a third polar off-centre displacement.[1] I will present experimental results[2] here showing that this picture is correct to the first approximation for $Ca_3Ti_2O_7$ and that the coupling of these three modes is linear in amplitude in accordance with theoretical predictions. However, for $Ca_3Mn_2O_7$ we find a phase coexistence over a large temperature range (Figure 1) between the ferroelectric structure and a previously unreported centrosymmetric structure. These phases are not related to each other by a group-subgroup relationship and this intermediate centrosymmetric phase is at odds with the predicted nature of the phase transition of this improper ferroelectric material.

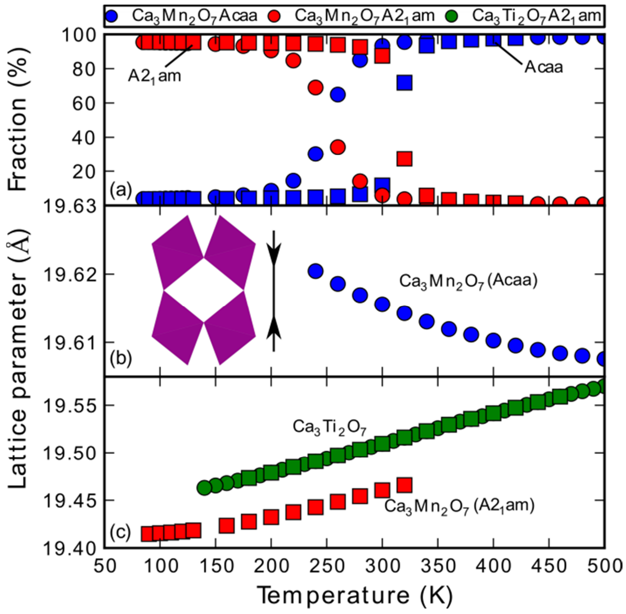

Figure 1: (*a*) phase coexistence between ferroelectric (*A2₁am*) and centrosymmetric *Acaa* phase. (*b*) NTE in *Acca* phase and (*c*) the expected positive thermal expansion in *A2₁am* phase of Ca3Ti2O7 and Ca3Mn2O7.

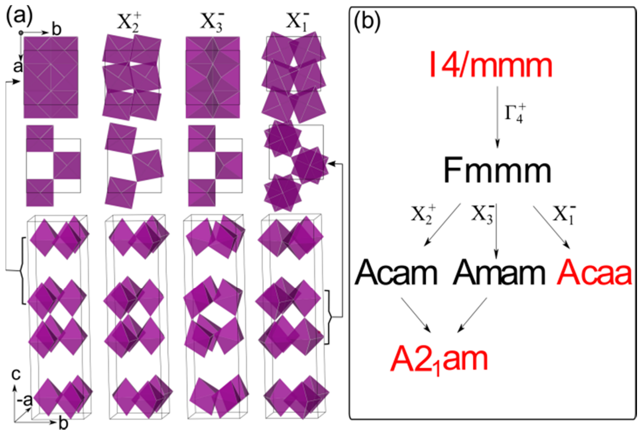

Figure 2: (a) Rotation and tilt modes for the relevant competing phases in $Ca_3Mn_2O_7$ with respect to the idealised high symmetry I4/mmm structure. (b) The ferroelectric *A2₁am* and centrosymmetric *Acaa* phase are not related to each other by a group subgroup relationship.

The competing centrosymmetric phase in $Ca_3Mn_2O_7$ is found to have pronounced uniaxial negative thermal expansion (NTE, Figure 1) over a large temperature range, representing the only sizable NTE reported in these and related perovskite materials to data. This unusual thermal expansion behaviour is not present in either the ferroelectric phases of $Ca_3Ti_2O_7$ or $Ca_3Mn_2O_7$.

Symmetry analysis of the two competing phases (Figure 2) allows us to infer the character of the soft phonon modes responsible for the NTE. This phonon mode, which represents a tilting of the MO_6 octahedra exerting a tension effect on the lattice, appears to become “trapped” in the metastable centrosymmetric phase.

I will explore in the rest of my talk how chemical control of these two closely competing phases can be used to tune their thermal expansion properties systematically, demonstrating how symmetry analysis of two closely competing phases alone can lead to a mechanistic understanding of a phenomenon which is not a ground state property but arises solely due to lattice dynamics. I will show that this approach may be more generally applied to understand the thermal expansion properties in the extended family of Ruddlesden-Popper oxides and that the engineering of closely competing phases will provide a general means to designing materials with desired thermal expansion properties.

References:

[1] N. A. Benedek and C. J. Fennie, Phys. Rev. Lett. **106**, 107204 (2011).
[2] M.S. Senn, A. Bombardi, C.A. Murray, C. Vecchini, A. Scherillo, X. Luo, and S.W. Cheong, Phys. Rev. Lett. **114**, 23 (2015).

High-temperature electromagnons in Z-type hexaferrite $(Ba_xSr_{1-x})_3Co_2Fe_{24}O_{41}$ and ferroelectric soft mode in improper ferroelectric 2H-$BaMnO_3$

Stanislav Kamba,[1] Filip Kadlec,[1] Christelle Kadlec,[1] Veronica Goian,[1] Dmitry Nuzhnyy,[1] Jakub Vít,[1] Fedir Borodavka,[1] Rujun Tang,[2] Viktor Bovtun,[1] Martin Kempa,[1] Valentin Laguta,[1] Jan Drahokoupil,[1] Josef Buršík,[3] Róbert Úhrecký,[3] Jan Prokleška,[4] and Bogdan Dabrowski[5]

[1]*Institute of Physics, Czech Academy of Sciences, Prague, Czech Republic*
[2]*Jiangsu Key Laboratory of Thin Films, Soochow University, Suzhou 215006, P. R. China*
[3]*Institute of Inorganic Chemistry, Czech Academy of Sciences, Řež, Czech Republic*
[4]*Faculty of Mathematics and Physics, Charles University, Prague, Czech Republic*
[5]*Department of Physics, Northern Illinois University, DeKalb, IL, USA*

Improper ferroelectric phase transition connected with a tripling of unit cell was discovered in hexagonal $BaMnO_3$ antiferromagnet at $T_C = 130$ K. New polar phonon activates in THz and Raman spectra below T_C due to folding of Brillouin zone. This mode has K_3 symmetry above T_C, hardens on cooling below T_C according to Cochran law and saturates near 26 cm^{-1} at 5 K.

Multiferroic $(Ba_xSr_{1-x})_3Co_2Fe_{24}O_{41}$ with Z-type hexaferrite structure also belongs to improper ferroelectrics, but here the polarization is induced by a spin order below $T_C \simeq 500$ K. We discovered one electromagnon in microwave dielectric and magnetic permeability spectra, which exhibits anomalous softening towards T_C. Second electromagnon seen in THz spectra also softens on heating, but it becomes overdamped above 250 K. Both electromagnons are active at highest temperatures observed yet and they are activated in the dielectric spectra by a dynamic magnetoelectric coupling.

In proper ferroelectrics, the phase transition parameter (PTP) is the polarization and the large dielectric anomaly observed at Curie temperature T_C is caused by softening of some polar excitation. In pseudoproper and improper ferroelectrics, the PTP is not polarization but some other quantity like antiferromagnetic order parameter, strain or phonon eigenvector with wavevector outoff Brillouin zone (BZ) center.[1,2] In this case the ferroelectric polarization arises below T_C due to coupling of the polarization with the primary PTP and usually only small dielectric anomaly appears near T_C. A question arises: Can be observed some soft mode in IR or Raman spectra near improper or pseudoproper phase transitions? If the improper ferroelectric phase transition is accompanied with multiplication of unit cell, some phonon from BZ boundary should soften around T_C. Nevertheless, in the paraelectric phase, this phonon can be studied only using inelastic neutron or X-ray scattering and only in the ferroelectric phase this phonon can become IR and Raman active. Below we will demonstrate that in two-layered hexagonal $BaMnO_3$ (abbreviated as 2H-$BaMnO_3$) the ferroelectric soft mode becomes both IR and Raman active below T_C due to tripling of unit cell in the ferroelectric phase. We will also show that electromagnons, i.e. electrically active magnons can exhibit anomalous softening around spin-induced ferroelectric phase transitions and therefore they can be responsible for a small dielectric peak at T_C. In Z-type hexaferrite $(Ba_xSr_{1-x})_3Co_2Fe_{24}O_{41}$ we even observed two electromagnons in microwave and THz regions.

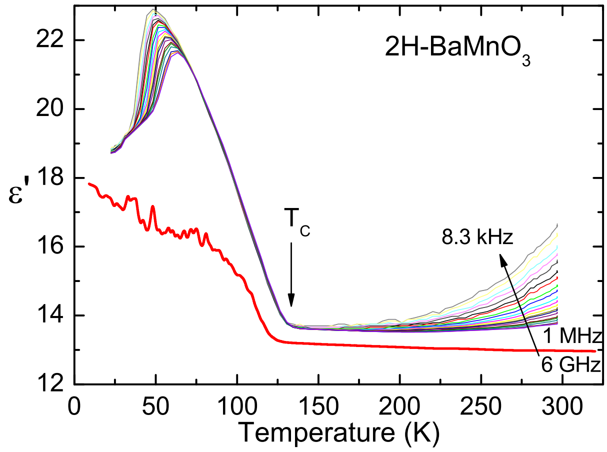

FIG. 1: Temperature dependence of dielectric permittivity in 2H-$BaMnO_3$ ceramics.

Improper ferroelectric phase transition in antiferromagnetic 2H-$BaMnO_3$ has been recently predicted from first-principles calculations[3] and $T_C = 130$ K was very recently confirmed in structural studies.[4] High-temperature $P6_3mc$ structure transforms to polar $P6_3cm$ space group and the unit cell triples at low temperatures. Antiferromagnetic order appears at 58 K.[5] We measured dielectric permittivity of 2H-$BaMnO_3$ ceramics and discovered increase of permittivity (see Fig. 1) below T_C typical for improper ferroelectrics. High-temperature dielectric dispersions is caused by Maxwell-Wagner polarization due to finite conductivity of the ceramics. Below T_C, THz and Raman spectra reveal the same new phonon, which hardens on cooling (see Fig. 2a). Above T_C, the phase transition is driven by the soft zone-boundary phonon of K_3 symmetry with $q = (1/3,1/3,0)$ which is coupled with the zone-center Γ_2^- mode.[3] Below T_C the BZ folding occurs due to tripling of unit cell and therefore the K_3 symmetry soft mode becomes zone center mode, which activates in our IR and Raman spectra and hardens on cooling. This mode is very weak in the

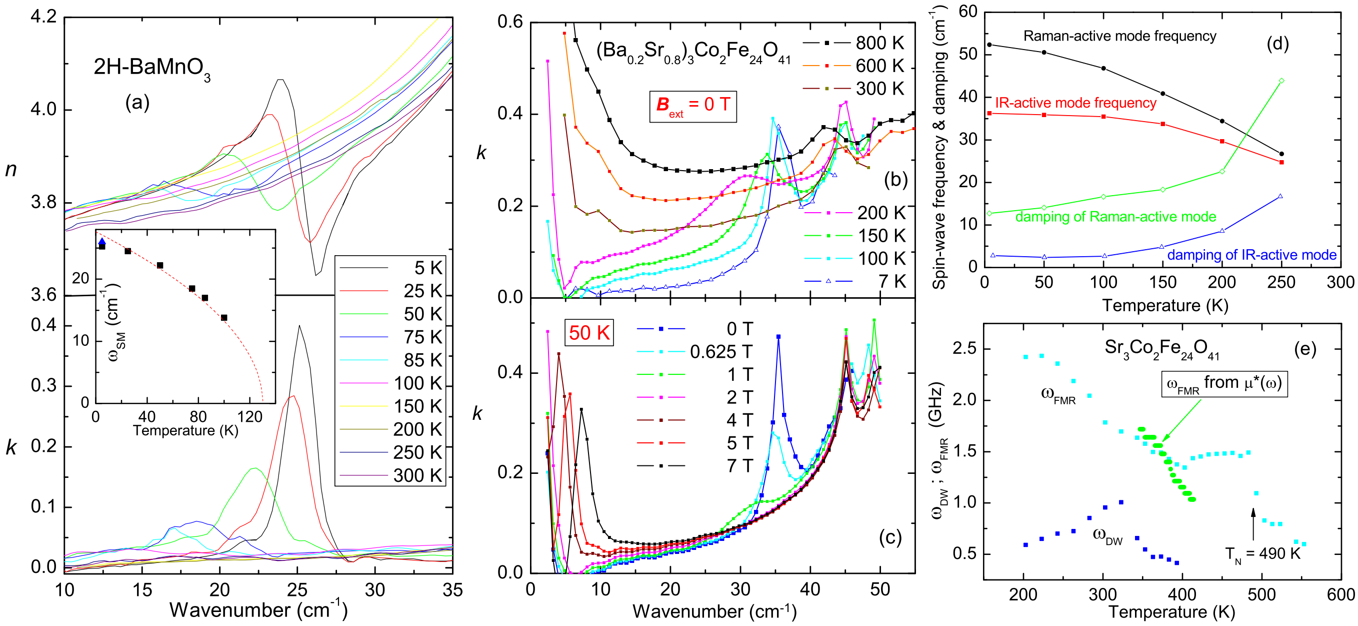

FIG. 2: (a) THz complex dielectric spectra of 2H-BaMnO$_3$ ceramics show activation of a new phonon below T$_C$ = 130 K. Temperature dependence of the soft mode frequency is seen in the inset. (b) Temperature and (c) magnetic field dependence of THz extinction coefficient of (Ba$_{0.2}$Sr$_{0.8}$)$_3$Co$_2$Fe$_{24}$O$_{41}$ ceramics. Ferrimagnetic resonance peak is seen below 10 cm^{-1} only in magnetic field above 4 T, electromagnon near 30 cm^{-1} disappears at 2 T and phonon near 45 cm^{-1} exhibits only small shift with temperature. (d) Temperature dependence of frequencies and dampings of the spin excitations observed in THz and Raman spectra of (Ba$_{0.2}$Sr$_{0.8}$)$_3$Co$_2$Fe$_{24}$O$_{41}$ ceramics. (e) Temperature dependence of resonance frequencies obtained from microwave magnetic permeability (marked by arrow) and dielectric permittivity spectra of Sr$_3$Co$_2$Fe$_{24}$O$_{41}$ ceramics. High-frequency resonance marked ω_{FMR} corresponds to a ferrimagnetic resonance, which activates in dielectric spectra due to magnetoelectric coupling. The low-frequency resonance ω_{DW} is probably frequency of domain-wall vibrations. Due to frequency and temperature limitation of our microwave instrument, ω_{FMR} seen in magnetic permeability spectra $\mu^*(\omega)$ was determined only between 350 and 415 K, but it is probably active also below and above this temperature interval.

THz spectra. Even thought its dielectric strength $\Delta\varepsilon$ increases on cooling and at 5 K $\Delta\varepsilon = 0.3$, it cannot itself explain the observed one order of magnitute larger increase of microwave and low-frequency ε' below T$_C$ = 130 K (Fig. 1). Additional dielectric relaxation must be present in the microwave region below T$_C$. This dielectric relaxation is probably caused by a ferroelectric domain walls motion. On cooling, this temperature-activated process slows down and distribution of relaxation frequencies increases. For that reason a relaxor-like dielectric dispersion is seen below 70 K in Fig. 1.

Second part of this contribution is devoted to studies of spin-induced ferroelectric (Ba$_x$Sr$_{1-x}$)$_3$Co$_2$Fe$_{24}$O$_{41}$ with Z-type hexaferrite crystal structure. Below 700 K this material is a collinear ferrimagnet and near 500 K its magnetic structure changes to transverse conical and a ferroelectric polarization arises due to inverse Dzyaloshinskii-Moriya interaction.[6] Here we discovered two kinds of electromagnons. High-frequency electromagnon seen near 30 cm^{-1} becomes underdamped below 250 K and markedly hardens on cooling (Fig. 2b,c,d). In external magnetic field this excitation softens, overdamps and disappears from THz spectra in the field 2 T (Fig. 2b,c). Ferrimagnetic resonance has also signature of electromagnon, because it is seen near 1 GHz in both microwave dielectric permittivity and magnetic permeability spectra (Fig. 2e). This electromagnon softens on heating towards T$_C$ = 500 K, below which the ferroelectric order is induced. This is the first electromagnon observed above room temperature. Moreover, this excitation shifts to THz region with external magnetic field above 4 T (Fig. 2b,c). Magnetoelectric character of the ferrimagnetic resonance was confirmed also in EPR spectra under external electric field.

This work was supported by the Czech Science Foundation, Project No. 15-08389S.

---

[1] V. Dvořák, Ferroelectrics **7**, 1 (1974).
[2] P. Tolédano, Phys. Rev. B **79**, 094416 (2009).
[3] J. Varignon and P. Ghosez, Phys. Rev. B **87**, 140403 (2013).
[4] T. N. Stanislavchuk et al., Phys. Rev. B **92**, 134308 (2015).
[5] E. Cussen and P. Battle, Chem. Mater. **12**, 831 (2000).
[6] S. H. Chun et al., Phys. Rev. Lett. **108**, 177201 (2012).

Domain Topology and Conducting Ferroelectric Walls in a Hybrid Improper Ferroelectric

F.-T. Huang[1], F. Xue[2], B. Gao[1], L. H. Wang[3], X. Luo[3], W. Cai[1], X. Lu,[4] J. M. Rondinelli[4], L. Q. Chen[2], and S.-W. Cheong[1,3*]

[1] Rutgers Center for Emergent Materials, Rutgers University, Piscataway, New Jersey 08854, USA,

[2] Department of Materials Science and Engineering, The Pennsylvania State University, University Park, Pennsylvania 16802, USA

[3] Laboratory for Pohang Emergent Materials and Max Plank POSTECH Center for Complex Phase Materials, Pohang University of Science and Technology, Pohang 790-784, Korea,

[4] Department of Materials Science and Engineering, Northwestern University, USA

Hybrid improper ferroelectricity (HIF), which describes a state with the polarization induced by a hybridization of two non-polar lattice instabilities, holds great promise toward the realization of room-temperature multiferroelectricity[1,2]. The key idea is to design new materials in which ferroelectricity and (anti)ferromagnetism can be coupled by the same lattice instability, therefore providing an indirect but strong coupling between polarization and magnetism[1]. Example compounds with HIF include the double-layered Ruddlesden-Popper (RP) perovskites with the chemical formula of $A_3B_2O_7$ (A^{2+} = alkali metal; B^{4+} = transition metal). Unexpectedly, charged ferroelectric domain walls (FE DWs), some of which are highly conducting, were also found to be mysteriously abundant in the recently discovered RP-type HIF $(Ca,Sr)_3Ti_2O_7$ crystals[3]. Head-to-head and tail-to-tail 180° FE DWs exhibit an approximately 100 times conduction difference in the conductive atomic force microscopy (c-AFM) measurements[3].

Figure 1a shows the two characteristic lattice modes in HIF $A_3B_2O_7$: the BO_6 octahedra in-phase rotations in either clockwise (sign of the rotation is +) or counterclockwise (-) about the [001] direction also denoted as $a^0a^0c^+$ in the Glazer notation or the X_2^+ mode and the BO_6 octahedral tilting about two $<100>_{orth}$ axes, i.e. apical oxygen-motions toward four directions (labeled as 1-4 quadrants) also denoted as $a^-a^-c^0$ or the X_3^- mode. Below a FE phase transition temperature, the X_3^- mode ($a^-a^-c^0$) adopts one of the four tilting directions (1-4), and the X_2^+ mode ($a^0a^0c^+$) adopts + or -, which leads to eight degenerate states (labeled as 1±, 2±, 3±, and 4± in Fig. 1a). Thus, antiphase boundaries (APBs) such as walls between state 1+ and 3- should exist in HIF $A_3B_2O_7$; however, they are hidden in the polarized optical image (POM, Fig. 1b) and the piezoresponse force microscopy measurement (PFM, Fig. 1c), which is usually a good method to map out FE domain configurations[3]. In order to unveil the origin of these abundant charged FE DWs in the HIF $(Ca,Sr)_3Ti_2O_7$, we explore the complete connectivity of DWs and domain topologies in $(Ca,Sr)_3Ti_2O_7$ single crystals, particularly with mapping of APBs using dark-field Transmission Electron Microscopy (DF-TEM). Compared with PFM, DF-TEM under systematic controlled diffraction conditions allows us to investigate domains induced directly by local structural deformations. For the first time, we discovered that there exists four possible polarization directions, each polarization state is degenerated with two antiphase domains in HIF $(Ca,Sr)_3Ti_2O_7$ crystals, and these eight structural variants form a Z_4xZ_2 domain structure with Z_3

vortices (three domains/domain walls merging at the vortex cores always). Figures 1d-f show a series of DF-TEM images demonstrating a typical Z_3 vortex pattern within a FA domain. In this talk, we will unveil the connection between the presence of charged FE DWs and the macroscopic DW connectivity/topology. Our results demonstrate the unexpectedly rich nature of hybrid improper ferroelectricity.

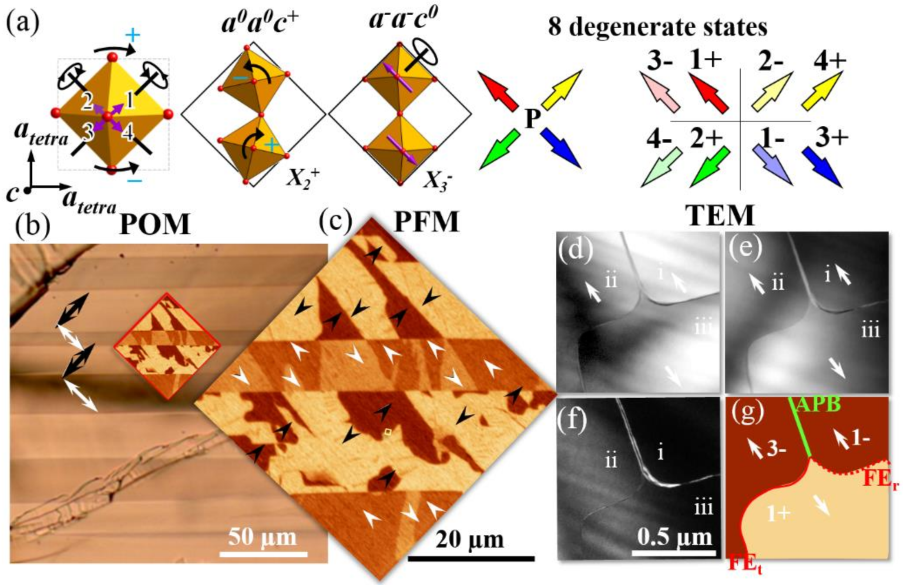

Figure 1 In-plane correlation of ferroelastic, ferroelectric and antiphase domains in $Ca_{2.46}Sr_{0.54}Ti_2O_7$ crystal. a, TiO_6 octahedra with tilting along the $<110>_{tetra}$ directions and rotation around the $[001]_{tetra}$ direction. The straight arrows with eight colors denote the eight domain variants as listed. There exist four polarization directions and two antiphase domains for each polarization direction. **b,** A POM image in 0.17 mm x 0.17 mm on the cleaved (001) plane at room temperature. White and black double arrows indicate the *a*-axes in an alternative way. **c,** The corresponding in-plane PFM image to the area in the red box in (b). The direction of spontaneous in-plane polarization were indicated by black and white arrows. **d,** A DF-TEM image taken using superlattice spots $g+ = 3/2(1, 1, 0)_{tetra}$ along [001] direction. **e,** A DF-TEM image taken using superlattice spots $g- = 3/2(-1, -1, 0)_{tetra}$. (c)-(d) were taken under two-beam conditions where the reversed contrast demonstrates the characteristic of 180^{o}-type ferroelectric domains. **f,** A DF-TEM image taken using superlattice g- spots under a larger tilting angle in order to tune contrast through enhancing excitation error. **g,** The schematic domain configuration demonstrates a typical Z_3 vortex pattern, composed of three 180^{o}-ferroelectric domains with DWs FE_r (red-dotted), FE_t (red-solid) and APB (green-solid) merging at one point. White arrows denote the polarization direction in each domain.

Ref: [1] Benedek, N. A. & Fennie, C. J. *Phys. Rev. Lett.* **106**, 107204 (2011). [2] Mulder, A. T., Benedek, N. A., Rondinelli, J. M. & Fennie, C. J. *Adv. Funct. Mater.* **23**, 4810–4820 (2013). [3] Oh, Y. S., Luo, X., Huang, F.-T., Wang, Y. & Cheong, S.-W. *Nat. Mater.* **14**, 407–413 (2015).

First-principles study of the layered oxides with hybrid improper ferroelectricity

Xue-Zeng Lu[*] and James M. Rondinelli[†]

Department of Materials Science and Engineering, Northwestern University, Evanston, IL 60208, USA

Hybrid improper ferroelectricity (HIF) was first theoretically proposed in $Ca_3B_2O_7$ (B=Mn,Ti) [1], in which the in-plane polarization is induced by the trilinear coupling among the polarization (P), oxygen octahedral rotation (Q_R) and tilt (Q_T) modes. The trilinear coupling significantly contributes to the stabilization of the polar ground state, and produces the polarization $P \propto Q_R Q_T$. Although subsequent theoretical studies report that hybrid improper ferroelectricity should exist in other n=2 Ruddlesden-Popper materials with different chemistries [2], few have been reported experimentally. Very recently the first experimental demonstration of hybrid improper ferroelectricity was reported in $Ca_3Ti_2O_7$ (CTO) [3]. The authors also showed the switchable polarization with unexpectedly low switching electric fields. Although explanations according to the simple trilinear coupling terms were presented, the model does not completely describe the switching behavior of the material.

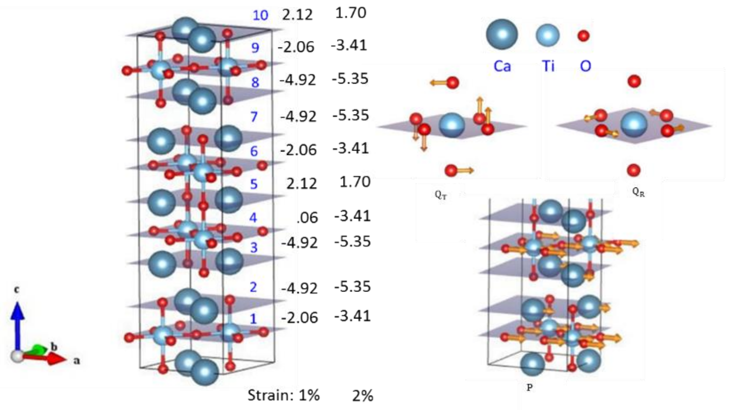

Figure 1. Left panel: reference structure with the space group of *I*4/*mmm*. Right panel: schematic illustration of in-plane [110] polarization, oxygen octahedral rotation around [001] and tilt around [110]. The values (i.e., 1, 2, 3…) in the structure indicate the layer numbers and the layer resolved polarizations in units of 10^{-2} eÅ, respectively. Layer resolved polarizations for 1% and 2% strains are shown.

Here, we investigated the CTO system by expanding the total energy using a Landau phenomenological model with order parameters for the in-plane polarization, oxygen octahedral tilt and rotation (i.e., P, Q_R and Q_T), respectively. By fitting the coefficients in the Landau model within the density functional theory (DFT) calculations, we find an accurate expansion for CTO. Fifth order terms must be included to more precisely reproduce the total energy (the error is less than 5meV per formula) and the magnitudes of the order parameters (the error is less than 3%) of the bulk system. Furthermore, we studied the strain effects on HIF by both formulating a Landau model based on thin-film boundary conditions and self-consistent DFT calculations. Here we find that the electric polarization increases with strain, upon going from -4 to 4% strain, although the amplitude of the polarization order decreases with tensile strain. We find that P increases with increasing tensile strain mainly owing to the oxygen displacements in the TiO_2 layers that align to favor the in-plane polarization (Fig. 1), which is revealed by examining the *ab* layer polarizations. Our study may gain insights into the importance of the higher order multi-mode interaction terms other than the trilinear term and be useful for the future model study in the materials with HIF.

*****xuezenglu2014@u.northwestern.edu

[†] jrondinelli@northwestern.edu

[1] N. A. Benedek & C. J. Fennie, Phys. Rev. Lett. **106**, 107204 (2011).

[2] A. T. Mulder, N. A. Benedek, J. M. Rondinelli, and C. J. Fennie, Adv. Funct. Mater. **23**, 4810-4820 (2013).

[3] Y. S. Oh, X. Luo, F.-T. Huang, Y. Zhang & S.-W. Cheong, Nature Mater. **14**, 407 (2015).

Coupling and electrical control of structural, orbital and magnetic orders in perovskites

Nicholas Bristowe

Department of Materials, Imperial College London, London SW7 2AZ, U.K.

The possibility of tuning the magnetic properties of a material with an applied electric field has recently received great interest for low energy consumption spintronic devices. In this regard, a promising route to achieve ferroelectricity in magnets is *via* the so-called hybrid improper ferroelectricity [1-4]. This concept is related to an unusual coupling of lattice modes, giving rise in the free energy expansion to a trilinear term $-\lambda P.R_1.R_2$ linking the polar mode P to two independent non-polar motions R_1 and R_2, which are typically antiferrodistortive (AFD) motions in magnetic perovskites and related materials. Recent experiments are beginning to confirm the existence of hybrid improper ferroelectrics [1,5,6], and this trilinear coupling is appearing as a practical way to achieve electrical control of non-polar AFD motions associated to the rotation of the oxygen octahedra, i.e. monitoring P with an electric field will directly and sizably tune the non-polar modes R_1 and/or R_2. The AFD modes in turn can influence spin-exchange interactions, such as the Dzyaloshinskii-Moriya interaction, and hence weak ferromagnetism, for example.

In general, however, these AFD motions are only relatively weakly coupled to the electronic properties of perovskites. It would be interesting to explore whether a similar trilinear coupling instead involving non-polar motions R_1 and R_2, that are more intimately connected to the electronic degrees of freedom. An obvious choice common to perovskites is the Jahn-Teller (JT) distortion, which traditionally manifests due to the Jahn-Teller effect in order to remove an electronic degeneracy, opening a band gap and favouring a particular orbital ordering, which in turn can affect magnetic ordering. It is interesting to note that, supposing a system was discovered whereby a $-\lambda P.R_1.R_2$ term exists and R_1 and/or R_2 has the symmetry of a JT distortion, the existence of this trilinear term could force into the system the JT distortion, even in traditionally non-JT active materials. Furthermore, this trilinear term would then allow the electrical control of JT modes, which would open novel functionalities in perovskites as it will have consequences on related electronic properties, for instance, optical and magnetic properties as well as the tuning of metal-insulator phase transitions.

This talk highlights preliminary work aimed at discovering and utilizing the coupling of P with JT distortions, through the trilinear term. Using first principles calculations and symmetry analyses the concept is demonstrated on a few different perovskite-based systems where it is shown that the coupling can strongly influence, and allow the electrical control of, the magnetic ground state [7,8] and electronic band gaps [9], for example.

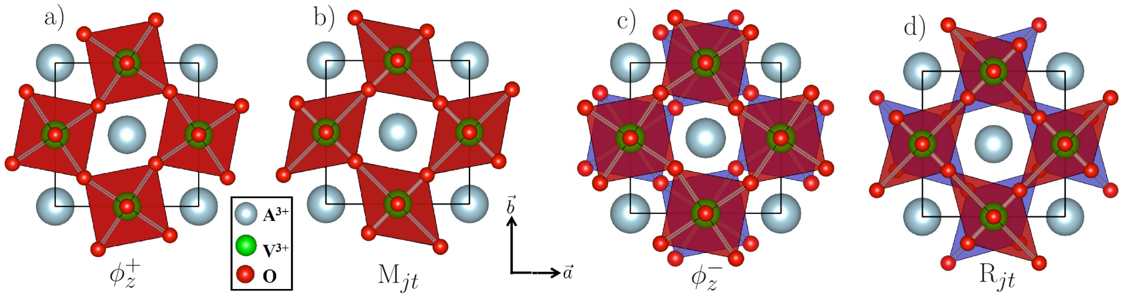

Comparison of JT and AFD motions; (**a**) in-phase ϕ_z^+ AFD motion (M_2^+ mode); (**b**) in-phase JT motion (M_3^+ mode); (**c**) anti-phase ϕ_z^- motion (R_5^- mode); (**d**) anti-phase JT motion (R_3^- mode). In the first demonstration of hybrid-improper ferroelectricity in $SrTiO_3$-$PbTiO_3$ superlattices a P. ϕ_z^+. ϕ_z^- coupling was found [1]. In vanadate superlattices a P. M_{jt}. R_{jt} trilinear term exists [8].

[1] E. Bousquet *et al.*, Nature Letters **452**, 732 (2008)
[2] T. Fukushima, A. Stroppa, S. Picozzi & J.M. Perez-Mato, Phys. Chem. Chem. Phys. **13**, 12186 (2011)
[3] N. A. Benedek & C. J. Fennie, Phys. Rev. Lett. **106**, 107204 (2011)
[4] J. Rondinelli & C. J. Fennie, Adv. Mater. **24**, 1961 (2012)
[5] M.S. Senn *et al.*, Phys. Rev. Lett. **114**, 035701 (2015)
[6] Y.S. Oh *et al.*, Nature Materials **14**, 407 (2015)
[7] N.C. Bristowe *et al.*, Nature Communications **6,** 6677 (2015)
[8] J. Varignon, N.C. Bristowe, E. Bousquet & P. Ghosez, Sci. Rep. **5**, 15364 (2015)
[9] J. Varignon, N.C. Bristowe & P. Ghosez, Phys. Rev. Lett. (accepted 2015)

Probing Magnetoelectric Heterostructures with Polarized Neutron Reflectometry

Alexander Grutter, NIST Center for Neutron Research

Direct electric field control of magnetism is among the most important goals in nanoscale magnetics research, but it is only recently that progress has been made in exploring new pathways to giant magnetoelectric coupling effects. Thus far, the most popular routes towards achieving magnetoelectric coupling have focused on heterostructures incorporating multiferroics or ferroelectrics. Although successful attempts to induce magnetoelectric behavior without multiferroicity or magnetoelasticity remain relatively rare, systems incorporating oxide/oxide or oxide/metal interfaces are promising. As with many magnetoelectric heterostructures, the magnetic response of such systems is often quite small and may be localized near the interface. Thus, it is critical to directly and unambiguously identify the magnetic response to an applied voltage and to understand the depth dependence of magnetoelectricity in these heterostructures. Polarized neutron reflectometry is an ideal tool for achieving both of these goals, and in this talk we will discuss several recent examples — voltage-controlled charge transfer at the $CaRuO_3/CaMnO_3$ interface, and voltage-induced oxygen migration at the GdO_X/Co interface.

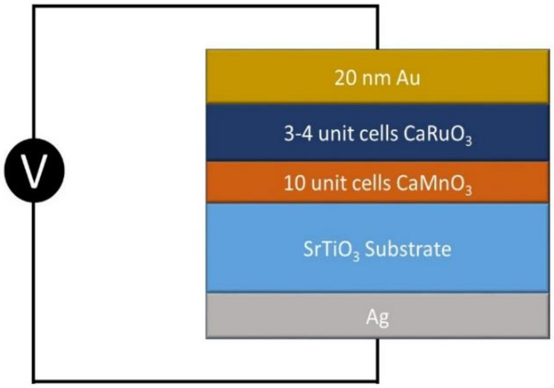

Figure 1 – Sample geometry, showing $CaRuO_3/CaMnO_3$ bilayer on a $SrTiO_3$ substrate with Au and Ag electrodes connected to a high-voltage power supply.

In the first case, we have demonstrated electric field control of ferromagnetism at the $CaRuO_3/CaMnO_3$ interface where the constituent materials are paramagnetic and antiferromagnetic in the bulk, respectively.[1-4] Due to interfacial charge transfer from the $CaRuO_3$, the interfacial Mn ions are in a canted antiferromagnetic state balanced between antiferromagnetic superexchange and ferromagnetic double exchange interactions.[1-4] Such a state is expected to be very sensitive to interfacial charge transfer and changes in carrier density, which can be modulated through electric fields. We have shown that direct electric field control of the interfacial magnetization may be achieved through the application of electric fields as small as ±8 kV/cm. We have used polarized neutron reflectometry to measure the magnetization of a single magnetic interface at 10 K as a function of applied voltage and found that a three-fold increase in magnetization can be induced. Without charge transfer, the ferromagnetic interactions are suppressed and the system becomes exclusively antiferromagnetic. In contrast, increasing the charge transfer results in a purely ferromagnetic state. Thus, we have successfully tuned the interfacial magnetic state of $CaRuO_3/CaMnO_3$ heterostructures and have demonstrated the selection of any state between fully parallel and fully antiparallel alignment of the interfacial Mn moments.

In the $CaRuO_3$/$CaMnO_3$ system, the primary challenge to overcome was the confinement of the ferromagnetic layer and magnetoelectric response to a single unit cell in the interfacial $CaMnO_3$. In consequence, the net magnetic moment was vanishingly small. Detection of the interfacial ferromagnetism, as well as the voltage induced modulation, relied on the extreme sensitivity of neutron reflectometry measurements, as well as the ability to exclude extrinsic magnetization sources such as sample contamination. Additionally, since the structure is not expected to change with the application of a bias voltage, any changes in the reflectivity may be reliably attributed to changes in the magnetization. However, in many systems magnetoelectricity is mediated through structural changes.

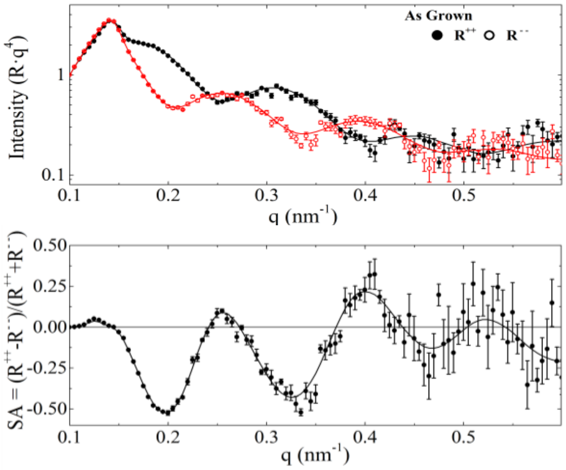

Figure 2 – Sample neutron reflectometry curve and spin asymmetry of a GdO_X/Co heterostructure

Recently, Bauer *et al.* and Bi *et al.* demonstrated stable, reversible electric field control of both magnetization and magnetic anisotropy at the interface between GdO_X and ultrathin (~1 nm) Co layers. Through heating and the application of a bias voltage, the Co layer may have its easy axis driven either into the film plane or along the film normal axis. Longer voltage and heating treatments can suppress the magnetization or cause it to recover. However, little is known about the mechanisms of oxygen transport in this system, the effects of the heat and voltage treatments on sample structure and interface quality, or the length scales over which the effect may be applied. Neutron reflectometry is ideally suited to answering such questions. Therefore, we have grown GdO_X/Co heterostructures and characterized the nuclear and magnetic depth profiles after a series of electric field and heat treatments. We find that the treatments drastically alter the interfacial structure and that the microstructure of the layers plays an important role in enabling reversible oxygen transport. Furthermore, we demonstrate that beyond a critical penetration depth, reversibility of oxygen transport into and out of the Co layer declines considerably. Despite considerable changes to the interfacial roughness and oxygen stroichiometry of the heterostructure, neutron reflectometry allows the simultaneous tracking and correlation of oxygen content with the magnetic properties of the system. Thus, we can see that neutron reflectometry is an ideal tool for the examination of a wide variety of magnetoelectric phenomena.

References

1. K. S. Takahashi et al., Applied Physics Letters 79, 1324 (2001)
2. C. He et al., Physical Review Letters 109, 197202 (2012)
3. A. J. Grutter et al., Physical Review Letters 111, 087202 (2013)
4. B. R. K. Nanda et al., Physical Review Letters 98, 216804 (2007)
5. U. Bauer et al., Nature Materials 14, 174 (2015)
6. C. Bi et al., Physical Review Letters 113, 267202 (2014)

Deterministic polarization switching in multiferroic bismuth ferrite nanoislands for magnetoelectric memories.

A.Morelli*[1], F. Johann[2], and J.M. Gregg[1]

[1]Centre of nanostructured media, School of Physics and Mathematics, Queen's University Belfast, University Road, BT7 1NN Belfast, United Kingdom
[2] Asylum Research, an Oxford Instruments company, Borsigstrasse 15a, 65205 Wiesbaden, Germany

*e-mail: alessio.morelli.pfm@gmail.com

Electric field driven magnetization switching could lead to reduction in power consumption and overheating in current nanoelectronic devices. In this regard, multiferroic magnetoelectric materials are the focus of attention, and in particular room temperature ferroelectric antiferromagnetic bismuth ferrite (BFO) is widely studied due to its unique properties[1]. It has been shown that in ferromagnetic/$(001)_p$BFO mesostructures electric field driven magnetization rotation can be achieved via an exchange bias mediated interfacial magnetoelectric effect[2,3]. In order to attain unequivocal control of magnetization in perpendicular heterostructures, deterministic ferroelastic/ferroelectric polarization switching in $(001)_p$BFO firstly needs to be achieved: to this effect investigations are currently ongoing[3,4]. However, switching procedures in thin films or mesostructures are influenced by the boundary conditions imposed on the area under investigation by the ferroelectric state of the surrounding matrix material[5]. Therefore, in order to fully understand and control such mechanism in $(001)_p$BFO, it would be desirable to study the phenomenon in free standing nanoislands.

Here we apply an ion beam milling fabrication procedure[6] to obtain BFO nanoislands out of a thin film. The switching properties are investigated by piezoresponse force microscopy (PFM). Switching is achievable in nanoislands down to 250nm diameter, with good retention properties witnessing preservation of ferroelctricity after nanostructuring. We demonstrate that deterministic switching is achievable by use of a trailing field originated by scanning a DC biased SPM probe over single nanoislands (FIG.1). In such way, while applying an out-of plane field to the structure, the in-plane polarization component can be selected, therefore being able to select between a 71°, 109° or 180° switching process.

Such degree of control on deterministic switching in BFO nanoislands will lead to BFO-based magnetoelectric multiferroic heterostructures, where magnetization can be switched by out-of plane electric field. Such investigations will yield a deeper understanding of the switching mechanism in BFO, and would eventually lead to utilization of composite multiferroics for nanoelectronic devices.

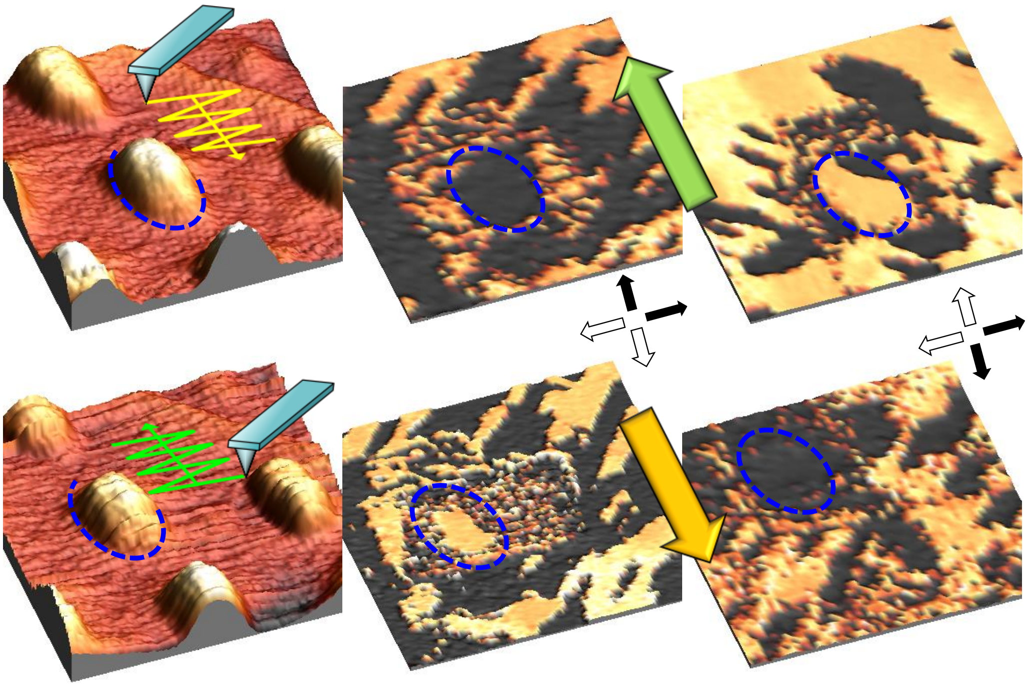

FIGURE 1: Deterministic switching in BFO nanoislands. Topography (left) showing graphically the scanning direction used while applying negative bias via the SPM probe. Lateral piezoresponse with sample tilting 0° (centre) and 90° (right), with respective in-plane polarization arrow maps, associating in-plane polarization direction with the image contrast. Arrows in between centre and right image indicate the actual in-plane polarization direction as resulting after vector PFM reconstruction. It results that it is possible to toggle the polarization direction by appropriate choice of scanning direction. Image size is 2x2µm^2.

1. Epitaxial $BiFeO_3$ multiferroic thin film heterostructures, Wang J et al., Science 299, p.1719 (2003).
2. Electric-field control of local ferromagnetism using a magnetoelectric multiferroic, Chu Y H et al., Nat. Mat 7, p.478 (2008).
3. Deterministic switching of ferromagnetism at room temperature using an electric field, Heron J T, et al., Nature 516, p.370 (2014).
4. Deterministic control of ferroelastic switching in multiferroic materials, Balke N, et al., Nat. Nan. 4, p.868 (2009).
5. Ferroelastic switching for nanoscale non-volatile magnetoelectric devices, Baek S H et al., Nat. Mater. 9, p.309 (2010).
6. Mask assisted fabrication of nanoislands of $BiFeO_3$ by ion beam milling, Morelli A et al., J. Appl. Phys. 113, p.154101 (2013).

Designing high response lead free piezoelectrics: From first principles

Valentino R. Cooper

Materials Science and Technology Division, Oak Ridge National Laboratory, Oak Ridge, TN 37830, USA

The past two decades have seen an unprecedented explosion in the use of computational methods in scientific research ranging from drug discovery to the design of new materials for electrodes in Li-ion batteries. This growth has largely been fueled by a steady increase in computational resources coupled with new algorithms that take advantage of larger, faster, massively parallelized computers. Electronic structure methods, such as density functional theory, excel at the characterization of macroscopic properties in materials that have yet to be grown. However, predicting synthesizability and operability is less straightforward. Temperature, pressure and the stability of competing phases are among the many factors that determine whether a material can be made or will exhibit favorable properties under the required operating conditions.

Here we shall review our progress towards developing an approach for designing and discovering novel functional oxides for piezoelectric applications. The focus will be on the use of first principles calculations to predict materials with *enhanced properties* that *can be synthesized* and *remain active* under device relevant conditions. The working hypothesis is that a comprehensive understanding of stability with respect to oxide impurity phases will facilitate the prediction-to-synthesis process. The standard model has been to (1) use computation to predict materials properties and then (2) to attempt to grow the most promising materials. The potential for discovering materials in this manner is great. However, materials predicted by theory/computation are often either difficult to synthesize, requiring extreme conditions such as high temperatures and pressures, or are simply unstable and thus segregate into secondary phases. Experimental feedback can be used to train the computational sets, but this is time consuming and can even be quite expensive. A third cornerstone of the prediction-to-synthesis triangle should therefore include a theoretical assessment of the phase stability of predicted materials. Identification of the energetics of competing phases with different structures and stoichiometries will

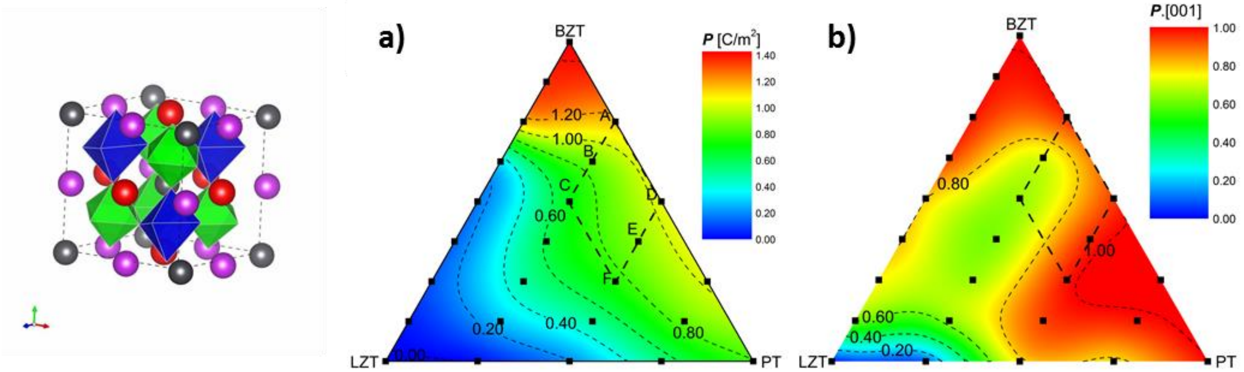

Figure 1(left) Atomic arrangement for a 3BiZnTiO$_3$-3LaZnTiO$_3$-2PbTiO$_3$ (BZT-LZT-PT) supercell. Green and blue polyhedra denote Ti and Zn octahedra, respectively. Pink, red and black atoms represent Bi, La and Pb, respectively. (right) BZT-LZT-PT ternary diagrams for (a) |P| and (b) P·[001]. For the P·[001] ternary diagram, the red, yellow and green regions indicate areas that are tetragonal, monoclinic and rhombohedral, respectively. The blue regions have little or no polarization. Black squares denote the compositions modeled. The dashed diamond defines the predicted optimal piezoelectric.

not only give a clear understanding of which structure is the ground state, but may give insight into which routes need to be taken to prepare the desired material. Similarly, understanding phase transition or critical temperatures speak to the usefulness of a material under device relevant conditions. Together, this has the potential for reducing the steps needed to get from property predictions to experimental realization. Unfortunately, an understanding of the complex energy landscape of many materials remains elusive and one of the great challenges in theoretical condensed matter physics today.[1]

In this presentation, I will present example studies that integrate properties prediction, experimental validation and phase stability to develop and build upon chemical concepts to design new materials with enhanced properties, in the context of ferroelectrics and piezoelectrics. In particular, I will examine our efforts to map out the phase diagram of a Bi based oxide solid solution in order to identify the presence of a morphotropic phase boundary (a possible region of high piezoelectric response) that may be favorable for experimental synthesis (see Fig.).[2,3] Naturally, I will discuss the use and development of techniques to treat chemical disorder,[4] relative stability of competing phases[3] and ferroelectric phase transitions.[5] Also, I will discuss our efforts to understand the enhanced piezoelectric response observed in strained $BiFeO_3$ thin films. Ultimately, we intend to develop a framework through which solid solutions of oxides can be routinely studied to give experimentally realizable predictions. Research was sponsored by the US DOE, Office of Science, BES, MSED and Early Career Research Programs.

[1] Woodley, S. M. & Catlow, R. "Crystal structure prediction from first principles", *Nat Mater* **7**, 937-946, (2008)

[2] Cooper, V. R., Henry, A. S., Takagi, S. & Singh, D. J. "First principles prediction of a morphotropic phase boundary in the $Bi(Zn_{1/2}Ti_{1/2})O_3$-$(Bi_{1/2}Sr_{1/2})(Zn_{1/2}Nb_{1/2})O_3$ alloy", *Appl. Phys. Lett.* **98**, 122903, (2011)

[3] Cooper, V. R., Morris, J. R., Takagi, S. & Singh, D. J. "La-driven morphotropic phase boundary in the $Bi(Zn_{1/2}Ti_{1/2})O_3$ - $La(Zn_{1/2}Ti_{1/2})O_3$-$PbTiO_3$ solid solution", *Mater. Chem.* **24**, 4477 (2012)

[4] Voas, B. K. *et al.* "Special quasirandom structures to study the $(K_{0.5}Na_{0.5})NbO_3$ random alloy", *Phys. Rev. B* **90**, 024105 (2014)

[5] Grinberg, I. & Rappe, A. M. Nonmonotonic "T_C Trends in Bi-Based Ferroelectric Perovskite Solid Solutions", *Phys. Rev. Lett.* **98**, 037603, (2007)

First-principles prediction of supertetragonal phases in perovskite oxide films: the case of $BiMnO_3$

O. Diéguez[(a)] and J. Íñiguez[(b)]

[(a)] *Department of Materials Science and Engineering, Faculty of Engineering,*
and The Sackler Center for Computational Molecular and Materials Science,
Tel Aviv University, IL-69978 Tel Aviv, Israel

[(b)] *Materials Research and Technology Department, Luxembourg Institute of Science and Technology (LIST), 5 avenue des Hauts-Fourneaux, L-4362 Esch/Alzette, Luxembourg*

Béa and collaborators[1] reported in 2009 the ferroelectric switching of $BiFeO_3$ films with giant axial ratio ($c/a = 1.23$) and monoclinic symmetry grown by pulsed laser deposition on $LaAlO_3$. First-principles studies had anticipated that similar $BiFeO_3$ structures might exist[2-4]. Although some of these films have monoclinic symmetry and some have tetragonal symmetry, they are often called *supertetragonal* because they are similar. Other synthesized supertetragonal materials are $PbVO_3$[5], $BiCoO_3$[6], and Bi_2ZnTiO_6[7]. Before these works, a first-principles study by Íñiguez, Vanderbilt, and Bellaiche predicted large c/a ratios for some phases of $BiScO_3$ and $BiYO_3$[8]. Supertetragonal perovskite oxides have the largest dielectric polarizations known, above 100 μC/cm^2.

In this talk I will report our first-principles calculations prediction that $BiMnO_3$ should also display a supertetragonal structure when grown on a substrate of lattice constant similar to that of $YAlO_3$. Bulk $BiMnO_3$ and bulk $BiFeO_3$ are very different—the former is a paraelectric ferromagnet, while the latter is a ferroelectric antiferromagnet. However, our results show that as compressed or strained epitaxial films these materials show similar properties.

We optimized bulk $BiMnO_3$ structures derived from metastable phases that appear in bulk $BiFeO_3$[9]. Several of these are also local minima of the bulk $BiMnO_3$ energy surface. The supertetragonal ones are likely to be stable if grown as films in compressive strains, as it happens for $BiFeO_3$. At tensile strains, our calculations predict that $BiMnO_3$ crystalizes in a phase akin to that of $BiFeO_3$ under similar conditions or in bulk. These epitaxial phases show polarizations of around 100 μC/cm^2 and and they are antiferromagnetic (with ferromagnetic ordering in plane). Some of their properties are shown in the Figure below; a particularity of the supertetragonal $BiMnO_3$ films is that their band gap is smaller than in most perovskite oxides. More information about our calculations is given in Ref. [10].

References:

[1] H. Béa, B. Dupé, S. Fusil, R. Mattana, E. Jacquet, B. Warot-Fonrose, F. Wilhelm, *et al.*, *Evidence for Room-Temperature Multiferroicity in a Compound with a Giant Axial Ratio*, Physical Review Letters **102** 217603 (2009).

[2] C. Ederer and N.A. Spaldin, *Effect of Epitaxial Strain on the Spontaneous Polarization of Thin Film Ferroelectrics*, Physical Review Letters **95**, 257601 (2005).

[3] P. Ravindran, R. Vidya, A. Kjekshus, H. Fjellvåg, and O. Eriksson, *Theoretical Investigation of Magnetoelectric Behavior in* $BiFeO_3$, Physical Review B **74** 224412 (2006).

[4] D. Ricinschi, K.-Y. Yun, and M. Okuyama, *A Mechanism for the 150* $\mu C/cm^2$ *Polarization of* $BiFeO_3$ *Films Based on First-Principles Calculations and New Structural Data*, Journal of Physics: Condensed Matter **18**, L97 (2006).

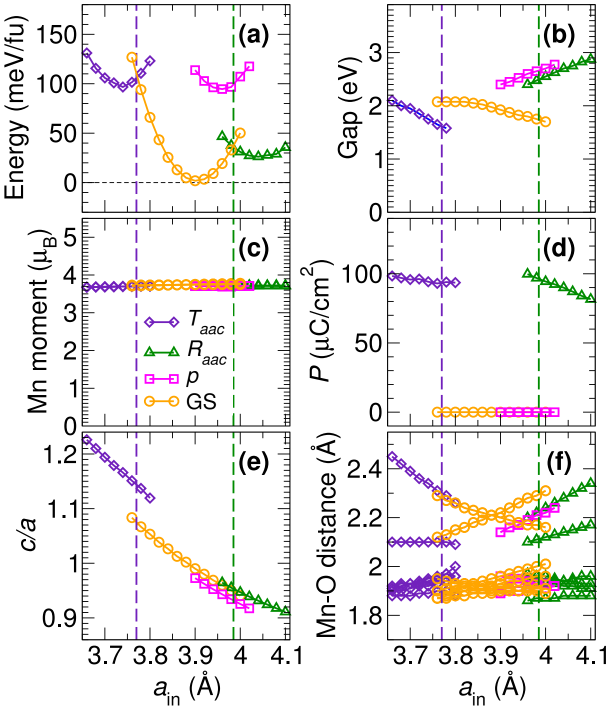

Figure 1: Properties of $BiMnO_3$ films as a function of the in-plane lattice parameter: (a) energy relative to the bulk ground state; (b) band gap; (c) magnetic moment of the Mn ions; (d) magnitude of the total macroscopic polarization; (e) c/a ratio; and (f) Mn–O distances. The four structures mentioned in the legend of (c) have been considered in their favored magnetic ordering (FM for GS and A-AFM for the rest). The phase labeled as T_{aac} is supertetragonal with space group Cc; phase R_{aac} is similar to that of bulk $BiFeO_3$, but also with space group Cc; the p phase is paraelectric with $Pnma$ space group, a phase that shows up in many perovskite oxides and it is stable in $BiFeO_3$ and $BiMnO_3$ at high pressures; GS labels a phase similar to the ground state of bulk $BiMnO_3$, but slightly distorted to match the substrate.

[5] R.V. Shpanchenko, V.V. Chernaya, A.A. Tsirlin, P.S. Chizhov, D.E. Sklovsky, E.V. Antipov, E.P. Khlybov, *et al.*. *Synthesis, Structure, and Properties of New Perovskite* $PbVO_3$, Chemistry of Materials **16** 3267 (2004).

[6] A.A. Belik, S. Iikubo, K. Kodama, N. Igawa, S. Shamoto, S. Niitaka, M. Azuma, *et al.*, *Neutron Powder Diffraction Study on the Crystal and Magnetic Structures of* $BiCoO_3$, Chemistry of Materials **18**, 798 (2006).

[7] M.R. Suchomel, A.M. Fogg, M. Allix, H. Niu, J.B. Claridge, and M.J. Rosseinsky, Bi_2ZnTiO_6*: A Lead-Free Closed-Shell Polar Perovskite with a Calculated Ionic Polarization of 150* $\mu C/cm^2$, Chemistry of Materials **18**, 4987 (2006).

[8] J. Íñiguez, D. Vanderbilt, and L. Bellaiche, *First-Principles Study of* $(BiScO_3)_{1-x}$-$(PbTiO_3)_x$ *Piezoelectric Alloys*, Physical Review B **67**, 224107 (2003).

[9] O. Diéguez, O.E. González-Vázquez, J.C. Wojdeł, and J. Íñiguez, *First-Principles Predictions of Low-Energy Phases of Multiferroic BiFeO3*, Physical Review B **83**, 094105 (2011).

[10] O. Diéguez, and J. Íñiguez, *Epitaxial Phases of* $BiMnO_3$ *from First Principles*, Physical Review B **91**, 184113 (2015).

First-Principles Calculations of Electric Field Induced Ferroelectric Phase Transition in $AgNbO_3$

Hiroki MORIWAKE[1], Ayako KONISHI[1], Takafumi OGAWA[1], Craig A. J. FISHER[1],
Akihide KUWABARA[1], Desheng FU [2]

[1] Nanostructures Research Laboratory, Japan Fine Ceramics Center, Nagoya, Aichi, JAPAN
[2] Department of Electronics & Materials Sciences, Shizuoka University, Hamamatsu, 432-8561, JAPAN

Silver niobate, $AgNbO_3$, and related materials are attracting attention as parent phases for developing lead-free piezoelectric materials to replace lead zirconate titanate (PZT). Soon after the discovery of ferroelectric behavior in $AgNbO_3$ at room temperature, well-controlled stoichiometric ceramic samples were synthesized and characterized, and it was found that this compound exhibits a large polarization of 52 $\mu C/cm^2$ with a large electric field induced strain under a high electric field of 220 KV/cm.[1] However, the precise structure of the ferroelectric phase and thus the origin of its ferroelectricity is still not well understood. In this study, a possible electric field induced ferroelectric phase transition in $AgNbO_3$ is examined using detailed first-principles calculations of the structural changes and stabilities of different phases of this compound. As shown in Fig.1, our calculations reveal that under an electric field of 9 MV/cm along b-axis, the symmetry of the $AgNbO_3$ crystal switches from antiferroelectric *Pbcm* to ferroelectric $Pmc2_1$. (Fig.2) The calculated spontaneous polarization (0.61 C/m^2) under this field compares well with the experimental value of 0.52 C/m^2. After transforming, the structure remains in the ferroelectric state even after the electric field is removed, although energetically the structure is metastable. As shown in Fig.3, the energy difference between the antiferroelectric *Pbcm* and ferroelectric $Pmc2_1$ phases is only +0.5 meV/f.u. and at 40 meV/f.u. the potential energy barrier between them is comparable to thermal fluctuation energies, it is possible for these two phases to coexist at temperatures well below the paraeletric-antiferroelectric transition temperature (~626 K). Coexistence of the two phases can explain the experimentally observed polarization–electric field hysteresis loop better than either phase on its own.

.

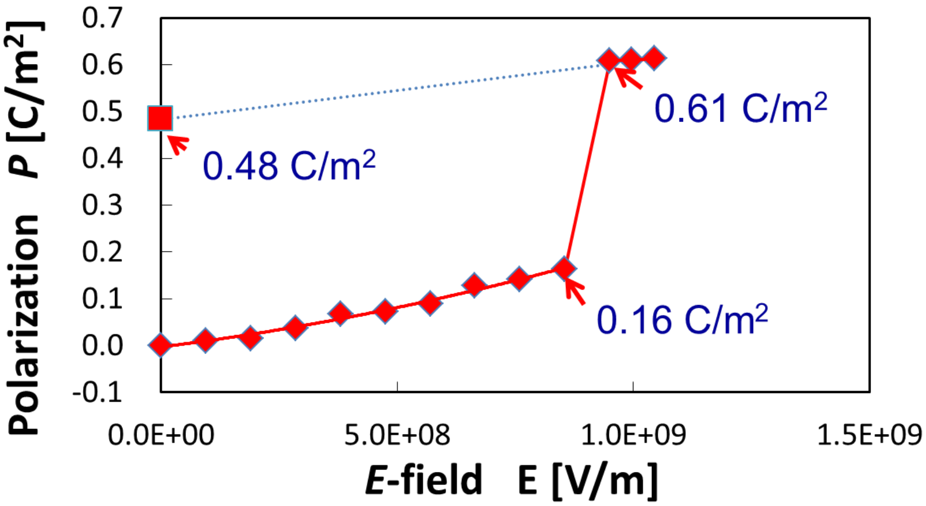

Fig. 1 Polarization change under electric field along b-axis. Under an electric field of 9 MV/cm along b-axis, the symmetry of the $AgNbO_3$ crystal switches from antiferroelectric *Pbcm* to ferroelectric $Pmc2_1$.

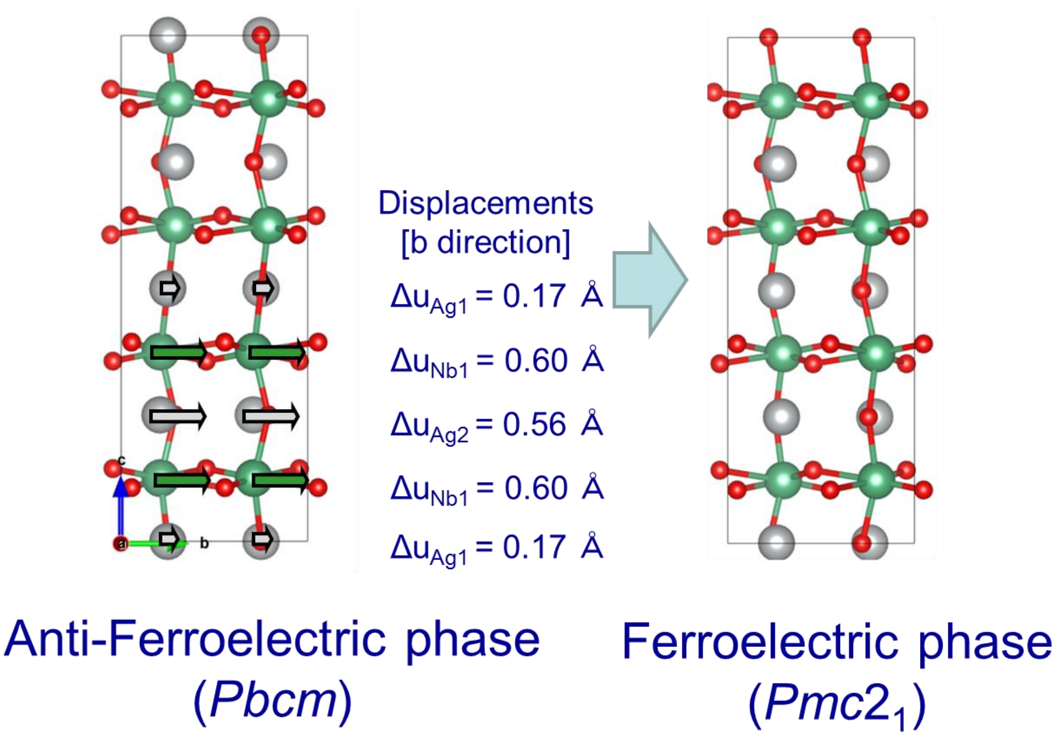

Fig. 2 Crystal structures of $AgNbO_3$: antiferroelectric *Pbcm* phase and ferroelectric *Pmc*2_1 phase. The atomic displacements under an electric field are shown. Displacement of the ions by electric field induced phase transition reduces the symmetry from *Pbcm* to *Pmc*2_1.

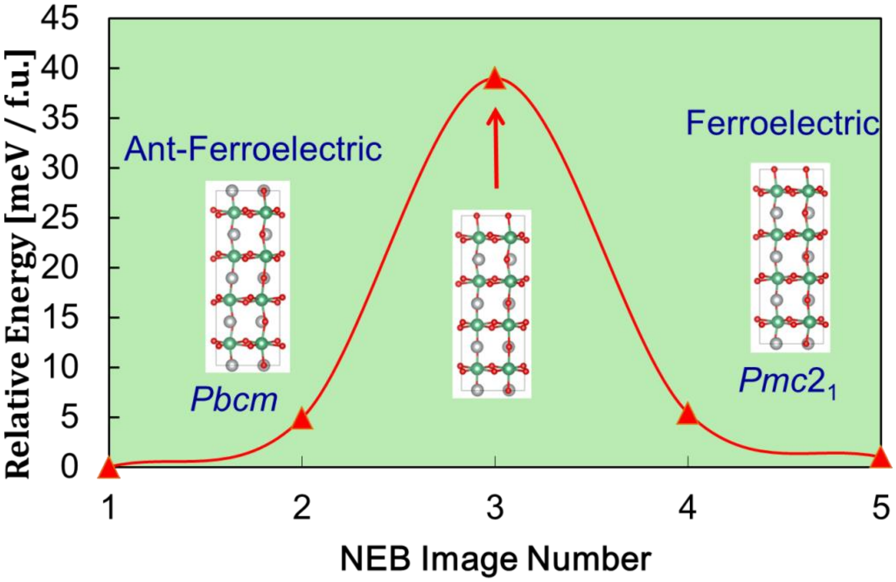

Fig. 3 Potential surface experienced by $AgNbO_3$ during the ferroelectric phase transition from *Pbcm* to *Pmc*2_1 under a finite electric field.

References

[1] D. Fu, M. Endo, H. Taniguchi, T. Taniyama, and M. Itoh: Appl. Phys. Lett. 90 (2007) 252907.

Record-High Ferroelectric Polarization by Spins and Non-Reciprocal Directional Dichroism in $BiFeO_3$

Jun Hee Lee
Ulsan National Institute of Science & Technology, Ulsan, Korea

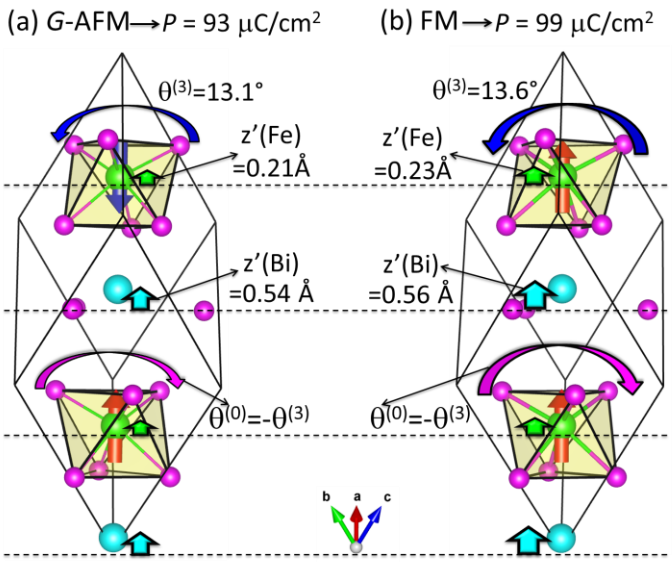

Fig 1. Huge spin-driven ferroelectric polarization and antiferrodistortive rotation by comparing ferromagnetic **(a)** and antiferromagnetic **(b)** ordering from first principles.

Intrinsic measurements such as neutron scattering and Terahertz-spectroscopy are powerful tools to uncover all the hidden couplings of the order parameters such as spin, polarization, and lattice and consequent multiferroicity. In particular, measurements combined with first-principles calculations and spin models display synergic capabilities to understand microscopic origins of the strong couplings and subsequent phenomena.

First, as a representative case for revealing hidden multiferrocities with neutron, we show record-high spin-driven ferroelectric polarizations in a type-*I* multiferroic $BiFeO_3$. Although $BiFeO_3$ is one of the most investigated multiferroics, its magnetoelectric couplings are barely understood on an atomic level. By combining a first-principles approach with a spin-cycloid model, we report hidden but huge spin-driven polarizations at room temperature in bulk $BiFeO_3$ as in Fig. 1. One of the ferroelectric polarizations reaches ~3.0 μC/cm², which is larger than any other spin-driven polarization in a bulk material by one order of magnitude

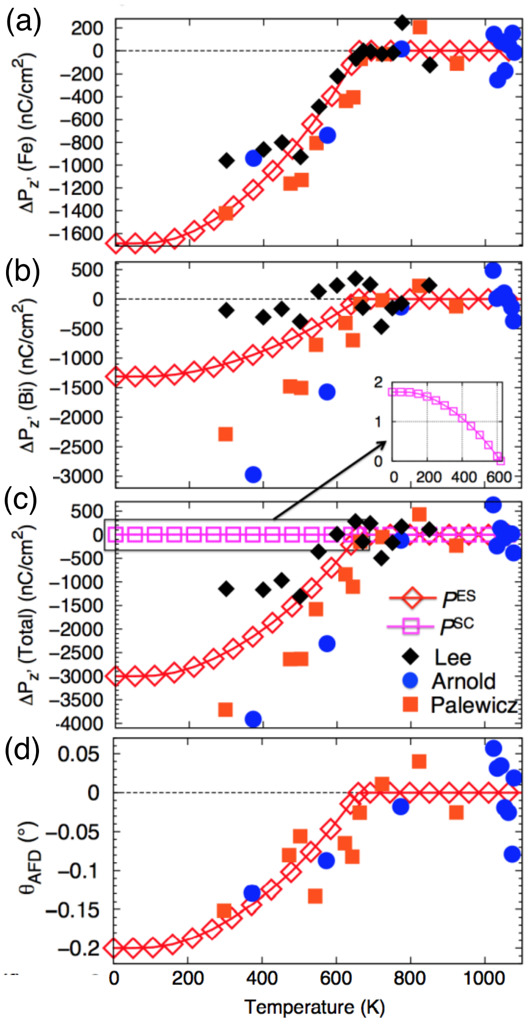

Fig 2. Spin-driven ferroelectric polarizations by **(a)**Fe **(b)**Bi **(c)**Fe+Bi **(d)**oxygen from first principles (lines) and elastic neutron scattering (dots).

[1] as shown with our results (lines) compared to elastic neutron scattering (dots) in Fig. 2. The broken inversion symmetries of the *R*3c $BiFeO_3$ induce the strong response of the magnetic interactions to an electric field and are responsible for the associated huge spin-driven polarizations. This neutron study rekindles the investigation of hidden spin-driven ferroelectric polarizations in various type-*I* multiferroics including $YMnO_3$ and $BiMnO_3$, as well as $BiFeO_3$, whose macroscopic magneto-capacitance measurements are critically limited.

Second, we show strong THz non-reciprocal directional dichroism induced by the spin-driven polarizations in bulk $BiFeO_3$. The broken inversion symmetries of the *R*3c structure are responsible for the huge spin-driven polarizations and subsequent uni-directional light propagation at room temperature. Beyond the spin-current polarization governed by the inverse Dzyaloshinskii-Moriya interaction, various spin-current polarizations derived from both ferroelectric and antiferrodistortive distortions cooperatively produce the strong non-reciprocal directional dichroism (Fig. 3) or the asymmetry in the absorption of counter-propagating light in $BiFeO_3$ [2]. Our systematic approach can be generally applied to any multiferroic material, laying the foundation for exploiting optical magnetoelectric effects in the next generation of technological devices such as optical diodes [3,4].

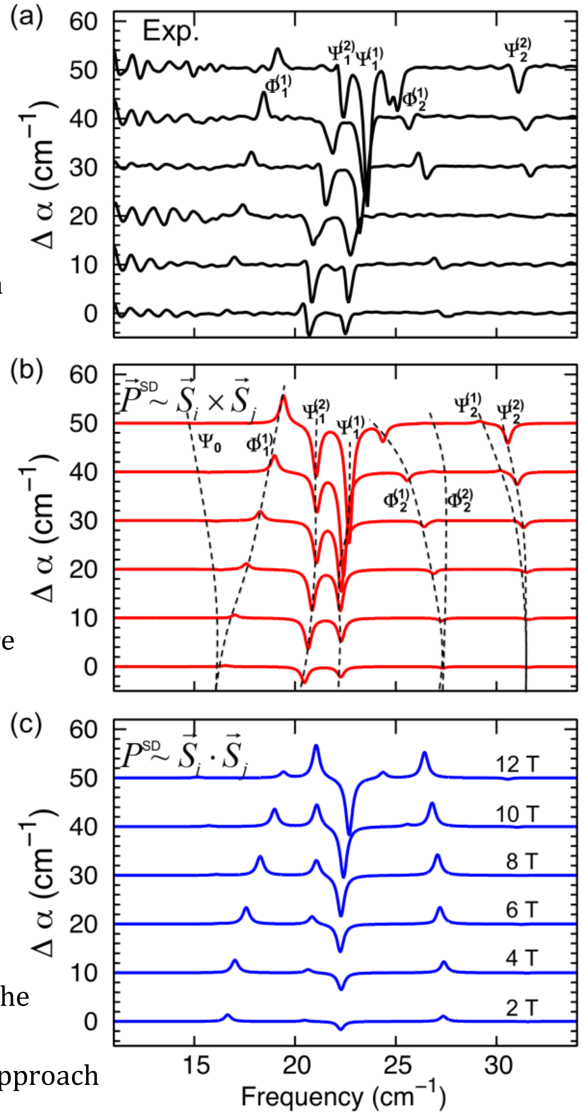

Fig 3. (a) The experimental non-reciprocal directional dichroism (NDD, $\Delta\alpha$) with static magnetic field from 2 to 12 T and oscillating electric field along [1,-1, 0]. The predicted NDD using spin-current **(b)** and exchange-striction **(c)** polarizations. All the parameters for spin-driven polarizations are calculated from first principles.

[1] **J. H. Lee*** and R. Fishman, **Physical Review Letters** 115, 207203 (2015).

[2] R. Fishman, **J. H. Lee***, *et al.*, **Physical Review B** 92, 094422 (2015).

[3] I. Kezsmarki, U. Nagel, S. Bordacs, R. S. Fishman, **J. H. Lee*** *et al.*, **Physical Review Letters** 115, 127203 (2015)

[4] **J. H. Lee*** and R. Fishman (In review by **New Journal of Physics**).

* These works have been collaborated with R. Fishman (ORNL), I. Kezsmarki (Budapest), U. Nagel, T. Room (Tallinn), and S.-W.Cheong (Rutgers).

High-throughput first principles search for new ferroelectrics

Kevin F. Garrity*
Material Measurement Laboratory, National Institute of Standards and Technology, Gaithersburg MD, 20899

(Dated: December 3, 2015)

There has been increasing interest in recent years in discovering both new ferroelectric materials and new mechanisms for creating switchable polar displacements[1–7]. Recently discovered ferroelectrics have already displayed a variety of interesting behaviors that are rare in well-studied perovskite ferroelectrics, including multiferroelectricity, hyperferroelectricity, semiconducting band gaps, etc. Furthermore, new ferroelectrics may allow for interfacing ferroelectricity with new compounds. In this work, we perform a high-throughout first principles search of the inorganic crystal structure database (ICSD) for new ferroelectrics. We find that the ICSD, which consists of experimentally determined atomic positions and unit cells, contains many previously synthesized materials which fulfill our requirements as candidate ferroelectrics.

To identify ferroelectrics, we look for materials which are a) insulating, b) have a polar ground state, and c) have a higher symmetry reference structure that is close in energy to the polar structure, which we take as an indication the material is likely to be switchable in an external electric field (see Fig. 1 for examples). Our search consists of two main strategies. The first is to start with a known non-polar structure and to look for previously unrecognized energy-lowering polar distortions. We do this in steps by first performing a Γ-point phonon calculation and looking for unstable polar modes. For materials with such an instability, we then search for the ground state structure by performing a full phonon calculation, freezing in combinations of unstable modes, and relaxing. If the lowest energy structure is polar, the material is a candidate ferroelectric. The second search strategy consists of starting with a known polar material and using symmetry analysis to identify possible related higher-symmetry structures. We then calculate the energy difference between the polar and new structure, and if the difference is small, the material is likely switchable.

As shown in table I, both of our search strategies have produced several candidate structures with

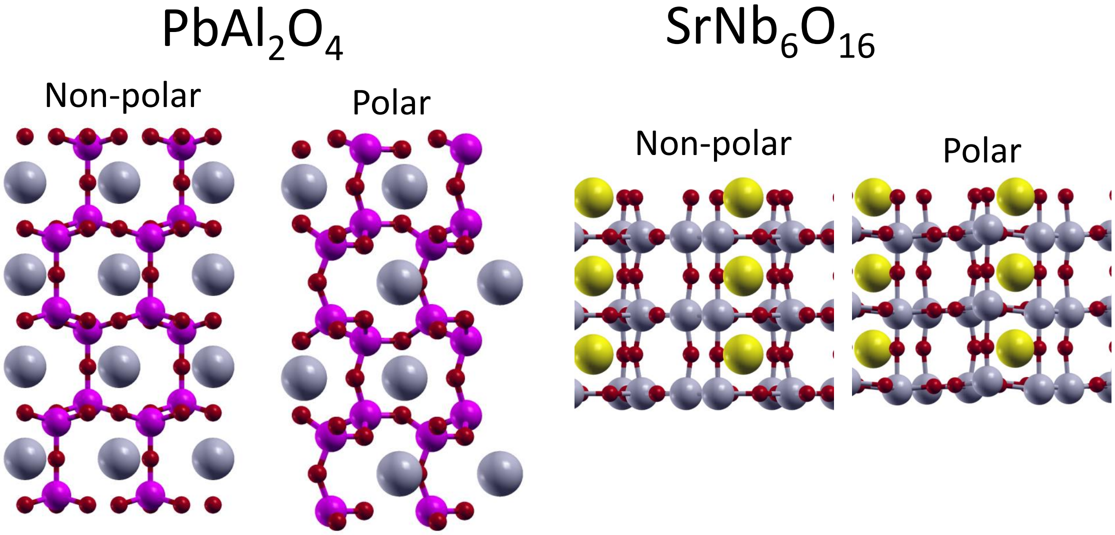

FIG. 1: Polar and non-polar structures of $PbAl_2O_4$ (left) and $SrNb_6O_{16}$ (right). The large atoms are Pb/Sr, the medium atoms are Al/Nb, and the smallest atoms are O.

Composition	High Sym. Space Grp.	Polar Space Grp.	Energy Diff. (meV/atom)	Polarization C/m^2
$SrNb_6O_{16}$	38	8	5.5	0.07
$NaNb_6O_{16}F$	38	5	9.5	0.06
$RbCa_2Nb_3O_{10}$	123	7	46.6	0.23
$BaBi_2Ta_2O_9$	139	4	15.7	–
$LiScAs_2O_7$	5	1	1.6	0.07
YSF	194	186	11	0.01
$CuBiW_2O_8$	2	1	0.3	0.06
$PbGa_2O_4$	190	40	108	0.23
$PbAl_2O_4$	190	40	75	–
LiV_2O_5	59	31	0.4	0.09
$NaVO_2F_2$	11	4	0.3	0.18
SbW_2O_6	14	4	4.4	0.21
V_2MoO_8	65	35	83.8	1.08
Zn_2BrN	64	33	1.3	0.014
Zn_2ClN	62	33	2.4	0.015
$AlAgO_2$	62	33	71	0.002

TABLE I: Data on candidate ferroelectrics, found by starting from high symmetry (top) and low symmetry (bottom) structures. The second and third columns are space groups of the high and low symmetry structures, column four is the energy difference in meV/atom, and the last column is the polarization in C/m^2.

energy differences which are in the range of known switchable ferroelectrics like $PbTiO_3$ (≈20 meV/atom) and $Ca_3Ti_2O_7$ (≈100 meV/atom), indicating that they may be switchable. In addition, we find a variety of interesting behaviors, the analysis of which is ongoing. These behaviors include possible hyperferroelectrics, weak ferroelectrics, multiferroics, and materials with large polarization.

---

[*] Electronic address: `kevin.garrity@nist.gov`

[1] J. W. Bennett, K. F. Garrity, K. M. Rabe, and D. Vanderbilt, Phys. Rev. Lett. **109**, 167602 (2012).

[2] J. W. Bennett, K. F. Garrity, K. M. Rabe, and D. Vanderbilt, Phys. Rev. Lett. **110**, 017603 (2013).

[3] K. F. Garrity, K. M. Rabe, and D. Vanderbilt, Phys. Rev. Lett. **112**, 127601 (2014).

[4] N. A. Benedek and C. J. Fennie, Phys. Rev. Lett. **106**, 107204 (2011).

[5] C. J. Fennie and K. M. Rabe, Physical Review B **72**, 100103 (2005).

[6] N. A. Benedek, Inorganic Chemistry **53**, 3769 (2014), pMID: 24678981.

[7] J. W. Bennett, Phys. Proc. **34**, 14 (2012).

Efficient Computation of Spontaneous Polarization Using Wannier Center Displacements

John R. Bonini, Oscar Paz, David Vanderbilt, Karin M. Rabe
Department of Physics and Astronomy
Rutgers University, Piscataway, NJ 08854

The materials genome initiative has motivated the development of high-throughput methods for screening large families of underdeveloped materials for exceptional properties using first principles methods. The discovery of new ferroelectrics is amenable to this approach as we can compute the spontaneous polarization which characterizes a ferroelectric.[1] The *Modern Theory of Polarization* has rigorously defined the spontaneous polarization of a crystalline solid as the difference in the 'formal polarization' between the polar structure and a centrosymmetric reference structure. An important subtlety arises from the fact that due to the periodicity of the crystal structure the formal polarization is a multivalued lattice quantity defined modulo a 'polarization quantum'.[2,4] The aforementioned change in the formal polarization then must be computed with both formal polarization values on the same branch of this 'polarization lattice'. The standard approach to resolving ambiguities stemming from this branch choice has been to calculate the (formal) polarization for a number of structures along the deformation path between the centrosymmetric and polar structures.[3] In this work we outline a symmetry based method to obtain the spontaneous polarization *using only one self-consistent calculation* by inferring the displacements of individual Wannier centers between oppositely polarized states.

Material	$P_{Standard}(\mathrm{C/m^2})$	$P_{New\,method}(\mathrm{C/m^2})$
$BaTiO_3$	0.34	0.34
$PbTiO_3$	0.95	0.95
$KNbO_3$	0.39	0.39
LiBeSb	0.51	0.56
LiBeP	0.77	0.77
BN	2.13	2.15

TABLE I. Results comparing values of $P_{spontaneous}$ computed two different ways. $P_{Standard}$ was found using calculations at intermediate steps along the deformation path from the centrosymmetric structure. $P_{New\,method}$ was found using a single self consistent calculation.

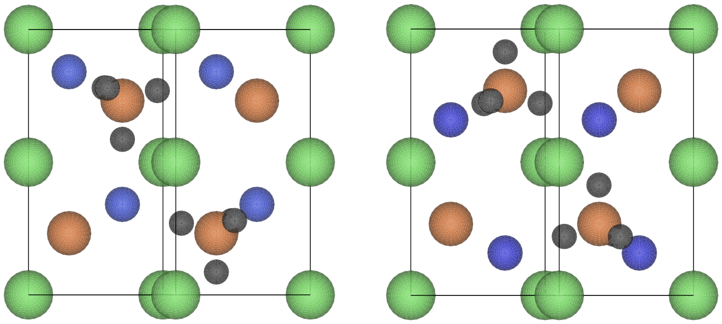

FIG. 1. Up and Down polar states of an LiGaGe structure. Black balls represent Wannier Centers. The correct branch choice in the computation of the spontaneous polarization corresponds to a smooth evolution of the Wannier centers as the material switches between these two states.

---

[1] Bennett, J. W., and K. M. Rabe (2012), Journal of Solid State Chemistry **195**, 21 , polar Inorganic Materials: Design Strategies and Functional Properties.

[2] King-Smith, R. D., and D. Vanderbilt (1993), Phys. Rev. B **47**, 1651.

[3] Spaldin, N. A. (2012), Journal of Solid State Chemistry **195**, 2 , polar Inorganic Materials: Design Strategies and Functional Properties.

[4] Vanderbilt, D., and R. D. King-Smith (1993), Phys. Rev. B **48**, 4442.

Accurate Geometric and Energetic Properties of Ferroelectrics and Related Materials from an Efficient Density Functional

Jianwei Sun[1], Yubo Zhang[1], John P. Perdew[1,2], and Xifan Wu[1]
[1]Department of Physics, [2]Department of Chemistry, Temple University, Philadelphia, PA 19122, USA

The first-principles approach based on density functional theory (DFT) plays an important role in studies of ferroelectrics and related materials. It is used to study the microscopic origins and mechanisms of properties of these materials [1]. Recent years have also witnessed the trend to rationally design materials with the desired ferroelectric and related properties by DFT [2]. Although DFT is exact in principle for the ground state total energy of a system of electrons under a multiplicative external potential, its applications are limited by the accuracy and efficiency of practical approximations to its exchange-correlation energy (E_{xc}).

The local density approximation (LDA) [3] and the Perdew-Burke-Enzerhof (PBE) generalized gradient approximation (GGA) [4] are the two most widely-used approximations in solid studies due to their efficiency and reasonable accuracy (e.g., typical errors are usually 1-2% in lattice constants). However, even such small errors cannot be tolerated in studies of ferroelectric materials because the spontaneous electric polarization due to structural instabilities there is extremely sensitive to their structures. This motivates the developments of GGAs for solids [5-7], pioneered by Wu and Cohen [5]. To further improve the accuracy, Bilc et al. [8] hybridized the WC GGA with the nonlocal exact exchange energy, which however deteriorates the efficiency dramatically. B1WC was designed by mixing 16% of exact exchange energy with 84% of WC GGA exchange to fit the properties of $BaTiO_3$, a prototypical ferroelectric material.

A promising yet less studied type of functional is meta-GGA. In addition to the electron density and its gradient that are used in GGAs, it includes the electron kinetic energy density as an input to model E_{xc}, and therefore is still semilocal and efficient in computation. The inclusion enables meta-GGAs to recognize and accordingly treat different chemical bonds (e.g., covalent, metallic, and even weak bonds), which no LDA or GGA can [9]. The non-empirical strongly constrained and appropriately normed (SCAN) meta-GGA [10] satisfies all 17 exact constraints appropriate to a meta-GGA, and is appropriately normed on or fitted to systems for which semilocal functionals can be exact or nearly-exact. Although SCAN uses no bonded information in its construction, it shows excellent accuracy for diversely-bonded systems (including covalent, metallic, ionic, hydrogen, and van der Waals bonds) and thus displays genuine non-empirical predictive power [11].

We demonstrate the accuracy of SCAN on geometric and energetic properties of ferroelectric materials with the prototypical $BaTiO_3$ and $PbTiO_3$. Interactions between ionic species there are primarily electrostatic in origin, but also have a significant component of vdW interactions among highly-polarizable negative ions, which makes the description of such systems challenging. PBE, for example, is particularly poor in its description of these materials, as it predicts spurious supertetragonality (too large c/a) in $BaTiO_3$ and $PbTiO_3$. Table I shows that B1WC predicts volumes for these two materials in excellent agreement with the experimental results, and also very accurate c/a ratios and polarizations for $BaTiO_3$ and $PbTiO_3$. On the other hand, the more commonly used HSE hybrid GGA [12] inherits the spurious supertetragonality for $BaTiO_3$ and $PbTiO_3$ from its parent PBE GGA [4] (although less severely), and predicts too large polarizations. SCAN is overall almost comparable to the computationally expensive B1WC, and much better than PBE for the above properties. The SCAN energy differences between the cubic and tetragonal phases are much closer to the B1WC values than either LDA, PBE, or even HSE. More discussions on band gaps of ferroelectric materials and magnetic properties of multiferroic materials will be given. These results show that SCAN matches or improves upon the accuracy of a computationally expensive hybrid functional for ferroelectric and related materials, at almost-GGA cost.

Table I. Properties of prototypical ferroelectric ($BaTiO_3$ and $PbTiO_3$) materials predicted by LDA, PBE, SCAN, and hybrid GGAs. The B1WC hybrid GGA[21] designed for ferroelectric materials is used as the reference in the second last columns. V ($Å^3$) is the volume, c/a the ratio of the lattice constants c and a, and Ps (C/m^2) the polarization of the tetragonal phases. ΔE(meV/cell) is the total energy difference between the cubic and tetragonal phases. The B1WC and experimental results for $BaTiO_3$ and $PbTiO_3$ are from Ref. 8.

systems	Property	LDA	PBE	HSE	SCAN	B1WC	Expt.
$BaTiO_3$	V	62.1	67.5	64.5	65.1	63.2	64.0
	c/a	1.011	1.054	1.039	1.029	1.015	1.010
	Ps	0.24	0.47	0.41	0.35	0.28	0.27
	ΔE	5.0	56.1	53.8	25.1	24	-
$PbTiO_3$	V	60.4	70.4	65.2	64.9	62.4	62.6
	c/a	1.045	1.239	1.158	1.122	1.097	1.071
	Ps	0.80	1.26	1.14	1.06	1.03	0.5~1.00
	ΔE	58.1	204.8	194.1	122.7	110.6	-

[1] R.D. King-Smith and D. Vanderbilt, Phys. Rev. B **49**, 5828 (1994).

[2] J.W. Bennett, et al, Phys. Rev. Lett. **109**, 167602 (2012).

[3] J.P. Perdew and Y. Wang, Phys. Rev. B **45**, 13244-13249 (1992).

[4] J. P. Perdew, K. Burke, and M. Ernzerhof, Phys. Rev. Lett. **77**, 3865-3868 (1996).

[5] Z. Wu and R.E. Cohen, Phys. Rev. B **73**, 235116 (2006).

[6] R. Armiento and A. E. Mattsson, Phys. Rev. B **72**, 085108 (2005)..

[7] J.P. Perdew, et al, Phys. Rev. Lett. **100**, 136406 (2008).

[8] Bilc, D.I., et al., Phys. Rev. B **77**, 165107 (2008)

[9] J. Sun et al., Phys. Rev. Lett. **111**, 106401 (2013).

[10] Sun, J., Ruzsinszky, A., and Perdew, J.P., Phys. Rev. Lett. **115**, 036402 (2015).

[11] J. Sun, et al, http://arxiv.org/abs/1511.01089.

[12] J. Heyd, G.E. Scuseria, and M. Ernzerhof, J. Chem. Phys. **118** 8207-8215 (2003).

Tuesday’s Abstracts

Understanding the dynamics of ferroelectric domain walls with molecular dynamics simulations

Shi Liu
Geophysical Laboratory, Carnegie Institution for Science, Washington D.C. 20015, USA

Ferroelectric materials possess switchable macroscopic polarization. In many cases, ferroelectrics adopt a multi-domain state where domains with polarization uniformly oriented in one direction are bounded by domains with polarization pointing in other directions. The interface separating regions of different polarities is called the domain wall. The internal structure and the motion of domain walls in ferroelectric materials can have a profound influence on the dielectric, piezoelectric, pyroelectric, and electronic properties of ferroelectrics. The ability to manipulate domain walls with an external stimulus offers a powerful paradigm for novel device engineering at the nanoscale.

Despite intense studies of domain walls, achieving controlled material design and device optimization for ferroelectrics remains a significant challenge, due to the lack of a microscopic and universal understanding of the mechanism of domain wall motion. Experimentally, the observed dynamics of domain walls are usually explained as the behavior of an elastic interface pinned by a random potential generated by defects, which appear to be strongly sample-dependent. Theoretically, it is difficult to connect 0 K first-principles-based microscopic quantities (e.g., domain wall energy) to finite-temperature macroscopic properties (e.g., coercive field) that are critical for material design and device performance. Molecular dynamics (MD) simulation is a powerful tool to examine the dynamics of complex nanoscale events at finite temperature, allowing direct comparison between theory and experiments.

We investigate the nature of switching in $PbZr_{0.2}Ti_{0.8}O_3$ thin films with a combination of thin film epitaxy, macro- and nanoscale property and switching characterization, and MD simulations. Differences are demonstrated between (001)-/(101)- and (111)-oriented films, with the latter exhibiting complex, nano-twined ferroelectric domain structures with high densities of 90º domain walls and broadened switching characteristics. Our MD simulations predict both 180º ferroelectric and 90º ferroelastic switching and these processes are subsequently observed in stroboscopic piezoresponse force microscopy. These observations provide insight into a previously unexplored aspect of ferroelectric switching in thin films and highlight the complexity of these materials. Such results have implications for our understanding of ferroelectric switching and offer opportunities to change domain reversal speed and potentially lead to interesting multi-state devices.

For many years, the Miller-Weinreich (MW) model of nucleation on the domain wall has been considered to be correct and has been parameterized with domain wall energies that allowed the fitting of the electric-field/domain-wall-velocity relationships in many experiments. However, first-principles calculations of domain wall energy per unit area were dramatically higher than the fit values, and conversely, inserting the accurate calculated values into the MW model gave velocities dramatically lower than experimentally observed. Previous theoretical studies on 180º domain wall motion reveal that the critical nucleus is a diffuse beveled square instead of a tall narrow sharp triangle assumed by MW. However, the mechanism of domain wall motion on 90º walls is not as well understood, and the relationship between the 180º and 90º wall motion has not been discussed. Taking the 90º domain walls in $PbTiO_3$ as an example, we explore the intrinsic ferroelectric response of domain walls in MD simulations under a wide range of temperatures and electric fields. We find the experimentally observed pinning/depinning behavior has intrinsic origin and can be accounted for even with no material defects. The depolarizing energy that was assumed to be the dominant energy term in MW model turns out to be neglectable. By mapping non-180º domain walls to a 180º domain wall, we propose a simple universal nucleation-and-growth-based analytical model that is able to quantify the dynamics of all types of domain walls in various ferroelectrics; this enables the prediction of the temperature- and frequency-dependence of coercive fields at finite temperature.

At last, we explore the domain structures in organometal halide perovskites, a promising solar-cell material for next-generation photovoltaic applications. We find that organometal halide perovskites can form both charged and uncharged domain walls, due to the flexible orientational order of the organic molecules. The presence of charged domain walls will reduce the band gap. We demonstrate that charged domain walls could serve as segregated channels for the diffusion of charge carriers.

Funding: ONR, NSF, Carnegie Institution for Science, HPCMO

Novel Ferroelectric Nanobubble Domains in Strained Prototypical Thin Films

Jacob B. J. Chapman[1,2], J. Marty Gregg[3], Alina Schilling[3], Anna V. Kimmel[1,2], Dorothy M. Duffy[1]

1. Department of Physics and Astronomy, University College London, Gower Street, London, WC1E 6BT, UK

2. Division of Mathematics and Modelling, National Physical Laboratory, Hampton Road, Teddington, TW11 0LW, UK

3. Centre for nanostructured Media, IRCEP, School of Maths and Physics, Queen's University Belfast, Belfast, BT7 1NN, UK

Classical molecular dynamics, with a shell model forcefield, is used to model the effects of strain and temperature on domain patterns in a nanofilm of $PbTiO_3$ under open circuit boundary conditions. Using the model on $PbTiO_3$ and experimental Piezo Force Microscopy on $BaTiO_3$, a new high temperature nanobubble domain pattern is revealed near Tc. The new domain morphology is shown to be caused by domain wall wandering in flux-closure domains near the Curie temperature under compressive strain.

Ferroelectric ultrathin films have shown huge potential for the next generation of emergent technologies that aim to develop concepts to integrate and exploit exotic and novel phenomena in dimensionally constrained materials. Domain walls in thin films have shown promising functionalities through induced electrical and magnetic properties, and unusual phases not present in the bulk domain interior. Recent direct observation of so-called wandering domain walls in thin films [1] and the ability to control the direction of the domain wall normal offer gateways for tuning intrinsic ferroelectric and piezoelectric properties.

In this work the properties of strained $PbTiO_3$ ultra-thin films (UTF) were studied using molecular dynamics implemented in the DL POLY code [2] applying an adiabatic core-shell forcefield derived in ref. [3]. Three dimensional periodic boundary conditions were imposed so the UTF is continuous and infinite along the pseudocubic $[100]_p$ and $[010]_p$ directions. A 100 Å vacuum gap in the growth direction $[001]_p$ was used to separate slab-image interactions. The initial slab configuration was set to include two ideal Kittel domains. A Pertsev (misfit-strain vs temperature) diagram for the $PbTiO_3$ was calculated using this model, demonstrating the local behaviour of polarisation with the domains.

In addition to the previously predicted flux-closure and in-plane domain morphologies [4,5], our model predicts an entirely new domain phase at temperatures above the flux-closing Landau-Lifshitz stripe domain patterning (c^d) but below Tc. Our simulations show that in the compressive strain regime, in vicinity of the effective Curie temperature, the homogeneity of the stripe c^d domains along the in-plane $[010]_p$ direction breaks down. This is due to diffuse nucleation and growth of the reverse domain on the domain walls, shown previously as a growth mechanism in bulk prototypical systems under an activation field using a Landau-Ginzburg-Devonshire model [6]. This first presents by the distortion of the 180° domain wall alignment with (100) planes, so-called '*wandering*' [1,4]. Here we observed that with further temperature increases leading to polarisation reduction, the degree of the anisotropy increases resulting in the domain wall pattern changing from linear stripe domains into the bubble domain pattern (Fig. 1).

We also observed bubble domains in an experimental study of $BaTiO_3$ crystals. Vertical PFM data was taken on a thin single crystal of flux-grown $BaTiO_3$. The total thickness of the crystal was of the order of 25 µm. After successive cooling and heating through the Curie temperature, the PFM surface contrast progressively changed. Initially ferroelastic stripe domains were observed evolving to finely spaced bubble patterns of 180° domains with polarisation in and out of the surface plane (Fig. 1 a). The observed domain morphology bears a striking similarity to the modelled morphology (Fig. 1 b-c). Imaging on a transmission polarized optical microscope reveals that the ferroelastic domains remained but were not evident in the surface region imaged by PFM. We conclude the observed bubble domains were a feature of the skin layer only and representable by our strained UTF model.

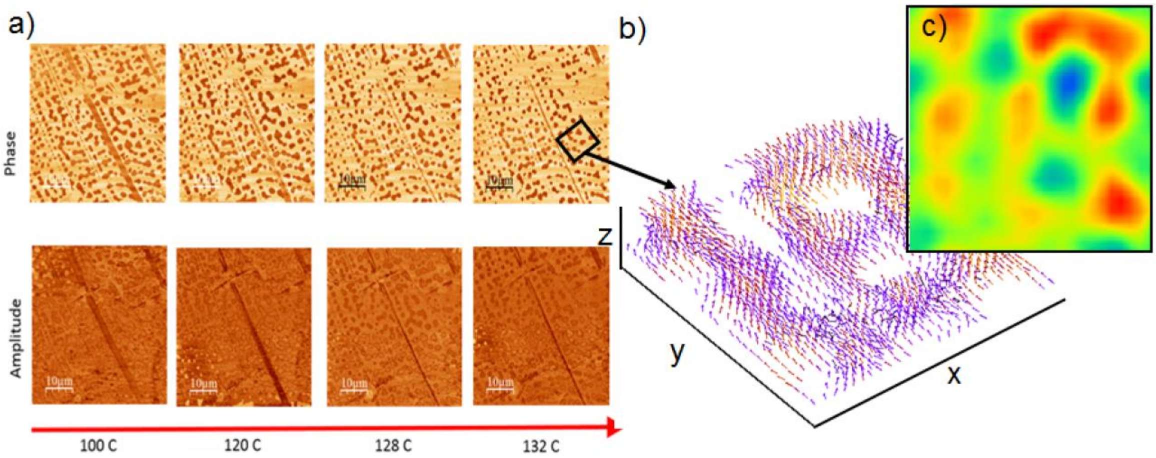

Figure 1. New ferroelectric domain morphology – nanobubble domains (c^b). (a) v-PFM on skin-layer of 25µm thick BaTiO3 in the tetragonal phase cycled about T_c. (b) Local dipoles of cb domains in compressively strained PbTiO3 calculated using a core-shell model forcefield at $0.8Tc^{FF}$ in a 26x26x10 unit cell supercell. Only dipoles with $P_z>0$ plotted for clarity leaving voids where $P_z<0$. Out of plane contour map of the polarisation in the centre of the simulated ultrathin film showing remarkable agreement with the skin layer experiment.

[1] C.-L. Jia *et al,* Science **331**, 1420 (2011)

[2] I.T. Todorov *et al,* J. Mater. Chem. **16**, 1911 (2006)

[3] O. Gindele, A.V. Kimmel & D.M.Duffy, J. Phys. Chem. C **119**, 17784 (2015)

[4] N.A. Pertsev, A.G. Zembilgotov & A.K. Tagantsev, Phys. Rev. Lett. **93**, 196104 (2004)

[5] Z. Jiang *et al*, Phys. Rev. B **89**, 214113 (2014)

[6] Y.-H.Shin *et al*, Nature **449**, 881 (2007)

Experimental evidences of defects stabilized by neutral domain walls

G. F. Nataf[1,2], M. Guennou[1], T. Granzow[1], A. Haußman[3], N. Barrett[2], E. K. H. Salje[1], J. Kreisel[1,4]

[1]Materials Research and Technology Department, Luxembourg Institute of Science and Technology, 41 Rue du Brill, 4422 Belvaux, Luxembourg
[2]SPEC, CEA, CNRS, Université Paris-Saclay, CEA Saclay 91191 Gif-sur-Yvette France
[3]Institut für Angewandte Photophysik, Technische Universität Dresden, George-Bähr-Str. 1, 01069 Dresden, Germany
[4]Physics and Materials Science Research Unit, University of Luxembourg, 41 Rue du Brill, 4422 Belvaux, Luxembourg

Since the 80's, studies of the interaction of charge defects and ferroelectric domain walls have focused on pinning-depinning mechanisms [1-3] and their influence on polarization fatigue [2-3]. More recently, this topic has received a renewed interest due to the emerging field of so-called domain wall nanoelectronics [4], which hold the promise of using the distinct functional properties of domain walls in electronic devices. Within this context, the crucial role of defects in the electrical conductivity of domain walls has been amply pointed out. For instance, in the case of multiferroic $BiFeO_3$, defects and specifically oxygen vacancies are proposed to play an important role in the conduction at the walls [5-7]. In $Pb(Zr,Ti)O_3$ thin films, it has been argued that defect segregation could explain conduction at domain walls via hopping between trapped states [8]. However, direct experimental evidences of the accumulation of defects at domain walls are rare [9].

We used Raman spectroscopy to investigate the interaction between domain walls and defects in lithium niobate ($LiNbO_3$) [10].

Figure 1 shows the evolution of the frequency of three Raman modes for line-scans across a domain wall in samples doped with magnesium. The frequency shift for $E(TO_1)$ and $E(TO_8)$ at the domain wall is negative below 5% of magnesium but positive above 5%, while it is always positive for $A_1(LO_4)$ and nearly independent on the amount of magnesium.

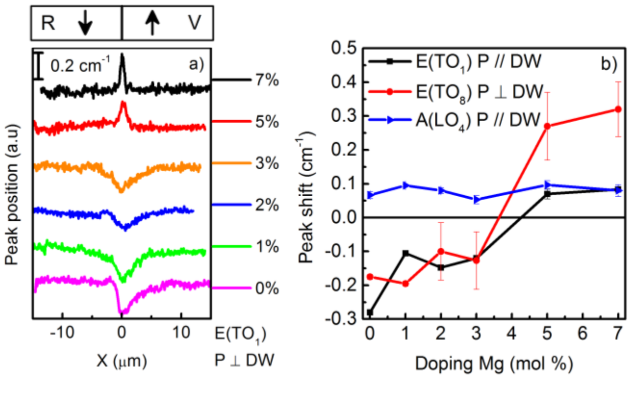

Figure 1 (a) Peak position of $E(TO_1)$ across a domain wall after annealing. (b) Peak shifts at the domain wall.

It is clear that an intrinsic electric field alone cannot account for all the observations since it would not explain the doping-dependence of the frequency shifts of the E modes. On the other hand, detailed examination shows that the frequency pattern at the domain wall differs from the signature of polar defects as observed in the bulk, notably because the doping-dependence is different. This can be understood in two ways: (1) the frequency shifts observed involve a combination of effects resulting from the defect structure and the electric (strain) field in the vicinity of the wall or (2) new defect structures have been stabilized at domain walls.

In order to get a better understanding of the defects evidenced by Raman spectroscopy measurements, we performed dielectric measurements on periodically poled single crystals – with high domain wall densities - and on monodomain single crystals [11]. In both cases, a relaxation can be observed, revealed by a peak in the imaginary part of permittivity with a maximum near 10 kHz. Figure 2 details the temperature evolution of the peak in the periodically poled single crystals. Its position is nearly temperature-independent. This relaxation has a semi-circular shape on a Cole-Cole plot.

The behavior of monodomain and periodically poled samples differ upon annealing. Annealing monodomain samples causes the relaxation to vanish, due to a rearrangement of the defect structure, particularly the Li vacancies, while the relaxation persists after annealing in periodically poled samples.

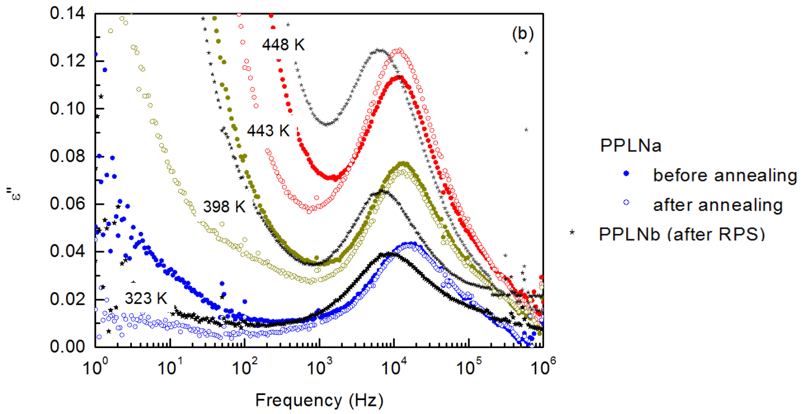

Figure 2 Imaginary part of the permittivity as a function of the excitation frequency for temperatures between 323 K and 448 K (before and after high temperature measurements).

The relaxation is unlikely to stem from the motion of the domain walls themselves since the coercive field in LiNbO$_3$ is very large. The origin of the relaxation is therefore likely to be of electronic nature. It would be compatible with the bi-polaron energy of $E = 0.27$ eV discussed by Schirmer et al. [12] provided that the hopping energy is $E/2$, as usually assumed for (bi-)polarons. We conclude that the ferroelectric 180° domain walls stabilize the charged defect structures.

References

[1] T. J. Yang, V. Gopalan, P. J. Swart, and U. Mohideen, Phys. Rev. Lett. **82**, 4106 (1999).
[2] A. K. Tagantsev, I. Stolichnov, E. L. Colla, and N. Setter, J. Appl. Phys. **90**, 1387 (2001).
[3] J. F. Scott and M. Dawber, Appl. Phys. Lett. **76**, 3801 (2000).
[4] G. Catalan, J. Seidel, R. Ramesh, and J. F. Scott, Rev. Mod. Phys. **84**, 119 (2012).
[5] J. Seidel *et al.*, Phys. Rev. Lett. **105**, 197603 (2010).
[6] S. Farokhipoor and B. Noheda, Phys. Rev. Lett. **107**, 127601 (2011).
[7] O. Diéguez, P. Aguado-Puente, J. Junquera, and J. Íñiguez, Phys. Rev. B **87**, 024102 (2013).
[8] J. Guyonnet, I. Gaponenko, S. Gariglio, and P. Paruch, Adv. Mater. **23**, 5377 (2011).
[9] A. Pramanick , A. D. Prewitt, J. S. Forrester and J. L. Jones, Crit. Rev. Solid State **37**, 243–75 (2012).
[10] G. F. Nataf, M. Guennou, A. Haußmann, N. Barrett and J. Kreisel. Phys. Stat. Sol. (RRL), (in-press - 2015).
[11] G. F. Nataf, O. Aktas, T. Granzow and E. K. H. Salje. J. Phys. Condens. Matter, (in-press - 2015).
[12] O. F. Schirmer, M. Imlau, C. Merschjann and B. Schoke, J. Phys. Condens. Matter **21**, 123201 (2009).

Learning through ferroelectric domain dynamics in solid-state synapses

V. Garcia[1], S. Boyn[1], G. Lecerf[2], B. Xu[3], S. Fusil[1], S. Girod[1], C. Carrétéro[1], L. Bellaiche[3], S. Saïghi[2], M. Bibes[1], A. Barthélémy[1], J. Grollier[1]

[1]Unité Mixte de Physique, CNRS, Thales, Univ. Paris-Sud, Université Paris-Saclay, 91767, Palaiseau, France
[2]Univ. Bordeaux, IMS, UMR 5218, F-33405 Talence, France
[3]Department of Physics and Institute for Nanoscience and Engineering, University of Arkansas, Fayetteville, Arkansas 72701, USA

In the brain learning is achieved through the ability of synapses to reconfigure the strength by which they connect neurons (*1*) (synaptic plasticity). Artificial hardware with performances emulating those of biological systems requires electronic nanosynapses endowed with such plasticity. In promising solid-state synapses called memristors, conductance can be finely tuned by voltage pulses (*2*) and set to evolve according to a biological learning rule called spike-timing-dependent plasticity (*3*). Future neuromorphic architectures will comprise billions of such nanosynapses (*4*), which requires a clear understanding of the physical mechanisms responsible for plasticity. Here we report on synapses based on ferroelectric tunnel junctions (*5*) comprising ultrathin films of super-tetragonal $BiFeO_3$ (*6*, *7*) (Fig. B). We show that spike-timing-dependent plasticity (Figs. C, D) can be harnessed from intrinsically inhomogeneous ferroelectric polarization switching. Through combined scanning probe imaging, electrical transport experiments, and atomic-scale dynamic simulations, we demonstrate that conductance variations can be accurately controlled and modeled by the nucleation-dominated switching (*8*) of domains with opposite polarizations. Our results show that ferroelectric nanosynapses learn in a reliable and predictable way, opening the path towards unsupervised learning in spiking neural networks.

(We acknowledge financial support from the European Research Council (ERC Advanced Grant FEMMES, No. 267579. B.X. and L.B. acknowledge the financial support from the Department of Energy, Office of Basic Energy Sciences, under contract ER-46612.))

1. D. O. Hebb, *The Organization of Behavior* (Wiley & Sons, New York, 1949).
2. J. J. Yang, D. B. Strukov, D. R. Stewart, Memristive devices for computing. *Nature Nanotechnol.* **8**, 13–24 (2013).
3. C. Zamarreño-Ramos *et al.*, On spike-timing-dependent-plasticity, memristive devices, and building a self-learning visual cortex. *Front. Neurosci.* **5**, 26 (2011).
4. D. B. Strukov, R. S. Williams, Four-dimensional address topology for circuits with stacked multilayer crossbar arrays. *Proc. Natl. Acad. Sci. USA*. **106**, 20155–20158 (2009).

5. V. Garcia, M. Bibes, Ferroelectric tunnel junctions for information storage and processing. *Nature Commun.* **5**, 4289 (2014).
6. H. Yamada *et al.*, Giant Electroresistance of Super-Tetragonal $BiFeO_3$-Based Ferroelectric Tunnel Junctions. *ACS Nano*. **7**, 5385–5390 (2013).
7. M. Marinova *et al.*, Depth Profiling Charge Accumulation from a Ferroelectric into a Doped Mott Insulator. *Nano Lett.* **15**, 2533–2541 (2015).
8. J. Y. Jo *et al.*, Domain Switching Kinetics in Disordered Ferroelectric Thin Films. *Phys. Rev. Lett.* **99**, 267602 (2007).

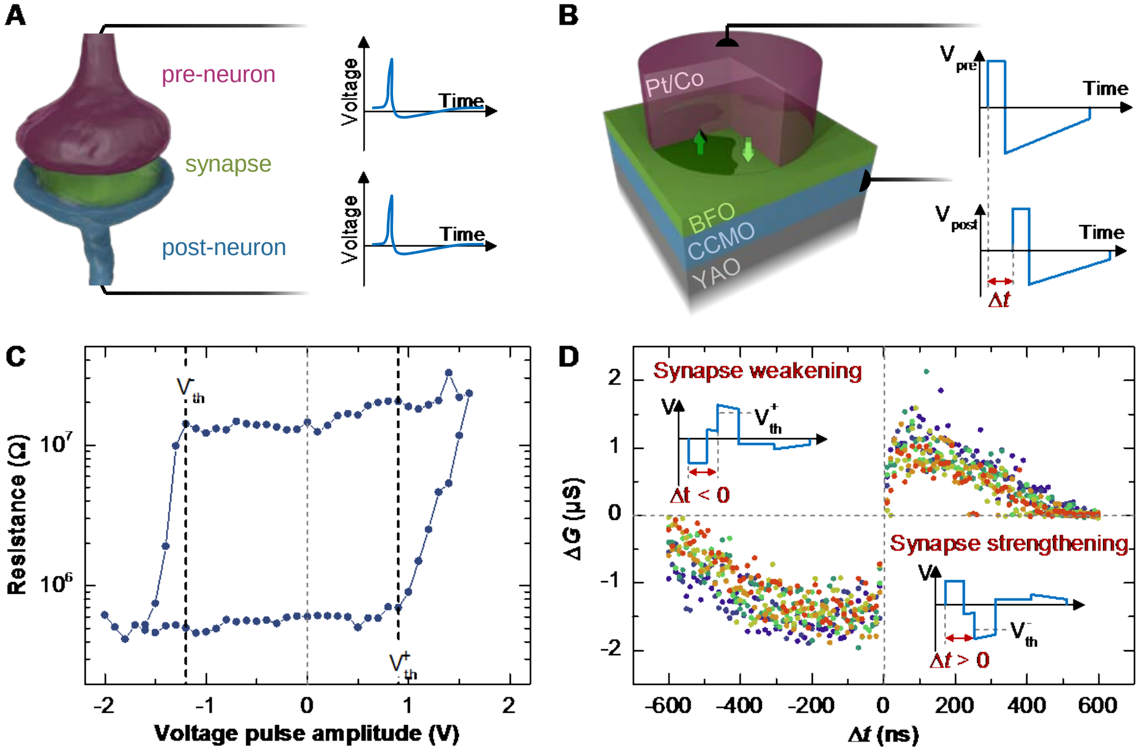

Figure: Artificial synapses based on ferroelectric tunnel junctions. A, *Sketch of pre- and post-neurons connected by a synapse. The synaptic transmission is modulated by the causality of neuron spikes.* ***B,*** *Sketch of the ferroelectric memristor where a ferroelectric tunnel barrier of BFO is sandwiched between a bottom electrode of CCMO and a top submicron pillar of Pt/Co.* ***C,*** *Single pulse hysteresis loop of the ferroelectric memristor displaying clear voltage thresholds.* ***D,*** *Measurements of spike-timing-dependent plasticity in the ferroelectric memristor. Modulation of the device conductance as a function of the time difference between pre- and post-synaptic spikes. Seven data sets were collected on the same device showing the reproducibility of the effect.*

Observation of domain wall dynamics in ferroelectrics by means of x-ray photon correlation spectroscopy

Alexei A. Bokov[1], Semën Gorfman[2], Mario Reiser[2] Y. Xie[1], Arman Davtyan[2], Nan Zhang[1], Alexei Zozulya[3], Michael Sprung[3], Ullrich Pietsch[2], Christian Gutt[2], Zuo-Guang Ye[1]

[1]Department of Chemistry and 4D LABS, Simon Fraser University, Burnaby, BC, Canada
[2]Department of Physics, University of Siegen, Siegen, Germany
[3]Deutsches Elektronen-Synchrotron DESY, Notkestrasse 85, D-22603 Hamburg, Germany

Many applications of ferroelectric materials are based on the properties, which are related largely to the motion of domain walls under external electric field or stress. For example, polarization switching in ferroelectric random access memory devices proceeds through the domain wall motion. This motion can contribute greatly to the piezoelectric response of piezoelectric sensors and actuators and to the dielectric constant of capacitor materials. While the static properties of domain walls and their structure on the atomic scale are studied extensively, the experimental characterization of domain wall dynamics is a challenging task. Accordingly, the underlying mechanisms remain unverified. In particular, while it is commonly accepted that domain wall motions can be described by a multi-well energy landscapes, the firm experimental confirmation of it is still missing.

In the present work, we developed the methodology for investigating the nanoscale dynamics of ferroelectric /ferroelastic domain walls using the X-ray Photon Correlation Spectroscopy (XPCS). This novel technique based on analysing the correlation between the speckle patterns (extremely detailed scattering patterns of highly coherent X-ray beam) has been applied during the last two decades for studying slow dynamics in soft matter system (polymers, colloidal gels, emulsions etc.) [1].

Our XPCS experiment was performed at the coherent beam X-ray scattering beamline (P10) of the PETRAIII storage ring. The multidomain $PbZr_{0.56}Ti_{0.46}O_3$ single crystal was studied in which the transitions were observed (by polarized light microscopy) on cooling from paraelectric to macroscopically tetragonal and further to monoclinic phase. The coherent beam was focused to a 3x5 μm^2 spot. The speckle patterns were collected with 2D detector at the angle of ~ 0.5° from the exact 100 Bragg position during slow (~1 K/min) cooling of the sample from 650 K to 320 K (Fig.1). To quantify the overall thermally induced speckles changes we calculated the correlation coefficients, $C(T_1, T_2)$, between all possible pairs of speckle patterns collected at temperatures T_1 and T_2. The results are shown in Fig. 2.

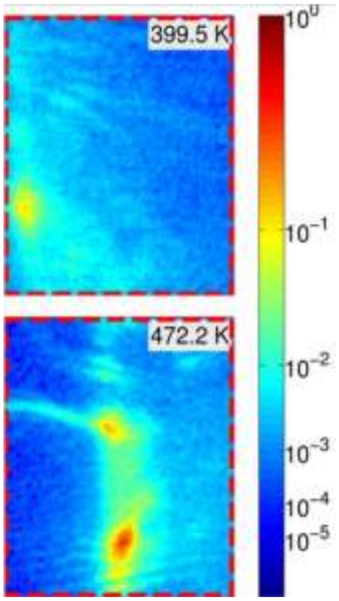

Figure 1. Examples of high-resolution X-ray speckle patterns at selected temperatures.

The correlation spectra, i.e. the set of decay functions $C(T, T+\Delta T)$ vs ΔT were further considered. We proposed the algorithm of the deconvolution of the spectra based on the statistical analysis that allows to distinguish the domain wall and the lattice strain dynamics and resolve the spectra into constituent contributions of various modes of domain wall motion. Fundamentally different behaviors are found in monoclinic and tetragonal phases. In the tetragonal phase, where temperature-induced displacements of walls is not expected, the Gaussian statistics is found, while in the monoclinic phase, where the domain walls should change the position with temperature, the statistics is of Poisson type and, therefore, C is a discreet variable. This is consistent with stop-and-go motions (jerks) arising from the complex interaction between domain walls and randomly distributed obstacles (pinning centres).

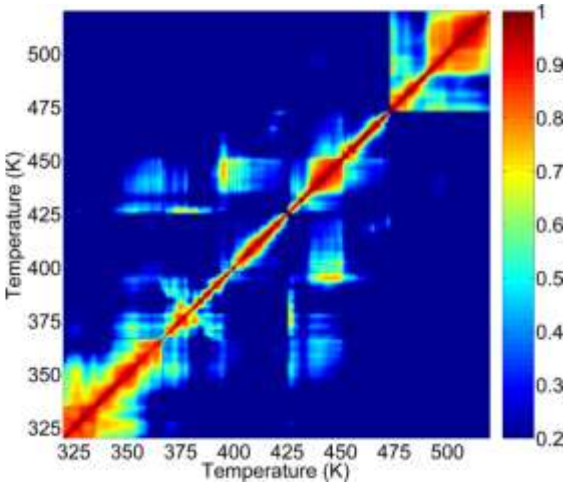

Figure 2 . The false-color map of the correlation matrix. The correlation coefficients $\boldsymbol{C(T_1, T_2)}$ between pairs of speckle patterns, collected at the temperatures T_1 and T_2

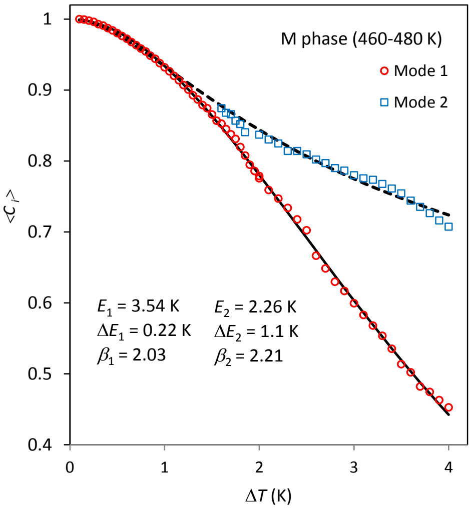

Figure 3. Example of deconvolution of the XPCS spectrum. Correlation decay related to two modes of domain wall dynamics active in the temperature range of 460-480 K

To characterize the correlation decay quantitatively the modified compressed exponential function was proposed:

$$C(T, T+\Delta T) = \exp\{-\left(\frac{\Delta T}{E+\Delta E \Delta T}\right)^{\beta}\}, \beta>1$$

which differs from the function used previously by the presence of the term $\Delta E \Delta T$. Different modes of domain wall motion can be characterized by different parameters E, E_1, β (Fig. 3). The expressions were derived relating the measured parameters with the microscopic characteristics of domain wall motion.

Our results also suggest that (in contrast to some previous reports) the regions of monoclinic symmetry are absent in tetragonal phase of PZT as the temperature-induced domain wall displacements would have been observed in a phase of monoclinic symmetry.

The work was supported by the U.S. Office of Naval Research (Grant No.N00014-12-1-1045) and the Natural Science & Engineering Council of Canada (NSERC).

[1] Sutton M, Mochrie SGJ, Greytak T, et al. *Nature*, **352**, 608–610 (1991).

Complex Nano-/micro Domain Structure in Tetragonal $PbZr_{1-x}Ti_xO_3$ Single Crystals

Bixia Wang[1], Alexei A. Bokov[1], Mingmin Zhu[2], Yujuan Xie[1], Wei Ren[2] and Zuo-Guang Ye[1,2*]

E-mail address: zye@sfu.ca

1) Department of Chemistry and 4D LABS, Simon Fraser University, Burnaby, BC, V5A 1S6, Canada

2) Electronic Materials Research Laboratory, Key Laboratory of the Ministry of Education & International Center for Dielectric Research, Xi’an Jiaotong University, Xi’an 710049, China

Abstract

$Pb(Zr_{1-x}Ti_x)O_3$ (PZT) ceramics are the most extensively used piezoelectric materials owing to their good piezoelectric and electromechanical properties near the morphotropic phase boundary (MPB). However, the microstructures of this class of materials and the atomistic phenomena that cause the outstanding performance have not been thoroughly understood yet. Therefore, it is of particular interest to grow single crystals of PZT, which are not only necessary for thorough characterization of the anisotropic properties of this system, but also are expected to exhibit superior piezo-/ferroelectric performance over their ceramic counterparts.

In this work, single crystals of $PbZr_{0.46}Ti_{0.54}O_3$ (PZT46/54) were grown by a top-seeded solution growth method. X-ray diffraction analysis indicates that the single crystals have a tetragonal symmetry. However, the analysis of domain structure by polarized light microscopy (PLM) reveals that the $(001)_{cub}$ platelet of the tetragonal crystal behaves like cubic, showing extinction at any positions under crossed polarizers [Figures 1(a) and 1(b)]. On the other hand, the $(011)_{cub}$ platelet exhibits birefringence with extinction at 0°/90° to the $<100>_{cub}$ direction [Figures 1(c) and 1(d)], which is consistent with the optical behavior of a tetragonal symmetry.

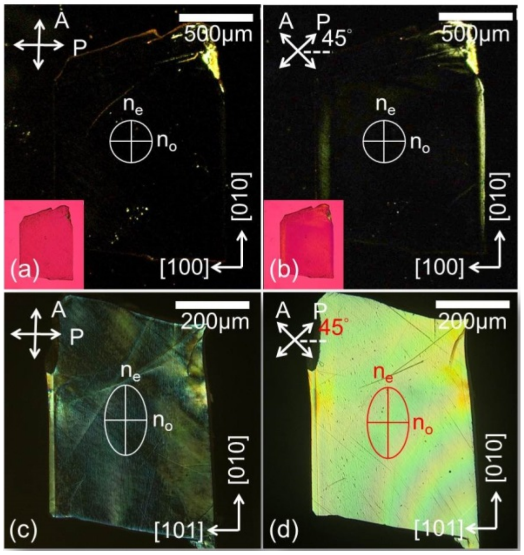

Figure 1. Room temperature PLM images of a $(001)_{cub}$ (a, b) and a $(011)_{cub}$ (c, d) PZT46/54 platelets with different polarizer/analyzer configurations: (a) and (c) are parallel to the $<010>_{cub}$ direction; (b) and (d) are at 45° to the $<010>_{cub}$ direction. The inserted photos in (a) and (b) were taken with a sensitive tint plate (λ = 530nm) placed between the sample and analyzer.

This discrepancy is attributed to the presence of differently oriented miniaturized domains or nanodomains. The arrangements of these domains compensate almost completely, in other words, the overall birefringence $\Delta n = \sum n_e - \sum n_o \approx 0$, when measured on the $(001)_{cub}$ platelet. Therefore, the platelet behaves like an isotropic crystal. In the case of a $(011)_{cub}$-cut platelet, the compensation is not completed due to the different orientations and shapes of the indicatrix sections of domains. Therefore, relation $\Delta n = \sum n_e - \sum n_o \neq 0$ is satisfied, and relatively small residual birefringence could be observed.

In addition, square-shaped domains with edges oriented in $<110>_{cub}$ direction are observed by PLM when an external dc electric field is applied along $<100>_{cub}$ direction (Figure 2). They are confirmed to be 180° ferroelectric domains with an average size of 12 μm by piezoresponse force microscopy (PFM) analysis. The interpretation of these domains is referred to the nucleation and growth of 180° flux-closure state in the crystal. A circular 180° flux-closure domain is first nucleated in the tetragonal nanodomain state [Figure 3(a)]. The circular flux-closure domain grows into a large one. The growth velocity along $<100>_{cub}$ is faster than that of $<110>_{cub}$ direction [Figure 3(b)]. Therefore, the newly formed domain ends up as a square with edges oriented in $<110>_{cub}$ direction [Figure 3(c)]. Furthermore, a monoclinic (M_C) phase is induced in the tetragonal nanodomains by application of an electric field.

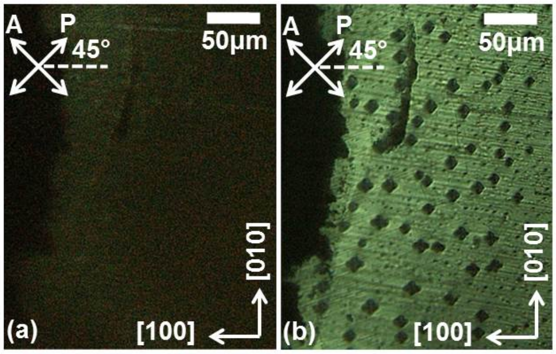

Figure 2. PLM images obtained before (a) and after (b) applying external electric field.

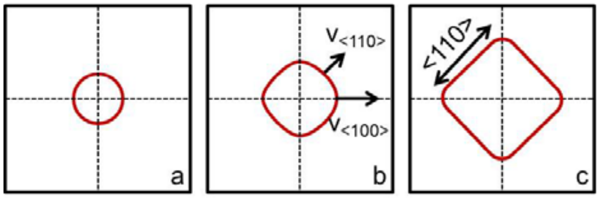

Figure 3. Schematic showing the formation of square-shaped ferroelectric domains: (a) a circular flux-closure is nucleated; (b) the domain wall expands through side-wall motion; (c) a square-shaped domain formed due to the different velocity along <100>cub and <110>cub directions.

The work was supported by the U.S. Office of Naval Research (Grant No. N00014-12-1-1045) and the Natural Science & Engineering Research Council of Canada (NSERC).

Towards improved caloric responses using ferroelectrics

Y. Liu[1], Z.G. Luo[2], W. P. Geng[3], L.C. Phillips[4], M. Sanlialp[5], I.C. Infante[1], P.E. Janolin[1], X.J. Lou[2], XB Ren[2], A. Q. Jiang[3], V.V. Shvartsman[5], D.C. Lupascu[5], X. J. Meng[6], R. Mattana[4], M. Bibes[4], A. Barthélémy[4], L. Bellaiche[7], J. F. Scott[8], B. Dkhil[1]

[1]Laboratoire Structures, Propriétés et Modélisation des Solides, UMR8580, CentraleSupélec, CNRS, Université Paris-Saclay, 92290 Châtenay-Malabry, France
[2]Multi-disciplinary Materials Research Center, Frontier Institute of Science and Technology, and State Key Laboratory for Mechanical Behavior of Materials, Xi'an Jiaotong University, Xi'an 710049, P. R. China
[3]State Key Laboratory of ASIC and System, School of Microelectronics, Fudan University, Shanghai, 200433, P. R. China
[4]Unité Mixte de Physique, CNRS, Thales, Univ. Paris-Sud, Université Paris-Saclay, 91767, Palaiseau, France
[5]Institute for Materials Science, University of Duisburg-Essen and Center for Nanointegration Duisburg-Essen (CeNIDE), Essen 45141, Germany
[6]National Laboratory for Infrared Physics, Shanghai Institute of Technical Physics, Chinese Academy of Sciences, Yu Tian Road 500, Shanghai 200083, P. R. China, University of Chinese Academy of Sciences, No. 19A Yuquan Road, Beijing 100049, China
[7]Physics Department and Institute for Nanoscience and Engineering, University of Arkansas, Fayetteville, 72701 Arkansas, USA
[8]Department of Physics, Cavendish Laboratory, University of Cambridge, Cambridge CB3 0HE, UK and Departments of Chemistry and Physics, St. Andrews University, St. Andrews, Scotland KY16 9ST

Email: brahim.dkhil@centralesupelec.fr

The search for alternative solid-state refrigeration materials to hazardous gases in conventional and cryogenic cooling devices is a very active field of condensed matter [1]. The use of phase transitions is a powerful tool to achieve giant caloric effects in ferroic materials in which magnetization, polarization, strain and/or volume can be strongly tuned under a moderate external stimulus. Here, we explore various strategies using ferroelectrics to reveal their potentialities as solid state coolers. By using Landau-based phenomenological calculations, we will briefly show the elasto- and electro-caloric properties of the model and ecofriendly $BaTiO_3$ that we studied in details including bulk and thin film form, the role of the external uniaxial stress, electric field, substrate, film thickness and electrodes [2-8]. Specifically, we will show that ferroelectrics are natural multicaloric materials in which both giant elasto- and electro-caloric responses can be achieved near room temperature and that the 2nd-order nature of transitions can be beneficial.

We also investigated how multiphase points composition can be used to enhance electrocaloric effects [9,10]. Moreover, in addition to conventional electrocaloric effect, we show that negative effect can be also generated efficiently and thus used as a supplemental tool for designing enhanced caloric responses [2, 11]. Finally, we will also discuss the effect of dual stimuli in ferroelectric/magnetic system with the goal to suppress the detrimental hysteresis losses due to 1st order nature of the phase transitions [12].

References:

1. X. Moya *et al.*, Nat. Mater. **13**, 439 (2014)
2. Y. Liu *et al.*, Adv. Mater. **26**, 6132 (2014)
3. Y. Liu *et al.*, Appl. Phys. Lett.**104**, 012907 (2014)
4. Y. Liu, *et al.*, Phys. Rev. B **90**, 104107 (2014)
5. Y. Liu *et al.*, Appl. Phys. Lett. **106** , 032901 (2015)
6. Y. Liu *et al.*, Appl. Phys. Lett. **100**, 192902 (2012)
7. Y. Liu *et al.*, Phy. Rev. B **88**, 024106, (2013)
8. Y. Liu *et al.*, Appl. Phys. Lett. **104**, 082901 (2014)
9. Z. Luo *et al.*,, Appl. Phys. Lett. **105**, 102904 (2014)
10. M. Sanlialp *et al.*, Appl. Phys. Lett. **106**, 062901 (2015)
11. W. Geng *et al.*, Adv. Mater. **27**, 3165 (2015)
12. Y. Liu *et al.*, Nat. Comm., submitted

Piezocaloric effect in antiferroelectric $PbZrO_3$ from atomistic simulations

Joseph Cuozzo, S. Lisenkov, B. K. Mani, I. Ponomareva
Department of Physics, University of South Florida, Florida 33620, USA

I. ABSTRACT

Caloric effects in functional materials are presently under intense investigation owing to both the discoveries of giant caloric effects in several ferroics [1] and their technological promise for solid state refrigeration. They are defined by either an adiabatic temperature change or by an isothermal entropy change upon application of an external field such as an electric or stress field. In this study we examine the piezocaloric effect (PCE) in antiferroelectric $PbZrO_3$. The aims of this work are as follows: (i) to predict the (co)existence of large positive and negative PCE in antiferroelectric $PbZrO_3$; (ii) to reveal the intrinsic features and atomistic origin of the effect; (iii) to report a high tunability of the PCE by an applied stress, and how it may improve the refrigeration cycle; (iv) to propose an experimental setup to demonstrate the PCE.

In this study, bulk $PbZrO_3$ is simulated using a 16x16x16 supercell periodic along the three Cartesian directions. The total energy of the supercell is given by the first-principles-based effective Hamiltonian of Ref. [2]. The Hamiltonian correctly reproduces many of the electrical and thermodynamical properties of $PbZrO_3$ [2]. In particular, it accurately predicts the antiferroelectric phase transition and the dipole pattern associated with it, electric hysteresis loops, and the $PbZrO_3$ behavior under pressure.

Before PCE computations were carried out, the simulated sample was annealed from 1200 K to 5 K in steps of 5 K using the Metropolis Monte Carlo (MC) simulations. PCE simulations were carried out on equilibrated samples using the adiabatic MC approach proposed in Ref. [3]; that is, the caloric change in temperature is computed during the application or removal of the stress field under adiabatic conditions. Technically, the normal uniaxial stress field, σ, in the range of -2 GPa to 2 GPa was simulated. The stress field was chosen to act either on [100], or [010], or [001] crystallographic planes. In each of our simulations, the stress field was slowly applied and then removed at a rate of 2 kPa per MC sweep. We computed the temperature and structural properties at each MC sweep and averaged them over 10,000 MC sweeps.

Our computations predict that the stress has a pronounced effect on the magnitude of all order parameters as well as the Curie point. In particular, we find that in the antiferroelectric phase, both the antiferroelectric and antiferrodistortive order parameters are weakened under tensile stress and strengthened under compressive stress. The same observation is true for the strain along the orthorhombic c-axis. Consequently, the Curie point is lowered under tensile stress and raised under compressive stress. Such sensitivity of the structure to the external stress is suggestive of a strong piezocaloric response which relies on the possibility to influence the structural order by the applied stress.

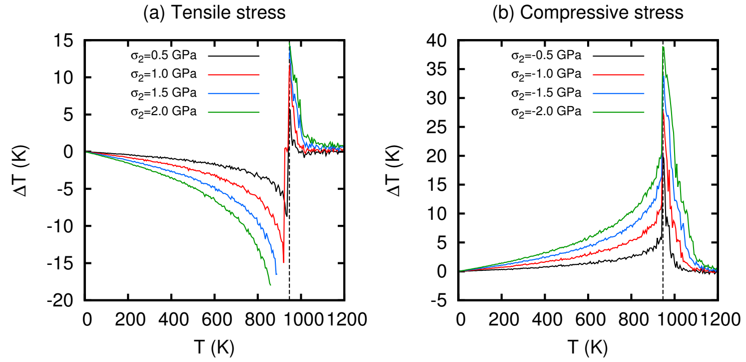

FIG. 1: Dependence of the piezocaloric ΔT on the temperature. Vertical lines indicate computational transition temperatures.

Figure 1 gives the computational data for the piezocaloric ΔT as a function of temperature. The largest values of the PCE are near the Curie point. Also notice that below the Curie temperature, the sign of the PCE ΔT for compressive and tensile stress are opposite of each other. This suggests that the nature of the stress uniquely determines the sign of the piezocaloric ΔT. The robustness of the effect in a very wide range of temperatures is attractive for potential applications.

We have also estimated the piezocaloric ΔT from the Maxwell relation equation $\Delta T = -\int_0^\sigma \frac{T}{c\rho}(\frac{\partial \eta}{\partial T})_\sigma d\sigma$ (the indirect approach), where T is the initial temperature, c is the specific heat under constant stress, and ρ is the density. The results are given in figure 2. We notice that this method substantially underestimates the piezocaloric ΔT at the Curie point as it does not take into account the entropy change at the first-order phase transition.

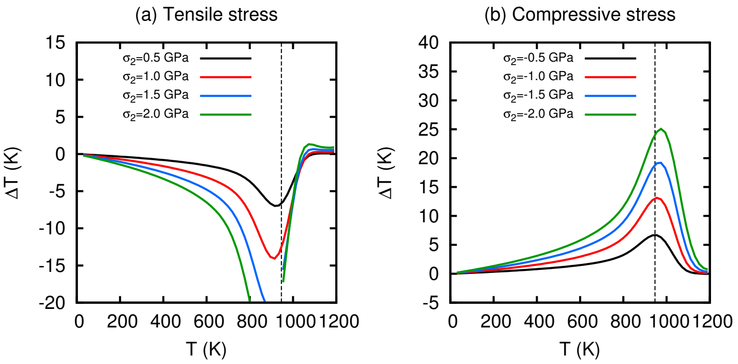

FIG. 2: Dependence of the piezocaloric ΔT on the temperature computed using the indirect approach. Vertical lines indicate computational transition temperatures.

In figure 3, we propose an experimental setup to achieve the required compressive and tensile stresses experimentally. In such a setup, a thin layer of $PbZrO_3$ is deposited on top of a substrate. Bending of the substrate creates tensile or compressive stress in the $PbZrO_3$ layer. From the mechanics of beam bending we estimate that achieving 1 GPa of compressive or tensile stress in a micron thick $PbZrO_3$ film deposited on a few micron thick $SrTiO_3$ substrate requires a bending radius of 45 microns.

In summary, we studied the intrinsic PCE in an antiferroelectric $PbZrO_3$ sample using the first-principles-based effective Hamiltonian approach. Our computations predict the existence of a very large PCE when the external stress acts along the orthorhombic *c*-axis. The coexistence of both the positive and negative PCE in the same material is very attractive for potential application, as it allows enhancement of the overall caloric response.

Financial support for this work provided by the National Science Foundation Grant No. DMR-1250492.

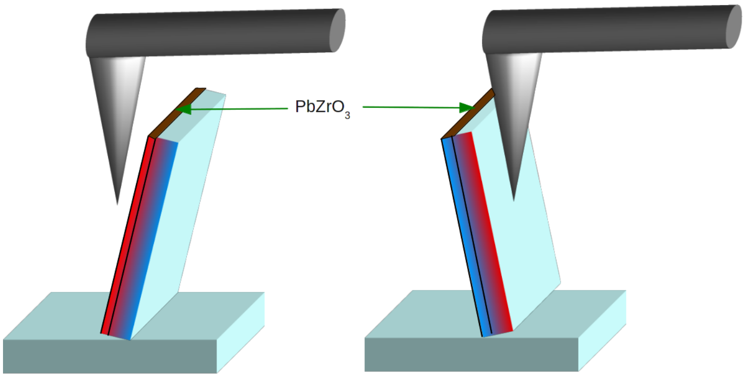

(a) Tensile stress (b) Compressive stress

FIG. 3: Schematic view of the bending setup for experimental demonstration of the PCE. The red and blue colors schematically indicate tensile and compressive stresses. respectively, that develop in the structure upon bending.

---

[1] V. K. Pecharsky and J. K. A. Gschneidner, Phys. Rev. Lett. **78**, 4494 (1997).
[2] B. K. Mani, S. Lisenkov, and I. Ponomareva, Phys. Rev. B **91**, 134112 (2015).
[3] I. Ponomareva and S. Lisenkov, Phys. Rev. Lett. **108**, 167604 (2012).

Antiferroelectric Rare-Earth-Substituted BiFeO$_3$:

A Lead-Free system for Large Energy Storage Density

Bin Xu[1], Jorge Íñiguez[2], Laurent Bellaiche[1]

[1]Physics Department and Institute for Nanoscience and Engineering, University of Arkansas, Fayetteville, Arkansas 72701, USA
[2]Materials Research and Technology Department, Luxembourg Institute of Science and Technology (LIST), 5 avenue des Hauts-Fourneaux, L-4362 Esch/Alzette, Luxembourg

A rapidly increasing proportion of electricity comes from renewable resources; however, the intermittent nature of some primary sources (e.g., wind, solar energy etc.[1]) throws a challenge on maintaining the balance between production and demand. Storing the energy temporarily or for a prolonged period of time composes one indispensable solution, but most of the available technologies, e.g., compressed air, pumped hydro, or even advanced batteries lack the ability to respond fast enough (less than a second). High-power energy storage systems, in particular the electrostatic capacitors with response time on millisecond scale or less, is uniquely suitable for effectively managing the energy resources with dramatic fluctuations.[2][3]

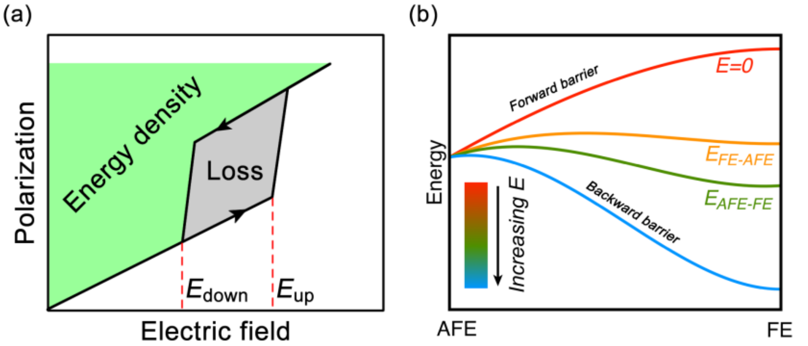

Figure 1. Schematic illustrations. (a) The definition of stored energy density and energy loss from the AFE *P-E* hysteresis loop; (b) the energetic path and barriers connecting the AFE and FE phases with increasing E-field.

In fact, storage applications using electrostatic capacitors are largely absent due to their relatively low energy densities. Continuous efforts have been devoted to find new materials with high energy density, and antiferroelectrics (AFE) are especially promising because of their characteristic polarization-electric field (*P-E*) double hysteresis loops (Figure 1a).[4] Large energy density of about 50 J cm^{-3} has been achieved in PbZrO$_3$-based films,[5][6][7] but more attention is directed to the environmentally friendly lead-free systems. [8][9][10][11] Among them, the (Bi$_{1/2}$Na$_{1/2}$)$_{0.9118}$La$_{0.02}$Ba$_{0.0582}$(Ti$_{0.97}$Zr$_{0.03}$)O$_3$ (BNLBTZ) epitaxial relaxor thin film can reach an energy density of 154 J cm^{-3},[10] i.e., comparable to that of good electrochemical supercapacitors;[12] however, despite the complexity in composition, the performance relies on the coexistence of ferroelectric/antiferroelectric (FE/AFE) phases near the morphotropic phase boundary, which is relatively sensitive to the change of composition and temperature. A much simpler and more robust system (AFE Hf$_x$Zr$_{1-x}$O$_2$ thin films) has been reported by Park *et al.* recently,[11] but the energy storage density is about five times lower than that of BNLBTZ.

It is therefore of great interest to generalize the characteristics about how to achieve high energy-storage performance. We rationalize the basic principles that can lead to high energy density and efficiency of a common AFE structure, i.e., the *Pnma* phase, and demonstrate with a novel material for energy storage, i.e., rare-earth substituted BiFeO$_3$ (BRFO), which is an excellent example as it provides good flexibility for tuning the energy landscape by composition and polymorphs depending on the E-field orientations. By conducting simulations using a newly-developed effective Hamiltonian[13], we find this system very promising for its energy storage performance, temperature stability and chemical simplicity. The storage

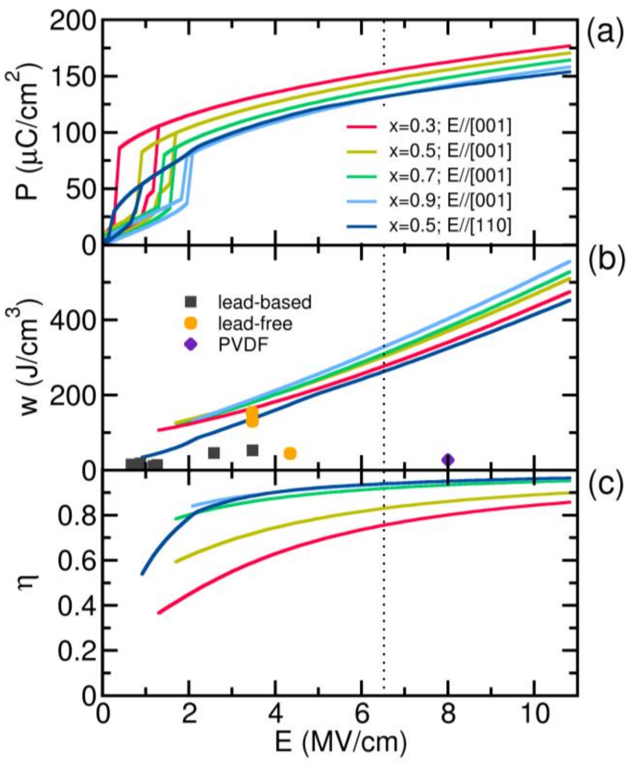

Figure 2. The calculated energy storage performance of selected $Bi_{1-x}Nd_xFeO_3$ solid solutions as a function of the electric field. a) The *P-E* hysteresis curves. b) The energy density. Discrete symbols represent the best available experimental data (lead-based, [5][6][15][16][17] **lead-free,[11][10] and PVDF**[15]**). c) The efficiency. The dotted vertical line denotes the electric field that has been applied in BFO thin films.[14]**

ability is expected to be achievable for a variety of rare-earth elements, and we predict that $Bi_{1-x}Nd_xFeO_3$ (BNFO) has an energy density higher than 250 J cm^{-3} for x>0.3 and a maximum electric field of 6.5 MV cm^{-1} (note that such field was achieved in BFO thin films experimentally[14]) and at the same time good efficiency (75-94%). The dependence of storage properties on the composition, E-field orientation, temperature, and strain are studied in details.

Acknowledgements This work is financially supported by the Department of Energy, Office of Basic Energy Sciences, under contract ER-46612 (B.X. and L.B.). J.I. is financially supported by the Fond National de Recherche Luxembourg through a PEARL grant (FNR/P12/4853155/Kreisel). J.I. and L.B. also thank the support of INTER/MOBILITY/15/9890527 GREENOX

References

[1] R. Gross, *et al.*, *Environ. Int.* **2003**, *29*, 105.
[2] L. Haspert, *et al.*, *Energy Environ. Sci.* **2013**, *6*, 2578.
[3] S. Sherrill, *et al.*, *Phys. Chem. Chem. Phys.* **2011**, *13*, 20714.
[4] X. Hao, *J. Adv. Dielectr.* **2013**, *03*, 1330001.
[5] B. Ma, *et al.*, *J. Mater. Res.* **2009**, *24*, 2993.
[6] B. Ma, *et al.*, *Mater. Lett.* **2009**, *63*, 1353.
[7] X. Hao, *et al.*, S. An, *Appl. Phys. Lett.* **2013**, *102*
[8] B. Chu, *et al.*, *Sci.* **2006**, *313* , 334.
[9] T. Correia, *et al.*, *J. Am. Ceram. Soc.* **2013**, *96*, 2699.
[10] B. Peng, *et al.*, *Adv. Electron. Mater.* **2015**, *1*, 1500052.
[11] M. Park, *et al.*, *Adv. Energy Mater.* **2014**, *4*, 1400610.
[12] K. Xie, *et al.*, *Nanoscale* **2011**, *3*, 2202.
[13] B. Xu, *et al.*, *Adv. Funct. Mater.* 25, 552 (2015).
[14] H. Yamada, *et al.*, *ACS Nano* **2013**, *7*, 5385.
[15] K. Yao, *et al.*, *IEEE Trans. Ultrason. Ferroelectr.*
[16] M. Ye, *et al.*, *J. Am. Ceram. Soc.* **2011**, *94*, 3234.
[17] X. Hao, *et al.*, *J. Am. Ceram. Soc.* **2011**, *94*, 1647.

Structural (in)stability of complex perovskites for solid oxide fuel cells: first principles calculations

M.M. Kuklja[1], E.A. Kotomin[2,3], D. Fuks[4], Yu. A. Mastrikov[3], J. Maier[2]

[1]Materials Science and Eng. Department, Univ. Maryland, College Park, MD, USA
[2]Max Planck Institute for Solid State Research, Heisenbergstr. 1, Stuttgart, Germany
[3]Institute for Solid State Physics, University of Latvia, Kengaraga str. 8, , Latvia
[4]Dept Materials Engineering, Ben Gurion University of the Negev, Beer Sheva, Israel

Among advanced materials for clean energy, non-stoichiometric $Ba_xSr_{1-x}Co_{1-y}Fe_yO_{3-\delta}$ (BSCF) and $La_xSr_{1-x}Co_{1-y}Fe_yO_{3-\delta}$ (LSCF) are considered as promising materials for cathodes in solid oxide fuel cells (SOFC) and oxygen permeation membranes [1-3]. BSCF exhibits the best oxygen exchange performance among similar materials, mixed ionic and electronic conductivity, high oxygen vacancy concentration, and low oxygen diffusion activation barrier, which largely define the oxygen reduction kinetics. However, it tends to decompose at low temperatures into a mixture of cubic and hexagonal perovskite phases, which strongly affects its practical applications.

To understand the mechanism(s) of this unwanted process, the first principles quantum mechanical calculations of BSCF and LSCF crystals with different non-stoichiometry and Frenkel/Schottky defects were performed and possible decomposition scenarios were studied [3,4]. It is shown that interstitial oxygen ions form dumbbell configuration with a regular host O ions (Fig.1). The formation energies of oxygen vacancies in the cubic and hexagonal phases of BSCF differ considerably and also behave in quite different ways depending on non-stoichiometry (Fig.2); in fact, it is the oxygen non-stoichiometry that makes the cubic phase more stable than the hexagonal phase. In comparison, LSCF is shown to be much more stable with respect to both the phase transformation and phase decomposition.

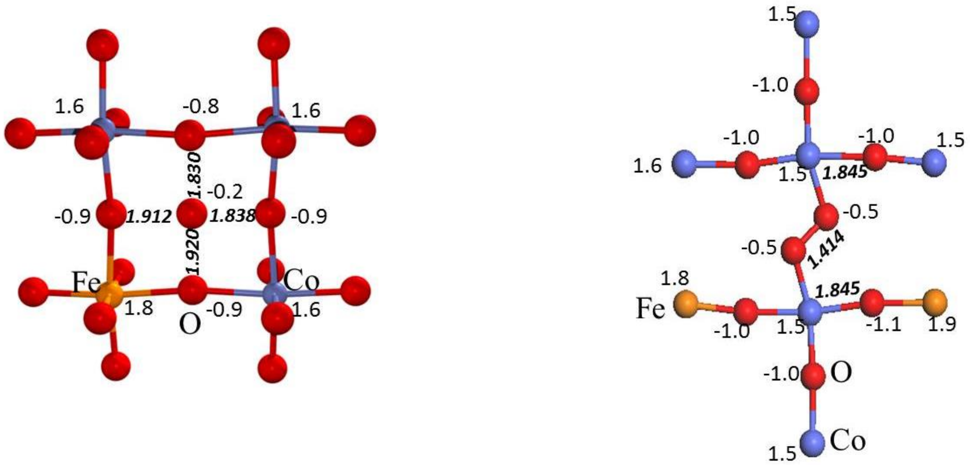

Fig.1. The oxygen hollow (left) and split (right) interstitial configurations, their atomic charges (e), and inter-atomic distances (Å) [4].

.

First principles calculations were performed also for a series of related perovskite solid solutions with a detailed thermodynamic analysis of the conditions under which a cubic phases are stable (Fig. 3) [5], in good agreement with experimental data.

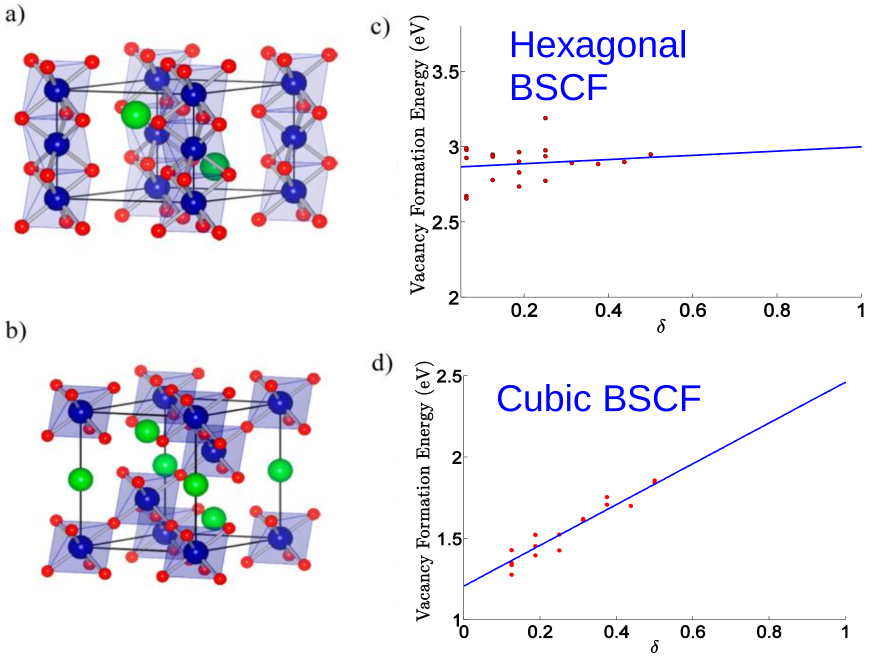

Figure 2. The lattice structure of a) hexagonal 2H and b) cubic BSCF82 phases, and calculated vacancy formation energies c) and d) as a function of oxygen nonstoichiometry δ [2]. Different energies for the same δ reflect variations in cation and vacancy configurations in the supercells.

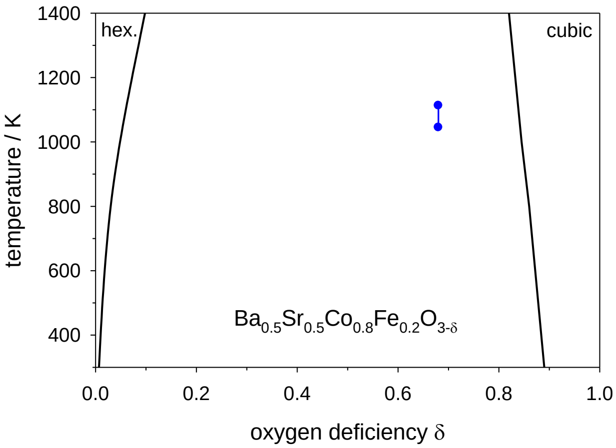

Figure 3. Phase diagram of hexagonal/cubic BSCF5582 from thermodynamic modeling [5] based on *ab inito* total energies. The black line (solvus) shows the stability boundary. Blue symbols show the stability limit for cubic BSCF82 as extracted from experiments in 0.01-0.2 bar O_2.

[1] J. A. Kilner et al, Ann. Rev. Mater. Res. 44, 365 (2014).
[2] M. Kuklja, et al, Phys. Chem. Chem. Phys. **15**, 5443 (2013).
[3] Yu. Mastrikov et al, Phys. Chem. Chem. Phys. **15**, 911 (2013).
[4] M.M. Kukla et al, J Phys Chem C 116, 18605 (2012).
[5] D. Fuks et al. J. Mater. Chem. A **1**, 14320 (2013)

Semiconducting Ferroelectric Photovoltaics

Jonathan E Spanier
Department of Materials Science & Engineering and Department of Physics
Drexel University, Philadelphia PA USA

In classic solid-state photovoltaic devices photo-generated charges are separated by the field at a *p-n* junction, a dye-sensitizer interface, or a domain boundary, or due to the Dember effect. All of these photovoltaic effects have in common the following: an inhomogeneous excitation or spatially-inhomogeneous medium; and the photovoltage does not exceed the band gap E_g. The bulk photovoltaic effect[1,2,3] (BPVE) in non-centrosymmetric crystals is a striking physical phenomenon: the photovoltage generated by the BPVE can greatly exceed the band gap E_g, but the direct conversion of light energy to electricity is extremely low. Over the past decade, photovoltaic effects in polar materials have attracted renewed attention. Also known as the anomalous photovoltaic effect, the BPVE can be observed in crystals which belong to twenty point groups lacking a center of inversion symmetry. I will first discuss recent advances in understanding the BPVE light-matter interaction, charge carrier separation and energy conversion in ferroelectric perovskite oxides.

Ferroelectric oxides possess band gaps that are generally far too large to be considered for practical photovoltaic solar energy conversion. Recent efforts focusing on cation substitution chemistries promoting generation of Ni^{2+}-O vacancy pairs have been shown to significantly increase the long-wavelength visible optical absorption without loss of ferroelectricity, enabling a completely new family of visible light-absorbing ferroelectric solid-solution semiconductors.[4] In the second part of my talk I will discuss the structural and ferroelectric phase evolution in the bulk ceramic $(1-x)KNbO_3$ - $xBa(Ni,Nb)O_{3-\delta}$ solid solution (KBNNO) probed by temperature-dependent Raman scattering spectroscopy, comparing results to those obtained in end member $KNbO_3$. I will also present and discuss our recent progress in characterizing the electronic structure and properties of KBNNO in epitaxial film form grown by physical vapor deposition, highlighting challenges and opportunities.

Work supported by the ARO under W911NF-14-1-0500 and NSF under DMR 1124696.

---

[1] A. A. Grekov, *et al.*, *Sov. Phys. Crystallogr.* 15, 423 (1970).
[2] V. M. Fridkin *et al.*, *Ferroelectrics* 8, 433 (1974).
[3] A. M. Glass *et al.*, *Appl. Phys. Lett.* 25, 233 (1974).
[4] I. Grinberg, *et al. Nature* 503, 509 (2013).

From soft harmonic phonons to fast relaxational dynamics in $CH_3NH_3PbBr_3$:

C. Stock-***School of Physics and Astronomy, University of Edinburgh***
I. Swainson-***National Research Council, Chalk River***
S. Parker and J. W. Taylor- ***ISIS Facility, Rutherford Appleton Labs***
L. Van Eijck-***ILL and Reactor Institute Delft***
M. Russina-***Helmholtz Zentrum Berlin fur Materialien and Energy***

The lead-halide perovskites, including $CH_3NH_3PbBr_3$, are components in cost effective, highly efficient photovoltaics, where the interactions of the molecular cations with the inorganic framework are suggested to influence the electronic and ferroelectric properties. $CH_3NH_3PbBr_3$ undergoes a series of structural transitions associated with the orientational order of the CH_3NH_3 (methylammonium) molecular cation and tilting of the $PbBr_3$ host framework. We apply high-resolution neutron scattering to study the soft harmonic phonons associated with these transitions, and find a strong coupling between the $PbBr_3$ framework and the quasistatic CH_3NH_3 dynamics at low energy transfers. At higher energy transfers we observe a $PbBr_6$ octahedra soft mode driving a transition at 150 K from bound molecular excitations at low temperatures to relatively fast relaxational excitations that extend up to 50-100 meV. We suggest that these temporally overdamped dynamics enables possible indirect band gap processes in these materials that are related to the enhanced photovoltaic properties.

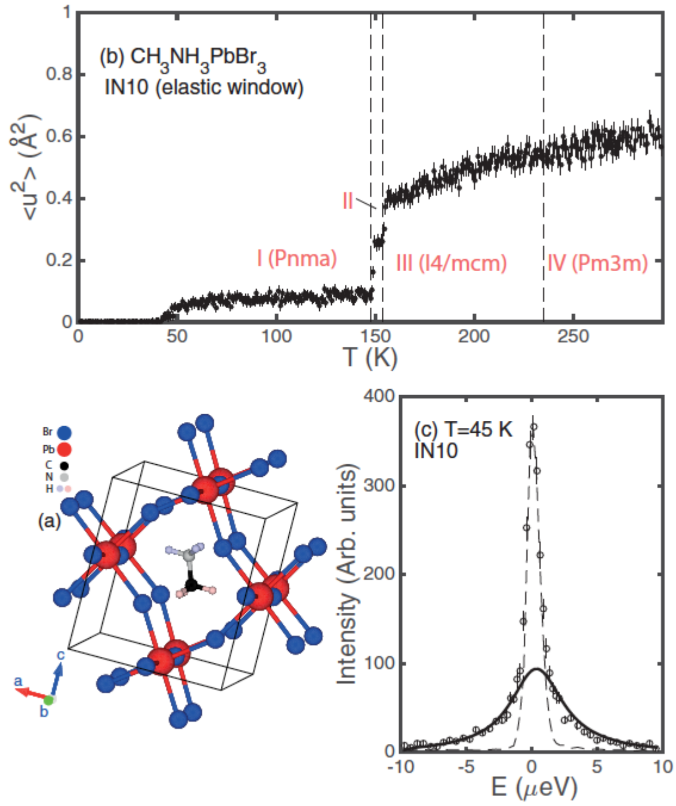

Figure 1: (a) An illustration of the structure. (b) shows the mean-squared displacement of the H-atoms. (c) plots a quasielastic scan at 45 K.

Organic-inorganic, hybrid perovskites (OIPs) are materials based upon an inorganic perovskite host framework with an organic molecular cation occupying the interstitial space. These materials have been studied for quite some time, but interest has recently surged owing to their use in photovoltaic devices and to possible ferroelectricity [1]. While earlier work centered on Sn-based OIPs as possible sensor materials, recent interest has been focused towards Pb-based OIPs, due to their potential advantages in inexpensive photovoltaic devices, with efficiencies of the order of 20% [2].

The OIPs are composed of two sublattices (Fig. 1 (a) for $CH_3NH_3PbBr_3$): the inorganic sublattice, consisting of a fully corner-bonded framework of octahedra ($PbBr_6^-$); and the organic sublattice consisting of the MA molecular cation, ($CH_3NH_3^+$). At high temperatures, the structure of $CH_3NH_3PbBr_3$ is cubic (space group Pm3m), and below 235 K has a tetragonal structure in symmetry I4/mcm. At 150 K, a transition to an unknown structure (believed to be incommensurate) occurs followed by further distortion to orthorhombic (Pnma) at 148 K. Neutron diffraction measurements have suggested that these transitions originate from tilting of the $PbBr_6$ octahedra and orientational ordering of the MA cation. We note that despite minor differences in the phase diagrams, for all $MAPbX_3$ (X=Cl,Br,I), a transition to an ordered phase, in which the octahedra are tilted and the MA cations have relatively well-defined orientations, occurs in the temperature range 150-175 K [3].

The various structural phase transitions as a function of temperature can be seen in Fig. 1 a) which plots the average mean squared displacement of the hydrogen ions as a function of temperature. The data was derived from the incoherent cross section measured on IN10 integrating energy transfers of +/- 1 μeV. Because the neutron incoherent cross section of hydrogen is over an order of magnitude larger than those of the non-H atoms, the angular-independent neutron scattering intensity is dominated by H dynamics. The temperature scans illustrate an onset of fluctuations near 50 K where dynamic processes enters the resolution of the IN10 spectrometer. With increasing temperature, this is followed by an abrupt change at the I--II and II-III structural transitions of 148 K and 154 K, respectively, from where the mean-squared displacement evolves continuously with increasing temperature.

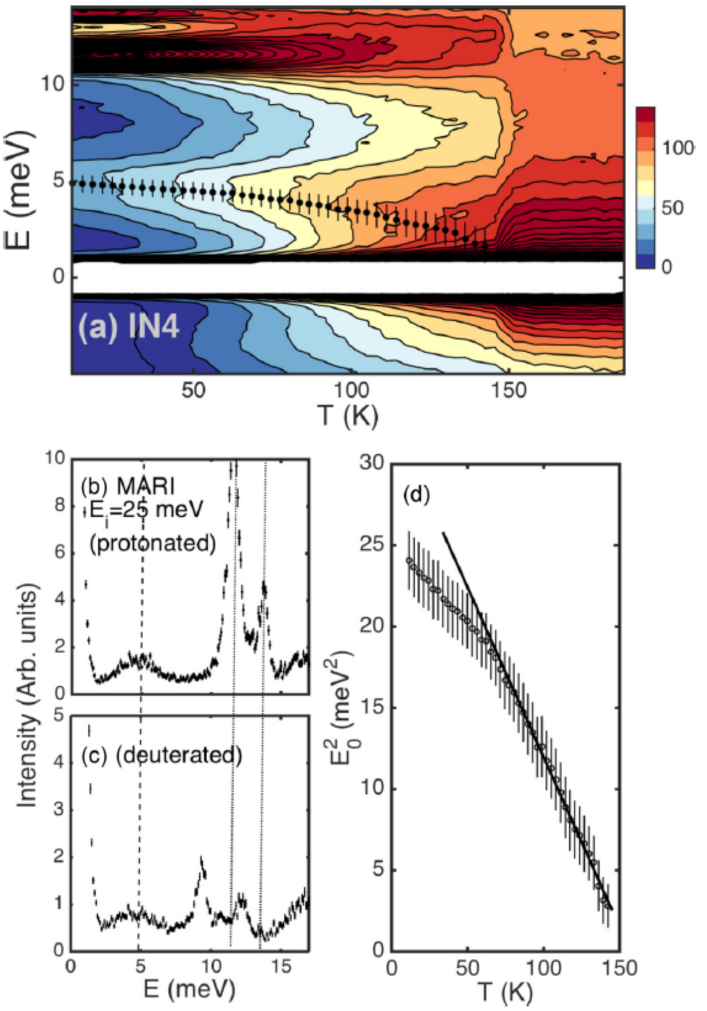

Figure 2: (a) displays inelastic scans vs temperature. (b) and (c) show momentum integrated scans on fully protonated and deuterated samples. (d) shows the square of the $PbBr_6$ octahedra phonon frequency vs T.

To study the dynamics of the host $PbBr_3$, we used the IN4 and MARI direct geometry chopper spectrometers. The results of these experiments are displayed in Fig. 2. Panel (a) shows the powder averaged spectrum on IN4 as a function of temperature. A distinct soft mode is seen and highlighted by the filled points. A plot of the frequency squared as a function of temperature is shown in panel (d) illustrating that the soft mode follows "Cochran's Law" from 50 K up to the transition at 150 K. A deviation is observed at around 50 K where molecular quasistatic dynamics are onset (Figure 1). We associate this soft mode with the $PbBr_3$ framework based upon two reasons. First, on deuteration the mode frequency does not shift (panels b-c) and second, first principles calculations assign this mode to the framework lattice.

An interesting observation in Figure 2 is that above 150 K the molecular dynamics cross over from being quasistatic to being relaxational with a large energy width. Further work on MARI finds these quasistatic dynamics to extend up to 50 -100 meV.

In summary, we report a neutron inelastic scattering study of the coupled molecular and framework dynamics in $CH_3NH_3PbBr_3$. We observe quasistatic molecular fluctuations coupled to a soft mode associated with tilting of the $PbBr_3$ framework. The low-temperature harmonic fluctuations cross over to fast overdamped relaxational dynamics at higher temperatures.

This work was funded by the Carnegie Trust for the Universities of Scotland and the EPSRC. This talk is based on work published in Phys. Rev. B ***92****, 100303(R) (2015).*

References:

[1] R. Wyckoff, Am. J. Sci. **16**, 349 (1928); A. Kojima *et al.* J. Am. Chem. Soc. **131**, 6050 (2009).
[2] N. G. Park, Phys. Chem. Lett. **4**, 2423 (2013).
[3] I. P. Swainson *et al.* J. Solid State Chem. **176**, 97 (2003).

Ferroelectric domains in the presence of molecular orientational disorder in hybrid perovskites

Liang Z. Tan, Fan Zheng, and Andrew M. Rappe

The Makineni Theoretical Laboratories, Department of Chemistry,
University of Pennsylvania, Philadelphia, Pennsylvania 19104-6323, USA

The hybrid organometallic halide perovskites, well known for their large and growing photovoltaic power conversion efficiencies [1,2], display ferroelectric phenomena which is at present still poorly understood. Experiments demonstrate the presence of ferroelectric domains [3], while also reporting extensive dynamical disorder of the molecular dipoles [4]. In this work, using first-principles density functional theory calculations and large-scale Monte Carlo simulations, we show that partial ordering of molecular components gives rise to a relaxor-like state of coexisting finite polarization and molecular disorder.

We show that the emergence of this state is a consequence of short-range hydrogen bonding between the molecules and the inorganic PbI_3 lattice, and the long-range interactions between molecular dipoles, two factors unique to the hybrid perovskites. The effects of the hydrogen-halide bonds is two-fold: (i) their presence results in a large number local molecular configurations nearly degenerate in energy, and (ii) they give rise to an intricate effective molecule-molecule interaction mediated by the inorganic PbI_3 lattice. We systematically enumerate hydrogen-bonding modes as well as inorganic lattice distortions by generating an unbiased first-principles structure-energy database. Statistical analysis and progressive refinement of this database enables the identification of dominant bonding patterns and PbI_3 distortions, which we find include octahedral rotations and ferrodistortive displacements. Using these insights, we deduce a low-energy Hamiltonian to describe these short-range interactions as well as the long-range intermolecular dipole interactions. We perform Monte Carlo simulations at experimentally relevant length scales, showing the coexistence of ferroelectric domains and glassy behavior.

This work was supported by the Office of Naval Research under grant number N00014-14-1-0761.

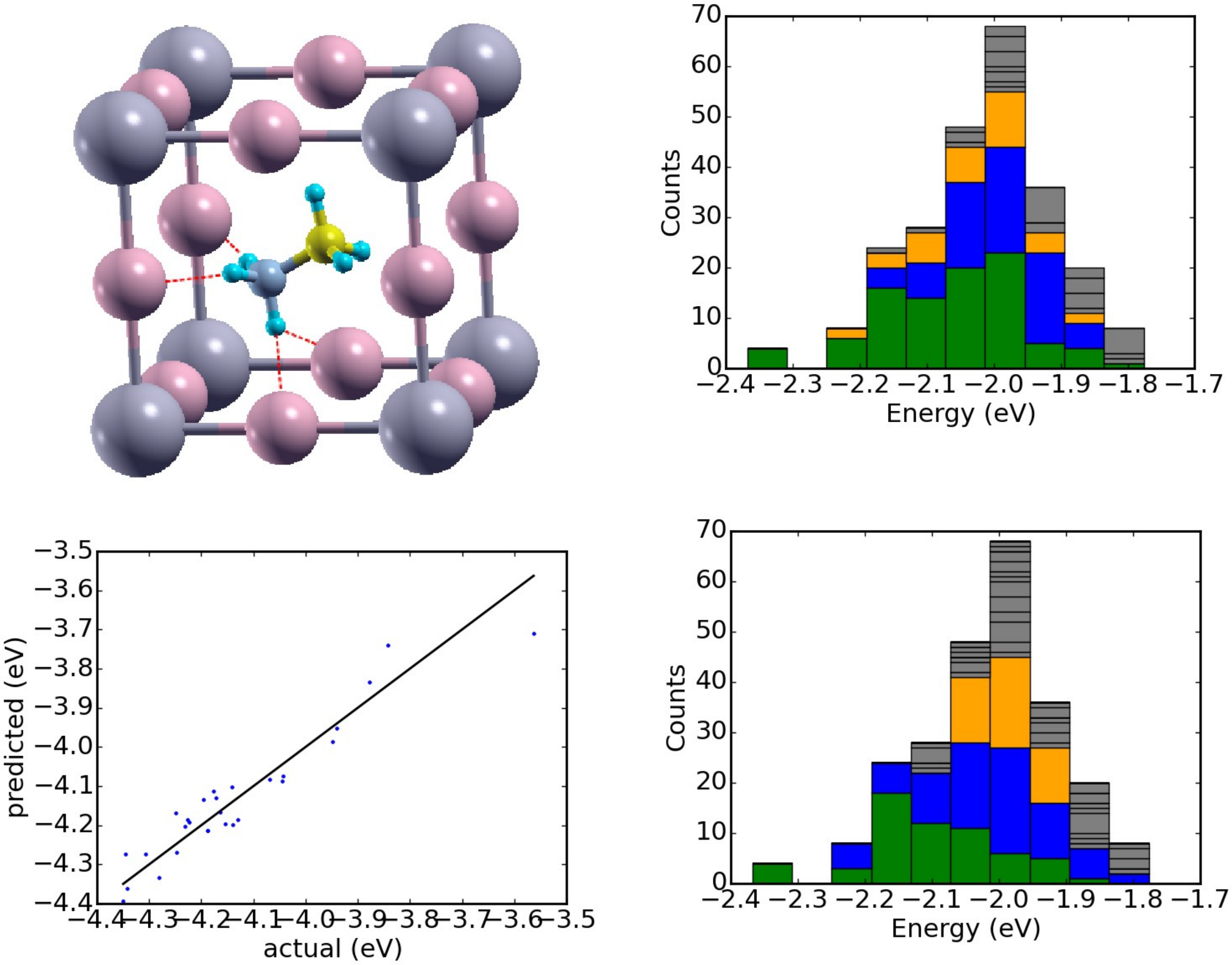

FIG. 1: (Clockwise, from top right) Top left: primitive unit cell of $MAPbI_3$, showing one of the dominant hydrogen-bonding modes in the tetragonal phase. Top right: histogram of hydrogen-bonding modes as a function of energy. The three most dominant modes are colored green, blue, and orange. The mode colored in blue is displayed in this figure. Bottom right: histogram of PbI_3 inorganic lattice distortion modes as a function of energy The three most dominant modes are colored green (pure octahedral tilting), and blue and orange (ferrodistortive). Bottom right: Comparison of predicted energies of model Hamiltonian and DFT calculated energies of a number of tetragonal phase structures.

References

[1] S. D. Stranks, G. E. Eperon, G. Grancini, C. Menelaou, M. J. P. Alcocer, T. Leijtens, L. M. Herz, A. Petrozza, and H. J. Snaith, Science 342, 341 (2013).
[2] T. M. Brenner, D. A. Egger, A. M. Rappe, L. Kronik, G. Hodes, and D. Cahen, The Journal of Physical Chemistry Letters 6, 4754 (2015).
[3] Y. Kutes, L. Ye, Y. Zhou, S. Pang, B. D. Huey, and N. P. Padture, The Journal of Physical Chemistry Letters 5, 3335 (2014).
[4] A. M. A. Leguy, J. M. Frost, A. P. McMahon, V. G. Sakai, W. Kochelmann, C. Law, X. Li, F. Foglia, A. Walsh, B. C. ORegan, et al., Nature Communications 6 (2015).

Synthesis and characterization of predicted oxynitride perovskite $YSiO_2N$.

Muhtar Ahart,[1] Maddury Somayazulu,[1] Rajasekarakumar Vadapoo,[1] Nicolas Holtgrewe,[1, 2] Yue Meng,[3] Russell J. Hemley,[1] and R. E. Cohen[1, 4, *]

[1]Extreme Materials initiative, Geophysical Laboratory, Carnegie Institution for Science, Washington, DC 20015 USA. [2]Department of Mathematics, Howard University, Washington DC 20059, USA. [3]HPCAT, Geophysical Laboratory, Carnegie Institution for Science, Argonne, Illinois 60439,USA. [4]Department of Earth and Environmental Sciences, Ludwig Maximilians University, Munich, Germany.

Attempts to produce polar oxynitrides have mostly been unsuccessful [1,2]. Caracas and Cohen explored possible polar ordered oxynitride ABO_2N perovskites using a materials by design approach[3]. They predicted $YSiO_2N$ to have a giant effective spontaneous polarization (130 μC/cm^2) and non-linear optic coefficients. They found the structure to be stable with P4mm symmetry (Fig. 1). Using a high-pressure and high-temperature method we have successfully synthesized the predicted polar ordered oxynitride.

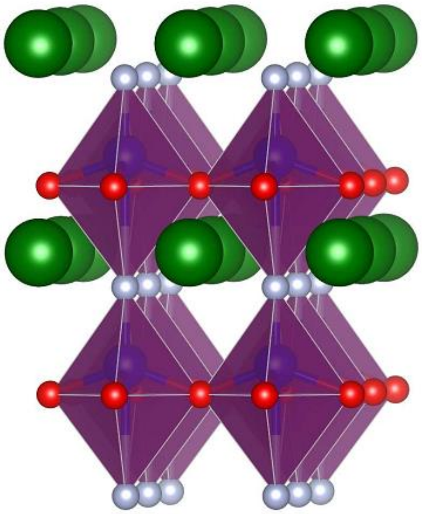

Fig. 1. polar P4mm structure of oxynitride perovskites ($YSiO_2N$), Where Y, Si, O and N represent by green, blue, red and grey balls respectively.

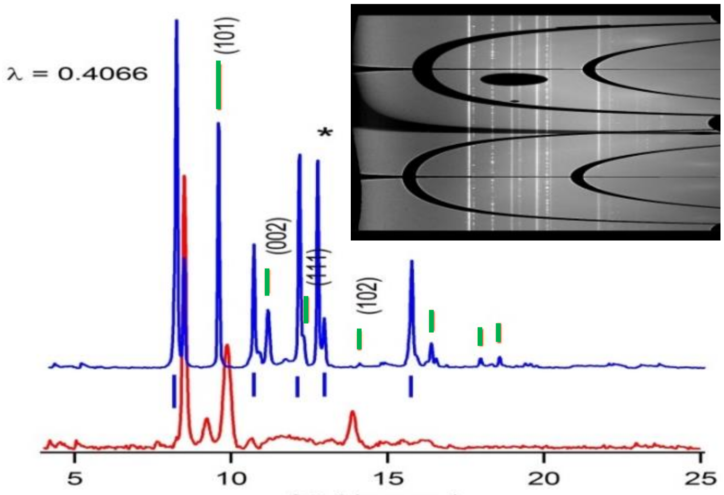

Fig. 2. X-ray diffraction pattern of high-pressure and high-temperature synthesized sample at 20 GPa, 2000 K (blue pattern). Red pattern is the parent material at 20 GPa before laser heating. The blue vertical line corresponds to stishovite and green vertical line corresponds to the theoretically predicted $YSiO_2N$ structure. Insert shows the corresponding CCD image of the diffraction lines at 20 GPa. * denotes unidentified peak.

We finely grind the stoichiometric yttrium nitride (YN) and amorphous silica together in an argon atmosphere. We loaded the fine ground parent material to the diamond anvil cell (DAC) and compressed to 20 GPa and then heated using double sided laser heating. The sample is analyzed for its structural properties and its polar nature. We used the synchrotron X-ray diffraction (XRD) at the Advanced Photon Source beam line 16-IDB for the X-ray studies. The diffraction pattern (Fig. 2, blue pattern indexed peaks) confirm synthesize of $YSiO_2N$ predicted by theory and the lattice parameter is calculated to be a=3.09 Å and c= 4.25 Å within P4mm along with the stishovite peaks. We can also see the unreacted YN and an unassigned peak along with the synthesized material.

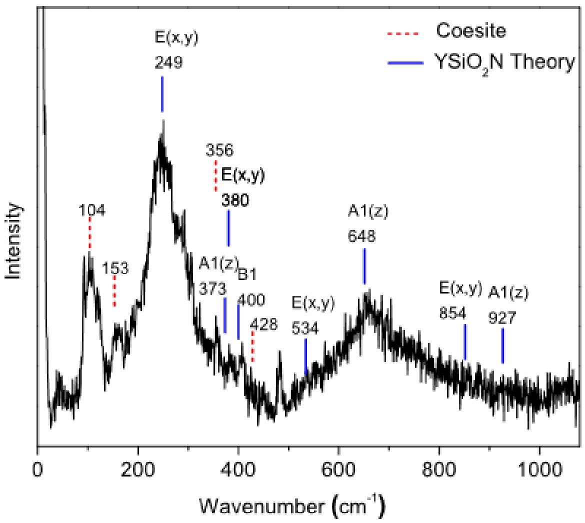

Fig. 3. Raman spectra of the $YSiO_2N$ synthesized at high-pressure and high-temperature method at 12 GPa, 1200 K and measured at 3 GPa.

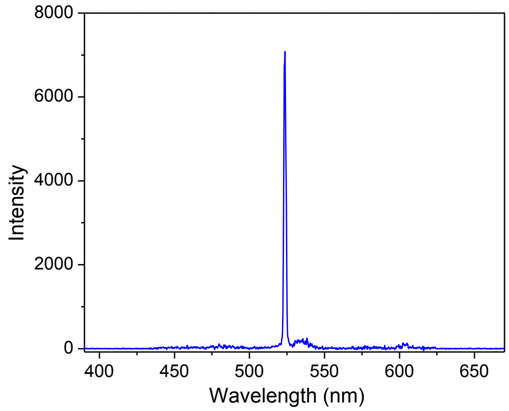

Fig. 4. Observation of strong optical second harmonic generation of synthesized $YSiO_2N$ excited by a near IR 1064 nm pulsed laser.

We find that $YSiO_2N$ formed at 12 GPa or above and 1200 K. The Raman spectra show the dominant modes are in good agreement with predicted modes by theory along with the Coesite modes (Fig. 3). The synthesized material is characterized for its inversion symmetry by Second Harmonic Generation and shows very strong signal thus confirming its polar nature (Fig.4).

Acknowledgement: This work is supported by ONR and CDAC.

References:

[1] Fuertes, A. *Journal of Materials Chemistry* **22**, 3293 (2012)

[2] Ebbinghaus, S. G. *et al. Progress in Solid State Chemistry* **37**, 173–205 (2009)

[3] Caracas, R. & Cohen, R. E. *Applied Physics Letters* **91**, 092902 (2007)

Atomistic Simulations of Complex Problems in Ferroelectrics

A. Al-Barakaty[1], L. Bellaiche[2], A. A. Bokov[3], B. Dkhil[4], Z. Gui[2], J. Hlinka[5], Yousra Nahas[2], Sergei Prokhorenko[2], S. Prosandeev[2], D. Wang[6], Lin-Wang Wang[7], and Z.-G. Ye[3,6]

[1] *Physics Department, Jamoum University College, Umm Al-Qura University, Makkah, Saudi Arabia*
[2] *Physics Department and Institute for Nanoscience and Engineering, University of Arkansas, Fayetteville, Arkansas 72701, USA*
[3] *Department of Chemistry and 4D LABS, Simon Fraser University, Burnaby, British Columbia V5A 1A6, Canada*
[4] *Laboratoire Structures, Proprietes et Modelisation des Solides, CentraleSupelec, CNRS-UMR8580, Grande Voie des Vignes, 92295 Chatenay-Malabry Cedex, France*
[5] *Institute of Physics, Academy of Sciences of the Czech Rep., Na Slovance 2, CZ-182 21 Praha 8, Czech Republic*
[6] *Electronic Materials Research Laboratory, Key Laboratory of the Ministry of Education and International Center for Dielectric Research, Xi'an Jiaotong University, Xi'an 710049, China*
[7] *Materials Science Division, Lawrence Berkeley National Laboratory, Berkeley, California 94720, USA*

In the last 25 years or so, the intensive use and development of first-principle-based methods have led to a better knowledge of ferroelectrics and related materials. However, some particularly challenging issues are still commonly believed to be too complex to be accurately tackled by atomistic simulations in these systems.

The aim of this talk is to report how it is, in fact, possible to investigate some of these issues, and what can be learnt from them. In particular and if time allows, the following topics will be discussed:

- (1) Investigating the electronic structure of electrical vortices:

An original *ab-initio* procedure is developed and applied to a ferroelectric nanocomposite, in order to reveal the effect of electrical vortices on electronic properties [1]. Such procedure involves the combination of two large-scale numerical schemes, namely an effective Hamiltonian (to incorporate ionic degrees of freedom) [2] and the linear-scaling three-dimensional fragment method (to treat electronic degrees of freedom) [3]. The use of such procedure sheds some light into the origin of the recently observed current that is activated at rather low voltages in systems possessing electrical vortices [4]. It also reveals a novel electronic phenomenon, that is a systematic control of the type of the band-alignment (i.e., type-I versus-type-II) within the same material via the temperature-driven annihilation/formation of electrical topological defects.

- (2) Mimicking finite-temperature properties of the prototype of relaxor ferroelectrics, that is Pb(Mg,Nb)O_3 (PMN):

An atomistic numerical scheme is developed and used to study PMN at finite temperature [5]. This scheme not only reproduces known complex macroscopic static properties of PMN, but also provides a deep microscopic insight into this puzzling system. In particular, relaxor properties of PMN are found to originate from the competition between (1) random electric fields arising from the alloying of Mg and Nb ions belonging to different columns of the periodic Table within the same sublattice; (2) the simultaneous condensation of several off-center k-points as a result of a specific short-range, antiferroelectric-like interaction between lead-centered dipoles; and (3) ferroelectric-like interactions. Such origins contrast with those recently proposed for the homovalent Ba(Zr,Ti)O_3 solid solution [6], despite the fact that these two materials have similar macroscopic properties -- which therefore leads to a deeper understanding of relaxor ferroelectrics.

- (3) Modeling the main dynamical features of relaxor ferroelectrics:

Here, we report first-principles-based Molecular dynamic simulations applied to the lead-free Ba(Zr,Ti)O_3 relaxor ferroelectric, which allow us to obtain the subterahertz dynamics of this material. This approach is demonstrated to reproduce the striking dynamical characteristics of relaxor ferroelectrics, including the relaxation of their dielectric response, the constant-loss behavior, the diffuse maximum in the temperature dependence of their dielectric susceptibility, the substantial widening of dielectric spectrum upon cooling, and the resulting Vogel-Fulcher law. The present simulations further reveal the origin of such features thanks to the decomposition of the dielectric response into several contributions, each associated with its own polarization mechanism.

This work is supported by ONR Grant N00014-12-1-1034, the Department of Energy, Office of Basic Energy Sciences, under contract ER-46612, NSF grant DMR-1066158, ARO grant W911NF-12-1-0085, DARPA grant HR0011-15-2-0038 and AFOSR grant FA9500-16-1-0065. Some computations were also made possible thanks to the MRI grant 0722625 from NSF, the ONR grant N00014-15-1-2881 (DURIP) and a Challenge grant from the Department of Defense.

References:

[1] Zhigang Gui, Lin-Wang Wang and L. Bellaiche, Nano Letters 15, 3224 (2015).

[2] L. Walizer, S. Lisenkov and L. Bellaiche, Phys. Rev. B 73, 144105 (2006).

[3] L.-W Wang, Z. Zhao and J. Meza, Phys. Rev. B 77, 165113 (2008).

[4] N. Balke et al, Nat. Phys. 8, 81 (2012).

[5] A. Al-Barakaty, S. Prosandeev, D. Wang, B. Dkhil and L. Bellaiche, Phys. Rev. B 91, 214117 (2015).

[6] A. R. Akbarzadeh, S. Prosandeev, E. J. Walter, A. Al-Barakaty and L. Bellaiche, Phys. Rev. Lett. 108, 257601 (2012).

Format: invited

To switch or not to switch: another probe microscopy perspective

Petro Maksymovych, Stephen Jesse, Qian Li, Arthur P. Baddorf, Sergei V. Kalinin, and Nina Balke
Center for Nanophase Materials Sciences
Oak Ridge National Laboratory, Oak Ridge, TN 37831

Piezoelectric and ferroelectric properties are broadly considered for information and energy technologies for converting mechanical to electrical energy or vice versa. Moreover, almost any mass transport in the material will be related to mechanical deformation, which recently enabled direct studies of ionic transport in energy storage materials. Local characterization of electromechanical response is often a preferred way to measure electromechanical response, particularly with respect to structure-function relationships of inhomogeneous materials. Unfortunately, existing approaches fail to provide quantitative values and pose significant ambiguity with respect to the origin of electromechanical response, for example to distinguish between the effects of charge injection and piezoelectricity.

Piezoelectric Force Microscopy (PFM) has become a very successful methodology to probe ferroelectric materials, by detecting surface deformation in the electric field of a biased microscope tip [1]. While PFM is an easily accessible characterization technique for thin films, quantification of the piezoelectric properties and the role of measurement artifacts are still poorly understood. Hysteresis of electromechanical response can originate from electrostatic interactions between the tip and sample involving slow surface charging or ionic mechanisms that mimic ferroelectric responses. Similarly, charge writing and strong electrostatic tip-sample interactions can appear as persistent domains in PFM. Distinguishing intrinsic and extrinsic contributions to the electromechanical sample response in oxide and chalcogenide-based films has been widely discussed, however, clear guidelines on how to distinguish them from ferroelectric responses is missing.

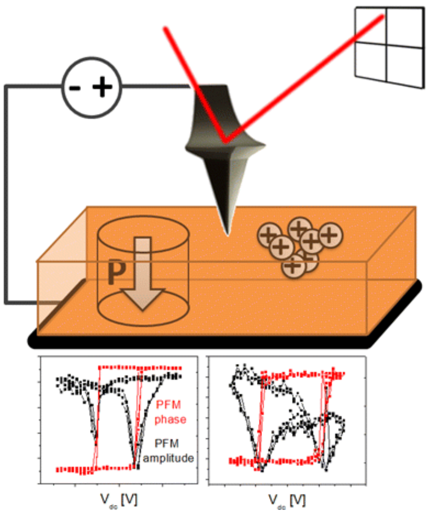

We will present a unified perspective on electromecahnical measurements that enables effective differentiation of ionic displacement, piezoelectric deformation and electrostatic interactions in the nanoscale contact geometry [2–4]. Furthermore, by modeling cantilever dynamics the surface displacements can be quantitatively extracted from the measurements, providing a systematic way to account for stochastic and deterministic variations in the experiments. These studies establish new opportunities for contact SPM to probe electroactive materials outside of the fairly limited family of strongly polarized ferroelectric materials, including ionic conductors, biological materials, electroactive polymers.

Support was provided by the U.S. Department of Energy, Basic Energy Sciences, Materials Sciences and Engineering Division through the Office of Science Early Career Research Program (NB) and US DOE MSED (SVK). Experiments were performed at the Center for Nanophase Materials Sciences, which is a DOE Office of Science User Facility.

[1] D. A. Bonnell, S. V. Kalinin, A. l. Kholkin, and A. Gruverman, MRS Bull. **34**, 648 (2009).
[2] N. Balke, P. Maksymovych, S. Jesse, I. I. Kravchenko, Q. Li, and S. V. Kalinin, Acs Nano **8**, 10229 (2014).
[3] N. Balke, P. Maksymovych, S. Jesse, A. Herklotz, A. Tselev, C.-B. Eom, I. I. Kravchenko, P. Yu, and S. V. Kalinin, ACS Nano **9**, 6484 (2015).
[4] N. Balke, S. Jesse, Q. Li, P. Maksymovych, M. B. Okatan, E. Strelcov, A. Tselev, and S. V. Kalinin, J. Appl. Phys. **118**, 072013 (2015).

First-principles theory of flexoelectricity

Massimiliano Stengel[1, 2]
[1]ICREA - Institució Catalana de Recerca i Estudis Avançats, 08010 Barcelona, Spain
[2]Institut de Ciència de Materials de Barcelona (ICMAB-CSIC), Campus UAB, 08193 Bellaterra, Spain

(Dated: December 23, 2015)

Flexoelectricity, the polarization response of an insulating material to a strain gradient, has sparked widespread interest in the past few years as a viable route towards novel electromechanical device concepts. [1–3] Flexoelectricity is a close relative of piezoelectricity, which describes the coupling between strain and polarization. Unlike the latter, which is present only in crystals that break inversion symmetry, it is a universal property of all insulators. The main drawback is that flexoelectricity is negligibly small in macroscopic samples, and this has limited its practical interest until very recently. The realization that, by downscaling the sample, one can enhance the effect in a proportion that is roughly inverse with its size, has motivated the current "revival". A number of interesting functionalities and potential device applications have been reported recently, including the possibility of rotating [4] or switching [5] the ferroelectric polarization by mechanical means, or of obtaining a pseudo-piezoelectric effect that is comparable in magnitude to the existing commercial units. [6]

Prior to practical exploitation it is crucial, however, to improve our understanding of how flexoelectricity works at the nanoscale. Being a higher-order effect, both the theoretical analysis and the interpretation of the experimental results are highly nontrivial, calling for advanced models and simulation techniques to cope with the many existing subtleties. [8] In this talk I will initially focus on three remarkable conceptual aspects of flexoelectricity that depart from the conventional picture of electromechanical phenomena:

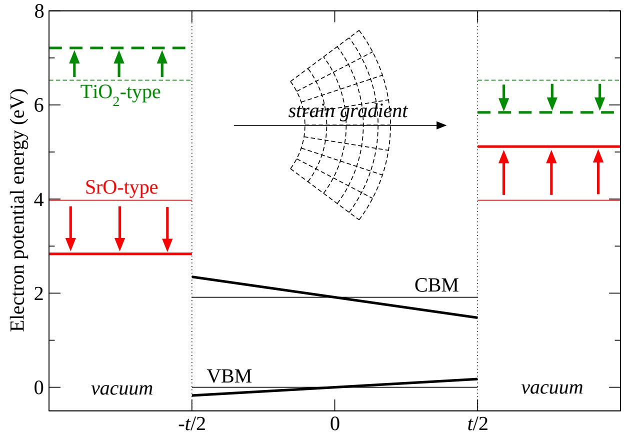

FIG. 1. Sketch of the relevant energy levels in a bent $SrTiO_3$ slab. Thin solid black lines indicate the flat conduction and valence band edges in the unperturbed system. Thin dashed black lines indicate the slab surfaces. Colored thin lines indicate the vacuum level. Upon bending, the band edges tilt and the vacuum levels shift (thick lines). An unrealistically large strain gradient, corresponding to a bending radius that is equal to slab thickness, is assumed for illustrative purposes. The inset illustrates the type (not the amplitude) of the deformation applied to the slab. From Ref. 7.

- First, a strain gradient is an inherently dynamical perturbation of the crystal lattice, and such a dynamic character propagates to the flexoelectric response coefficients. [9] (Unlike a uniform strain, which can always be produced via an appropriate combination of surface loads, some components of the strain-gradient tensor are only allowed in a sound wave, as they are associated with a local acceleration of the medium.) Yet, the flexoelectric polarization associated to a static deformation field is correctly described as a static property, as the explicit mass dependence disappears from any linear combination of the tensor components that is compatible with the mechanical equilibrium condition.

- Second, in a strain gradient the notion of macroscopic electric field becomes ambiguous, and depends on the choice of the energy reference that one uses to define the *deformation potential.* [7] (For example, in the interior of a bent slab the conduction band bottom, CBM, and valence band top, VBM, undergo different tilts, leading to two inequivalent possible definitions of the macroscopic electric field; see Fig. 1.) This points to a notable *gauge freedom* of a thermodynamic functional incorporating strain-gradient effects, whereby the flexoelectric coefficients (and hence the electrostatic energy of the corresponding electric fields) are, to a certain extent, arbitrary at the bulk level, but the actual physical observables are not.

- Third, the experimentally measured flexoelectric coefficients always contain a surface piezoelectric contribution that is of the same order as the bulk flexoelectric effect, even in the limit of a macroscopically thick sample. [10, 11] (A surface is always piezoelectric, as it breaks inversion symmetry by construction.) Such surface terms are affected by the same gauge arbitrariness as the bulk contributions, but with *opposite sign*, and are therefore

	Bulk	Surface (SrO)	Surface (TiO_2)
CBM	-0.87	3.15	-0.50
VBM	0.36	1.92	-1.73

TABLE I. Deformation potentials associated with static bending of a $SrTiO_3$ slab (plate-bending limit). The surface is assumed to be oriented along the [100] cubic direction. The label CBM or VBM refers to the choice of the reference energy in the slab interior. The bulk contributions consist in the tilts of the corresponding band edges that are illustrated in Fig. 1. The surface deformation potentials refer to the variation of the ionization potential (VBM) or electron affinity (CBM) under a uniform in-plane expansion (including Poisson ratio effects and full atomic relaxation) of the slab. The total (bulk and surface) deformation potentials are reference-independent and amount to: $D^{\mathrm{SrO}} = 2.28$ eV, $D^{\mathrm{TiO_2}} = -1.37$ eV. Values are in eV. From Refs. 16 and 7.

necessary for the total response of the system to be a well-defined physical quantity. [7, 10] Recent experimental measurements [12] indirectly confirm such predictions in the case of paraelectric $BaTiO_3$.

Even after clarifying the above points, calculating the relevant contributions to the flexoelectric response of a realistic system from first principles is no easy task. Strain gradients break the translational symmetry of the lattice, and this constitutes a major challenge for *ab initio* methods, which are traditionally based on periodic boundary conditions. An efficient workaround consists in describing strain gradients as the long-wavelength limit of an acoustic phonon perturbation. [13–15] By calculating the charge-density response of bulk and slab systems up to second order in the wavevector $\mathbf{q}$, [9] and by processing such information via an appropriate Poisson solver in curvilinear coordinates, [10] one can readily compute the full flexoelectric tensor, including both electronic and lattice-mediated effects.

As a practical demonstration, I will present results for the flexovoltage (i.e. open-circuit voltage induced by a strain gradient) response of a macroscopically thick $SrTiO_3$ slab. [16] In oder to demonstrate the surface dependence of the effect, I consider two different terminations of the (100)-oriented perovskite lattice, either of the SrO- or TiO_2-type. I will show that, upon static bending of the slab, one obtains a positive or a negative voltage response depending on the crystal lattice termination (Table I), which points to a dramatic dependence of the flexoelectric effect on the details of the sample surface.

This work was supported by MINECO-Spain through Grants No. FIS2013-48668-C2-2-P and No. SEV-2015-0496, and Generalitat de Catalunya (2014 SGR301). Calculations were performed at Supercomputing Center of Galicia (CESGA).

[1] P. Zubko, G. Catalan, and A. K. Tagantsev, "Flexoelectric effect in solids," Annu. Rev. Mater. Res. **43**, 387–421 (2013).

[2] Thanh D. Nguyen, Sheng Mao, Yao-Wen Yeh, Prashant K. Purohit, and Michael C. McAlpine, "Nanoscale flexoelectricity," Advanced Materials **25**, 946–974 (2013).

[3] P. V. Yudin and A. K. Tagantsev, "Fundamentals of flexoelectricity in solids," Nanotechnology **24**, 432001 (2013).

[4] G. Catalan, A. Lubk, A. H. G. Vlooswijk, E. Snoeck, C. Magen, A. Janssens, G. Rispens, G. Rijnders, D. H. A. Blank, and B. Noheda, "Flexoelectric rotation of polarization in ferroelectric thin films," Nature Materials **10**, 963–967 (2011).

[5] H. Lu, C.-W. Bark, D. Esque de los Ojos, J. Alcala, C. B. Eom, G. Catalan, and A. Gruverman, "Mechanical writing of ferroelectric polarization," Science **336**, 59–61 (2012).

[6] L. E. Cross, "Flexoelectric effects: Charge separation in insulating solids subjected to elastic strain gradients," J. Mater. Sci. **41**, 53 (2006).

[7] Massimiliano Stengel, "From flexoelectricity to absolute deformation potentials: The case of $SrTiO_3$," Phys. Rev. B **92**, 205115 (2015).

[8] M. Stengel and D. Vanderbilt, "First-principles theory of flexoelectricity," arXiv:1507.03440(2015).

[9] M. Stengel, "Flexoelectricity from density-functional perturbation theory," Phys. Rev. B **88**, 174106 (2013).

[10] M. Stengel, "Microscopic response to inhomogeneous deformations in curvilinear coordinates," Nature Communications **4**, 2693 (2013).

[11] A. K. Tagantsev, "Piezoelectricity and flexoelectricity in crystalline dielectrics," Phys. Rev. B **34**, 5883 (1986).

[12] Jackeline Narvaez, Sahar Saremi, Jiawang Hong, Massimiliano Stengel, and Gustau Catalan, "Large flexoelectric anisotropy in paraelectric barium titanate," Phys. Rev. Lett. **115**, 037601 (2015).

[13] R. Resta, "Towards a bulk theory of flexoelectricity," Phys. Rev. Lett. **105**, 127601 (2010).

[14] J. Hong and D. Vanderbilt, "First-principles theory of frozen-ion flexoelectricity," Phys. Rev. B **84**, 180101(R) (2011).

[15] J. Hong and D. Vanderbilt, "First-principles theory and calculation of flexoelectricity," Phys. Rev. B **88**, 174107 (2013).

[16] M. Stengel, "Surface control of flexoelectricity," Phys. Rev. B **90**, 201112(R) (2014).

,

Structure of Ultrathin Film Ba-Ti-O

Eric Cockayne*,[1] Marek Mihalkovič,[2] and Christopher L. Henley†[3]

[1] *Material Measurement Laboratory, National Institute of Standards and Technology, Gaithersburg, Maryland 20899 USA*
[2]*Institute of Physics, Slovak Academy of Sciences, 84511 Bratislava, Slovakia*
[3]*Department of Physics, Cornell University, Ithaca, New York 14850 USA*

$BaTiO_3$ is one of the best-known perovskite ferroelectrics, and has been extensively studied in its bulk and thin-film forms. Remarkably, a variety of new structures (including a dodecagonal *quasicrystal*) have recently been discovered in ultrathin Ba-Ti-O films fabricated via various multistep heat treatments of an initial thin film perovskite $BaTiO_3$ layer deposited on a Pt(111) surface.[1, 2] Experimental observations distinguish these structures from the perovskite phase: (1) photoemission spectra show the Ti ions have charge 3+, not 4+, and (2) the measured compositions are Ba and O deficient with respect to the perovskite composition. In this abstract, we give a tiling decoration model for the ultrathin film Ba-Ti-O structures that is fully consistent with experimental observations. The structure consists of a rumpled Ti-O network with each Ti threefold coordinated with O, and Ba nestled in the larger, mainly Ti_7O_7 pores.

In Fig. 1, we show models for two of the crystalline structures that have been observed in ultrathin film Ba-Ti-O.[1]. In Fig. 2, we present a model for a large approximant to the quasicrystalline structure. In all cases, the Ba, Ti, and O atoms overlying the Pt-111 surface project into the plane as shown. Connecting Ba atoms as shown creates tiles with Ba at the vertices. At least six different tiles are found, many of which recur in more than one structure: thin rhombus, triangle, square, pentagon, flat hexagon, and elongated curved decagon. Each tile has a unique decoration. The tiles join edge to edge, and can be combined in different ways to reproduce the experimentally observed structures as well as other as-yet hypothetical structures. A perfect quasicrystal can be created by combining the thin rhombus, triangle, and square tiles in the "C_a" tiling pattern of Gähler.[3]

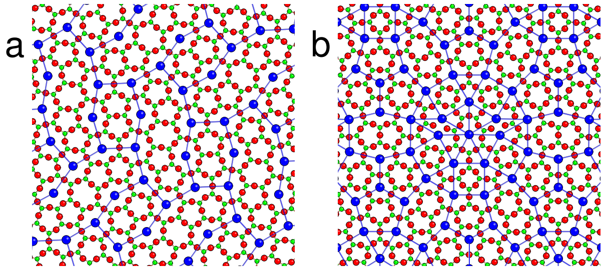

FIG. 1: (a), (b) Structure models for two large-period crystalline structures observed in ultrathin film Ba-Ti-O.[1] Ba atoms are large blue; Ti small green, and oxygen medium red.

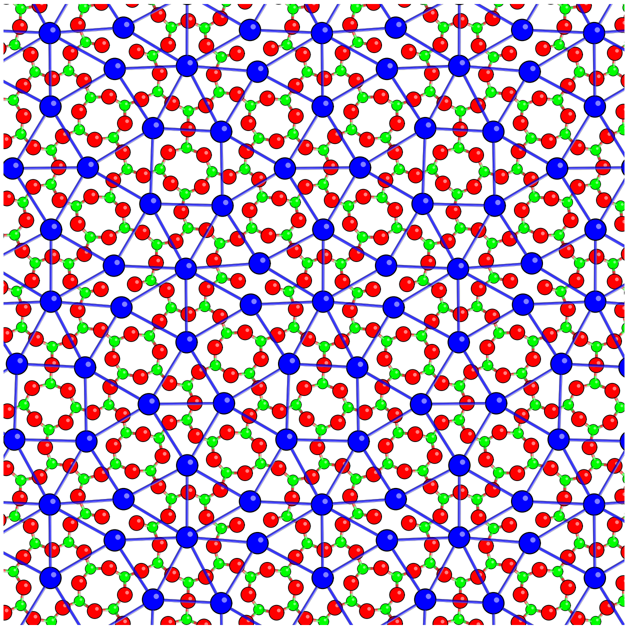

FIG. 2: Structure model for an ultrathin film Ba-Ti-O quasicrystalline approximant.

The compositions for all our ultrathin film Ba-Ti-O structure models is $Ba_xTiO_{1.5+y}$, with $0.23 \leq x \leq 0.37$ and $O \leq y \leq 0.05$, with $y > 0$ for structures containing thin rhombus tiles. The O:Ti ratio of approximately 1.5 is consistent with a 3+ charge on Ti. Note that the proposed structures do *not* satisfy charge balance. Therefore, it is unlikely that these structures could be grown as thicker film or bulk structures. We define "charge balanced analogs" to ultrathin film Ba-Ti-O as structural analogs with Ba removed, trivalent "B" ions in all tiles except for the thin rhombus, and quadrivalent "B" ions in the thin rhombus. Such hypothetical charge-balanced structures should be insulating and capable of existing as free 2D materials. It would be interesting to investi-

---

*Electronic address: eric.cockayne@nist.gov
†Deceased

gate the physical properties, such as dielectric response, of these novel structures.

The Ti and O in the structures form a Ti-O network, with each Ti threefold coordinated with O, that tessellates the plane into $\mathrm{Ti}_n\mathrm{O}_n$ rings (with one exception, associated with the thin rhombus tile, discussed below). The presence of three-fold coordinated Ti atoms in the quasicrystal Ba-Ti-O structure model along with $\mathrm{Ti}_n\mathrm{O}_n$ polygons with different values of n is reminiscent of three-fold coordinated network structure observed in other two-dimensional systems such as graphene[4] and bilayer SiO_2.[5, 6] For example, the Ti-O-Ti links in the Ba-Ti-O system are analogous to the C-C bonds in graphene.

With such a rich variety of observed structures, it becomes possible to elucidate their common features. Some observations: (1) The Ba-Ti-O systems show $\mathrm{Ti}_n\mathrm{O}_n$ rings with $n = 4$, 5, 6, and 7, but not $n = 8$ or greater; (2) The $n = 7$ rings are very common; and the $n = 6$ rings relatively rare; (3) The 7-rings always share a Ti-O-Ti edge with two or more other 7-rings to create a larger-scale network that can be represented as a tiling; (4) The 7-rings are always occupied by a Ba ion, the 6-rings partially occupied, and smaller rings empty.

The local structure associated with the thin rhombus can be viewed as the fusion of two $\mathrm{Ti}_7\mathrm{O}_7$-type pores to make a dumbbell-shaped pore. The two oxygen atoms that are coordinated with only one Ti serve as a buffer against Coulomb repulsion of the relatively close Ba-Ba pair. An analogous three-dimensional dumbbell-shaped pore was recently found in a zeolite structure,[7] and the best structural model in that case similarly had oxygen atoms inside the pore that were bound to only one Si each, instead of the normal two. The analogy with zeolites also suggests one possible application of the structures proposed here: if charged-balanced analogs could be created, they could act as ultrathin filters with a uniform pore size for gas separation, etc.

DFT calculations show the stability of the structures on a Pt-111 surface. The average heights above the topmost Pt layer in the relaxed structure are 3.1 Å, 2.2 Å, and 3.1 Å for Ba, Ti, and O, respectively. Ti-O distances range from 1.80 Å to 1.95 Å. The rumpling of the Ti-O network is driven by transfer of electrons from Ba to Pt; the negative surface charge on the Pt layer then attracts the positive Ti ions and repels the negative O ions.[8] Simulated scanning tunneling microscopy STM topographs for charge density 0.1 e nm^{-3} show only the Ba atoms, whose positions agree with the bright protrusions in the experimental STM images.[1, 2] The Ti-O network is predicted to be invisible unless very high-resolution STM is used.

It remains an open question how the various Ba-Ti-O structures are stabilized versus the processing conditions. In any case, the existence of detailed structure models for all these structures is a first step toward solving this problem.

The authors thank Terrell A. Vanderah (NIST) for helpful discussions. M. M. was supported by Slovak grants VEGA 2/0189/14 and APVV-0076-11. C. L. H. received support from DOE grant DE-FG02-89ER45405.

[1] S. Förster, K. Meinel, K.-M. Schindler, and W. Widdra, Surf. Interface Analysis **44**, 628 (2012).

[2] S. Förster, K. Meinel, R. Hammer, M. Trautmann, and W. Widdra, Nature (London) **502**, 215 (2013).

[3] F. Gähler, in *Quasicrystalline Materials*, edited by C. Janot and J. M. Dubois (World Scientific, Singapore, 1988), pp. 272–284.

[4] J. Kotakoski, A. V. Krasheninnikov, U. Kaiser, and J. C. Meyer, Phys. Rev. Lett. **106**, 105505 (2011).

[5] P. Y. Huang, S. Kurasch, A. Srivastava, V. Skakalova, J. Kotakoski, A. V. Krasheninnikov, R. Hovden, Q. Mao, J. C. Meyer, J. Smet, et al., Nano Lett. **12**, 1081 (2012).

[6] T. Björkman, S. Kurasch, O. Lehtinen, J. Kotakoski, O. V. Yazyev, A. Srivastava, J. Smet, U. A. Kaiser, and A. V. Krasheninnikov, Sci. Rep. **3**, 3482 (2013).

[7] S. Smeets, D. Xie, C. Baerlocher, L. B. McCusker, W. Wan, X. Zou, and S. I. Zones, Angew. Chem. Int. Ed. **53**, 10398 (2014).

[8] C. Wu, M. R. Castell, J. Goniakowski, and C. Noguera, Phys. Rev. B **91**, 155424 (2015).

Evolution of surface charge and domain structure through the ferroelectric paraelectric phase transition in $BaTiO_3(001)$ using MEM-LEEM

N. Barrett,[1,*] J. Dionot,[1] C. Mathieu,[1] and D. Martinotti[1]
[1]*SPEC, CEA, CNRS, Université Paris Saclay, CEA-Saclay, 91191 Gif sur Yvette cedex, France*

Polar structures in ferroelectric (FE) $BaTiO_3$ have been studied using mirror and low energy electron microscopy. At room temperature in (IP) and out-of-plane (OOP) polarized domains are observed with the surface charge screened by polar adsorbates. At higher temperature but still below the Curie temperature, T_C, contrast inverts due to adsorbate desorption. Polarized surface domains persist above T_C. Above 350 °C elastic strain at the OOP/IP domain walls is released whereas moderate heating preserves the original domain structure, providing a form of ferroelectric memory.

PACS numbers: 68.37.Xy, 71.15.Mb, 73.20.At, 77.80.Dj

Polar structures have been observed above the Curie temperature, T_C, in ferroelectric (FE) materials such as $BaTiO_3$ using Raman spectroscopy [1], diffuse X-ray scattering [2], X-ray absorption [3], birefringence [4] and resonant piezoelectric spectroscopy [5].

At the surface, atomic reconstruction and relaxation, and charge screening also determine polarity, elastic distortions and the domain ordering. Hoefer et al. have observed surface charge contrast up to 510 K in $BaTiO_3$ due to tetragonal distortion of the uppermost unit cells stabilized by ionic surface relaxation [6].

Low-energy electron microscopy (LEEM) is well suited for the study of FE surfaces. At low incident energy, called mirror electron microscopy (MEM), electrons are reflected by the electrostatic potential just above the surface. By scanning the incident energy, also called the start voltage (SV), the electrons approach closer to the surface until they penetrate the sample to be elastically backscattered. The transition between reflection and backscattering, called the MEM-LEEM transition, measures the local surface potential [7, 8]. Mapping the reflected or back-scattered electron intensity as a function of SV therefore provides full field, non-contact imaging of electric surface topography.

We study polar structures at the surface of $BaTiO_3(001)$. These structures persist above T_C up to ∼350 °C, above which strain relaxation occurs and the out-of-plane/in-plane (OOP/IP) contrast vanishes. For a moderate heating/cooling cycle up to 175 °C the original OOP/IP domain structure is conserved, suggesting that the polar structures play the role of a FE memory.

We tracked the FE-paraelectric (PE) phase transition using the surface displacement observed in LEEM. Figure 2 shows the movement during heating. At ∼140 °C a jump of 4.15 μm is measured due to the FE-PE phase transition and corresponds to a 0.04% lattice parameter difference. The offset in the Curie temperature is due to an instrumental artefact. The displacement is smaller than that between the tetragonal and cubic structure if the sample were a single domain but is quite reasonable considering that there are both OOP and IP domains.

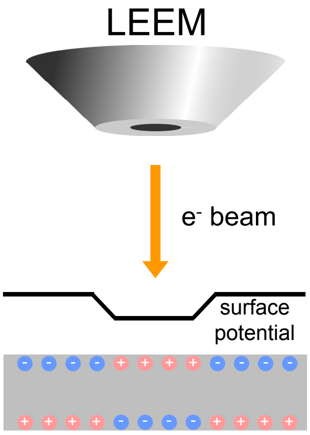

FIG. 1. Schematic representation of a MEM-LEEM experiment on a ferroelectric surface with out of plane polarization. Fixed surface polarization charge modulates the surface potential as seen by the incoming electrons.

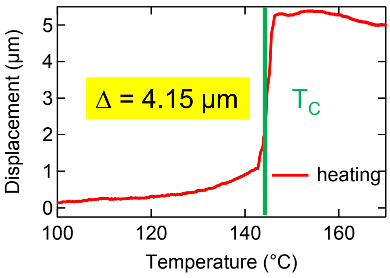

FIG. 2. Mechanical displacement as tracked by LEEM at SV = 0.65 V.

Figure 3 shows MEM images at (a) 21 (b) 100 (c) 120 (d) 140 (e) 160 and (f) 383 °C using SV = 0.65 V. The

[100] (pseudo-) cubic direction is horizontal and the [010] direction vertical. Three levels of intensity are observed, corresponding to outward and inward pointing OOP polarization and IP polarization. These are labelled P^+, P^- and P^{in}, respectively. The broad vertical stripes are OOP domains, whereas the finer vertical and horizontal structures inside the bright vertical stripes at 21 °C are IP domains.

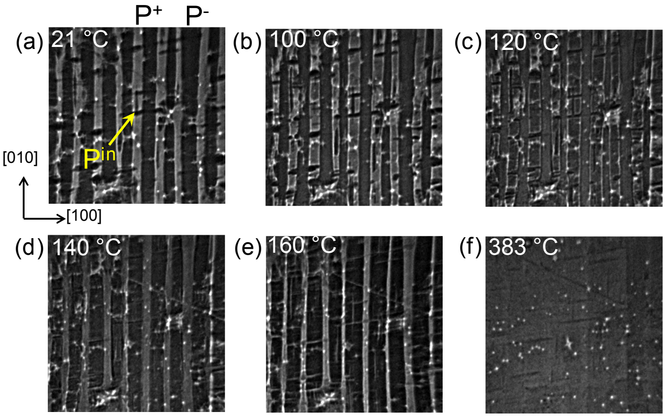

FIG. 3. MEM-LEEM images acquired using a start voltage of 0.65 V in a FoV of 20 μm at (a) 21 (b) 100 (c) 120 (d)140 (e) 160 and (f) 383 °C.

Above T_C (Fig. 3e), the contrast between the vertical stripe domains has inverted with respect to that at room temperature. The new bright stripes are narrower and the bright stripes at 21 °C have become dark and are broader. The contrast between OOP and IP domains has also inverted, the latter are now brighter than the surrounding P^+ region. At 350 °C the vertical stripes have started to fade and are no longer visible at 383 °C (Fig. 3f).

Screening OOP domains by polar adsorbates changes the sign of the surface charge [9, 10] as seen by the incoming electrons. In Fig. 3a, the bright vertical stripes have the highest surface potential (1.07 eV) corresponding to negative screening charge, i.e. to a P^+ surface fully screened by negatively charged adsorbates whereas the dark vertical stripes which have the lower potential (0.76 eV) are P^- domains (OOP polarized antiparallel to the surface normal) screened by positively charged adsorbates. The finer horizontal/vertical structures are IP polarized domains. As temperature increases two successive inversions in contrast are observed, first at 112 °C (between the OOP domains) and then at 128 °C (between OOP and IP domains). Since both temperatures are below the experimental T_C the polarization is still non-zero, suggesting that the change in sign of the surface charge is indeed due to desorption.

Although the bulk crystal has undergone a phase transition to the centrosymmetric cubic structure, at the surface OOP/IP-like contrast is still visible. The surface stress induced by the mismatch with the underlying cubic structure may be absorbed by OOP/IP ordering since DWs between OOP and IP polarized domains are also ferroelastic [11]. At high temperature (383 °C), however, the polar structures have almost completely disappeared suggesting that strain has been relaxed. This contrasts with the behaviour for a moderate heating cycle up to 175 °C where we observe almost a perfect FE memory. One must heat to 350 °C to unpin the domain structure and release the strain.

Finally, at the Curie temperature, we have observed the appearence of kinetic, transitory stripes, almost orthogonal to the domains in Fig. 3. We interpret these transitory stripes as ferroeastic twins similar to those observed by Streiffer et al. [12] in rhombohedral films.

J. D. is funded by ED107 (Ministère de l'Enseignement Supérieur et de la Recherche) and by the CEA. We gratefully acknowledge funding from the Agence Nationale de la Recherche project ANR-12-IS04-0001-01 CHEM-SWITCH and the Labex NanoSaclay COLNANO project.

---

[*] Correspondence should be addressed to nick.barrett@cea.fr

[1] U. M. Pasha, H. Zheng, O. P. Thakur, A. Feteira, K. R. Whittle, D. C. Sinclair, and I. M. Reaney, Applied Physics Letters **91**, 062908 (2007).

[2] R. Comes, M. Lambert, and a. Guinier, Solid State Communications **6**, 715 (1968).

[3] N. Sicron, B. Ravel, Y. Yacoby, E. A. Stern, F. Dogan, and J. J. Rehr, Phys. Rev. B **50**, 13168 (1994).

[4] A. Zibiska, D. Rytz, K. Szot, M. Górny, and K. Roleder, Journal of Physics: Condensed Matter **20**, 142202 (2008).

[5] O. Aktas, M. A. Carpenter, and E. K. H. Salje, Applied Physics Letters **103**, 142902 (2013).

[6] A. Höfer, M. Fechner, K. Duncker, M. Hölzer, I. Mertig, and W. Widdra, Physical Review Letters **108** (2012), 10.1103/PhysRevLett.108.087602.

[7] S. Cherifi, R. Hertel, S. Fusil, H. Béa, K. Bouzehouane, J. Allibe, M. Bibes, and A. Barthélémy, Physica Status Solidi (RRL) - Rapid Research Letters **4**, 22 (2010).

[8] N. Barrett, J. E. Rault, J. L. Wang, C. Mathieu, A. Locatelli, T. O. Mentes, M. A. Nino, S. Fusil, M. Bibes, A. Barthelemy, D. Sando, W. Ren, S. Prosandeev, L. Bellaiche, B. Vilquin, A. Petraru, I. P. Krug, and C. M. Schneider, Journal of Applied Physics **113**, 187217 (2013).

[9] S. Kalinin and D. Bonnell, Physical Review B **63**, 125411 (2001).

[10] S. V. Kalinin, C. Y. Johnson, and D. A. Bonnell, Journal of Applied Physics **91**, 3816 (2002).

[11] J. H. Park, J. Park, K. B. Lee, T. Y. Koo, H. S. Youn, Y. D. Ko, J. S. Chung, J. Y. Hwang, and S. Y. Jeong, Applied Physics Letters **91**, 012906 (2007).

[12] S. K. Streiffer, C. B. Parker, A. E. Romanov, M. J. Lefevre, L. Zhao, J. S. Speck, W. Pompe, C. M. Foster, and G. R. Bai, J. Applied Physics **83**, 2742 (2012).

Ferroelectric domain structures in low-strain $BaTiO_3$

Arnoud Everhardt[1]*, Sylvia Matzen[1,2], Neus Domingo[3], Gustau Catalan[3,4], Beatriz Noheda[1]

1 Zernike Institute for Advanced Materials, University of Groningen, 9747 AG Groningen, The Netherlands
2 Institut d´Electronique Fondamentale, UMR CNRS University Paris Sud 91405 Orsay CEDEX, France
3 Catalan Institute of Nanoscience and Nanotechnology (ICN2), CSIC and The Barcelona Institute of Science and Technology, Campus UAB, Bellaterra, 08193 Barcelona, Spain
4 ICREA, Barcelona, Spain

Epitaxial thin films offer enhanced control of the microstructure compared to bulk materials, as well as properties that can be vastly different from its bulk counterparts. Examples are the possibility to enhance the $BaTiO_3$ ferroelectric transition temperature by a few hundreds of degrees in highly-strained films [1], the polarization rotation that occurs in periodic a/c nanodomains of $PbTiO_3$ thin films by the induced flexoelectric effect [2] or an optimization of the piezoelectric coefficient by varying the growth direction [3]. This endows the material with an additional degree of freedom that might be beneficial for its piezoelectric properties, just like the rotated polarization in PZT close to the Morphotrophic Phase Boundary.

Ferroelectric $BaTiO_3$ thin films under low epitaxial mismatch strain have attracted the attention of the theorists, yielding rich phase diagrams [4,5], shown in **Fig 1**. Despite this interest, little experimental evidence of that region of the phase diagram exists.

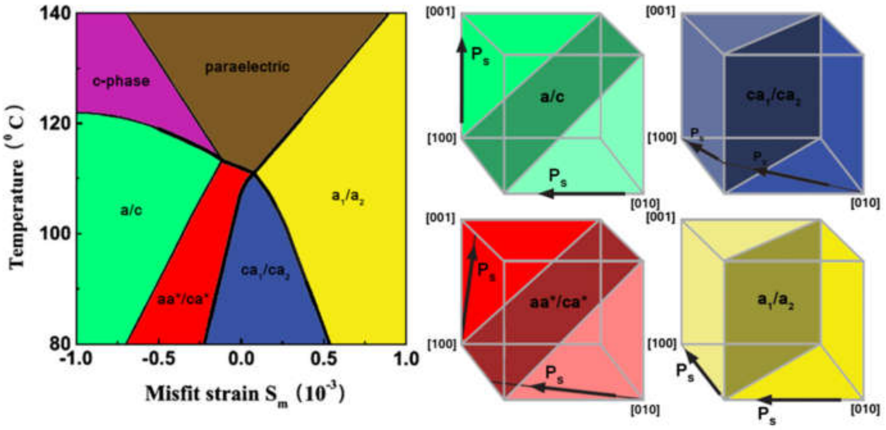

Fig 1. Pertsev phase diagram of temperature *versus* misfit strain for low-strained $BaTiO_3$. The predicted phases are tetragonal a/c or a_1/a_2 phases and monoclinic aa*/ca* and ca_1/ca_2 phases. Sketch adapted from reference [4].

In this work, high quality epitaxial $BaTiO_3$ thin films have been grown by Pulsed Laser Deposition on $NdScO_3$ substrates (strain ~0.1%) with a $SrRuO_3$ bottom electrode [6]. A monoclinic ca_1/ca_2 phase (a periodic 90 ° in-plane domain configuration with a small additional out-of-plane component of polarization) has been stabilized at room temperature. Above 50 °C this phase is transformed into an a/c phase with alternating in-plane and out-of-plane polarizations and forming zigzag domain walls between up-polarized and down polarized superdomains. These phases have been characterized by Piezoelectric Force Microscopy (**Fig 2**) where well-ordered periodic domains have been found. Substrate anisotropy is the reason for high anisotropy in domain size, direction and length.

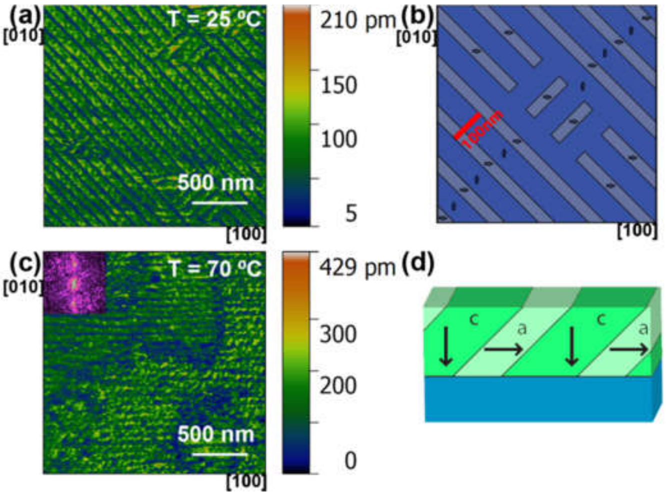

Fig 2. PFM images at a) 25 ºC and c) 70 ºC. b) Top-view model of the in-plane ca_1/ca_2 domain configuration and d) three-dimensional model of the a/c domain configuration.

Next to PFM, X-Ray Diffraction (XRD) (**Fig 3**) around (001) Bragg peaks gives additional information about the domain structures. High intensity domain peaks are observed for the a/c phase (**Fig 3b**), pointing to large out-of-plane polarization with a periodicity in agreement with the PFM images. For the ca_1/ca_2 phase, weak, but clear, domain peaks are observed corresponding to the same periodicity observed by PFM (**Fig 3a**). This reveals a weak out-of-plane polarization, as expected in the monoclinic ca_1/ca_2 phase (discarding, thus, a purely in-plane a_1/a_2 phase).

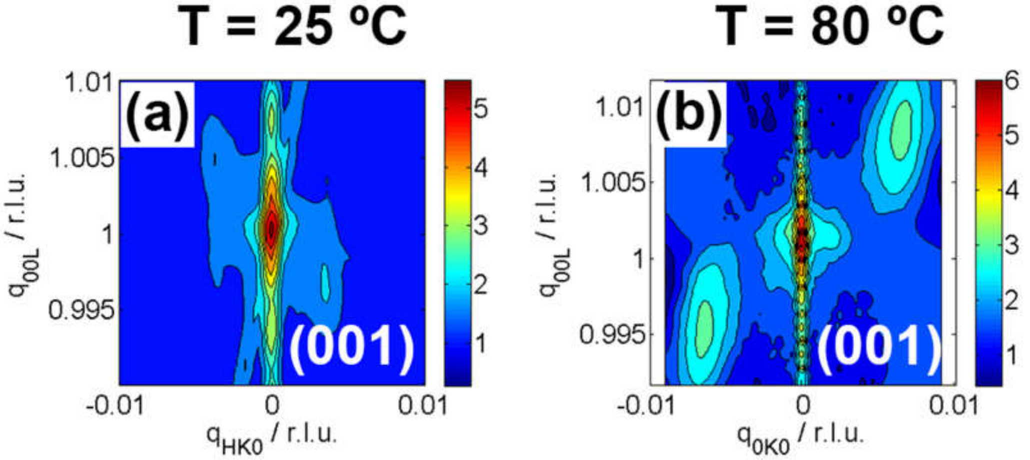

Fig 3. XRD Reciprocal Space Maps around (001) Bragg peaks at a) 25 ºC and b) 80 ºC.

The occurrence of a phase transition close to room temperature, a low symmetry ca_1/ca_2 phase and the formation of periodic domains make of this material a promising candidate for high piezoelectric response.

[1] K. J. Choi, M. Biegalski, et al., Science 306, 1005 (2004)
[2] G. Catalan, A. Lubk, A. H. G. Vlooswijk, E. Snoeck, C. Magen, A. Janssen, G. Rijnders, D.H.A. Blank and B. Noheda, Nature materials 10, 963 (2011)
[3] Z. Gui, L. Bellaiche, Phys. Rev. B 91, 020102 (2015)
[4] V. Koukhar, N. Pertsev and R. Waser, Phys. Rev. B 64, 214103 (2001)
[5] Y. L. Li, L. Q. Chen, Appl. Phys. Lett. (2006); O. Diéguez et al., Phys. Rev. B (2004); N. A. Pertsev et al., Phys. Rev. Lett. (1998); V. B. Shirokov et al., Phys. Solid State (2008); V. B. Shirokov et al., Phys. Rev. B (2007); M. Marathe, C. Ederer, Appl. Phys. Lett. (2014)
[6] A. S. Everhardt, S. Matzen, N. Domingo, G. Catalan, B. Noheda, Adv. Electron. Mater. 1500214 (2015)

Disorder in $BaTiO_3$ probed by angle-resolved polarized Raman scattering

Shinya Tsukada[1‡], Yasuhiro Fujii[2], Seiji Kojima[3], and Yukikuni Akishige[1]

[1]Faculty of Education, University of Shimane, Matsue, Shimane 690-8504, Japan
[2]College of Science and Engineering, Ritsumeikan University, Kusatsu, Shiga 525-8577, Japan
[3]Graduate School of Pure and Applied Sciences, University of Tsukuba, Tsukuba, Ibaraki 305-8573, Japan

The useful properties of $BaTiO_3$ are dependent on temperature and closely related with the phase transitions. However, micro- and mesoscopic pictures of phases and phase transitions are still uncertain. One important picture in history is the displacive model [1]. Although various properties of $BaTiO_3$ have been understood well on the basis of this simple model, inconsistencies of experimental results from the model have been apparent. For example, i) the diffuse x-ray scattering, ii) second harmonic generation signal, iii) x-ray fine structure and nuclear magnetic resonance, and iv) first-order Raman scattering indicate that Ti-ion displaces <111> in all phases.

In order to explain these experimental results inconsistent with the displacive model, temporal disorders due to the Ti-ion-hopping in eight-site (8g site with x=0.5+δ, where δ denotes the deviation from the center of oxygen-octahedron) have been considered as microscopic dipoles and ferroelectricity is induced by their interaction. In other words, Ti-ions are always located in one of eight minima along <111>-direction for all phases, and the average position of Ti-ions determines the macroscopic polarization [2].

From the view point of Raman scattering, Lambert, *et al.* explained the origin to be disorder on the basis of order-disorder eight-site model [3]. On the other hand, Barbosa, *et al.* attributed it to second-order process on the basis of the displacive model [4]. Even though the origin is still in controversy, Raman scattering from $BaTiO_3$ is widely used to evaluate the materials properties in applications for convenience. To understand $BaTiO_3$ more clearly and to apply Raman scattering from $BaTiO_3$ for evaluating electric components in the next generation, at the present stage, it is necessary to answer i) whether the Raman scattering is first-order or second-order, and ii) whether phonon mode or relaxation is related with the phase transitions. In order to solve these questions, angle-resolved polarized Raman scattering from $BaTiO_3$ was measured in the present study.

Figure 1(a) shows the Raman spectra at 700 K at various polarization angles. The schematic diagram of the measurement system is shown in Ref. [5]. Because T_C of $BaTiO_3$ is 400 K, 700 K is in the paraelectric cubic phase and is enough high to vanish the ferroelectric instability. By measuring both Stokes- and anti-Stokes-Raman scattering, we confirmed for two peaks at 200 and 500 cm^{-1} that ratio of the peak intensity between Stokes- and anti-Stokes-Raman scattering obeys the first-order process (Bose factor). Thus, we attribute peaks at 200 and 500 cm^{-1} to be first-order Raman scattering. The appearance of first-order Raman scattering is prohibited in cubic phase without disorder. On the basis of 3m point group of disorder in $BaTiO_3$, polarized-angle dependence of Raman scattering intensity was calculated as shown in FIG. 1(b). By fitting the experimental result with the calculated angular dependence, we attribute the quasi-elastic scattering and peaks to be E-mode and A-mode, respectively. In addition, we obtained the Raman tensor ratio to be a/b~3.0 and c/d~0.30 as shown in FIG 1(c). Because the quasi-elastic scattering shows marked narrowing toward T_C and no peak shift was found in others, our Raman scattering results capture the order-disorder eight-site model.

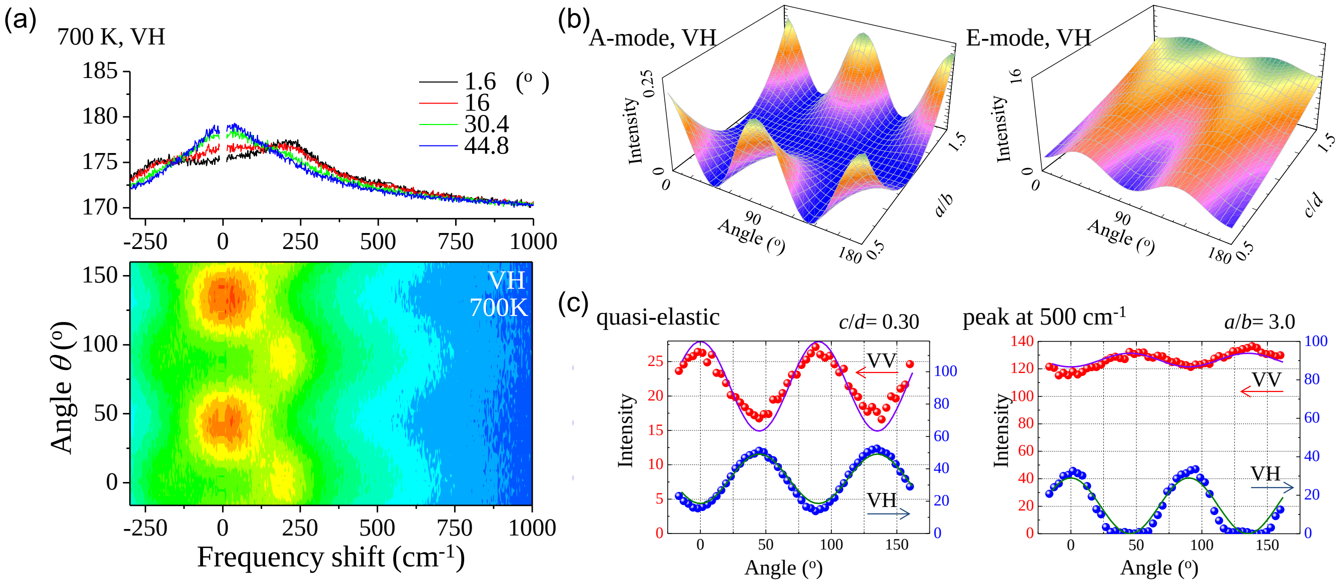

FIG. 1 : (a) Raman spectra of $BaTiO_3$ at 700 K in the backscattering geometry on (001) plane crystal. The angle denotes polarization direction of incident light. [100]-direction corresponds to 0°, while [010]-direction corresponds to 90°. (b) Calculated polarized-angle dependence of Raman scattering intensity on the basis of 3m point group of disorder in $BaTiO_3$. The angle dependence indicates that quasi-elastic scattering is attributed to E-mode, while peaks at 200 and 500 cm^{-1} are attributed to A-mode. (c) Angle dependence of light scattering intensity of quasi-elastic and Raman scattering. Raman tensor ratio a/b and c/d were determined by fitting.

References

[1] R. Blinc, *Advanced Ferroelectricity* (Oxford University Press, Kettering, 2011).

[2] R. Comes, M. Lambert, and A. Guinier, Solid State Commun. **6**, 715 (1968).

[3] M. P. Fontana and M. Lambert, Solid State Commun. **10**, 1 (1972).

[4] G. A. Barbosa, A. Chaves, and S. P. S. Porto, Solid State Commun. **11**, 1053 (1972).

[5] Y. Fujii, M. Noju, T. Shimizu, H. Taniguchi, M. Itoh, I. Nishio, Ferroelectrics **462**, 8 (2014).

Ab initio phase diagram of $\mathbf{BaTiO_3}$ under epitaxial strain revisited

Anna Grünebohm[1], Madhura Marathe[2], and Claude Ederer[2]
[1] *Department of Physics and Cenide, University of Duisburg-Essen, 47048 Duisburg, Germany*
[2] *Materials Theory, ETH Zürich, 8093 Zürich, Switzerland*

The optimization of ferroelectric materials by epitaxial growth and interface-mediated strain is nowadays a well-established and highly successful method. However, the experimental determination of strain-temperature phase diagrams is quite challenging and the theoretical modeling is highly important. Different levels of sophistication have been used to model the strain-dependent phase diagram of BTO, however, leading in part to conflicting results [1].

We revisit the phase diagram of $BaTiO_3$ under biaxial strain using a first principles-based effective Hamiltonian approach [3]. We show that, in addition to the tetragonal (c), quasi-rhombohedral (r), and quasi-orthorhombic (aa) ferroelectric phases that have been discussed previously [2], there are temperature and strain regions, in particular under tensile strain, where the system decomposes into multi-domain structures, see Fig. 1 (a)-(c). In such cases, the strained system, at least on a local level, recovers the same phase sequence as the unclamped bulk material. So far these multi-domain phases have been overlooked in *ab initio* based simulations [2] as they are not favorable in the small simulation cells used there. Furthermore, we extend these results from the case of "uniform" biaxial strain to the situation where the two in-plane lattice constants are strained differently and show that similar considerations apply in this case, see Fig.1(d)-(i).

References

[1] N. A. Pertsev *et al.*, Phys. Rev. Lett. **80**, 1988 (1998); N. A. Pertsev and V. G. Koukhar, Phys. Rev. Lett. **84**, 3722 (2000); K. Choi *et al.*, Science **306**, 1005 (2004); Y. L. Li and L. Q. Chen, Appl. Phys. Lett. **88**, 072905 (2006).

[2] Diéguez *et al.*, Phys. Rev. B **69**, 212101 (2004);
M. Marathe and C. Ederer, App. Phys. Lett. **104**, 212902 (2014).

[3] T. Nishimatsu *et al.*, Phys. Rev. B **78**, 104104 (2008); T. Nishimatsu *et al.*, Phys. Rev. B **82**, 134106 (2010).

[4] A. Grünebohm, M. Marathe, and C. Ederer, Appl. Phys. Lett. **107**, 102901 (2015).

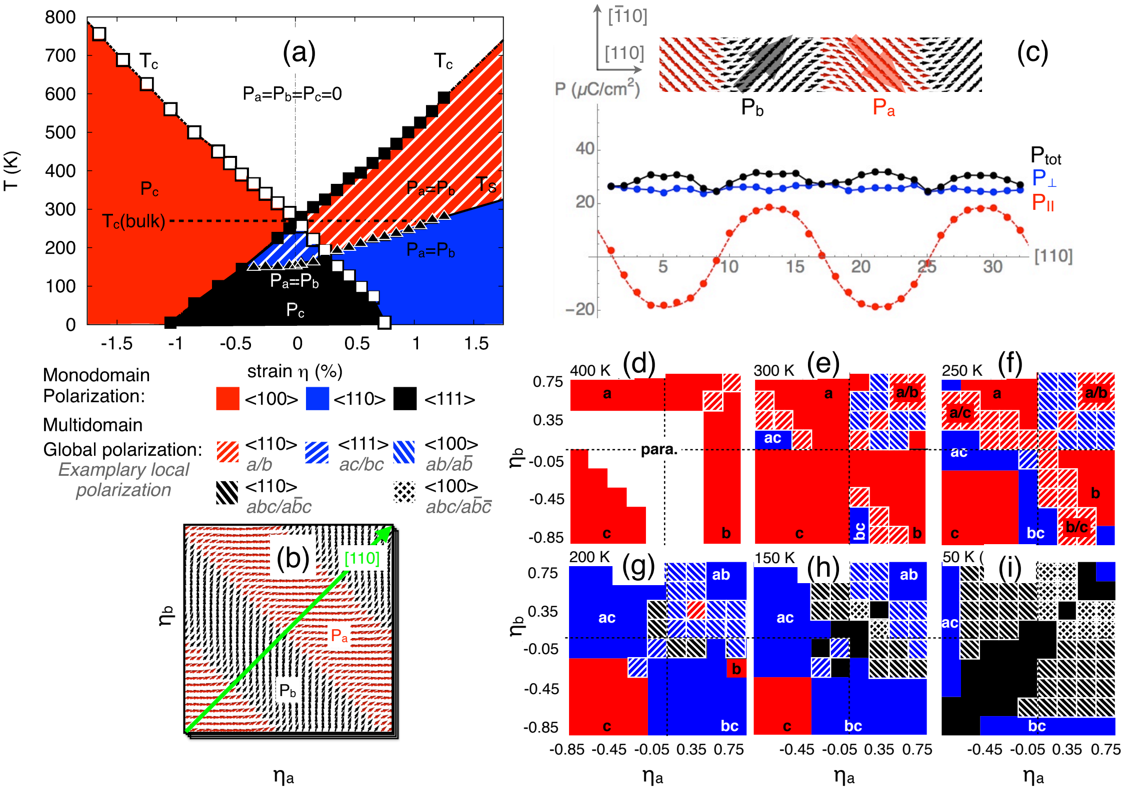

Figure 1: (a) Phase diagram of BaTiO$_3$ under biaxial strain ($\eta_a = \eta_b$). Colors/grayscale encode the paraelectric (white) and ferroelectric phases with local polarization along ⟨100⟩ (red/light gray), ⟨110⟩ (blue/dark gray), and ⟨111⟩ (black). Multi-domain configurations are indicated by striped regions as specified in the legend. (b) Domain structure under 0.75% tensile epitaxial strain (T=400 K). (c) Cross section of the polarization profile across the domain wall. Black: total polarization; Blue: polarization perpendicular to the wall ($P_\perp$); Red: polarization parallel to the wall ($P_{||}$). Dashed line: tanh-fit to the profile of $P_{||}$. (d)-(i) Phases found for general biaxial strain ($\eta_a \neq \eta_b$) for different temperatures. Figures taken from [4].

Wednesday’s Abstracts

Stabilization of highly polar $BiFeO_3$ like structure: a new interface design route for enhanced ferroelectricity in artificial perovskite superlattice

Hongwei Wang[1], Jianguo Wen[2], Dean J. Miller[2], Qibin Zhou[4], Mohan Chen[5], Ho Nyung Lee[3], Karin M. Rabe[4], and Xifan Wu[1]

1. Department of Physics, Temple University, Philadelphia, PA 19122, USA
2. Center for Nanoscale Materials, Argonne National Laboratory, Argonne, IL 60439, USA
3. Materials Science and Technology Division, Oak Ridge National Laboratory, Oak Ridge, Tennessee 37831, USA
4. Department of Physics and Astronomy, Rutgers University, Piscataway, NJ 08854-8019, USA
5. Department of Mechanical and Aerospace Engineering, Princeton University, Princeton, New Jersey 08544, USA

In ABO_3 perovskites, ferroelectricity is strongly coupled to oxygen octahedron rotations as a common structural distortion. However, this coupling behaves rather differently in various perovskite materials. It can promote large ferroelectricity in $BiFeO_3$ with *R3c* structure [1]. However, it suppresses ferroelectricity in $CaTiO_3$ with *Pbnm* symmetry [2]. For many $CaTiO_3$-like perovskite materials, the $BiFeO_3$ structure is a metastable phase. We report the stabilization of the highly-polar $BiFeO_3$-like phase of $CaTiO_3$ in the $BaTiO_3/CaTiO_3$ superlattice grown on a $SrTiO_3$ substrate. Stabilizing of this metastable phase is realized by a reconstruction of the oxygen octahedron rotations at the interface from the pattern in nonpolar bulk $CaTiO_3$ to a different pattern that is characteristic of a metastable $BiFeO_3$-like phase. This is shown through a combination of amplitude-contrast sub *0.1 nm* high-resolution transmission electron microscopy (HRTEM) as shown in Fig. 1 and first-principles calculations of the structure, energetics, and polarization of the superlattice and its constituents. By demonstrating the predicted new artificial ferroelectric materials under this mechanism, we argue that a large number of perovskites with the $CaTiO_3$ structure type, which include many magnetic representatives, are now good candidates for novel highly-polar multiferroic materials [3].

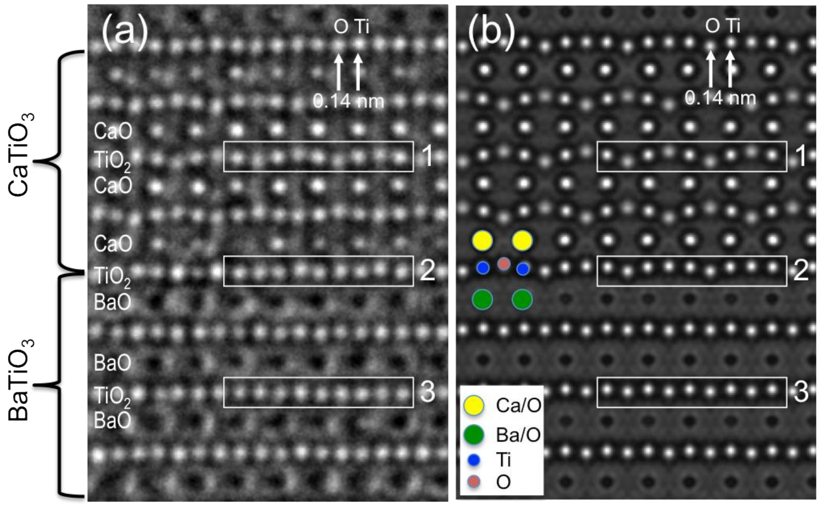

Fig. 1: Experimental and simulated HRTEM images showing oxygen octahedral tilts in the $4BaTiO_3/4CaTiO_3$ superlatice film grown on a $SrTiO_3$ substrate along [110]. (a). Experimental HRTEM image using an amplitude contrast imaging method ($Cs = 3\mu\ m$, $Cc=1\ \mu\ m$, $\Delta f=-1nm$). BaO columns (dark dots) and CaO columns (bright dots) show different channeling contrast. Oxygen atomic columns displace differently upward and downward with respect to the central Ti atoms in box 1, 2 and 3. *0.14 nm* indicates the spacing between Ti and O columns. Accumulated electron dose is 3×10^4 *electrons/nm*^{2}. (b). Simulated HRTEM image using the atomic positions obtained from first-

principles calculations. The simulated image matches well with the experimental image except a sharper column contrast in the simulated image compared to the experiment one because electron beam induced object excitations are omitted as pointed out by Kisielowski et al. [4].

1. J. B. Neaton, C. Ederer, U. V. Waghmare, N. A. Spaldin and K. M. Rabe, First-principles study of spontaneous polarization in multiferroic BiFeO3, Phys. Rev. B **71**, 014113 (2005).
2. N. A. Benedek and C. Fennie, Why are there so few perovskite ferroelectrics, J. Phys. Chem. C **117**, 13339-13349 (2013).
3. N. A. Spaldin, S. W. Cheong and R. Ramesh, Multiferroics: Past, present, and future, Phys. Today **63**, 38 (2010).
4. Kisielowski et al., Real-time sub-Angstrom imaging of reversible and irreversible conformations in rhodium catalysts and graphene, Phys Rev. B **88**, 024305, 2013.

Transition metal oxides: promising candidates for multifunctional applications

Annette Bussmann-Holder (oral)
Max-Planck-Institute for Solid State Research, Heisenbergstr. 1, D-70569 Stuttgart, Germany

Perovskite transition metal oxides are one the most challenging material classes in solid state physics since they display multiple coexisting and competing ground states which reach from superconductivity via magnetism to ferroelectricity. Typically, by doping or under stress, strain, electric, magnetic fields, transitions between these states are enabled. The key features of them are, however, coexisting phases where an interplay between different properties takes place to induce multifunctional properties as desired for novel device technologies.

An enormous challenge in this material class is the realization of multiferroic properties where magnetism and ferroelectricity not only coexist but couple strongly. This would permit to tune the polarity by a magnetic field and magnetism by an electric field. The realization of these desired properties is rare for rather simple reasons: ferroelectricity in perovskites is intimately related to a d^0 configuration at the transition metal site, whereas magnetism needs a d^n state there.

A way out of this obvious dilemma is to attribute magnetism to the perovskite A site, as e.g., realized in $EuTiO_3$ (ETO). The apparent similarity with the well investigated $SrTiO_3$ (STO) suggests multiple applications and enhanced functionality due to the high spin $4f^7$ state of Eu.

However, these states are strongly localized and have almost no overlap in ETO such that magnetic ordering occurs only at T_N=5.7K [1]. Even though a soft optic mode is present in ETO, reminiscent of a polar instability [2,3], its freezing temperature is as low as -170K. However, an unusually strong coupling between this mode and the antiferromagnetic order has been established, since at T_N a stabilization of the soft mode occurs which turns back into softening with a magnetic field [4].

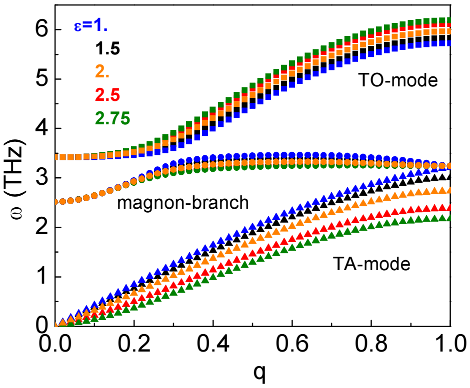

Fig. 1 dispersion of the lowest optic, acoustic and magnon mode at 300 K for different coupling strengths ε.

ETO and its mixed crystals with STO have been investigated in deep detail theoretically and experimentally. Theoretically it was predicted that paramagnons are active at high temperatures and couple strongly to phonons (Figure 1) [5, 6]. Even though there is no macroscopic magnetism, this coupling becomes evident by enabling a manipulation of the structural instability of ETO by a magnetic field [7] (Figure 2).

Even though the ultimate goal to realize high temperature magnetism in coexistence with ferroelectricity in ETO appears to be far from realizable, a new method is suggested which offers a way out of the above difficulties. This is achieved through domain wall engineering and manipulation. For STO it has been shown that the domain walls become polar [8]. A similar effect can be expected for ETO which in combination with domain wall related strain stabilizes magnetic properties. Since the structural phase transition in ETO is near room temperature [5], devices for practical applications are realizable through domain wall technology.

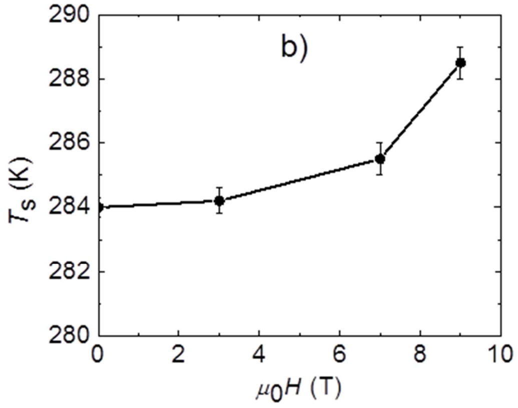

Fig. 2 Magnetic field dependence of the structural transition temperature

[1] McGuire T R, Shafer M W, Joenk R J, Halperin H A and Pickart S 1966 J. Appl. Phys. **37** 981

[2] Kamba S, Nuzhnyy D, Vaněk P, Savinov M, Knížek K, Shen Z, Šantavá E, Maca K, Sadowski M and Petzelt J 2007 Europhys. Lett. **80** 27002

[3] Goian V, Kamba S, Hlinka J, Vaněk P, Belik A A, Kolodiazhnyi T and Petzelt J 2009 J. Eur. Phys. B **71** 429

[4] Katsufuji T and Takagi H 2001 Phys. Rev. B **64** 054415

[5] Bussmann-Holder A, Köhler J, Kremer R K and Law J M 2011 Phys. Rev. B **83** 212102

[6] Guguchia Z, Keller H, Köhler J, and Bussmann-Holder A 2013 J. Phys. Cond. Mat. **24** 490021

[7] Guguchia Z, Keller H, Kremer R K, Köhler J, Luetkens H, Goko T, Amato A and Bussmann-Holder A 2014 Phys. Rev. B **90** 064413

[8] Catalan G, Seidel J, Ramesh R and Scott J F 2012 Rev. Mod. Phys. **84** 119

Broadband Dielectric Studies of Cobalt Ferrite doped Lead Zirconium Titanate Multiferroic Composites

J. Banys[1], A. Sakanas[1], R. Grigalaitis[1], C.E. Ciomaga[2], L. Mitoseriu[2], S. Kamba[3]
[1] Department of Radiophysics, Faculty of Physics, Vilnius University, Sauletekio av. 9, Vilnius, LT-10222 Lithuania
[2] Faculty of Physics, University "Al. I. Cuza", Iasi 700506, Romania
[3]Institute of Physics, Academy of Sciences of the Czech Republic, 182 21 Prague 8, Czech Republic
*e-mail: juras.banys@ff.vu.lt

Multiferroics belongs to class of materials in which the ferroelectric and ferromagnetic ordering occurs simultaneously in the same temperature range. Some of them can exhibit also a coupling between these orders, i.e. posses a magnetoelectric effect. It is not surprising that multiferroics are promising as multifunctional materials for various sensors, actuators, transducers, four state memory devices, etc [1] and are being intensively studied at the present. The most interesting multiferroic materials at the moment are so-called two-phase multiferroic composites due to the possibility to realize the "product property" referring to effects present in the composites but not in the individual phases. Lead zirconate titanate $PbZr_{x}Ti_{1-x}O_3$ is the well known ferroelectric perovskite with excellent electromechanical properties while cobalt ferrite $CoFe_2O_4$ exhibit good ferromagnetic and magnetostrictive properties. These above mentioned properties allow combining them together to form composite exhibiting multiferroic behaviour. Due to the lack of high frequency dielectric investigations the applicability of such multiferroics in GHz and THz range is still limited and the present work is dedicated to the broadband dielectric spectroscopy results of $Pb_{0.988}(Zr_{0.52}Ti_{0.48})_{0.976}Nb_{0.024}O_3$ (PZTN) and $CoFe_2O_4$ (CF) composite ceramics.

CF-PZTN composite ceramics with CF ratio of 10%, 20 % and 30% were prepared were prepared in situ by citrate–nitrate combustion by using PZTN-based template powders as described in [2]. Various devices and broadband dielectric spectroscopy methods were used in experiments to cover the wide range of temperatures and frequencies, spanning from 100 K to 500 K and from 20 Hz up to 50 GHz. Transmission mode time domain THz spectroscopy was employed in measurements of complex dielectric response in the range of 5 – 50 cm^{-1} with a resolution of 0.5 cm^{-1} at 20 – 800 K. In order to investigate phonon properties of composites, IR reflectivity and Raman spectra were collected of optically polished samples. Bruker IFS 113v Fourier-transform IR spectrometer was used in the range of 30 – 3000 cm^{-1} at the room temperature, and up to ~700 cm^{-1} in cooling and heating regimes with the resolution of 2 cm^{-1}. For Raman measurements, RENISHAW RM-1000 micro-Raman spectrometer was used in back-scattering geometry in the range of 20 – 1200 cm^{-1} with the spectral resolution below 2 cm^{-1}.

The obtained results show a broad dielectric anomaly around the temperature of 630 K, whereas steady increase of dielectric loss above this temperature is observed as well. The peak of permittivity in the temperature dependencies can be associated with the paraelectric-ferroelectric phase transition in the morphotropic phase boundary (MPB) PZT material, in accordance to the phase diagram of lead zirconate-lead titanate system [3]. Comparing ε' and ε'' temperature dependencies at a fixed frequency one can conclude that permittivity values decrease with an increase of cobalt ferrite concentration, as can be explained by a sum rule.

Dielectric spectra of (1-*x*)PZTN-*x*CF composites (Fig. 1) can be divided into three regions, where characteristic differences exist in each of them between soft and hard doped PZT.

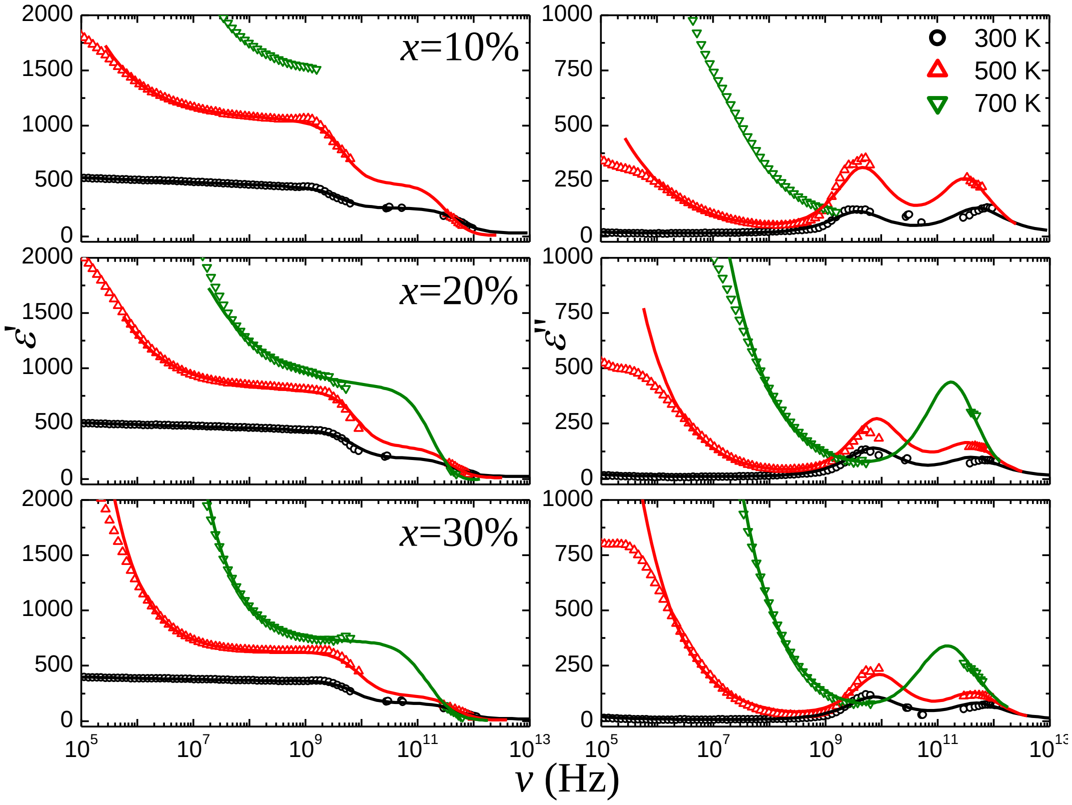

Fig 1. Dielectric spectra comparison of ε' and ε'' of (1-x)PZTN-xCF composites at selected temperatures. Solid lines are approximations by empirical relationships.

At low frequencies dielectric spectra are governed by electrical conductivity phenomena while in the midrange, they show monotonic increase of dielectric permittivity upon decreasing the frequency. Generally, such dispersion is called *Universal Dielectric Response*, or *Logarithmic Dispersion* law and it is believed that it is the reason of the existence of disorder in the materials. The origin of the dielectric relaxation in GHz range is of piezoelectric nature and possibly is caused by grain or domain wall resonance.

In IR spectra characteristic phonons of ferroelectric morphotropic phase boundary PZT are dominated in all (1-x)PZTN-xCF composites. While it is known that phonon mode close to 80 cm^{-1} is related to the ferroelectric behavior, the softening of central mode around 45 cm^{-1} is observed in our case. Furthermore, this softening is disturbed by the increasing concentration of CF. It seems that cobalt ferrite effectively disturbs the softening of ferroelectric IR phonon modes.

Acknowledgements:

This work was supported by CNCSIS-UEFISCSU project PN-II-PT-PCCA-2013-4-1119 and the European Social Fund under the Global Grant measure (project VP1-3.1-SMM-07-K-03-011).

References

[1] W. Eerenstein, N. D. Mathur, and J. F. Scott, Nature 442 (2006).

[2] A.R. Iordan, M. Airimioaei, M.N. Palamaru, C. Galassi, A.V. Sandu, C.E. Ciomaga, F. Prihor, L. Mitoseriu, A. Ianculescu, J. Eur. Ceram. Soc. 29 (2009) 2807.

[3] B. Noheda, D.E. Cox, G. Shirane, R. Guo, B. Jones, and L.E. Cross, Phys. Rev. B **63**, (2000).

Unveiling the room temperature magnetoelectricity of troilite FeS

FABIO RICCI[1] AND ERIC BOUSQUET[2]

[1,2]*Physique Théorique des Matériaux, Université de Liège, Sart Tilman, Belgium*
fabio.ricci@ulg.ac.be

The amazing possibility of certain compounds to couple electric and magnetic properties attract a lot of attention in material science. Since the discovery of magnetoelectric and multiferroic effects, numerous studies emerged with the aim to exploit these unique material properties in technologically appealing applications such as low-power-consumption spintronics. The main big challenge is to obtain room temperature magnetoelectricity: over the known magnetoelectric materials only a few exhibit the desired property at room temperature. In the present study, we show that the troilite phase of the iron sulphide based compound is a new room temperature magnetoelectric crystal.

From the planetary chemistry and dynamics studies and from high temperature and high pressure experiments, it is known that the outer core of some planets (Earth and Mars) is composed by a molten iron-rich material in which a substantial amount of light elements is dispersed. Among them, the sulphur is recognised to be the most abundant. A large portion of sulphur combines with iron such as the iron-sulphur alloys represent one of the fundamental building blocks for the understanding of planet's evolution [1]. The first discovery of the troilite phase of FeS alloys is due to an Italian Jesuite, Domenico Troili in 1766 [2]. This particular phase is mostly found in meteors originating from the Moon or Mars and naturally found in the Earth crust and allowed to carry out important informations about their chemical and physical characteristics. Interestingly, during the '60 and '70 there was a renewed interest of the scientific community on the troilite phase of FeS thanks to the discovery of a ferroelectric polarization at room temperature in several samples [3, 4].

At high temperature, FeS is metallic and paramagnetic and it crystallises in the the high symmetry hexagonal $P6_3/mmc$ space group, commonly called NiAs-type structure. Below $T_N \sim 588$ K, FeS undergoes an antiferromagnetic (AFM) phase transition with spins perpendicular to the hexagonal axis (c-axis) and around $T_s \sim 445$ K a spin-flip transition occurs where the spins align toward the c-axis [5]. At $T_\alpha = 413$ K a structural phase transition arises changing the crystal structure from the $P6_3/mmc$ space group to the so-called troilite structure with space group $P\bar{6}2_c$ [6].

Using *ab-initio* techniques we show that the zone boundary modes, driving the structural transition from the high symmetry $P6_3/mmc$ to the low symmetry $P\bar{6}2_c$ phase, are actually non polar. This means that even if the $P\bar{6}2_c$ is non-centrosymmetric the active phonon modes driving the structural phase transition are not polar. We appealingly found that the total electric polarization is zero because of a compensation a non-zero electric polarization in each spin channel (up and down) of opposite direction (see Fig. 1, left panel). This behaviour is linked to the so-called magnetoelectric monopolarization [7] such that even if the system is not ferroelectric, it is nevertheless magnetoelectric. The study of the

electric polarization as a function of an applied magnetic field (see Fig. 1, right panel) gives a magnetoelectric constant of $\alpha_{xx}^{tot} \simeq \alpha_{yy}^{tot} = 3.00$ ps/m. This value is three times larger than that found for the prototypical room temperature magnetoelectric compound Cr_2O_3. Then, FeS is potentially a very promising magnetoelectric crystal thanks to the fact that it is easy and cheap to find it in natural environments.
A more detailed description of the cited results can be found in Ref. [8].

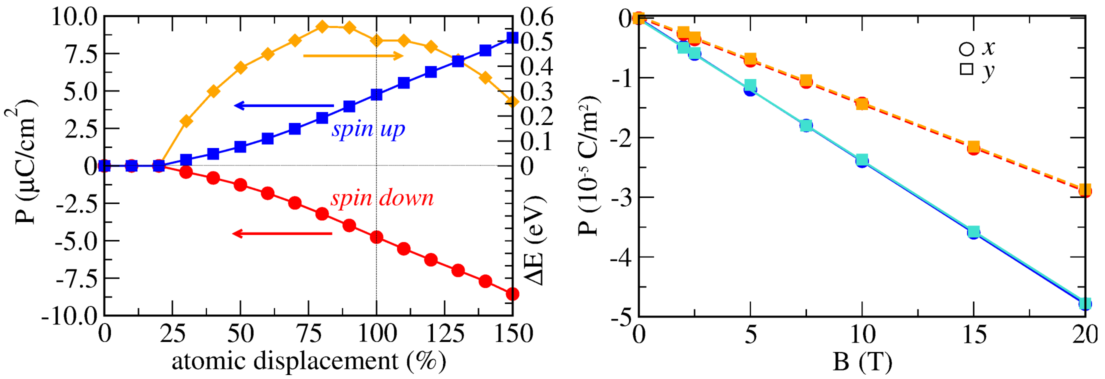

Figure 1: Left panel: spin resolved electronic contribution to the polarization (blue squares and red circles) and energy gap (orange diamonds) as a function of the displacement from $P6_3/mmc$ (0%) to the $P\bar{6}2_c$ (100%) phase. Right panel: polarization as a function of an in-plane magnetic field along the x (circles) and y (squares) directions. Solid and dashed lines represent the total and electronic contribution respectively.

References

[1] C. Allègre and G. Manhès and È. Lewin, Earth and Planetary Science Letters **8**, 49 (2001).

[2] Domenico Troili, *Ragionamento della caduta di un sasso* (1766).

[3] E. F. Bertaut, Bull. Soc. Franç. Minér. Crist. **79**, 276 (1956).

[4] C. B. van den Berg, Physica Status Solidi **40**, K65 (1970).

[5] K. Adachi and K. Sato, Journal of Applied Physics **39**, 1343 (1968).

[6] A. F. Andresen, Acta Chemica Scandinavica **192**, 73 (1960).

[7] N. A. Spaldin and M. Fechner and E. Bousquet and A. Balatsky and L. Nordström, Phys. Rev. B 88, 094429 (2013).

[8] F. Ricci and E. Bousquet, arXiv:1511.01327.

The macroscopic magnetoelectric monopolization in diagonal magnetoelectrics

Florian Thöle, Michael Fechner, and Nicola A. Spaldin
Materials Theory, ETH Zürich, Switzerland

We present a formalism to calculate the spin contribution to the macroscopic magnetoelectric (ME) monopolization from first principles within the density functional theory framework. The magnetoelectric multipoles form the second-order term in the interaction energy of the magnetization density $\boldsymbol{\mu}(\boldsymbol{r})$ with an inhomogeneous magnetic field $\boldsymbol{H}(\boldsymbol{r})$.[1] They are often represented as three irreducible components, the magnetoelectric monopole, the toroidal moment or anapole, and the magnetic quadrupole and occur in materials with broken time-reversal and space-inversion symmetries. Magnetic textures that correspond to each of these terms are shown in Fig. 1.

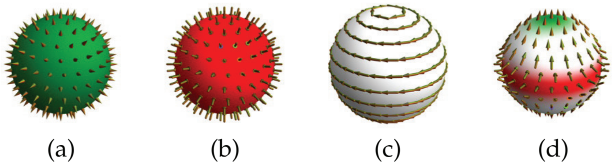

FIG. 1. Magnetic textures for (a), (b) positive and negative magnetoelectric monopole, (c) toroidal moment and (d) magnetic quadrupole. For (c) and (d), the figure corresponds to one of the possible three/five components.

The ME monopolization (that is the magnetoelectric monopole per unit volume) is given by

$$A = \frac{1}{3V} \int \boldsymbol{r} \cdot \boldsymbol{\mu}(\boldsymbol{r})\, d^3\boldsymbol{r} \quad . \tag{1}$$

We begin by deriving the fomalism for a Berry phase theory and showing the analogy to the modern theory of polarization. We then implement the corresponding Wannier function-based description in first-principles calculations within the density functional formalism. Currently, our approach can be used with Quantum Espresso[2] and Wannier90.[3]

We apply the formalism to $LiMnPO_4$ and Cr_2O_3 and then interpret the results for the bulk magnetoelectric monopolization of these compounds. In $LiMnPO_4$, the Berry phase theory agrees well with the previously introduced local moment approximation,[1]

$$A = \frac{1}{3V} \sum_i \boldsymbol{R}_i \cdot \boldsymbol{m}_i \quad , \tag{2}$$

where $\boldsymbol{R}_i$ is the position of an atom, $\boldsymbol{m}_i$ is its formal spin magnetic moment (5 μ_B in the case of $LiMnPO_4$), V is the volume of the unit cell and the sum is over the atoms in the unit cell. However, as the second example of Cr_2O_3 shows, the agreement between the Berry phase ME monopolization and Eq. 2 is not generally valid. Here, the local moment approximation and the Berry phase theory can be brought into agreement if a renormalized local magnetic moment is used in Eq. 2. We suggest that the value of $\boldsymbol{m}_i$ that provides this agreement between the local moment and the Berry phase monopolizations provides a practical definition of the magnetic moment in a magnetoelectric antiferromagnet without reference to projection schemes, which rely on a rather arbitrary definition of atomic spheres.

Finally, we discuss the correspondence between ME multipoles and the linear magnetoelectric effect, in which an electric polarization is induced by an applied magnetic field, $P_i = \alpha_{ij} H_j$, and a magnetization is induced by an applied electric field, $M_j = \alpha_{ij} E_i$. In the case of materials with a magnetoelectric monopolization, the magnetoelectric response is isotropic and diagonal, so that an applied electric field induces a parallel magnetization; a cartoon illustrating the response of a monopolar arrangement of spins interacting through Goodenough-Kanamori superexchange is shown in Fig. 2.

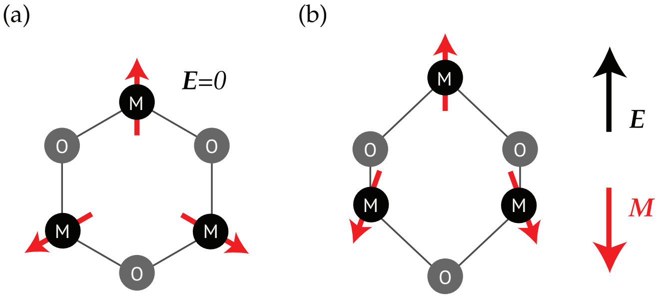

FIG. 2. Illustration of the correspondence between the magnetoelectric monopolization and the diagonal magnetoelectric effect. In (a) the frustrated antiferromagnetic superexchange between the almost 180°transition metal–oxygen–transition metal (M-O-M) interactions leads to 120°angles between the spins, and no net magnetization. (b) Under application of an electric field, the sublattices shift, and the M-O-M angles change, with the angle between the lower two M ions becoming close to 90°. Since 90°superexchange is ferromagnetic, the spins rotate as shown leading to a net magnetization. The reverse case (induced polarization under applied magnetic field) is illustrated in Ref. 1.

In Ref. 1, the following free energy expression was analyzed:

$$
\begin{aligned}
U = & \frac{1}{2\chi_e} P^2 - \boldsymbol{P}\cdot\boldsymbol{E} + \frac{1}{2\chi_m} M^2 - \boldsymbol{M}\cdot\boldsymbol{H} \\
& + \frac{1}{2}\beta A^2 + \frac{1}{4}\gamma A^4 + cA\boldsymbol{P}\cdot\boldsymbol{M} \quad ,
\end{aligned} \tag{3}
$$

where χ_e and χ_m are the electric and magnetic susceptibilities, A is the ME monopolization, c is a constant giving the coupling strength and β and γ are temperature-dependent coefficients. The relation between the ME monopolization and the magnetoelectric tensor following from this free energy is $\alpha = c\chi_e\chi_m A$. By including a Zeeman field in first-principles calculations,[4] we compute the magnetoelectric coefficients for Cr_2O_3 and $LiMnPO_4$ under the same conditions as our computed magnetoelectric monopolizations obtained with the Berry phase theory. We conclude by discussing the correspondence between the two quantities.

---

[1] N. A. Spaldin, M. Fechner, E. Bousquet, A. Balatsky, and L. Nordström, Phys. Rev. B **88**, 094429 (2013).

[2] P. Giannozzi, S. Baroni, N. Bonini, M. Calandra, R. Car, C. Cavazzoni, D. Ceresoli, G. L. Chiarotti, M. Cococcioni, I. Dabo, A. Dal Corso, S. de Gironcoli, S. Fabris, G. Fratesi, R. Gebauer, U. Gerstmann, C. Gougoussis, A. Kokalj, M. Lazzeri, L. Martin-Samos, N. Marzari, F. Mauri, R. Mazzarello, S. Paolini, A. Pasquarello, L. Paulatto, C. Sbraccia, S. Scandolo, G. Sclauzero, A. P. Seitsonen, A. Smogunov, P. Umari, and R. M. Wentzcovitch, J. Phys.: Condens. Matter **21**, 395502 (2009).

[3] A. A. Mostofi, J. R. Yates, G. Pizzi, Y.-S. Lee, I. Souza, D. Vanderbilt, and N. Marzari, Comput. Phys. Comm. **185**, 2309 (2014).

[4] E. Bousquet, N. A. Spaldin, and K. T. Delaney, Phys. Rev. Lett. **106**, 107202 (2011).

Ferroelectric and Magnetic Double Morphotropic Phase Boundaries in Dy-Modified $BiFeO_3$-$PbTiO_3$ Multiferroics

Jian Zhuang,[1,2] Lun-Wei Su,[2] Jinyan Zhao[1], Hua Wu,[3] Alexei A. Bokov,[2] Ming Liu,[1] Wei Ren,[1] and Zuo-Guang Ye[2,1*]

[1] *Electronic Materials Research Laboratory, Key Laboratory of the Ministry of Education & International Center for Dielectric Research, Xi'an Jiaotong University, Xi'an, 710049, P. R. China*

[2] *Department of Chemistry and 4D LABS, Simon Fraser University, Burnaby, British Columbia, V5A 1S6, Canada*

[3] *Department of Applied Physics, Donghua University, Songjiang District, 201620 Shanghai, P. R. China*

[*] *Email: <zye@sfu.ca>*

The presentence of morphotropic phase boundary in ferroelectric solid solutions (FE-MPB) is known to be crucial for the development of high-performance piezoelectrics. Similarly, magnetic MPB has been found to exist in a few ferromagnets and is proved to be greatly beneficial to the magnetostricitive response. Considering the fact that many ferroelectric systems show FE-MPB and similarly some ferromagnetic systems exhibit M-MPB, one naturally asks if in multiferroics that exhibit both ferroelectricity and (ferro-/antiferro-)magnetism, the FE-MPB and M-MPB could exist simultaneously, and if so, what the relation between these two kinds of MPB would be, and how they would affect the properties. In this study, we reported the finding of ferroelectric and magnetic double morphotropic phase boundaries in Dy-Modified $BiFeO_3$-$PbTiO_3$ Multiferroics.

The effects of dysprosium ion on the crystal structure and local polar domains of the bismuth ferrite-based systems have been investigated firstly in the Dy-substituted solid solutions of $0.66Bi_{1-x}Dy_xFeO_3$-$0.34PbTiO_3$, with $x = 0$, 0.05, 0.1, 0.15, 0.2, 0.3, 0.4 and 0.5. It is found that with increasing substitution amount of Dy, the crystal structure changes from a primarily tetragonal P4mm phase to the stable rhombohedral R3c phase, suggesting that the substitution of Dy for Bi can stabilize the R3c symmetry and hinder the formation of the P4mm phase. The unit cell volume generally decreases with increasing Dy content due to the relatively small radius of Dy^{3+} compared with Bi^{3+}. Interestingly, with increasing concentration of Dy, the ferroelectric phase transition temperature T_C first decreases for compositions with $x < 0.1$ and then increases for compositions with $x \geq 0.1$. This is explained by the competition between two processes arising for the Dy-substitution: the effect of the dilution of the ferroelectrically active Bi^{3+} ion which would reduce T_C, and the effect of the structural transformation from the P4mm phase to the R3c phase with a more stable ferroelectric ordering and thereby increased T_C. The former is dominant in the compositions with $x < 0.1$, resulting in a slight decrease in T_C, while the latter prevails in the compositions with $x \geq 0.1$, giving rise to an increase in T_C. The Piezoresponse Force Microscopy (PFM) imaging reveals the formation of 180^o polar domains for the compositions with $x = 0.15$, as shown in Fig. 1(a), which can be poled and switched by applying an electric field through the PFM tip, confirming the ferroelectricity. The results show that the substitution of Dy can affect the structural symmetry and phase component of the $BiFeO_3$-based multiferroic solid solution, and thereby enhance its ferroelectric order.

A (weak) ferromagnetic state is induced at room temperature by Dy for the rhombohedral compositions with $x \geq 0.10$. On the other hand, although each Fe^{3+} ion couples primarily antiferromagnetically with its neighbouring Fe^{3+} ions below the Néel temperature, the canted spins due to the Dzyaloshinskii-Moriya (D-M) coupling are present in the *R3c* (or Cc) phase, giving rising to the appearance of weak ferromagnetism. On the other hand, the incorporated Dy^{3+} ions themselves are magnetically active and expected to couple with the Fe^{3+} ions through the Dy-O-Fe superexchange, possibly leading to enhanced canting of the spins of Fe^{3+} ions. All in all, the introduction of Dy into $0.66BiFeO_3$-$0.34PbTiO_3$ leads to the breaking of its antiferromagnetic structure below Néel temperature and thereby the formation of (weak) ferromagnetic ordering at room temperature when the substitution rate exceeds a critical value ($x \geq 0.10$), making the $0.66Bi_{1-x}Dy_xFeO_3$-$0.34PbTiO_3$ system one of rare room-temperature ferromagnetic and ferroelectric materials, i.e. a true multifrroic.

Upon cooling down from room temperature, the tetragonal compositions ($x \leq 0.05$) only show one magnetic phase transition from the paramagnetic to antiferromagnetic phase while the rhombohedral compositions exhibit a series of magnetic phase transitions from the (weak) ferromagnetic state to an antiferromagnetic order then to another weak ferromagnetic phase. A comprehensive ferroelectric-magnetic phase diagram has been established in terms of temperature and composition that depicts the coexistence of a ferroelectric morphotropic phase boundary and a magnetic morphotropic phase boundary, as shown in Fig. 1(b). Interestingly, these two kinds of MPBs are found to overlap with each other. Such an unusual coincidence of both magnetic MPB and ferroelectric MPB, the so-called double MPB, points to new kinds of couplings among the multiple physical quantities. It is reasonable to expect that such effects as magnetoelectricity, magnetostrictive and piezoelectricity, could be enhanced within or near the overlapping MPB region.

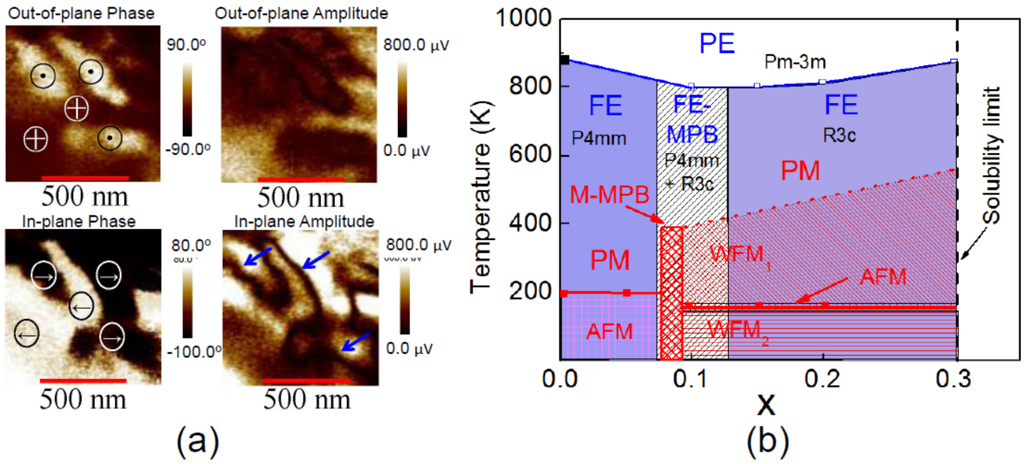

Fig. 1. (a) PFM images of as–sintered ceramic surface of compositions with $x = 0.15$, and (b) The structural and ferroelectric-magnetic phase diagram of the $0.66Bi_{1-x}Dy_xFeO_3$-$0.34PbTiO_3$ solid solution system, indicating the following phase regions: PE = Paraelectric Phase, FE = Ferroelectric Phase, PM = Paramagnetic Phase, AFM = Antiferromagnetic Phase, WFM = Weak Ferromagnetic Phase, FE-MPB = Ferroelectric/structural Morphotropic Phase Boundary, and M-MPB = Magnetic Morphotropic Phase Boundary. The red dots are an estimated line dividing the PM and WFM_1 phases.

The work was supported by the U.S. Office of Naval Research (Grant No. N00014-12-1-1045) and the Natural Science & Engineering Research Council of Canada (NSERC).

References:

1). S. Yang, H. Bao, C. Zhou, Y. Wang, X. Ren, Y. Matsushita, Y. Katsuya, M. Tanaka, K. Kobayashi, X. Song, and J. Gao, “Large Magnetostriction from Morphotropic Phase Boundary in Ferromagnets”, *Phys. Rev. Lett.*, **104**, 197201 (2010)

2). J. Zhuang, L.-W. Su, J. Zhao, H. Wu, A. A. Bokov, W. Ren and Z.-G. Ye, “Structure and Local Polar Domains of Dy-Modified $BiFeO_3$-$PbTiO_3$ Multiferroic Solid Solution”, *J. Mater. Chem. C,* **3**, 12450 – 12456 (2015)

3). J. Zhuang, L.-W. Su , H. Wu, A. A. Bokov, M. Liu, W. Ren, and Z.-G. Ye, “Coexisting Ferroelectric and Magnetic Morphotropic Phase Boundaries in Dy-Modified $BiFeO_3$-$PbTiO_3$ Multiferroics”, *Appl. Phys. Lett.*, **107**, 182906 (2015).

Emergence of Room-Temperature Ferroelectricity at Reduced Dimensions

D. Lee[1], H. Lu[2], Y. Gu[3], S.-Y. Choi[4], S.-D. Li[5], S. Ryu[1], T. R. Paudel[2], K. Song[6], E. Mikheev[7], S. Lee[1], S. Stemmer[7], D. A. Tenne[8], S. H. Oh[6], E. Y. Tsymbal[2], X. Wu[5], L.-Q. Chen[3], A. Gruverman[2], C. B. Eom[1]

[1]Department of Materials Science and Engineering, University of Wisconsin–Madison, Madison, Wisconsin 53706, USA.

[2]Department of Physics and Astronomy & Nebraska Center for Materials and Nanoscience, University of Nebraska, Lincoln–Nebraska, Nebraska 68588, USA.

[3]Department of Materials Science and Engineering, Pennsylvania State University, University Park, Pennsylvania 16802 USA.

[4]Advanced Characterization and Analysis Group, Korea Institute of Materials Science, Changwon 641-831, Korea.

[5]Department of Physics, Temple University, Philadelphia, Pennsylvania 19122, USA.

[6]Department of Materials Science and Engineering, Pohang University of Science and Technology, Pohang 790-784, Korea.

[7]Materials Department, University of California–Santa Barbara, Santa Barbara, California 93106-5050, USA.

[8]Department of Physics, Boise State University, Boise, Idaho 83725-1570, USA.

The enhancement of the functional properties of materials at reduced dimensions is crucial for continuous advancements in nanoelectronic applications. Here, we report that the scale reduction leads to the emergence of an important functional property – ferroelectricity, challenging the long-standing notion that ferroelectricity is inevitably suppressed at the scale of a few nanometers. A combination of theoretical calculations, electrical measurements, and structural analyses provides evidence of room-temperature ferroelectricity in strain-free epitaxial nanometer-thick films of otherwise non-ferroelectric $SrTiO_3$. We show that electrically-induced alignment of naturally existing polar nanoregions is responsible for the appearance of a stable net ferroelectric polarization in these films [1]. This finding can be useful for the development of low-dimensional material systems with enhanced functional properties relevant to emerging nanoelectronic devices.

References

[1] D. Lee, H. Lu, Y. Gu, S.-Y. Choi, S.-D. Li, S. Ryu, T. R. Paudel, K. Song, E. Mikheev, S. Lee, S. Stemmer, D. A. Tenne, S. H. Oh, E. Y. Tsymbal, X. Wu, L.-Q. Chen, A. Gruverman, C. B. Eom, *Science*, **349**, 1314, 10.1126/science.aaa6442 (2015)

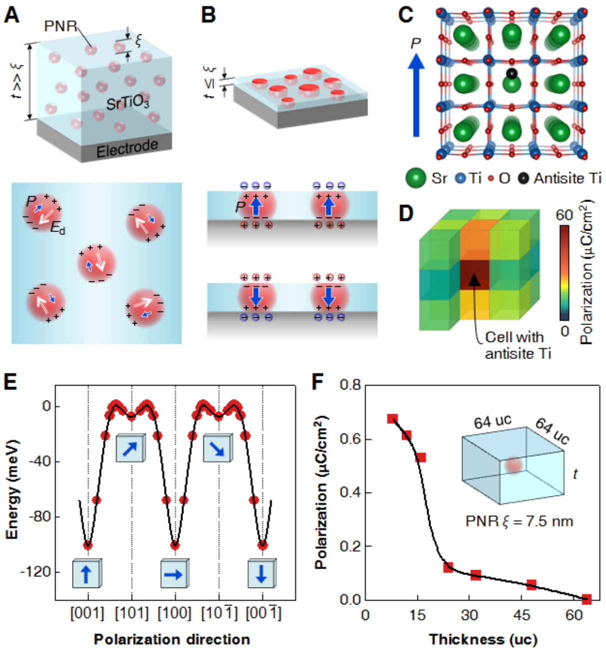

Fig. 1. Theoretical calculations showing the emergence of ferroelectricity in ultrathin films of otherwise non-ferroelectric $SrTiO_3$. (**A** and **B**) Dimensional engineering of the polarization (*P*) stability in PNRs: schematics of PNRs and their *P* in thick $SrTiO_3$ (**A**) and ultrathin $SrTiO_3$ (**B**). (**C**) Calculated atomic structure near the off-center antisite Ti atom. (**D**) Profile of local *P* around the antisite Ti atom in a 3×3×3 supercell obtained from DFT calculations. (**E**) Calculated energy barrier between the polarization states. (**F**) Remnant polarization of the model system, where a single spherical PNR is embedded in $SrTiO_3$ with a thickness *t*, obtained by phase-field simulations. The lateral dimension of $SrTiO_3$ was fixed as 64 uc×64 uc..

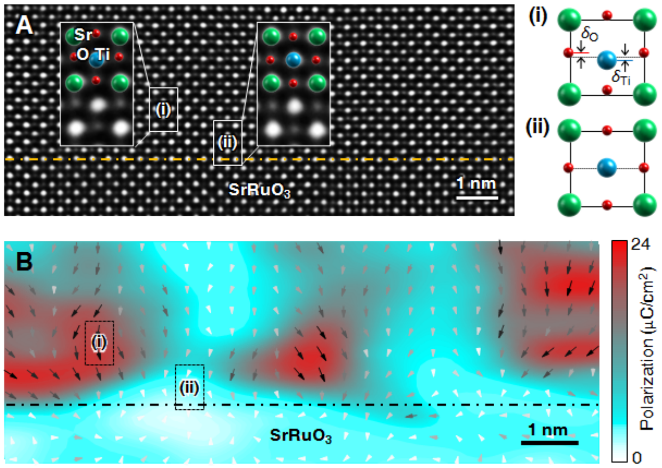

Fig. 2. Atomic-scale imaging of polar nanoregions. (**A**) Filtered ABF-STEM image, including all atomic positions. The (i) and (ii) regions are examples of polar and nonpolar regions, respectively. (**B**) Polarization vectors for each unit cell, estimated from atomic displacements in A. Arrows denote the polarization direction; the stronger polarization, the darker the arrow color. Strength of polarization is also expressed as a color map, ranging from white (weak) to red (strong).

Ab-initio approach to structural, electronic and ferroelectric properties of Antimony Sulpho-iodide

Danila Amoroso[1] and Silvia Picozzi[2]

[1] *Univerisitá degli Studi di L'Aquila, 67100 L'Aquila, Italy*

[1] *Physique Théorique des Matériaux, Université de Liège (B5), B-4000 Liège, Belgium*

[2] *Consiglio Nazionale delle Ricerche (CNR-SPIN), 66100 Chieti, Italy*

Abstract. This work analyzes the structural, electronic and ferroelectric properties of the ferroelectric semiconductor Antimony sulfo-iodide (SbSI), by means of an *ab-initio* approach based on Density Functional Theory (DFT). Despite SbSI being known since many years, its theoretical characterization is rather poor, and few non-exhaustive *ab-initio* studies exist in the literature.

SbSI in both paraelectric and ferroelectric phases is orthorhombic and has four SbSI molecules (12 atoms) per unit cell. The space group is $D_{2h}^{16} - Pnam$ in the paraelectric phase above the Curie temperature ($T_c > 298\ K$) and $C_{2v}^{9} - Pna2_1$ in the ferroelectric phase below the Curie temperature ($T_c < 298\ K$). SbSI is characterized by a quasi-one-dimensional structure composed of zigzag chains of $[Sb_2S_4I_4]_n$ dimers stacked along the crystallographic c axis, as shown in Fig. (1). It was suggested [1] that the interaction between two double chains of SbSI crystal is negligible, i.e. chains of atoms parallel to the z axis are linked only via a weak van-Der-Waals-type interaction. It is found that standard DFT fails to reproduce the experimentally observed ferroelectric phase, whereas a more advanced approach, based on Hybrid Functionals within the Heyd-Scuseria-Erzenhof (HSE) approximation, correctly works. Changes in the atomic positions, between the paraelectric and ferroelectric phases, take place along the z direction: Sb and S shift along the polarization c axis with respect to iodine by 0.18 Å and 0.05 Å, respectively, in excellent agreement with experiments [2]. The calculated electronic band structures shows that SbSI has an indirect gap in both phases. Because of the presence of heavy elements, by using HSE with SOC,

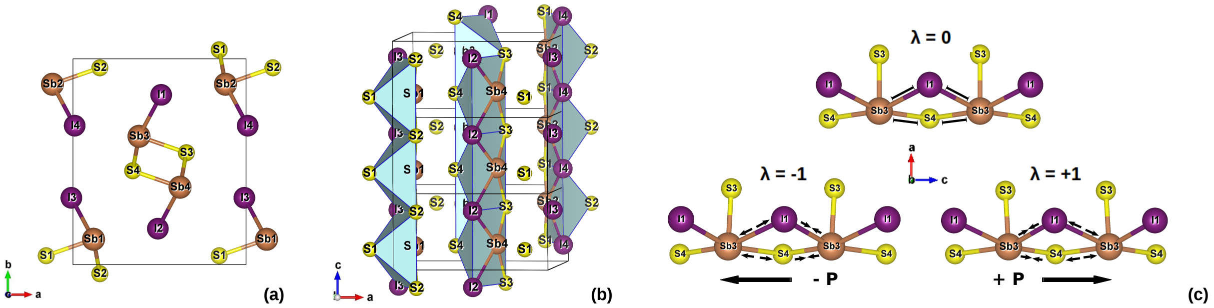

Figure 1: Schematic representation of SbSI: **(a)** Atomic positions in the x-y plane in the crystalline unit cell. **(b)** SbSI crystal highlighting both the rhombic-bypiramidal atomic arrangement, as well as a quasi-one-dimensional structure composed of zigzag chains of $[Sb_2S_4I_4]_n$ dimers stacked along the crystallographic c axis. **(c)** Zoom over relevant ions, showing the switching between shorter and long bond lengths in the FE state, according to the polar mode amplitude $\lambda = \pm 1$, compared with those in the PE phase $\lambda = 0$. The directions of small (large) arrows highlight the shorter and longer Sb-S bonds (polarization direction along the c axis).

the indirect gap ($X - U \rightarrow S$) amounts to $\simeq 2.15\ eV$ in the ferroelectric phase, whereas the smallest direct gap is along the $\Gamma - Y$ line in the first Brillouin zone and it is about $2.3\ eV$. The energy gap range is consistent with the experimental estimate $E_g \simeq 1.80\ eV$. The calculated spontaneous polarization $P \simeq 20\ \mu C/cm^2$ is in good agreement with the experimental values [3]. When comparing the FE polarization within PBE and HSE, the changes in the magnitude of polarization were found to be less than few percent, confirming the validity of GGA to study the electronic and ferroelectric properties of SbSI (at fixed geometry), even though it fails in estimating the correct energetics of the system. In Fig. (2) we report the variation of the total energy from the centrosymmetric ($\lambda = 0$) to the non-centrosymmetric ($\lambda = \pm 1$) structures as a function of the amplitude of the polar mode, within HSE. We found a bistable energy profile characteristic of a ferroelectric material, with an energy barrier of about 6 meV/unit cell; it is also evident how polarization behaves almost linearly as a function of λ. An analysis of the density of states and anomalies in the Born Effective charges reveal a large covalency in the bonding nature of SbSI, based on a strong $s - p$ hybridization between Sb and S ions, in turn ionically bonded to iodine anions. Finally, the interplay between ferroelectricity and spin-orbit coupling has been investigated by focusing on the spin texture of the conduction bands along the $k_x^*(\Gamma - X)$ and the $k_y^*(\Gamma - Y)$ directions perpendicular to the FE polarization. It reveals sizeable k-dependent spin-splitting and a coexistence of Dresselhaus and Rashba relativistic effects. The spin texture can be reversed by switching the polarization [4, 5] (i. e. with an external electric field), so that SbSI can be classified as a member of the interesting class of "ferroelectric relativistic semiconductors" with appealing potential in spintronics.

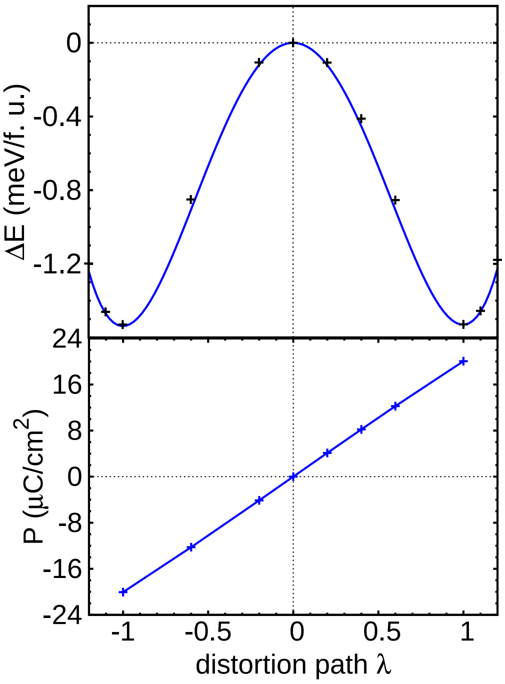

Figure 2: Variation of HSE total energy (top) and polarization (bottom) as a function of the amplitude of the polar mode distortion between centric ($\lambda = 0$) and polar ($\lambda = \pm 1$) configurations.

References

[1] E. Furman, O. Brafman, J. Makovsky, *Phys. Rev. B*, **13**, 1703 (1974).

[2] A. Kikuchi, Y. Oka, E. Sawaguchi, *J. Phys. Soc. Japan*, **23**, 337 (1967).

[3] E. Fatuzzo, G. Harbeke, W. J. Merz, R. Nietsche, H. Roetschi, W. Ruppel, *Phys. Rev.*, **127**, 2036 (1962).

[4] A. Stroppa, D. Di Sante, P. Barone, M. Bokdam, G. Kresse, C. Franchini, M.-H. Whangbo, S. Picozzi, *Nature Communications*, **5**, 5900 (2014).

[5] D. Di Sante, P. Barone, R. Bertacco, S. Picozzi, *Adv. Mater.*, **25**, 509 (2013).

Ferroelectric switching pathways in $Ca_3Ti_2O_7$ from first principles

Elizabeth A. Nowadnick, Andrew T. Mulder, and Craig J. Fennie
School of Applied and Engineering Physics, Cornell University, Ithaca, NY 14853, USA

(Prefer ORAL presentation)

Materials that possess an electrical polarization coupled to non-polar order parameters offer an opportunity to control functionality, such as magnetism, orbital order, or electronic bandwidth, with an electric field. A promising set of materials for this type of application are hybrid improper ferroelectrics, where polarization can be induced via a trilinear coupling to two octahedral rotations of different symmetry. Because this mechanism does not require conventional zone-center distortions, it opens the possibility of realizing ferroelectricity in a wider range of chemistries. Hybrid improper ferroelectricity was predicted theoretically in A-site cation ordered superlattices[1,2] and in n=2 Ruddlesden-Popper (RP) materials.[3] Recently, hybrid improper ferroelectricity was experimentally demonstrated in the n=2 RP compound $Ca_3Ti_2O_7$.[4] The observation of an unexpectedly low ferroelectric switching barrier and abundant structural domains suggests that these domains may be critical to the switching process. Key issues that remain to be understood include what are the specific structural properties of $Ca_3Ti_2O_7$ that enable this low-energy switching, and how these properties could be further optimized.

To address these questions, in this talk we analyze possible ferroelectric switching pathways that are facilitated by the presence of orthorhombic twin domains and vertical stacking faults in the n=2 RP structure of $Ca_3Ti_2O_7$. Utilizing group theoretical methods and Landau expansions, we first analyze the crystal structure and domains of $Ca_3Ti_2O_7$ with the goal of identifying likely low-energy switching pathways. Then, using first principles calculations, we compute the energy barriers of the various switching pathways and study the evolution of the octahedral rotation and polar order parameters during these switching processes. Our results offer insight into what is the likely switching mechanism in $Ca_3Ti_2O_7$, and which order parameter is primarily responsible for controlling the energy barriers.

The ground state ferroelectric structure (space group $A2_1am$) of $Ca_3Ti_2O_7$ is shown in Fig. 1. This structure consists of perovskite slabs of thickness n=2, separated by a rocksalt layer. Due to the trilinear coupling between the two octahedral rotation order parameters and the polarization, the simplest possibility for switching the polarization by 180° is a one-step process where either one of the octahedral rotations is turned off, and then turned on again, with the opposite rotation "sense". These two switching pathways were already considered in Ref. 3.

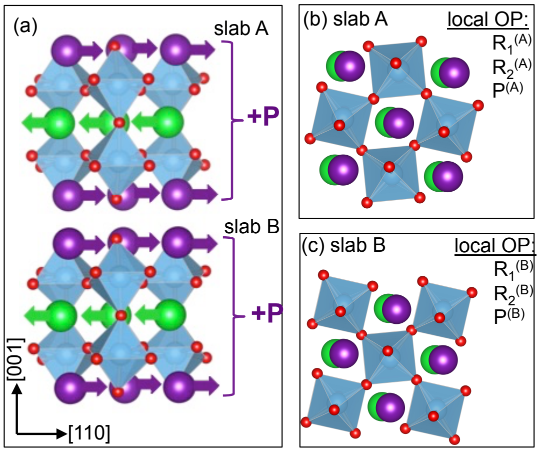

FIG. 1. (a) Ferroelectric $A2_1am$ ground state structure of $Ca_3Ti_2O_7$. (b) and (c) show a top view of slabs A and B, respectively, looking down the [001] axis, and list the local order parameters defined for that slab. The purple/green represents the Ca ions moving to the right/left, respectively.

What are other possible ferroelectric switching pathways facilitated by the n=2 RP structure? To elucidate other possibilities, we introduce a language of order parameters *local* to adjacent perovskite slabs A and B, as defined in Fig. 1 (previous works use irreps of $I4/mmm$ as order parameters). In our local picture, in each slab $\alpha = (A, B)$, there are two octahedral rotations, R_1^α and R_2^α, coupled trilinearly to the polarization P^α in that slab:

$$F \sim R_1^{(A)} R_2^{(A)} P^{(A)} + R_1^{(B)} R_2^{(B)} P^{(B)}. \tag{1}$$

(one arrives at an equivalent formal Landau theory regardless of whether one works with these local order parameters or order parameters that transform like irreps of $I4/mmm$).

A new possibility for ferroelectric switching can be understood by comparing Fig. 1(a) and Fig. 2. In Fig. 1(a), a net polarization develops because the Ca ions in both slabs move in the same 2-against-1 pattern. In contrast, Fig. 2 depicts a structure where the Ca ions in slabs A and B move with opposite 2-against-1 patterns, so the resulting structure is anti-polar with no net polarization. In this anti-polar structure, each perovskite slab has two octahedral rotations that couple trilinearly to the polarization in that slab (space group $Pnma$); it can be obtained from the structure in Fig. 1(a) by switching the sense of one of the octahedral rotations in one of the perovskite slabs. Thus, the ferroelectric and

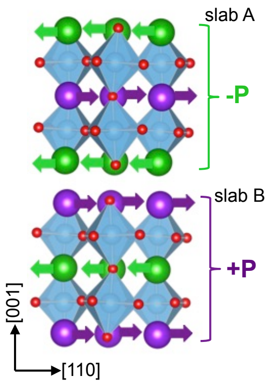

FIG. 2. Anti-polar structure *Pnma*.

Switching path	Energy/Ti [meV]
1-step: reverse $a^-a^-c^0$ rotation	93
1-step: everse $a^0a^0c^+$ rotation	57
2-step: orthorhombic twin	41
2-step: anti-polar	32

TABLE I. Energy barriers calculated from first principles for $Ca_3Ti_2O_7$ ferroelectric switching pathways.

anti-polar structures are quite similar, so we expect them to be close in energy. Our first principles calculations confirm this: we find that the anti-polar structure in Fig. 2 is only 7 meV/Ti higher in energy than the ferroelectric ground state. Therefore, a “two-step” switching process, where first the polarization in one slab is reversed, bringing the structure to an anti-polar intermediate state, and then the polarization in the other slab is reversed, is likely low energy.

A second possibility is polarization switching via an orthorhombic twin domain,[4] an example of which is illustrated in Fig. 3. The $A2_1am$ structure has eight structural domains which are determined by combinations of the octahedral rotation order parameters.[4,5] Starting with a domain with, for example, polarization along [110], as shown in Fig. 3(a), the polarization could be reversed by a two-step process: first rotating the polarization by 90° (b), and then again by 90° to a domain with polarization along [-1-10] (c). Changes to both the octahedral rotations accompany this rotation of the polarization vector, but both octahedral rotations are non-zero throughout the switching process (in at least one of the slabs). In both the two-step ferroelectric switching processes considered here, either via an anti-polar intermediate or an orthorhombic twin domain, the trilinear coupling remains non-zero throughout, which is a key difference compared to the one-step switching processes previously discussed.

Having gained intuition from this analysis, we then use first principles methods to calculate the energy barriers for the various switching pathways described above; the results are presented in Table I. While a full description of the dynamic ferroelectric switching process is belong the scope of $T = 0$ first principles calculations, these results can offer insight into the likely pathways. We find that both two-step switching pathways are lower energy than the one-step possibilities. In addition, we use our first principles calculations to carefully analyze how the octahedral rotation and polar order parameters evolve throughout the switching process, which offers insight into which structural distortion is the most significant determining factor for the energy barriers.

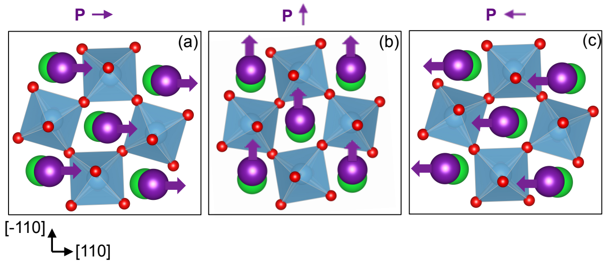

FIG. 3. Schematic of polarization switching via an orthorhombic twin domain. Here the structure is viewed along the [001] axis. Note that only one perovskite slab is shown here for simplicity.

Finally, we discuss how the ferroelectric switching barriers can be modified via biaxial strain and Sr-doping, and comment on our results in light of the experimental results from Ref. 4 on $Ca_{3-x}Sr_xTi_2O_7$.

---

[1] E. Bousquet, M. Dawber, N. Stucki, C. Lichtensteiger, P. Hermet, S. Gariglio, J.-M. Triscone, and P. Ghosez, Nature **452**, 732 (2008).

[2] J. M. Rondinelli and C. J. Fennie, Advanced Materials **24**, 1961 (2012).

[3] N. A. Benedek and C. J. Fennie, Phys. Rev. Lett. **106**, 107204 (2011).

[4] Y. S. Oh, X. Luo, F.-T. Huang, Y. Wang, and S.-W. Cheong, Nature Materials **14**, 407 (2015).

[5] A. B. Harris, Phys. Rev. B **84**, 064116 (2011).

Shearing-mediated ferroelectricity: polarization switching caused by the bond recombination of cations

Mitsuru Itoh[1,*], Yosuke Hamasaki[1], Shintaro Yasui[1], Akiko Ito[1], Tomoyasu Taniyama[1], Takao Shimizu[2], Ayako Konishi[3], Takafumi Ogawa[3], Hiroki Moriwake[3]

[1]Materials and Structures Laboratory, Tokyo Institute of Technology, 4259 Nagatsuta, Midori-ku, Yokohama 226-8503, Japan.
[2]Center for Elemental Research, Tokyo Institute of Technology, 4259 Nagatsuta, Midori-ku, Yokohama 226-8503, Japan.
[3]Nanostructures Research Laboratory, Japan Fine Ceramics Center, 2-4-1 Mutsuno, Atsuta-ku, Nagoya 456-8587, Japan

Introduction Sesquioxides of A_2O_3 or ABO_3 (A, B = Al, Fe, Ga) show a polymorphism. For example, Al_2O_3 has intermediate phases of χ-Al_2O_3, κ-Al_2O_3, κ'-Al_2O_3, η-Al_2O_3, θ-Al_2O_3, and δ-Al_2O_3 through the crystallization process of aluminum hydrates into final stable phase of α-Al_2O_3. Gallium nitrates decompose into stable β-Ga_2O_3 through intermediate metastable phases of γ-Ga_2O_3, α-Ga_2O_3, δ-Ga_2O_3, and ε-Ga_2O_3. Iron compounds decompose into stable phases of FeO (wüstite), Fe_3O_4 (magnetite), and α-Fe_2O_3 (hematite) depending on the oxygen partial pressure. Nanoparticle of metastable phase of γ-Fe_2O_3(maghemite) with a defect spinel structure crystalizes into ε-, β-, and finally to α-Fe_2O_3, depending on their sizes. Among sesquioxides above, κ-Al_2O_3, ε-Fe_2O_3, and ε-Ga_2O_3 have the structure (hereafter, we call as κ-Al_2O_3-structure). Figure 1(a) shows the κ-Al_2O_3 structure compared with the structures of corundum (Fig1(b)) and spinel (Fig.1(c)). In the textbook of crystal chemistry, the structures of corundum and spinel are classified as oxygen-closed-packed system. κ-Al_2O_3-structure is also characterized as an oxygen-close-packed system, but the sequence of oxygen-close-packed layers is expressed as **ACABACAB**….., whereas corundum and spinel structures have the sequences of **ABAB**……. and **ABCABC**, respectively. ε-Fe_2O_3 has recently attracted researchers' attention for its large coercive field of 20 kOe [1]. Ferroelectric hysteresis loop for epitaxially grown ε-Fe_2O_3 thin film gives a polarization of 2 μC/cm^2 at room temperature [2]. ε-Fe_2O_3 and its related compounds have become a key material, like $BiFeO_3$, as a target of the multiferroic. ε-Fe_2O_3 allows to be dissolved by trivalent ions, such as Al^{3+} and Ga^{3+}, keeping the same structure, and the solid solution also shows a ferroelectricity and ferrimagnetism. Among κ-Al_2O_3–type complex oxides, only $Ga_xFe_{2-x}O_3$ $(0.8 \leqq x \leqq 1.2)$ exists as stable phase at ambient temperature, while $Al_xFe_{2-x}O_3$ does as a high temperature phase (x~1.0, $1310 \leqq T \leqq 1500$ ℃). Epitaxially grown $GaFeO_3$ film shows a clear P-E hysteresis of the magnitude of 1 μC/cm^2, which is much smaller than the calculated value, 25 μC/cm^2, derived from the first principle calculation [3]. The reason for the difference between the calculated and experimental values of one order in magnitude is not clear at the present time.

In this study, we report *ab initio* calculation of the magnitude of the polarization and the energy for polarization switching in κ-Al_2O_3-type compounds of κ-Al_2O_3, ε-Ga_2O_3, and ε-Fe_2O_3 in the first part. Secondly, we report the structure and ferroelectric properties of $AFeO_3$ (A=Ga, Al, Sc, and In) thin films.

Results and discussions Previous report on the *ab initio* calculation for $GaFeO_3$ [3] assumes the non-polar phase of *Pnna* during polarization switching between polar structures of *Pna*2_1. In the present study, we used *Pbcn* structure as an intermediate phase for the switching of κ-Al_2O_3, ε-Ga_2O_3, and ε-Fe_2O_3. Then we found that the activation energy for the polarization switching is the 0.08 ~ 0.16 eV, which is fairly smaller than the reported value of 0.5 eV[3]. Fig.2 shows the HAADF-STEM image for GFO0.8 viewing from the same direction of Fig.1(a). The cation arrangement in Fig.2 corresponds to that of Fig.1(a), manifesting the upward polarization of GFO0.8 on the $SrTiO_3$ substrate. We confirmed that all the $AFeO_3$ (A=Ga, Al, Sc, and In) films with κ-Al_2O_3 structure showed a ferroelectricity. Fig.3 shows *P-E* loop for $ScFeO_3$ film. The Polarization switching is closely related to the shearing of the oxygen-closed-packed layers, and the detail will be explained in the presentation.

References [1] Jin and Ohkoshi, Adv. Mater., 16, 48 (2004). [2] Gich et al., Adv. Mater., 26, 4645 (2014). [3] Stoeffler, J. Phys.:Condensed Matter 24, 185502 (2012).

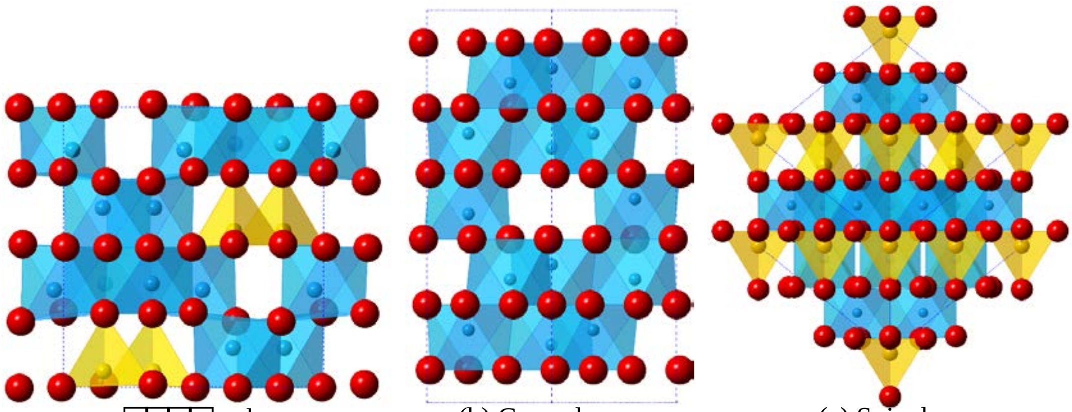

□□□□κ-alu (b) Corundum (c) Spinel

Fig.1 Comparison of three structures of κ-alumina, colundum, and spinel.

Fig.2 HAADF image for GFO0.8.

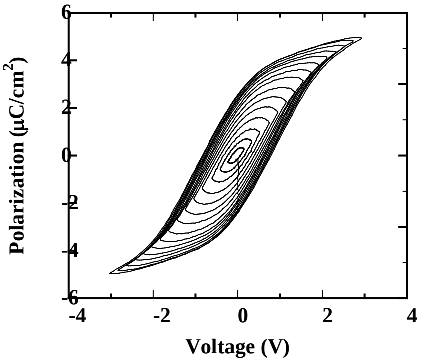

Fig.3 *P-E* loop for $ScFeO_3$.

Ferroelectricity in corundum derivatives

Meng Ye and David Vanderbilt
Department of Physics and Astronomy, Rutgers University, Piscataway, New Jersey 08854-8019, USA

Ferroelectricity requires a material to have a spontaneous electric polarization that can be reversed by an external electric field. The search for new ferroelectric (FE) materials holds promise for broadening our understanding of FE mechanisms and extending the range of application of FE materials. Recently, the research on multiferroics, in which FE and ferromagnetic orders coexist in the same material, further extends the application of FE materials.

The most intensively studied family of FE oxides is that of the perovskite oxides such as $BaTiO_3$. Perovskite oxides have the chemical formula ABO_3 with the A cation much larger than the B cation. The FE distortion is usually driven by B-site off-centering and typically requires an empty d shell on the B cation, which is not compatible with magnetism.

The corundum derivatives ABO_3 and $A_2BB'O_6$ can be derived from the corundum structure with cation ordering. They have a 10-atom rhombohedral unit cell as shown in Fig. 1. Most corundum derivatives are polar and thus can potentially be new ferroelectrics. A well-known example of a FE corundum derivatives is $LiNbO_3$ (LNO). The polarization in these materials is driven by the small A cation, so that the B and B' cations are not required to be in the d^0 configuration. The huge number of combinations of A, B and B' cations in the corundum derivatives open the possibility to achieve not only ferroelectricity but also multiferroicity.

In this work, we have used first-principles density-functional methods to systematically study the polar structure, the coherent and domain-wall-mediated FE reversal barriers for a variety of corundum derivatives. We have also identified the conditions under which the magnetic ordering is compatible with ferroelectricity. Finally, several empirical measures were found that can provide a rule of thumb for estimating the barrier energies.

In the corundum derivatives, the cations are spaced along the three-fold rotation axis and each one is surrounded by a distorted oxygen octahedron. Based on the combinations and arrangements of cations, corundum derivatives can be classified into four types, which we denote as follows. An oxygen octahedron with an A or B cation inside is written as "A" or "B", and if an oxygen octahedron is cation-vacant, the octahedron is denoted by "$-$". Then we use this notation to represent the six face-sharing oxygen octahedra in the unit cell for each of the four different types of corundum derivatives, i.e., LNO-type ABO_3 is $AB-AB-$, ilmenite ABO_3 is $AB-BA-$, ordered-LNO $A_2BB'O_6$ is $AB-AB'-$, and ordered-ilmenite $A_2BB'O_6$ is $AB-B'A-$.

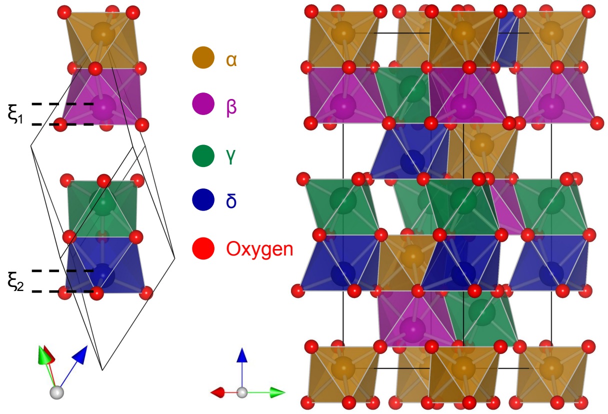

FIG. 1. Structure of corundum derivatives. The unit cell in the rhombohedral setting is shown at the left; an enlarged hexagonal-setting view is shown at right. The cations α, β, γ, and δ are are all identical in the A_2O_3 corundum structure. For LNO-type ABO_3, $\beta=\delta=A$, $\alpha=\gamma=B$; for ilmenite ABO_3, $\beta=\gamma=A$, $\alpha=\delta=B$; for ordered-LNO $A_2BB'O_6$, $\beta=\delta=A$, $\gamma=B$, $\alpha=B'$; for ordered-ilmenite $A_2BB'O_6$, $\beta=\gamma=A$, $\delta=B$, $\alpha=B'$. At left, ξ_1 (or ξ_2) is the distance between β (or δ) and the oxygen plane that it penetrates during the polarization reversal.

The polarization reversal process in corundum derivatives can in principle be associated with the motion of either A or B cations along the rhombohedral axis, such that the cation penetrates an oxygen plane and migrates into an adjacent unoccupied oxygen octahedron [1-2]. In our notation, the polarization reversal process interchanges A or B with $-$. For example, the LNO-type structure changes from $AB-AB-$ to $-BA-BA$. We insist that the structures before and after the reversal should be related by inversion symmetry; this consideration eliminates ilmenite and ordered-ilmenite structures from consideration as FE candidates.

For the LNO-type and ordered-LNO FE candidates, we studied the energy profiles of the coherent and domain-wall-mediated FE reversal barriers. In all cases the smaller cations are on the A sites and are the ones which are responsible for the polarization reversal. As illustrated in Fig. 1, we defined ξ_1 and ξ_2 as the distance between each A cation and the oxygen plane that is penetrated as the A atom moves along its path. Then we used $\xi_1+\xi_2$ as a structural constraint and the energy profile of the reversal path was calculated by controlling the constraint. For the coherent barrier, every unit cell undergoes the same polarization reversal process simultaneously. On the other hand, for the domain-wall-mediated barrier calculation-

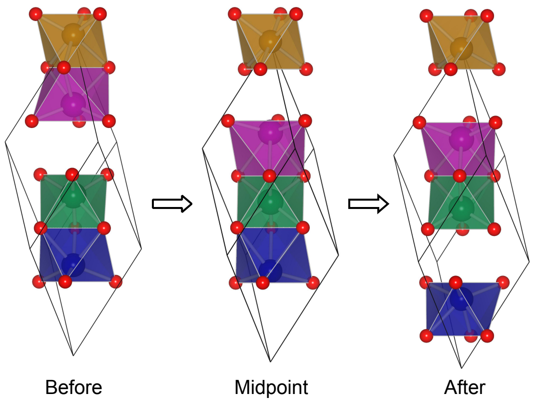

FIG. 2. The structural evolution along the polarization reversal path of LNO-type and ordered-LNO corundum derivatives. “Before” and “After” are the initial and final structures on the polarization reversal path, while “Midpoint” denotes the structure halfway between these.

TABLE I. Coherent FE barrier $E^{\mathrm{Coh}}_{\mathrm{barrier}}$, domain-wall-mediated FE barrier $E^{\mathrm{DW}}_{\mathrm{barrier}}$, and spontaneous polarization P_{S} for the materials covered by this study. A notation like “*udu*” describes a magnetic state in which spins are up (“*u*”) or down (“*d*”) on atoms β, δ and γ in that order.

	magnetic order	$E^{Coh}_{\mathrm{barrier}}$ (meV)	$E^{DW}_{\mathrm{barrier}}$ (meV)	P_{S} (μC/cm^2)
$LiNbO_3$	—	259	98	82
$LiTaO_3$	—	129	55	57
$ZnSnO_3$	—	241	86	57
$FeTiO_3$	AFM	763	—	105
$MnTiO_3$	AFM	468	220	94
Li_2ZrTeO_6	—	57	28/39	33
Li_2HfTeO_6	—	61	32/42	32
Mn_2FeWO_6	*udu*	215	—	63
Mn_3WO_6	*uud*	240	161/210	69
Mn_3WO_6	*udu*	272	170/205	70
Zn_2FeOsO_6	FiM	92	—	52

s, we constructed two adjacent domains with opposite polarizations, and only the unit cell at the domain wall undergoes polarization reversal.

We applied the above methods to the LNO-type corundum derivatives $LiNbO_3$, $LiTaO_3$, $ZnSnO_3$, $FeTiO_3$, and $MnTiO_3$, and to the ordered-LNO corundum derivatives Li_2ZrTeO_6, Li_2HfTeO_6, Mn_2FeWO_6, Mn_3WO_6, and Zn_2FeOsO_6. The structural evolution along the polarization reversal path is illustrated in Fig. 2, and the sequential movements of the A cations are depicted by ξ_1 and ξ_2 quantitatively in Fig. 3. The “Before” and “After” structures in Fig. 2 correspond to the points at the top right and bottom left corners of Fig. 3 respectively. The ideal “Midpoint” structure would correspond to the origin on the plot, but we find that the reversal path does not pass through this point because of an unstable mode along the $\xi_1 = -\xi_2$ direction. Our “Midpoint” in Fig. 2 is thus displaced from the origin along the dashed line $\xi_1 = -\xi_2$. The path for ordered-LNO is similar, except that the the ground-state symmetry does not enforce $\xi_1 = \xi_2$.

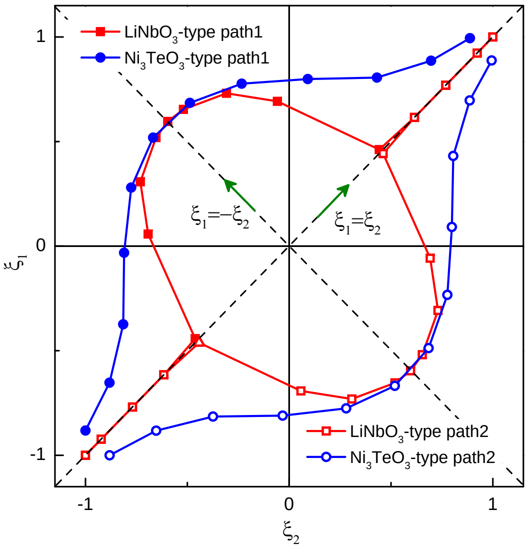

FIG. 3. Movements of A atoms in LNO-type and ordered-LNO corundum derivatives along the polarization reversal path. ξ_1 and ξ_2 are the distances from A atoms to the oxygen planes that are penetrated in the polarization reversal procedure, here rescaled to a range between −1 and 1. The “path1” (filled symbol) is related to the “path2” (open symbol) by interchanging the definitions of ξ_1 and ξ_2.

The coherent barrier energy $E^{\mathrm{Coh}}_{\mathrm{barrier}}$, the domain-wall-mediated barrier energy $E^{\mathrm{DW}}_{\mathrm{barrier}}$, and the spontaneous polarization P_{S} of these FE candidates are summarized in Table I. The domain walls of the ordered-LNO are asymmetric depending on the relative position between the P_{S} and $-P_{\mathrm{S}}$ domains, so there are two domain-wall-mediated energy barriers for each ordered-LNO material. Our results predicted several corundum derivatives with low coherent barrier and low domain-wall-mediate barrier energy, which are possible new FE materials. In the calculations, we also found that some materials with transition-metal cations, such as Mn_2FeWO_6, becomes conducting during the FE reversal; only d^3, d^5, and d^8 spin configurations were compatible with insulating FE path. Finally, we discovered that the coherent barrier is correlated with the off-center position of the A cations in the octahedron, while the domain-wall-mediated barrier is determined by how loosely the A cation is bonded in the oxygen octahedron.

[1] I. Inbar and R. E. Cohen, Phys. Rev. B **53**, 1193 (1996).
[2] M. Veithen and Ph. Ghosez, Phys. Rev. B **65**, 214302 (2002).

Underlying topological features in ferroelectrics

Y. Nahas* [1], S. Prokhorenko[1], I. Kornev[2], L. Bellaiche[1]

[1] *Physics Department and Institute for Nanoscience and Engineering*
University of Arkansas, Fayetteville, AR 72701, USA
[2] *Laboratoire Structures, Propriétés et Modélisation des Solides*
Ecole Centrale Paris, Chtenay-Malabry, 92290, France

∗ yousra.nahas@gmail.com

Topological defects such as vortices and antivortices are now widely recognized as constituting a prime topic in different areas of physics, ranging from cosmology to liquid crystals and, to a lesser extent, ferroelectrics. Here, we examine point topological defects, seeking to deepen the understanding of the means by which such features correlate to ferroelectric behavior.

1 Frustration and self-ordering of topological defects in ferroelectric nanocomposite[1]

Geometrical frustration is an inevitable feature of a wide variety of systems and has focused considerable interest on the unusual phenomena it prompts, among which are spin ice and spin liquid phases. Unlike the frustration inherent to disordered systems such as spin glasses wherein competing interactions fail to be simultaneously satisfied, geometrical frustration can manifest in well-defined structures as a result of the incompatibility between the geometry of the latter and the interactions governing the collective behavior of a set of degrees of freedom.

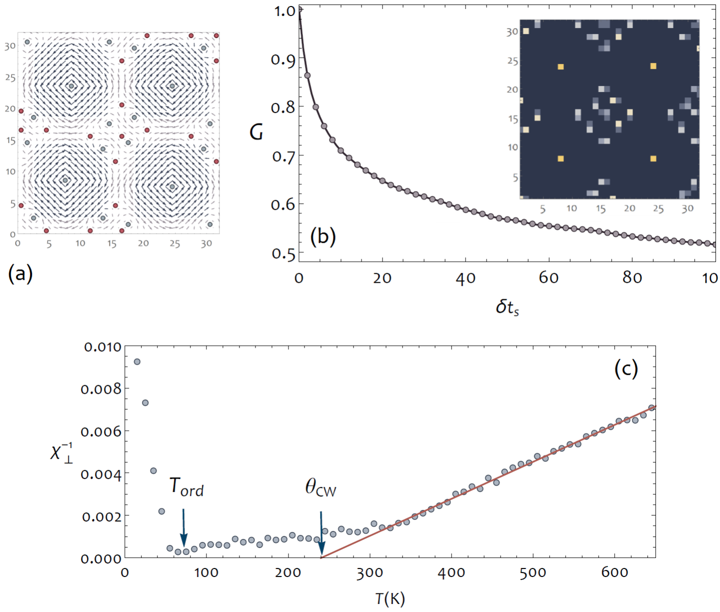

Fig. 1: **(a)** Microstructure (in-plane component of local modes and defects distribution) for a configuration with a checkerboard arrangement of the wires' chirality at 5 K. Blue (red) circles denote vortices (antivortices). Dark (light) arrows indicate the dipoles liying in the wires (matrices). **(b)** Monte Carlo time autocorrelation function $G(\delta t_s)$ of the spatial distribution of topological defects at 5 K. Inset shows the spatial probablity distribution of defects occurrence at 5 K. Yellow to dark blue gradient color indicates high to low probability of occurrence. **(c)** Temperature dependence of the inverse in-plane susceptibility $\chi_{\perp}^{-1}$. Vertical arrows indicate the transition temperature at which vortices and antivortices order in the matrix (T_{ord}), and the Curie-Weiss temperature (θ_{CW}). Red line is a linear fit of the high temperature values of $\chi_{\perp}^{-1}$.

Using a first-principles-based effective Hamiltonian (H_{eff}) technique[2] , we investigate a chiral ferroelectric nanocomposite consisting of a square array of $BaTiO_3$ nanowires embedded in a less polarizable matrix ($Ba_{0.15}Sr_{0.85}TiO_3$). We find that, as a result of the weak coupling between the chiralities of the wires, independent choices of spontaneous chiral symmetry breaking in each of the wires geometrically constrains the matrix to incompatible orientational boundary conditions. Assessment of the frustration index based on the dielectric susceptibility[3] attests of the geometrical frustration the system is subjected to. In response to frustration, the matrix locally accommodates such orientational incompabatibilities by featuring a self-assembled ordered structure of vortices and antivortices. Such structures are found to spatially fluctuate while preserving the energy, thereby pointing to a residual entropy at the origin of ground state degeneracy.

---

[1] Y. Nahas, S. Prokhorenko, and L. Bellaiche, "Frustration and self-ordering of topological defects in ferroelectrics", *submitted*

[2] L. Walizer, S. Lisenkov, and L. Bellaiche, Phys. Rev. B 73, 144105 (2006).

[3] A. P. Ramirez, Annu. Rev. Mater. Sci. 24, 453 (1994).

Following the theorem of Mermin and Wagner, thermal fluctuations preclude true long-range order at any finite temperature in two-dimensional (2d) systems with short-range interactions and O(2) symmetry. The behavior of these systems, which are described by the 2d XY-model, is cast into the BKT theory that provides a paradigmatic example of phase transitions mediated by topological defects; it predicts the occurrence of a transition from a disordered phase with exponentially decaying correlations, to a low-temperature quasi-long range ordered phase with correlations falling off as $1/r^{\eta}$ (where η is a temperature-dependent critical exponent), as a result of the pairing of vortices and antivortices. Although some systems, such as weakly interacting ultracold gases, effectively undergo such a transition, the situation described by the XY-model is scarcely met in experiments. A more realistic model has to account for crystal-field anisotropy and long-range dipolar interactions which may alter the nature of the transition.

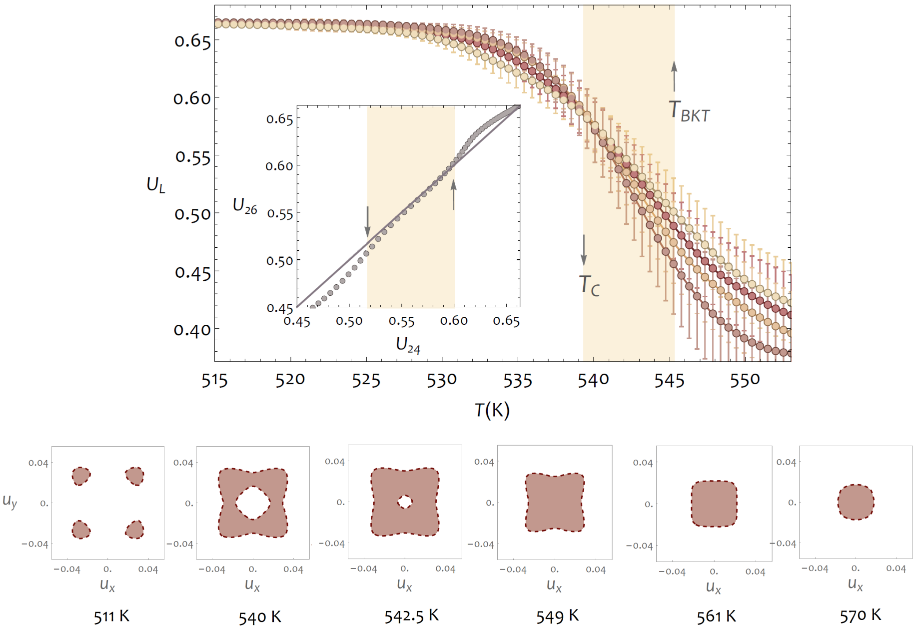

Fig. 2: Temperature dependence of Binder's fourth-order cumulant[4] U_L for different lateral sizes (L) of the periodic supercells. Inset provides the behavior of U_{26} vs U_{24}. A line of critical points for which U_{26}=U_{24} is clearly seen (shaded area). It is indicative of a correlation length exponentially divergent ($\nu = \infty$), sign of the existence of an intermediate BKT phase. Lower panel shows the temperature evolution of the symmetrized probability distribution of local dipole moments within L=30 supercell. The system transits from a uniform distribution characteristic of a disordered state at high-T to four isolated spots representative of a fourfold-degenerate ground state, through an approximate continuous rotational symmetry with nearly annular distribution at intermediate-T. The ring's distortion reflects the anisotropy of the underlying crystal lattice.

Seeking to address the question of the stability of BKT phase against the introduction of anisotropy and long-ranged dipolar interactions in ferroelectrics, we inspect the critical properties of $BaTiO_3$ thin film ($\sim$ 12 Å) under tensile strain (3%) using the H_{eff} scheme and finite-size scaling arguments. The system can be effectively regarded as quasi two-dimensional with the fluctuations of polarization constrained to lie within the film plane. At low temperatures, the fluctuations are sufficiently reduced leading to the stabilization of truly long-range ordered fourfold-degenerate ground state below a transition temperature T_C. Remarkably, we find evidence for a narrow critical phase above T_C with an emergent approximate continuous symmetry, reminiscent of the intermediate BKT phase between the low-T ordered phase and the high-T disordered phase of the square planar rotator model with small fourfold symmetry-breaking field[5]. The intermediate phase is a critical BKT phase exhibiting correlations of the order parameter that decay algebraically in space. Its upper critical temperature, T_{BKT}, marks the transition to the paraelectric phase and coincides with a value $\eta \sim 0.25$ of the extracted critical exponent. Inquiring into the behavior of point topological defects, we further corroborate the BKT nature of this intermediate phase $T_C < T < T_{BKT}$, as we find it to be concomitant with a bound state of vortices-antivortices pairs. The latter are found to unbound and proliferate for $T > T_{BKT}$ while they annihilate for $T < T_C$.

In summary, while the critical behavior is usually determined by the spatial dimensionality and the symmetry of the order parameter, in some cases such as the one here reported, at criticality, a higher, quasi-continuous symmetry of the discrete order parameter may emerge, rendering the associated critical behavior richer than expected. Indeed, while we find that the fourfold anisotropy is relatively irrelevant in the intermediate critical BKT phase where the 2d XY-model properties are recovered, it reasserts itself restoring the fourfold-symmetry at low temperatures.

This work is supported by ARO grant W911NF-12-1-0085 and DARPA grant HR0011-15-2-0038. Some computations were also made possible thanks to the MRI grant 0722625 from NSF, the ONR grant N00014-15-1-2881 (DURIP) and a Challenge grant from the Department of Defense.

---

[4] K. Binder, Z. Phys. B: Condens. Matter 43, 119 (1981).

[5] E. Rastelli, S. Regina, and A. Tassi, Phys. Rev. B, 70,174447 (2004).

Poster Session Abstracts

Understanding Negative Thermal Expansion in Improper Ferroelectric Ruddlesden-Popper Oxides from first principles

Chris Ablitt[1], Mark Senn[2], Arash Mostofi[1] and Nicholas Bristowe[1]

[1]*Department of Materials, and the Thomas Young Centre for Theory and Simulation of Materials, Imperial College London, London SW7 2AZ, UK*

[2]*Department of Chemistry, Inorganic Chemistry Laboratory, University of Oxford, South Parks Road, Oxford OX1 3QR, UK*

Lattice distortions and the coupling between them are important in controlling the electronic and mechanical behaviour of perovskites and related materials, such as Ruddlesden-Popper oxides. Examples include the emergence of the polar mode through a second order Jahn-Teller distortion in proper ferroelectrics [1] and as a secondary order parameter in improper ferroelectrics [2]. Another example is negative thermal expansion, which has also been shown to arise in a number of network structures by a 'tension mechanism' involving rigid unit modes, that is, lattice distortions of rigid oxide octahedral units [3,4]. Understanding how to control these modes and their coupling is a step towards developing the microscopic understanding required to design materials with different functionalities. Such design rules are becoming established in the field of ferroelectrics whereby non-polar modes couple to make polar modes by design [5,6,7,8].

Recent experiments have shown the existence of a paraelectric phase displaying strong uniaxial negative thermal expansion (NTE) which competes with an alternative phase exhibiting improper ferroelectricity (FE) in a Ruddlesden-Popper compound, $Ca_3Mn_2O_7$ [9]. The coincidence of NTE and FE in the same system is particularly interesting. Both FE and NTE have been argued to arise as a result of octahedral tilt modes [6,9]. However, whilst FE requires these tilts to be condensed into the system, such that the polar distortion may also condense due to trilinear coupling, NTE is thought to arise due to the dynamic appearance of these tilts as soft phonon modes, hence the competition between these NTE and FE phases.

We have performed a number of calculations on the Ruddlesden-Popper $(Ca,Sr)_{n+1}Ge_nO_{3n+1}$ system using first-principles density functional theory in order to understand this competition. From the results of these, I will discuss the origin of NTE in these materials and show that negative thermal expansion is caused by octahedral tilt and rotational modes and the strong couplings between these modes to one another and to the strain. I will also discuss why the Ruddlesden-Popper system is conducive to this type of NTE and how the level of NTE, both the magnitude and the temperature range, may be controlled through physical and chemical alterations.

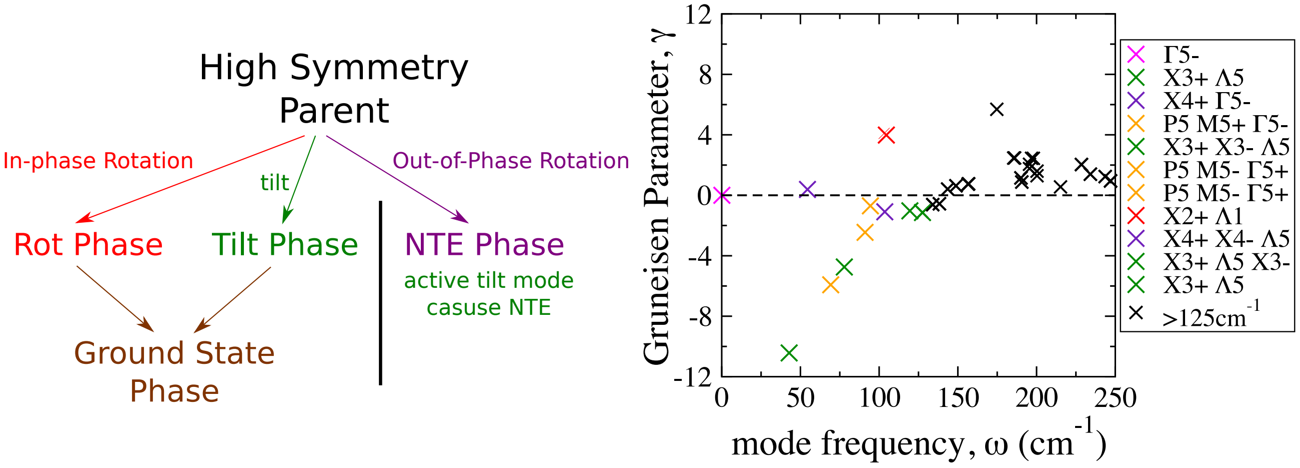

Figure 1: a) General scheme for competing phases in Ruddlesden-Popper oxides showing NTE b) Grüneisen parameters for lowest frequency modes in NTE phase.

References:

[1] R. E. Cohen, Nature, **358**, 136 (1992)
[2] A. P. Levanyuk and D. G. Samnikov, Sov. Phys. Usp. **17**, 199 (1974)
[3] M. T. Dove, V. Heine, and K. D Hammond. Min. Mag., **59,** 629 (1995)
[4] K. Takenaka. Sci. Technol. Adv. Mater., **13**, 013001 (2012)
[5] E. Bousquet *et al.*, Nature Letters **452**, 732 (2008)
[6] N. A. Benedek and C. J. Fennie, Phys. Rev. Lett. **106**, 107204 (2011)
[7] J. Rondinelli and C. J. Fennie, J. Phys. Chem. C **117**, 13339 (2013)
[8] T. Fukushima *et al.*, Phys. Chem. Chem. Phys., **13**, 12186 (2011)
[9] M. S. Senn *et al.,* Phys. Rev. Lett., **114**, 035701 (2015)

Finite-temperature properties of PMN-25PT nanodot from First-principles

A. Albarakati[1], S. Prosandeev[2,3], D. Wang[4], and L. Bellaiche[2]
[1] Physics Department, Umm Al-Qura University, Makkah, Saudi Arabia
[2] Physics Department and Institute for Nanoscience and Engineering, University of Arkansas, Fayetteville, Arkansas 72701, USA
[3] Research Institute of Physics, Southern Federal University, 344090 Rostov on Don, Russia
[4] Electronic Materials Research Laboratory, Key Laboratory of the Ministry of Education and International Center for Dielectric Research, Xi'an Jiaotong University, Xi'an 710049, China

Relaxor ferroelectric systems (bulk or nanostructure form) are very important because of their unusual properties and potential applications [1,2]. Interestingly, atomistic simulations can reveal many interesting features of bulk or nanostructured materials that may lead to new applications. For example, calculations of the dipole pattern in nanodots of $BaTiO_3$ and $PbZr_{1-x}Ti_xO_3$ [3,4] showed a vortex structure, which is characterized by a toroidal moment. In this study, we use first-principles-based techniques to investigate $Pb(Mg_{1/4}Nb_{1/2}Ti_{1/4})O_3$ nanodots, (denoted as PMN-25PT nanodot), for several sets of atomic and oxygen vacancies (OV) distributions. The aim of this study is to find the effects of nanodot's size (volume and shape) and the effects of atomic and OV distributions on the dipole pattern of PMN-25PT nanodots, and the dependence of this property on temperature.

In this work, we first extend the effective Hamiltonian developed in reference [5] to include the influence of surfaces and OV by adding energetic terms that characterize the interaction of surfaces and OV with local dipoles and strains. Then we use Monte-Carlo (MC) simulations to demonstrate the structure and properties of the system under investigation.

We numerically simulate two kinds of distributions (disordered and perfectly ordered distribution) of B-atoms (Mg/Ti/Nb) in several PMN-25PT nanodots of different sizes. In the disordered distribution, the three B-atoms are randomly distributed along the [001]c, [010] and [001]c directions, while in the perfectly ordered distribution, the three B-atoms are distributed in a special way, so that no net random electric field on B-sits, (random electric field results from the difference in valence charge between the three B-atoms). During simulations, the size of the dot, the distribution of B-site atoms and the OV distribution are kept fixed. The output of MC simulations are local modes (u_x,u_y,u_z), which are directly proportional to polarizations, homogenous strains, toroidal moments, and hyper-toroidal moments.

Our primary results reflect the importance of distribution of atoms and nanodots' size. First, as displayed in Fig.1 for the ideal open-circuit system (the parameter that controls the depolarizing field β=0.0), the vortex does not appear in the disordered nanodot of size 6x6x6 [cf. Fig.1(a)], while the dipole pattern does show some signature of vortex in the perfectly ordered nanodots of the same size as shown in Fig.1(b). However, the vortex clearly appears in VCA PMN-25PT nanodot, which does not have random field, of size 6x6x6, and in the disordered PMN-25PT nanodot of size 10x10x10 [cf. Fig. 1(c) and (d)]. Second, for the ideal short circuit condition (β=1.0), the low temperature phase of the disordered PMN-25PT nanodot of size (10x10x10) is tetragonal, ($u_x = u_y = 0.0$, $|u_z| > 0$), while it is monoclinic M_C ($u_x = 0$, $|u_y| > 0$, $|u_z| > |u_y|$) for the perfectly ordered PMN-25PT nanodot as seen in Fig. 2(a) and (b). However, the low temperature phase for disordered and perfectly ordered PMN-25PT *bulk* is rhombohedral ($|u_x| = |u_y| = |u_z| > 0$). Such difference is likely due to the depolarizing fields that is present in nanodots. These results, as well as others (e.g., the effects of OV distributions), will be discussed in detail.

This work is supported by King Abdulaziz City for Science and Technology under grant number 11-NAN1414-10.

References:

[1] Park S-E. and Shrout T.R., J. Appl. Phys. 82, 1804 (1997).

[2] Park S-E. and Shrout T.R., Ultrason. Ferroelectr. Freq. Control 44, 1140 (1997).

[3] H. Fu and L. Bellaiche, Phys. Rev. Lett. 91, 257601 (2003).

[4] Ivan I. Naumov, L. Bellaiche, and Huaxiang Fu, Natture 432, 737-740 (2004).

[5] Al-barakaty A., *Finite-temperature properties of complex perovskite from first principles calculations*, Ph.D thesis, University of Arkansas, 2004.

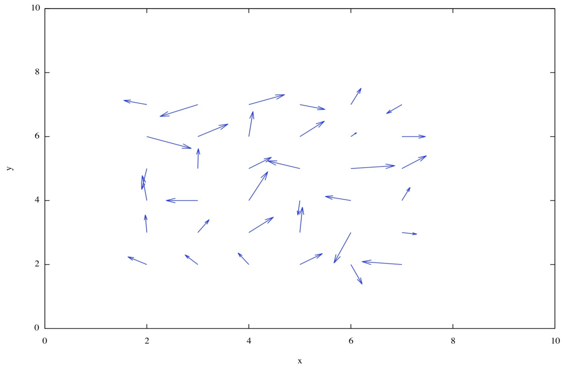

Fig.1(a): Local mode pattern in the x-y plane at T=100K for disordered PMN-25PT nanodot of size 6x6x6.

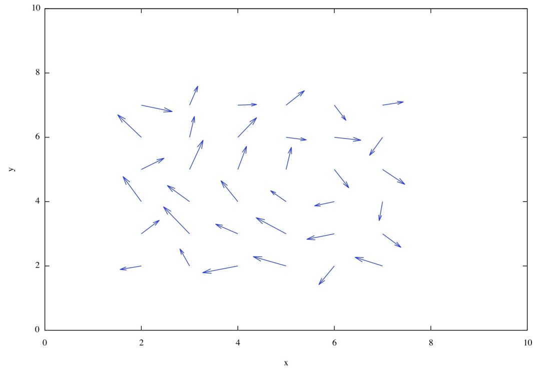

Fig1(b): Local mode pattern in the x-y plane at T=100K for the perfectly ordered PMN-25PT nanodot of size 6x6x6.

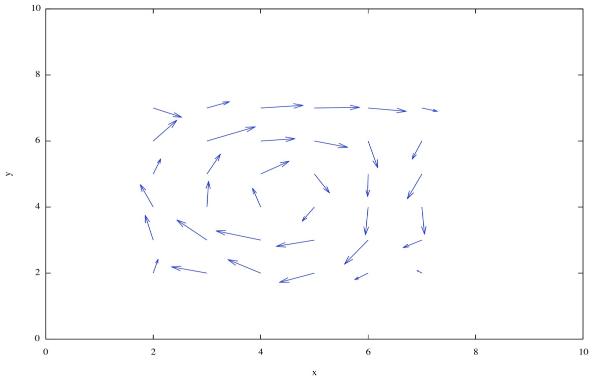

Fig.1(c): Local mode pattern in the x-y plane at T=100K for VCA PMN-25PT nanodot of size 6x6x6 .

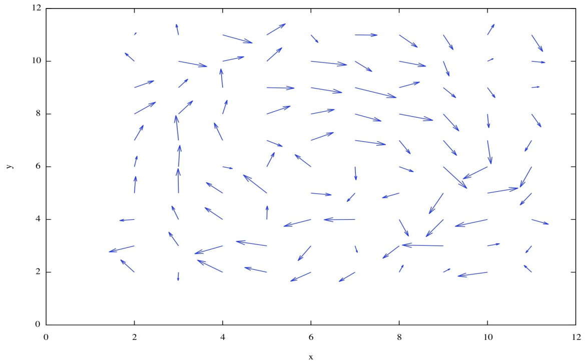

Fig.1(d): Local mode pattern in the x-y plane at T=100K for disordered PMN-25PT nanodot of size 10x10x10.

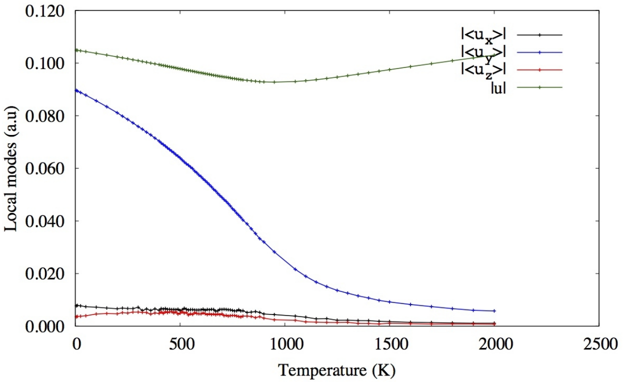

Fig.2(a): Local modes versus temperature for disordered PMN-25PT nanodot of size 10x10x10 and β=1.0.

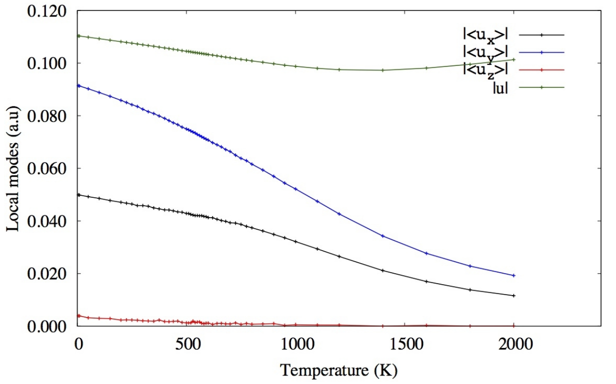

Fig2(b): Local modes versus temperature for perfect-ordered PMN-25PT nanodot of size 10x10x10 and β=1.0.

Charged domain walls and polar boundaries in $LiNbO_3$ and $CaTiO_3$ studied by Mirror Electron Microscopy

G. F. Nataf[1,2], D. Martinotti[1], C. Mathieu[1], P. Grysan[2], L. Tortech[3], R. Haumont[4], N. Barrett[1]

[1]SPEC, CEA, CNRS, Université Paris-Saclay, CEA Saclay, 91191 Gif-sur-Yvette, France
[2]Materials Research and Technology Department, Luxembourg Institute of Science and Technology, 41 Rue du Brill, 4422 Belvaux, Luxembourg
[3]Sorbonne Universités, UPMC Univ Paris 06, CNRS UMR 8232, Institut Parisien de Chimie Moléculaire, Université Pierre et Marie Curie, 4 place Jussieu, case courrier 42, F-75005 Paris CEDEX 05 , France and LICSEN, NIMBE, CEA, CNRS, Université Paris-Saclay, CEA Saclay 91191 Gif-sur-Yvette Cedex, France
[4]Institut de Chimie Moléculaire et Matériaux d'Orsay, UMR CNRS 8182, Bât 410, Université Paris Sud. 91405 Orsay cedex, France.

There is currently a growing interest for structural and electric properties of ferroelectric and ferroelastic domain walls. The emerging field of so-called domain boundary engineering [1,2] holds the promise of using the distinct functional properties of domain walls in and as devices. We are particularly interested in Mg-doped $LiNbO_3$, which has drawn attention after reports of photo-induced conductivity at their domain walls [3]; and $CaTiO_3$, for the experimental evidence of polar domain boundaries in an otherwise non-polar matrix [4,5].

$LiNbO_3$

We use a low energy electron microscope (LEEM) to observe out-of-plane ferroelectric domains of a Mg-doped $LiNbO_3$ single crystal. At very low electron kinetic energy, called mirror electron microscopy (MEM), electrons are reflected without penetrating the sample surface [6]. At higher kinetic energy, the electrons penetrate the surface. In between the reflectivity gives a measure of the local work function or surface potential [7].

Figure 1(a) shows the surface potential measured across microscopic region of the $LiNbO_3$ surface. Two domain walls are visible. As shown in Fig. 1(b), they are characterized by an asymmetry in the intensity arising from the electrons being deflected by the electric field due to the domain wall dipole. By studying samples with controlled topography (height difference between domains, step sharpness and surface roughness), we show that the changes in the signal due to local surface potential variations dominate those due to physical topography.

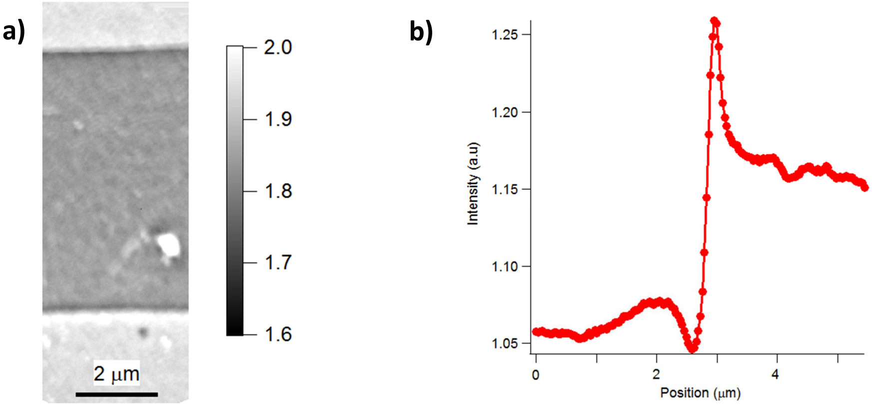

Figure 1 (a) Relative surface potential (in eV) and (b) intensity profile across domain wall extracted from MEM images.

CaTiO₃

Since MEM is sensitive to local surface charge, we use it to study the possible polar nature of $CaTiO_3$ domain boundaries. Figure 2(a) shows the electron image of the surface. As expected, adjacent domains present the same intensity because the material is non-polar and the work function is not expected to change from one domain to another. However, at twin domain boundaries, thin black and white lines are visible. In Fig. 2(b), an Atomic Force Microscopy image shows that the contrast depends on the orientation of the twin boundary. In particular, valleys, whose physical topography is expected to concentrate and enhance intensity are dark in the electron image, providing strong evidence for a polar domain wall. By adjusting the focusing conditions of the LEEM we observe behavior consistent with locally charged domain walls. We thus provide direct in-situ evidence of the polar nature of ferroelastic twins in $CaTiO_3$.

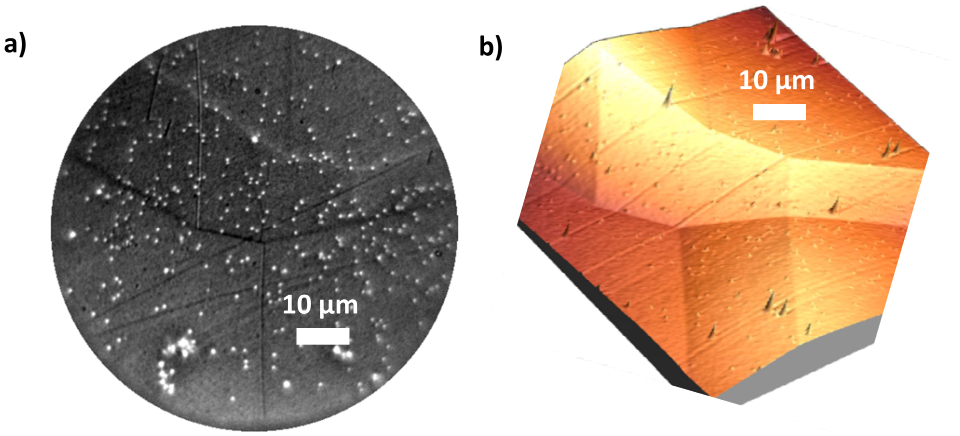

Figure 2 (a) Electron and (b) AFM image of the same region of the $CaTiO_3$ surface correlating electron reflectivity as a result of surface charge/potential and physical topography.

The ability to observe the domain boundary region in wide-band-gap oxides opens the path for a better understanding of domain walls in a whole range of functional oxides. This should be a real step forward in the characterization of domain wall engineering.

References

[1] G. Catalan, J. Seidel, R. Ramesh, and J. F. Scott, *Rev. Mod. Phys.* **84** 119 (2012).
[2] E. K. H. Salje and H. Zhang, Phase Transitions ***82***, 452–69 (2009).
[3] M. Schröder et al., *Adv. Funct. Mat.* ***22***, 3936–44 (2012).
[4] H. Yokota et al., *Phys. Rev. B* **89**, 144109 (2014).
[5] S. Van Aert et al., *Adv. Mater.* **24**, 523 (2012).
[6] N. Barrett et al., *J. Appl. Phys.* **113**, 187217 (2013).
[7] J. Rault et al. *Phys. Rev. Lett.* **109**, 267601 (2012).

Application of the Wang-Landau Monte-Carlo Formalism applied to Ferroelectrics materials

S. Bin-Omran[1], I. Kornev[2], and L. Bellaiche[3]

[1]King Saud University, Department of Physics and Astronomy, P.O.BOX: 2455, Riyadh 11451, Saudi Arabia

2 Laboratoire SPMS, UMR 8580 du CNRS, Ecole Centrale Paris, 92295 Chatenay-Malabry, France

3 Institute for Nanoscience and Engineering and Physics Department, University of Arkansas, Fayetteville, Arkansas 72701, USA

The conventional description of phase transitions in ferroelectrics is based on canonical thermodynamic functions and always assumes the thermodynamic limit of an infinite system. However, ferroelectrics at nanoscale recently became of high interest due to their potential applications in miniaturized devices. It is also very difficult to estimate the thermal average of some microscopic quantities with satisfactory accuracy by using standard Metropolis Monte Carlo and molecular dynamics methods due to the critical slowing down near the phase transition temperature. Moreover, these methods do not give direct access to thermodynamic potentials. It is thus timely and more appropriate to use the microcanonical ensemble when mimicking ferroelectric systems [1,2].

Interestingly, a Monte Carlo method based on the density of states (or microcanonical ensemble partition function) proposed by Wang and Landau [3] has the potential to overcome these difficulties. In principle, this technique provides a route to calculate the density of states g(E), which is defined by the number of all possible states (or configurations) for an energy E of the system of interest. Once g(E) is determined, one can then calculate most thermodynamical quantities for all temperature with one single simulation! Moreover, the free energy (F) and the entropy (S) can be readily calculated, unlike in conventional Monte Carlo Metropolis simulations – which allows the investigation of challenging but important quantities.

In this work [4], the Wang-Landau Monte Carlo algorithm is implemented within an effective Hamiltonian approach and used to conduct a detailed study of physical properties of $BaTiO_3$ bulk. In this presentation, we will show how this approach allows a highly-accurate and straightforward calculation of various thermodynamic properties, including phase transition temperatures, as well as polarization, dielectric susceptibility, specific heat and electrocaloric coefficient at any temperature.

This work is supported by the National Plan for Science, Technology and Innovation under the research project No. ADV-1498-2. L.B. thanks the financial support of DARPA grant HR0011-15-2-0038.

References:

[1] D. Gross, Microcanonical Thermodynamics: Phase Transitions in "small" Systems, World Scientific lecture notes in physics (World Scientific, 2001), ISBN 9789812798916.

[2] M. Pleimling and H. Behringer, Phase Transitions 78, 787 (2005).

[3] F. Wang and D. P. Landau, Phys. Rev. Lett. 86, 2050 (2001).

[4] S. Bin-Omran, I. Kornev and L. Bellaiche, submitted.

Proper and improper ferroelectricity in the n=3 Dion-Jacobson material $AA'_2Ti_2NbO_{10}$

Eric Bousquet,[1] Neil C. Hyatt,[2] and Emma E. McCabe[3]

[1] *Theoretical Materials Physics, University of Liege B-4000 Sart Tilman, Belgium*
[2] *Department of Materials Sciences and Engineering, University of Sheffield,*
Sir Robert Hadfield Building, Mappin Street, Sheffield S1 3JD, U.K.
[3] *School of Physical Sciences, Ingram Building, University of Kent, Canterbury, Kent, CT2 7NH, U.K*

Dion-Jacobson phases, of general formula $AA'_{n-1}B_nO_{3n+1}$, consist of perovskite layers composed of n layers of corner-linked BO_6 octahedra, separated by layers of alkali A' cations. Their layered perovskite structure is similar to that of the Aurivillius and Ruddlesden-Popper families in which the stacking arrangements of the layers is different. The structural chemistry of the Dion-Jacobson family is less understood than the two other families. Even though distortions similar to those found in Ruddlesden-Popper and Aurivillius materials can be expected in the Dion-Jacobson phases, the symmetries of the resulting Dion-Jacobson phase will not necessarily follow those determined for the Ruddlesden-Popper and Aurivillius crystals. Recently, Benedek has demonstrated the importance of hybrid-improper mechanisms for ferroelectricity in the n =2 Dion-Jacobson phases [1], which motivated several works proving the piezoelectric and ferroelectric properties of $ABiNb_2O_7$ (A = Cs, Rb) [2–4].

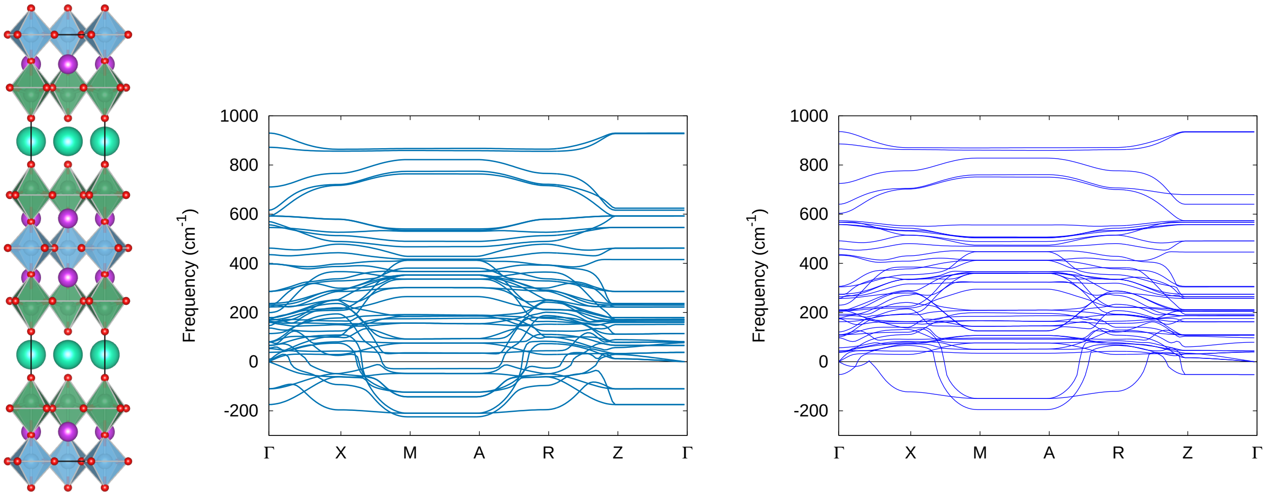

FIG. 1. (Left) Illustration of the $I4/mmm$ phase of $CsBi_2Ti_2O_{10}$ Dion-Jacobson material (big light green, small red, purple, blue and green spheres represent the Cs, O, Bi, and Ti/Nb atoms respectively). The central octahedra are represented in blue and the outer octahedra are represented in green. (Central) Calculated phonon dispersion curves of the $P4/mmm$ phase of $CsBi_2Ti_2O_{10}$. Negative values correspond to imaginary frequencies, *i.e.*, to unstable phonon modes. The coordinates of the high-symmetry points are X (1/2, 0, 0), M (1/2, 1/2, 0), A (1/2, 1/2, 1/2), R (1/2, 0, 1/2), and Z (0, 0, 1/2). From [5]. (Right) Same as the central panel but for $CsLa_2Ti_2O_{10}$ where Bi has been replaced by La.

Here we report from experiment and first-principles calculations [5] that the n =3 $CsBi_2Ti_2O_{10}$ Dion-Jacobson material adopts a proper ferroelectric structure below 545°C ($Ima2$ space group). Our structural studies from variable-temperature neutron powder diffraction (NPD) data on $CsBi_2Ti_2O_{10}$ show that it adopts a polar structure at room temperature involving two modes of octahedral rotation as well as ferroelectric displacements along the in-plane polar direction. At high temperature, $CsBi_2Ti_2O_{10}$ crystalises to a high symmetry tetragonal phase ($P4/mmm$ space group). These structural studies are consistent with second harmonic generation (SHG) measurements and its relatively low permittivity with maximum at 550°C. Our Density Functional Theory (DFT) analysis of the phonon instabilities of the $P4/mmm$ phase (see Figure 1 right) and their successive condensation

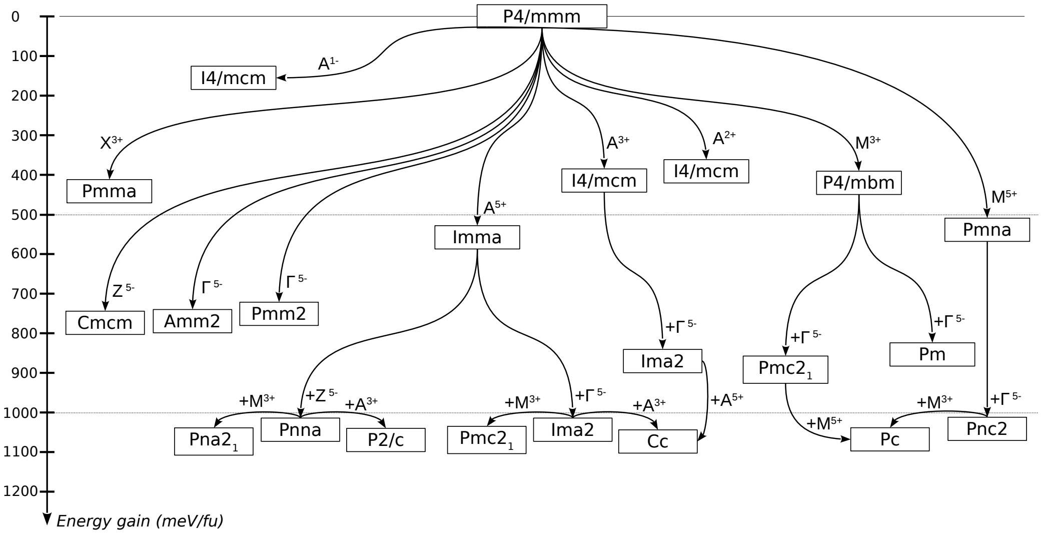

FIG. 2. DFT internal energy phase diagram of $CsBi_2Ti_2O_{10}$ after the condensation of different combination of unstable modes obtained in the $P4/mmm$ phase. From [5]

show that the $Ima2$ phase of $CsBi_2Ti_2O_{10}$ is a proper ferroelectric, unlike the $n = 2$ analogues. Additionally, the DFT calculations show that the phase diagram of $CsBi_2Ti_2O_{10}$ is complex and exhibits numerous metastable phases of relatively close energies (see Figure 2). The lowest energy phases suggest that further low-temperature phases combining proper and improper ferroelectricity together may exists.

Going further, we also investigate the influence of A and A$'$ cations in $AA'_2Ti_2O_{10}$ on the phonon instabilities of the $P4/mmm$ phase and the resulting low symmetry phase diagram. We explore mixtures of A= Cs and Rb and A$'$ = Bi, La, Nd and Y and show the cation sizes and chemistry can completely change the phase stability of the n =3 Dion-Jacobson materials (see Figure 1 for the $P4/mmm$ phonon dispersion curves comparison between $CsBi_2Ti_2NbO_{10}$ and $CsLa_2Ti_2NbO_{10}$), consistent with analysis of variable temperature NPD data [6].

BIBLIOGRAPHY

[1] N. A. Benedek, Inorganic Chemistry **53**, 3769 (2014).
[2] H. Sim and B. G. Kim, Phys. Rev. B **89**, 144114 (2014).
[3] G. Gou and J. Shi, EPL (Europhysics Letters) **108**, 67006 (2014).
[4] C. Chen, H. Ning, S. Lepadatu, M. Cain, H. Yan, and M. J. Reece, J. Mater. Chem. C **3**, 19 (2015).
[5] E. E. McCabe, E. Bousquet, C. P. J. Stockdale, C. A. Deacon, T. T. Tran, P. S. Halasyamani, M. C. Stennett, and N. C. Hyatt, Chemistry of Materials **27**, 8298 (2015).
[6] E. Bousquet and *et al.*, In preparation (2015).

Study on mixed crystals $[N(CH_3)_4]_2Zn_{1-x}Co_xCl_4$ (x=0, 0.5, 0.7, 0.9, and 1) by NMR

Jin-Hae Chang,[a,*] **Ae Ran Lim**[b]

[a]*Department of Polymer Science and Engineering, Kumoh National Institute of Technology, Gumi 730-701, Korea*

[b]*Department of Science Education, Jeonju University, Jeonju 560-759, Korea*

$[N(CH_3)_4]_2ZnCl_4$ and $[N(CH_3)_4]_2CoCl_4$ single crystals belong to the group of A_2BX_4-type crystals, many of which have an incommensurate (INC) phase in their phase transition sequence [1]. Crystals of this type have attracted considerable interest owing to their several phase transitions. $[N(CH_3)_4]_2ZnCl_4$ undergoes five phase transitions, which occur at 161 K, 181 K, 276.3 K, 279 K, and 296 K, respectively [2, 3]. On the other hand, $[N(CH_3)_4]_2CoCl_4$, undergoes six phase transitions, which occur at 122 K, 192 K, 276 K, 277.6 K, 280.1 K, and 293 K, respectively. It should be noted that $[N(CH_3)_4]_2CoCl_4$ undergoes successive phase transitions that are similar to those of $[N(CH_3)_4]_2ZnCl_4$ [6].

Here, $[N(CH_3)_4]_2Zn_{1-x}Co_xCl_4$ (x=0, 0.5, 0.7, 0.9, and 1) single crystals were grown from aqueous solutions using the slow evaporation method. We measured the temperature dependence of the cross-polarization/magic-angle spinning (CP/MAS) NMR spectrum for ^1H and ^{13}C nuclei of $[N(CH_3)_4]_2Zn_{1-x}Co_xCl_4$ in these solid solutions. In addition, spin-lattice relaxation times in the rotating frame, $T_{1\rho}$, for ^1H and ^{13}C nuclei in $[N(CH_3)_4]_2Zn_{1-x}Co_xCl_4$ according to the amount of impurity Co^{2+} ions were

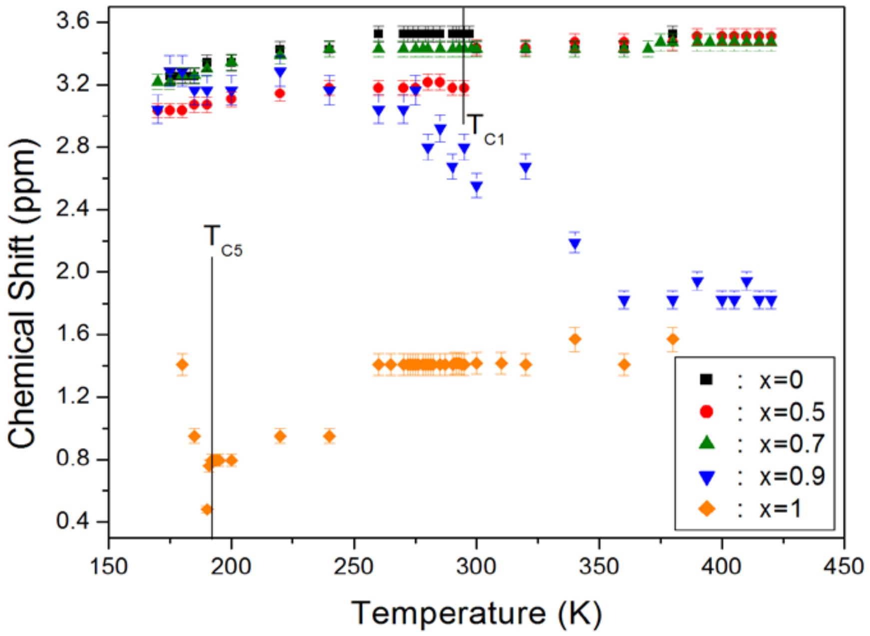

Fig. 1. Chemical shifts of the ^1H MAS NMR spectrum as a function of temperature in $[N(CH_3)_4]_2Zn_{1-x}Co_xCl_4$ (x=0, 0.5, 0.7, 0.9, and 1).

determined. This is the first investigation of the local structures of $[N(CH_3)_4]_2Zn_{1-x}Co_xCl_4$, and we use our results to analyze the environments of the $N(CH_3)_4$ ions. The results also enable us to compare the structural properties of $[N(CH_3)_4]_2ZnCl_4$ and $[N(CH_3)_4]_2CoCl_4$: we examined the effect of substituting Zn ions with Co ions in $[N(CH_3)_4]_2ZnCl_4$, with a focus on the effects of Co impurities on structural geometry and relaxation mechanisms.

The purpose of this study was to investigate how the local structure of pure crystal is affected by random presence of cations of different sizes and to determine the influence of such substitution on physical properties. After partial replacement of Zn^{2+} ions by Co^{2+} ions, the Co^{2+} ions occupy the same locations in the lattice as the Zn^{2+} ions previously did. Crystallographic structures in $[N(CH_3)_4]_2Zn_{1-x}Co_xCl_4$ (x=0, 0.5, 0.7, 0.9, and 1) can be understood by considering the differences due to chemical shifts of ^{1}H MAS NMR and ^{13}C CP/MAS NMR spectra. The NMR spectrum and $T_{1\rho}$ with x=0.5 and x=0.7 were similar to those for pure $[N(CH_3)_4]_2ZnCl_4$, whereas the NMR spectrum and $T_{1\rho}$ with x=0.9 were absolutely different. However, the presence of x=0.5 and 0.7 of Co^{2+} in the structure with does not lead to any differences in the chemical shift and relaxation behavior for ^{1}H and ^{13}C. Perhaps, this implies that the local environments surrounding ^{1}H and ^{13}C nuclei were not different. Consequently, $[N(CH_3)_4]_2Zn_{0.1}Co_{0.9}Cl_4$ showed structural properties of pure $[N(CH_3)_4]_2ZnCl_4$ as well as $[N(CH_3)_4]_2CoCl_4$. Our results indicate that the replacement of Zn^{2+} ions by a high concentration of Co^{2+} ions introduces a local distortion in structure of crystals.

References

[1] J. Berger, J.P. Benoit, C.W. Garland, P.W. Wallace, J. Phys. 47 (1986) 483.

[2] K. Hasebe, H. Mashiyama, N. Koshiji, S. Tanisaki, J. Phys. Soc. Jpn. 56 (1987) 3543.

[3] P.S. Gregoire, K. Tchakpele, T. Assih, Ferroelectrics 126 (1992) 319.

[4] G. Madariaga, F.J. Zuniga, J.M. Perez-Mato, M.J. Tello, Acta Cryst. B 43 (1987) 356.

[5] M. Ribet, S. Leon, F. Lefaucheux, M.C. Robert, J. Appl. Cryst. 23 (1990) 277.

[6] A.R. Lim, K.W. Hyung, K.S. Hong, S.Y. Jeong, Phys. Stat. Solidi (b) 219 (2000) 389.

Correct implementation of polarization constants in wurtzite materials and impact on III-nitrides

Cyrus E. Dreyer,[1, 2] Anderson Janotti,[2] Chris G. Van de Walle,[2] and David Vanderbilt[1]
[1] *Department of Physics and Astronomy, Rutgers University, Piscataway, NJ 08845-0849*
[2] *Materials Department, University of California, Santa Barbara, CA 93106-5050*

(Dated: 2 December 2015)

Wurtzite materials (space group $P6_3mc$) have piezoelectric and spontaneous polarization in the crystallographic c direction. Though this polarization is generally not switchable by an electric field, it is of extreme technological importance. For example, polarization differences between layers of a heterostructure allow for strong carrier confinement and the formation of a two-dimensional electron gas with high density; this is exploited at AlGaN/GaN interfaces in high electron mobility transistors (HEMTs). The effect of polarization can also be detrimental, for example causing the quantum-confined Stark effect in quantum wells of light-emitting diodes (LEDs) based on GaN and InGaN, which reduces radiative recombination rates and shifts the emission wavelength. For both HEMTs and LEDs, accurate values of the SP and PZ polarization constants are required for a fundamental understanding as well as for device design.

In this work, we consider two issues with the definition of polarization constants for WZ materials, the choice of reference for defining SP polarization, and the use of "proper" versus "improper" PZ constants. While our theoretical considerations are general, we choose the nitride semiconductors as a suitable example to illustrate the derivations because our findings have a significant impact on this materials system of high (and still increasing) technological importance.

Direct calculation of the formal polarizations by first-principles electronic-structure methods is conducted using the modern theory of polarization (MTP).[1,2] The calculations in this study are based on density-functional theory with the screened hybrid functional of Heyd, Scuseria, and Ernzerhof (HSE)[3] as implemented in the VASP code.[4]

The calculation of SP polarization requires the choice of a reference structure. In the case of WZ semiconductors, this has invariably been chosen to be zincblende[5,6] (ZB, space group $F\bar{4}3m$). Though ZB as a reference structure is intuitively appealing, it has a nonzero formal polarization in the [111] direction. We show that this results in a spurious contribution when effective SP polarizations have been implemented to determine polarization differences between materials, and demonstrate that a correction term must be included.

In order to avoid extensive changes in the simulation software, and to enhance physical insight, the SP polarization constants can be determined with respect to the centrosymmetric layered hexagonal (H) structure reference structure (space group $P6_3/mmc$), which can be obtained by an adiabatic (gap preserving) increase of the internal structural u parameter from $u \approx 0.37 - 0.38$ of the WZ structure to $u = 0.5$ (see Fig. 1). This is analogous to the method used to define SP in a ferroelectric.

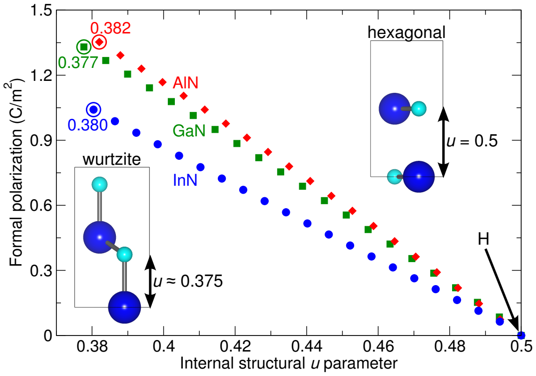

FIG. 1. Formal polarization of InN, GaN, and AlN for structures as a function of the internal structural parameter u, varying between fully relaxed WZ (circled symbols) and H ($u = 0.5$), as shown schematically by ball and stick models.

In addition, a complication that must be addressed is the choice between improper and proper PZ constants.[7] For implementation in device simulations, the PZ constants that should be used correspond to the improper case, since their role in the equation is to take into account the change in formal polarization of material with strain.[7] The current practice in the field, however, uses the proper PZ constants.

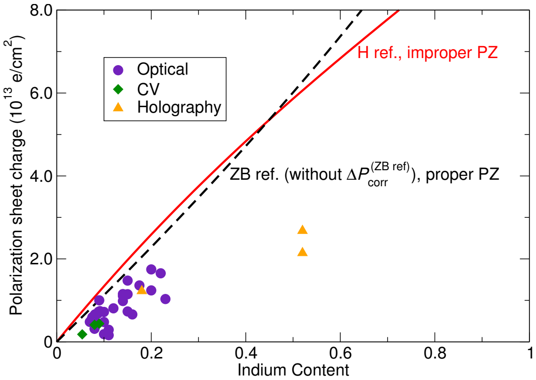

FIG. 2. Absolute values for polarization sheet charges at the InGaN/GaN interface as a function of alloy content predicted from the implementation recommended in this work (red solid curve), and the current practice in the field (black curve). Points are experimental values from the literature.

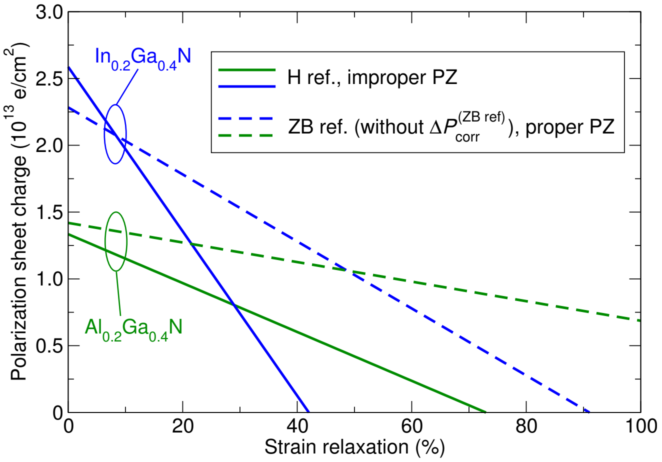

FIG. 3. Absolute values for polarization sheet charges at the $In_{0.2}Ga_{0.4}N$/GaN (blue) and $Al_{0.2}Ga_{0.4}N$/GaN (green) interface as a function percent strain relaxation (0% corresponding to the alloy coherently strained to GaN). Solid curves are the revised implementation of this work, dashed curves are the current practice in the field.

Figure 2 compares experimental measurements of polarization bound charge at InGaN/GaN interface, as a function of alloy content, along with predicted bound charges using the current practice in the field (SP constants referenced to the ZB structure without the necessary correction term, and proper PZ constants) and the implementation recommended in this work (H reference structure and the improper PZ constants).

We show that the success of current practice in the field has hinged on a fortuitous cancellation of errors between the spurious term from the use of the ZB reference for the SP polarization and the proper PZ constants instead of the improper ones. However, the two implementations differ significantly in the *relative* contributions of SP and PZ polarization. Fig. 3 shows the predicted polarization bound charges for $In_{0.2}Ga_{0.4}N$/GaN (blue curves) and $Al_{0.2}Ga_{0.4}N$/GaN (green curves) as a function of strain relaxation of the layer. For both InGaN/GaN and AlGaN/GaN, the revised implementation of this work predicts a much faster decrease in bound charge at the interface than the current practice in the field.

This work was supported by the U.S. Department of Energy (DOE), Office of Science, Basic Energy Sciences (BES) under Award DE-SC0010689, the Center for Low Energy Systems Technology (LEAST), one of the six SRC STARnet Centers, sponsored by MARCO and DARPA, and ONR Grant N00014-12-1-1035.

REFERENCES

[1] R. D. King-Smith and D. Vanderbilt, Phys. Rev. B **47**, 1651 (1993).
[2] R. Resta, Rev. Mod. Phys. **66**, 899 (1994).
[3] J. Heyd, G. E. Scuseria, M. Ernzerhof, J. Chem. Phys. **118**, 8207 (2003); *ibid.* **124**, 219906 (2006).
[4] G. Kresse and J. Furthmüller, Phys. Rev. B. **54**, 11169 (1996).
[5] F. Bernardini, V. Fiorentini, D. Vanderbilt, Phys. Rev. B **56**, R10024 (1997).
[6] F. Bernardini, V. Fiorentini, D. Vanderbilt, Phys. Rev. B **63**, 193201 (2001).
[7] D. Vanderbilt, J. Phys. Chem. Sol. **61**, 147 (2000).

Two type of domains in $CuInP_2Se_6$ layered crystal

Andrius Dziaugys[1], Marius Chyasnavichyus[2], Juras Banys[1], Yulian Vysochanskii[3], Petro Maksymovych[2]

[1]Faculty of Physics, Vilnius University, Vilnius, LT-01513 Lithuania

[2]The Institute for Functional Imaging of Materials and the Center for Nanophase Materials Sciences, Oak Ridge National Laboratory, Oak Ridge, Tennessee 37831, United States

[3]Institute of Solid State Physics and Chemistry, Uzhgorod University, 88000 Uzhgorod, Ukraine

email.: andrius.dziaugys@ff.vu.lt

After the discovery of a graphene with its extraordinary properties, other two-dimensional (2D) materials have got more scientific attentiont [1-2]. Among the 2D materials, metal chalcogenophosphate $A^IB^{III}P_2X_6$ (where A = Cu, Ag, B= In, Cr, Bi, and X= S, Se) crystals are an interesting group of materials with (anti)ferroelectric and/or (anti)ferromagnetic properties [3-4]. These materials have been known for a long time and widely studied in the past, and are now experiencing a resurgence of interest because it is possible mechanically exfoliate their crystals down to several tenth of monolayer flakes that maintain the stable structure of the bulk crystal [2]. Most extensively studied member is $CuInP_2S_6$. It is the only one known material showing ferroelectric polarization behavior as a layered crystal at room temperature and above [5-6]. This compound has a unique characteristics and shows interesting physical properties when In is doped with Cr [7-8] or S with Se [9]. For the layered crystals $CuInP_2S_6$ and $CuInP_2Se_6$ the d^{10} electronic configuration of Cu^+ cations determines possibility of second order Jahn – Teller effect and those cations shifting from by sulfur coordinated octahedral positions in middle of crystal layers to the quasi-trigonal positions near the layers edge [3-4, 10]. Such shift is supported by flexible ethane-like P_2S_6 groups, which are connected into enough rigid layers [11]. $CuInP_2Se_6$ is a new addition to this class of chalcogenophosphate materials. Calorimetric evidence for the occurrence of a broad phase transition between 220 and 240 K in this compound was given in paper [3]. A single-crystal X-ray diffraction study showed that the high- and low-temperature structures of $CuInP_2Se_6$ (trigonal space group *P*-31*c* and *P*31*c*, respectively) are very similar to those of $CuInP_2S_6$ in the paraelectric and ferrielectric phases, with the Cu^I off-centering shift being smaller in the former than in the latter [3]. There the thermal evolution of the cell parameters of $CuInP_2Se_6$ was obtained by full profile fits to the X-ray diffractograms. Both cell parameters a and c slightly increase on cooling, only at T=226 K a parameters show a local minimum.

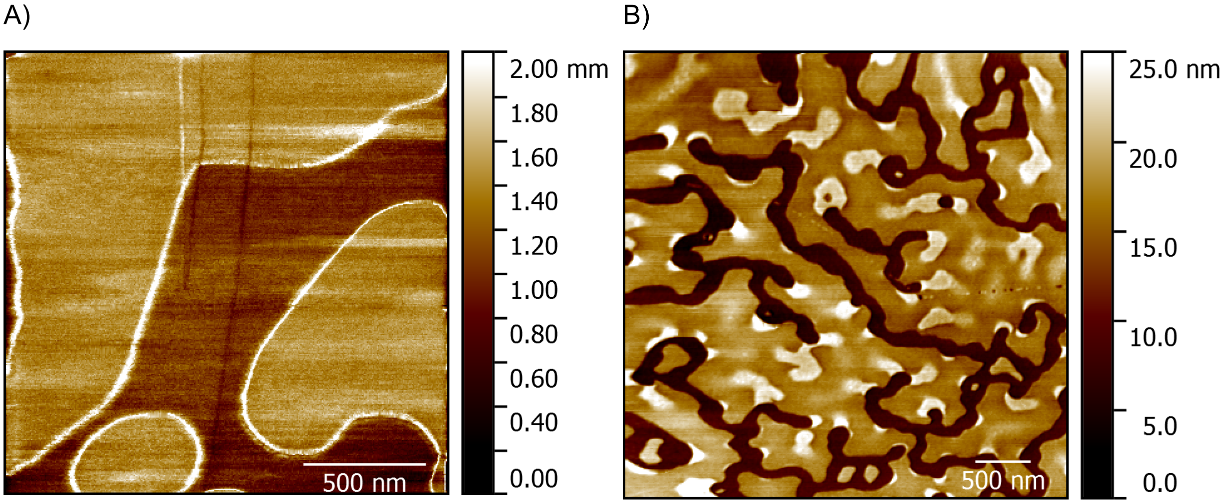

Fig. 1. $CuInP_2Se_6$ surface A) 1.8x1.8 µm single frequency amplitude image obtained in contact mode (SFPFM) at 120 K, B) 4x4 µm topographic image obtained by non-contact mode (KPFM) at 120 K.

This behaviour is quite different from the anomalous increases found in the cell parameters of $CuInP_2S_6$ when heating through the transition [4, 12]. The important feature of selenides is the higher covalence degree of their bonds. Evidently, for this reason the copper ion sites in the low-temperature phase of $CuInP_2Se_6$ are displaced only by 1.17 Å from the middle of the structure layers in comparison with the corresponding displacement 1.58 Å for $CuInP_2S_6$ [4, 13-14]. These facts enable to assume the potential relief for copper ions in $CuInP_2Se_6$ to be shallower than for its sulphide analog. Presumably, for this reason the structural phase transition in the selenide compound is observed at lower temperature than for the sulphide compound. Despite the multiplicity of the investigations, microscopic material properties are not well known. For this reason we focused our attention on the observation of domain structure temperature dependence and repolarization processes in $CuInP_2Se_6$ crystals by single frequency piezoresponse force microscopy (SFPFM) and Kelvin probe force microscopy (KPFM). The topography and domain structure of cleaved 2D ferroelectric $CuInP_2Se_6$ crystal is shown in Fig. 1. The main features in the topography are the steps created by the layers of a material. This crystal contains bands of domains extended across the entire sample. The domains are continuous over the layer steps. This result shows that this system has three dimensional ordering of spontaneous polarization. The domains look different using SFPFM or KPFM. There are three levels of contrast in KPFM image, which is not readily explained by binary polarization distribution. It may be the effect of some depth (3D) sensitivity. More interestingly SFPFM shows bright lines (like domain walls) of 20 nm width, where PFM amplitude increases instead of decreasing like in $CuInP_2S_6$ [2]. One more obvious point is different domain structure, what can be related with the fact that system has two order parameters (dipolar and some structural). This can be confirmed with the fact that these two types of domain walls disappear at different temperatures: 210 K and 230 K. Here we discus about the origin of the domain wall aspects.

Acknowledgement
We wish to acknowledgement the support of the CIEE / Baltic-American Freedom Foundation in funding this work.
These investigations were carried out as a user project at the Center for Nanophase Materials Sciences, Oak Ridge National Laboratory

Literature

[1] S. Z. Butler, S. M. Hollen, L. Cao, Y. Cui, J. A. Gupta, H. R. Gutiérrez, T. F. Heinz, S. S. Hong, J. Huang, A. F. Ismach, E. Johnston-Halperin, M. Kuno, V. V. Plashnitsa, R. D. Robinson, R. S. Ruoff, S. Salahuddin, J. Shan, L. Shi, M. G. Spencer, M. Terrones, W. Windl, and J. E. Goldberger, ACS Nano 7, 2898 (2013).
[2] A. Belianinov, Q. He, A. Dziaugys, P. Maksymovych, E. Eliseev, A. Borisevich, A. Morozovska, J. Banys, Y. Vysochanskii, and S. V. Kalinin, Nano Lett., 2015, 15 (6), pp 3808–3814
[3]. X Bourdon, V Maisonneuve, V.B Cajipe, C Payen, J.E Fischer, Journal of Alloys and Compounds 283 (1999)
[4]. V. Maisonneuve, V. B. Cajipe, A. Simon, R. Von Der Muhll, J. Ravez. Phys. Rev. B, 1997, v. 56, p. 10860
[5]. A. Belianinov, Q. He, A. Dziaugys, P. Maksymovych, E. Eliseev, A. Borisevich, A. Morozovska, J. Banys, Y. Vysochanskii, and S. V. Kalinin, Nano Lett., 2015, 15 (6), pp 3808–3814
[6] Michael A. Susner, Alex Belianinov, Albina Borisevich, Qian He, Marius Chyasnavichyus, Hakan Demir§, David S. Sholl§, Panchapakesan Ganesh, Douglas L. Abernathy, Michael A. McGuire, and Petro Maksymovych* ACS Nano, Article ASAP, DOI: 10.1021/acsnano.5b05682
[7]. A. Dziaugys, V. Shvartsman, J. Macutkevic, J. Banys, Yu. Vysochanskii, W. Kleemann. Phys. Rev. B, 2012, v. 85, p. 134105-1 - 134105-6.
[8]. W. Kleemann, V. V. Shvartsman, P. Borisov, J. Banys, Yu. M. Vysochanskii. Phys. Rev. B, 2011, v. 84, p. 094411-1 - 094411-8.
[9]. J. Macutkevic, J. Banys, R. Grigalaitis, and Yu. Vysochanskii, Phys. Rev. B 78, 064101
[10]. Y. Fagot-Revurat, X. Bourdon, F. Bertran, V.B., D. Malterre. J. Phys.: Condens. Matter, 2003, v. 15, p. 595 – 602.
[12]. A. Simon, J. Ravez, V. Maisonneuve, C. Payen, and V. B. Cajipe, Chem. Matter, 6, 1575 (1994).
[13]. V. B. Cajipe, J. Ravez, V. Maisonneuve, A. Simon, C. Payen, R. Von der Muhll and J. E. Fischer, Ferroelectrics 223, 43 (1999).
[14]. V. Maisonneuve, M. Evain, C. Payen, V. B. Cajipe, and P. Molinie, J. Alloys and Compdounds 218, 157 (1995).

Transitions between $BaTiO_3$ ca_1/ca_2 and a/c phases

Arnoud Everhardt and Beatriz Noheda

Zernike Institute for Advanced Materials, University of Groningen, 9747 AG Groningen, The Netherlands

In the abstract for the talk “Ferroelectric domain structures in low-strain $BaTiO_3$”, the different domain structures for a ferroelectric $BaTiO_3$ thin film under low epitaxial mismatch strain have been measured. A monoclinic ca_1/ca_2 phase and a transition at 50 ºC to a a/c phase has been reported experimentally [1].

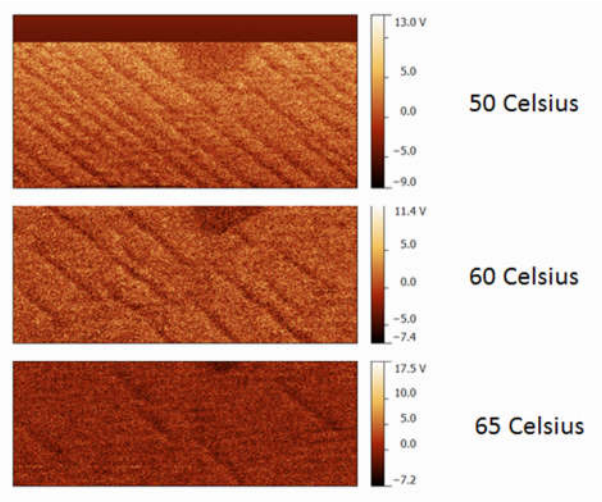

Fig 1. PFM images of a single area at different temperatures, measured from low to high temperature.

The transition from the ca_1/ca_2 phase towards the a/c phase with increasing temperature has been followed by Piezoelectric Force Microscopy (**Fig 1**). Through the phase transition ca_2 domains become ca_1 domains (with the domain walls disappearing nearly one by one), while at the same time long c domains form within the ca_1 domains (turning ca_1 into a/c). XRD measurements have revealed that the domain wall orientation is inclined 45 º with respect to the substrate in both phases. This is in disagreement with the expectations of vertical domain walls for the ca_1/ca_2 phase. The results could be consistent with a (111) domain wall . Such unexpected walls could form due to nucleation within the a/c (011) wall, subsequent growth and a kinetic trapping within this orientation. We also report here slim ferroelectric loops measured at room temperature in these films (see Fig.2)

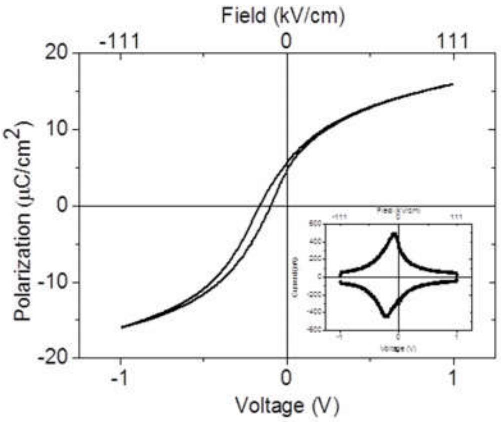

Fig 2. Macroscopic ferroelectric polarization loop for the $BaTiO_3$ thin film. The very small coercive field shows that the energy cost to rotate the polarization out of plane is very small, which is consistent with a monoclinic phase.

[1] A. S. Everhardt, S. Matzen, N. Domingo, G. Catalan, B. Noheda, Adv. Electron. Mater. 1500214 (2015)

Mode sequence, frequency change of non-soft phonons, and LO-TO splitting in strained tetragonal $BaTiO_3$

Aldo Raeliarijaona and Huaxiang Fu
Department of Physics, University of Arkansas, Fayetteville, Arkansas 72701, USA

(Dated: December 1, 2015)

PACS numbers:

A breakthrough was made in probing the lattice dynamics in nanoscale ferroelectrics (FE),[1–3] by using *ultraviolet* (UV) Raman spectroscopy rather than conventional Raman spectroscopy. The UV-Raman, utilizing UV-light with an energy larger than the band gaps of oxides, can be absorbed strongly by the FE thin films and thus can reveal the phonon structure of thin films with high resolution. Indeed, using UV-Raman, multiple sharp peaks were clearly observed in $BaTiO_3/SrTiO_3$ superlattices epitaxially grown on a $SrTiO_3$ substrate.[1,2]

Furthermore, interesting phonon physics was revealed.[1] For instance, a new and pronounced Raman peak was observed at frequency 540 cm^{-1}, and was assigned as the transverse TO_4 mode originated from the strained $BaTiO_3$.[1] However, in bulk $BaTiO_3$, the frequency of the TO_4 mode is merely 486 cm^{-1} (Ref.5). Whereas it is known that strain may cause a large frequency shift to the soft mode, note that TO_4 is not a soft mode, however. A very large strain-induced frequency shift that occurs to a non-soft mode is interesting itself. It further raises other intriguing questions: (i) What is the origin of the drastic frequency shift? (ii) Are there other non-soft modes that may also exhibit large frequency shifts, but have not been detected in experiments?

Previously there were many important works on the lattice dynamics in ferroelectrics, yielding critical understanding on the structural instability,[6,7] characteristic difference in phonon dispersion among different materials,[8] phonon in composition-modulated FE superlattices,[9] and finite electric-field induced phonon hardening in incipient ferroelectrics.[10,11] Most of these studies paid attention to the behaviors of soft modes in the high-symmetry *non-polar* phase, namely the phase before ferroelectric transition occurs. In contrast, relatively less attention is given to the *polar* phase[12] and to the non-soft phonon modes.

The experimental advance[1–3] also brings another issue of broad interest, namely how the sequence of phonon modes is altered by external conditions. Sequencing of phonon modes, namely the ordering of vibration modes according to frequencies, is of fundamental relevance for unveiling the interatomic interaction in solids,[13] because the sequence is determined by the microscopic nuclei-nuclei, nuclei-electron, and electron-electron interactions. In contrast to a *single* mode, the mode sequencing reflects collectively the behaviors of a *group* of modes. Since different modes respond to the external conditions (such as pressure, strain, and electric field) in different manners, it is nontrivial to determine how the mode sequence alters with external conditions. Determination of mode sequencing is also of practical importance, since in infrared or Raman experiments this sequence is much needed in order to correctly assign phonon modes to individual peaks and to determine the origin of these peaks.[4] This knowledge is particularly relevant when the mode sequence under the ambient condition is, after the external condition has changed, no longer valid.

Another subject of profound interest in FEs is the LO-TO splitting. Transverse optic (TO) modes interact with light, which is a key process that determines optical properties.[13] On the other hand, longitudinal optic (LO) modes interplay with electric fields, determining the dielectric responses of solids.[13] The LO and TO modes are thus of key importance both in optical and dielectric properties. Further, the LO and TO modes are also critical in testing the fundamental 2n-1 sum rule.[14] Moreover, the LO-TO splitting arises from the long-range Coulomb interaction, manifesting the influence of this interaction on the lattice dynamics and the origin of anomalous Born effective charge.[15,16]

A long-standing problem inhibits the *quantitative* study of the LO-TO splitting, however. That is, the splitting has not been fundamentally well defined. As have been realized by Zhong and Vanderbilt in a seminal work,[15] it is generally *not* possible to find a one-to-one correspondence between a LO mode and a TO mode. In fact, when lattice vibrations interact with electric fields via the long-range Coulomb interaction, more than one TO mode may contribute simultaneously—and all of them, significantly—to form a single LO mode as a result of the strong mode mixing caused by the Coulomb interaction. Here we give a concrete example to illustrate this spread mode mixing. We consider $BaTiO_3$ at a compressive strain of -2.5%. By quantitative mode projection, our first-principles calculations show that the $E(LO_4)$ mode at frequency ω =735 cm^{-1} has contributions from five TO modes with the contribution weights at 7%, 23%, 21%, 8%, and 40%, respectively, revealing that the contributions are indeed widespread and there is no dominating one. This mode mixing is fundamental and cannot be avoided. As a consequence, attempt to define the LO-TO splitting as the frequency difference between one LO mode and one TO mode cannot be justified. The lack of quantitative study of the LO-TO splitting hampers the efforts in obtaining insight knowledge about this important quantity. It also prevents us from investigating how the splitting may be quantitatively tuned by external conditions such as epitaxial strain and electric field.

Here, by mapping out the evolutions of individual phonon modes as a function of strain using first-principles density functional perturbation calculations,[18,19] we determine the mode sequence and strain-induced phonon frequency shifts in prototypical $BaTiO_3$. Our study[20] reveals that the mode sequence is drastically different when $BaTiO_3$ is strained to $SrTiO_3$ as compared to that in the unstrained structure, caused by multiple mode crossings. Furthermore, we predict that three other non-soft modes—$A_1(TO_2)$, $E(LO_4)$, and $A_1(TO_3)$—display even larger strain-induced frequency shifts than $E(TO_4)$. The strain responses of individual modes are found to be highly mode specific, and a mechanism that regulates the magnitude of the frequency shift is provided. As another key outcome of this study, we tackle a long-standing problem of LO-TO splitting in ferroelectrics. A rigorous definition for the LO-TO splitting is formulated, which allows this critical quantity to be calculated quantitatively. The definition immediately reveals a new finding, that is, a large LO-TO splitting not only exists for $E(LO_4)$, which is previously known and originates from a soft mode, it also occurs to a non-soft $A_1(LO_3)$ mode. The LO-TO splitting is shown to decrease drastically with compressive strain, and this decrease cannot be explained by the Born effective charges and high-frequency dielectric constants.

This work was supported by the Office of Naval Research.

---

[1] D. Tenne, A. Bruchhausen, N.D. Lanzillotti-Kimura, A. Fainstein, R.S. Katiyar, A. Cantarero, A. Soukiassian, V. Vaithyanathan, J.H. Haeni, W. Tian, D.G. Schlom, K.J. Choi, D.M. Kim, C.B. Eom, H.P. Sun, X.Q. Pan, Y.L. Li, L.Q. Chen, Q.X. Jia, S.M. Nakhmanson, K.M. Rabe, and X.X. Xi, Science **313**, 1614 (2006).

[2] D. A. Tenne, P. Turner, J. D. Schmidt, M. Biegalski, Y. L. Li, L. Q. Chen, A. Soukiassian, S. Trolier-McKinstry, D. G. Schlom, X. X. Xi, D. D. Fong, P. H. Fuoss, J. A. Eastman, G. B. Stephenson, C. Thompson, and S. K. Streiffer, Phys. Rev. Lett. **103**, 177601 (2009).

[3] D. A. Tenne, A. K. Farrar, C. M. Brooks, T. Heeg, J. Schubert, H. W. Jang, C. W. Bark, C. M. Folkman, C. B. Eom, and D. G. Schlom, Appl. Phys. Lett. **97**, 142901 (2010).

[4] P.Y. Yu and M. Cardona, *Fundamentals of Semiconductors Physics and Materials Properties* (Springer, Berlin, 2001).

[5] U. D. Venkateswaran, V. M. Naik, and R. Naik, Phys. Rev. B **58**, 14256 (1998), and references therein.

[6] R. Yu and H. Krakauer, Phys. Rev. Lett. **74**, 4067 (1995).

[7] D. J. Singh, Phys. Rev. B **53**, 176 (1996).

[8] Ph. Ghosez, E. Cockayne, U. V. Waghmare, and K. M. Rabe, Phys. Rev. B **60**, 836 (1999).

[9] C. Bungaro and K.M. Rabe, Phys. Rev. B **65**, 224106 (2004).

[10] I.I. Naumov and H. Fu, Phys. Rev. B **72**, 012304 (2005).

[11] X. Wang and D. Vanderbilt, Phys. Rev. B **74**, 054304 (2006).

[12] A. Garcia and D. Vanderbilt, Phys. Rev. B **54**, 3817 (1996).

[13] M. Born and K. Huang, *Dynamical Theory of Crystal lattices* (Oxford University Press, Oxford, 1954).

[14] A.S. Barker Jr., Phys. Rev. **136**, A1290 (1964).

[15] W. Zhong, R. D. King-smith, and D. Vanderbilt, Phys. Rev. Lett. **72**, 3618 (1994).

[16] Ph. Ghosez, J.-P. Michenaud, and X. Gonze Phys. Rev. B **58**, 6224 (1998).

[17] P. Hohenberg and W. Kohn, Phys. Rev. **136**, B864 (1964); W. Kohn and L.J. Sham, Phys. Rev. **140**, A1133 (1965).

[18] P. Giannozzi *et al.*, J. Phys. C **21**, 395502 (2009).

[19] P. Giannozzi *et al.*, http://www.quantum-espresso.org.

[20] A. Raeliarijaona and H. Fu, Phys. Rev. B **92**, 094303 (2015).

Evolution of the local structure of $PbZr_{0.5}Ti_{0.5}O_3$ under applied electric fields

O. Gindele[1,2], C.Vecchini[2], A. Kimmel[2], D. Duffy[1]

[1]Department of Physics and Astronomy, University College London, Gower Street, London, WC1E 6BT UK
[2]National Physical Laboratory, Hampton Road, Teddington, TW11 0LW, UK

One of the industrially most important piezoelectrics is $Pb(Zr_{(1-x)}Ti_x)O_3$ (PZT), which is a solid solution ABO_3 perovskite with two isovalent B-cations. The performance of PZT is strongly affected by the temperature and composition [1]. Although many studies have been performed at room temperature and above, the low temperature ($T < 200K$) properties of PZT are not well characterized. In this work we studied the temperature dependent ferroelectric response of morphotropic PZT with low temperature X-ray experiments and molecular dynamics (MD) simulations using a shell-model force field [2].

Through cycling of the electric field in quasi-static simulations we have reproduced polarization hysteresis loops for PZT similar to experimental ones. Here, we found an increase of the saturation polarization with temperature, while the coercive field (E_C) decreases with temperature (see figure 1). Both effects agree well with X-ray experimental observations and relate to thermally activated polarization switching. The difference in the experimental and theoretical exponential factors is due to the simulation cell being free of defects and domains.

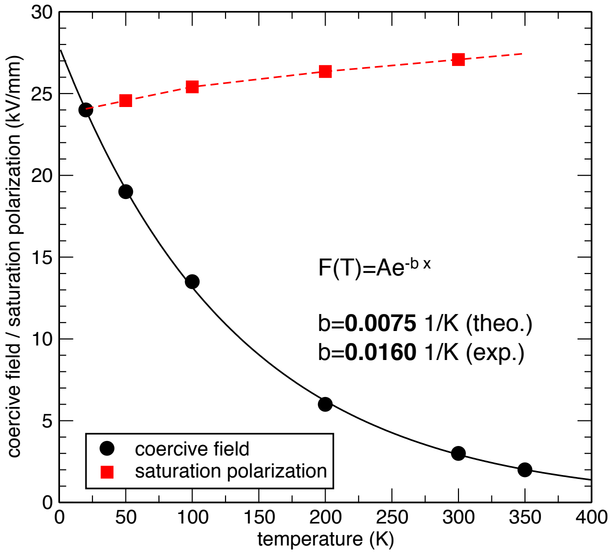

Figure 1: Coercive field and saturation polarization for $Pb(Zr_{0.5}Ti_{0.5})O_3$ at different temperatures calculated with molecular dynamics simulations. The coercive field follows an exponential behaviour for the modelling and the experimental data.

In further MD simulations on rhombohedral PZT we applied static electric fields along (001) and we found a field induced change in symmetry from rhombohedral to tetragonal where the c-axis aligns with the field direction (see figure 2). Polarization and strain vary linearly with small electric fields up to a critical field above which the system fully adopts a tetragonal state. At this critical field polarization and strain components exhibit a jump where Zr and Ti environments react differently to the symmetry change: Zr centred cells increase in volume, while the Ti ones decrease. Additionally, we report a different response of the local structure of PZT to an electric field depending on the local environment of the B-cations. Statistical analysis of polarization distributions demonstrates that a Ti-rich environment is highly polarizable, while a Zr-rich environment exhibits less sensitivity to an applied electric field and to its local environment.

Overall, we report that the response of the local structure of PZT to an electric field is not uniform and strongly depends on the type of B-cation and its local environment.

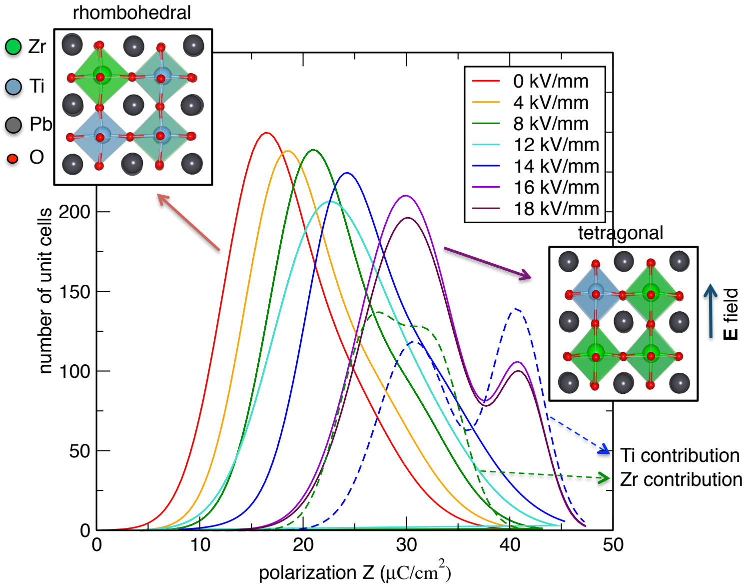

Figure 2: Distributions of the Z component of the polarization values calculated for each B-cation centred unit cell for different electric fields (along (001)). With increasing electric field the distributions shift to a higher polarization and become more asymmetric. Above a critical field (14 kV/mm) the polarization distribution splits into two peaks, which is related to the change in symmetry from rhombohedral to tetragonal. For 18 kV/mm the vastly different contributions of Ti and Zr based unit cells to the total polarization distribution are shown as dotted lines. The two insets show small extracts of the whole simulation box and they demonstrate the change from rhombohedral to tetragonal symmetry on the atomistic scale.

[1] N. Izyumskaya et. al, *Crit. Rev. Solid State Mater. Sci.* **2007**, 32, 111
[2] O. Gindele, A. Kimmel, M. Cain, D. Duffy, *J. Phys. Chem. C*, **2015**, *119* (31)

Presentation preference: ORAL

Electrocaloric properties of ferroelectric ultrathin films in the presence of residual depolarizing field

E. Glazkova, C.-M. Chang, S. Lisenkov, B. K. Mani, I. Ponomareva
Department of Physics,
University of South Florida, Florida 33620, USA,
e-mail: elenag@mail.usf.edu

Electrocaloric effect (ECE) has attracted a lot of attention recently owing to the discovery of giant ECE in $PbZr_{0.95}Ti_{0.05}O_3$ thin films [1] and other ferroelectric materials [2, 3]. Effect can be potentially used for solid state refrigeration and integrated circuit cooling [3–5]. Ferroelectric ultrathin films are considered to be excellent candidates for cooling devices as they allow application of very high electric fields. However, downsizing ferroelectric films reveals the depolarizing field that could critically alter or even destroy the films electrocaloric properties. In this work we reveal the critical and multifold role of the depolarizing field in the electrocaloric properties of ferroelectric ultrathin films and demonstrate the contribution of nanodomains to the ECE [6].

We used adiabatic Monte Carlo approach with first-principles-based effective Hamiltonian for nanostructures to simulate ECE for 4.8 nm thick $PbTiO_3$ films grown on $SrTiO_3$ substrate. The depolarizing field was altered by controlling the amount of charge compensation. The surface charge compensation mechanism was modelled as described in Ref.[7]. We simulated a supercell of 12x12x12 unit cells chosen to accommodate the equilibrium domain patterns. Periodic boundary conditions are applied along [100] and [010] pseudocubic directions to simulate a film of infinite area. The electric field was slowly applied and then removed along the film growth directions at a rate of 50 V/m to ensure reversibility.

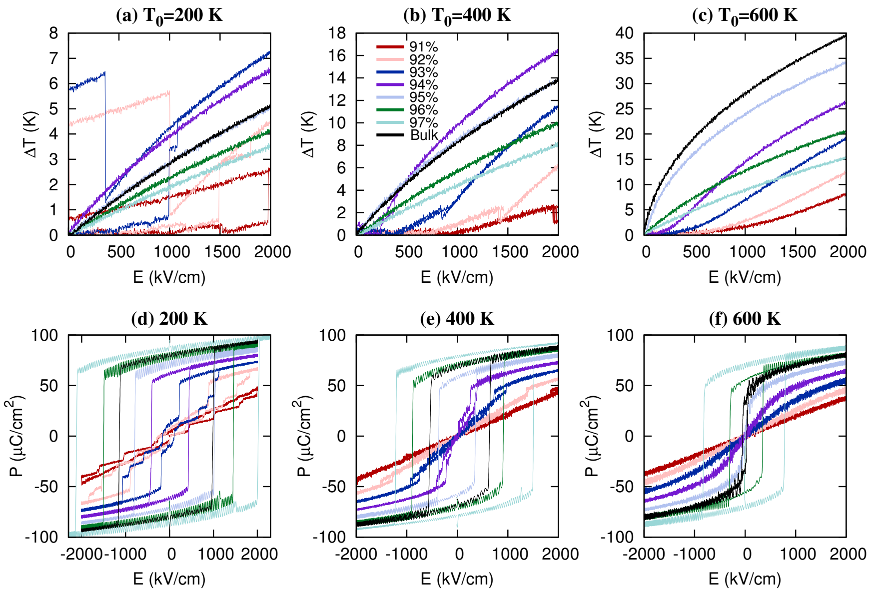

FIG. 1. Panels (a)-(c) give the electrocaloric change in temperature as a function of the applied electric field for three different initial temperatures, T_0 . Panels (d)-(f) show the polarization as a function of the electric field as obtained in isothermal simulations under an ac electric field of 1 GHz frequency.

The electrocaloric change in temperature in films with different percentage of charge compensation is giving on Fig.1. It can be seen that the residual depolarizing field could play a dual, but mostly negative, role in the electrocaloric properties of these films. If the films are compensated well enough (β >94 %) which lead to monodomain state then the depolarizing field significantly reduce the electrocaloric change in temperature. Furthermore, if the films are poorly compensated ($\beta \leqslant$93 %) which leads to formation of nanodomains, the electrocaloric response is either completely lost or significantly reduced due to the irreversible domain wall motion. Fig.2 confirms the analysis above and also shows that for β =94 % the depolarizing field is predicted to enhance the ECE response due to a competition between the monodomain and nanodomain states. We will report our findings about the role of the partial charge compensation on the electrocaloric properties of $PbTiO_3$ ultrathin films and discuss the possibility of potential enhancement of electrocaloric effect for ferroelectric ultrathin films.

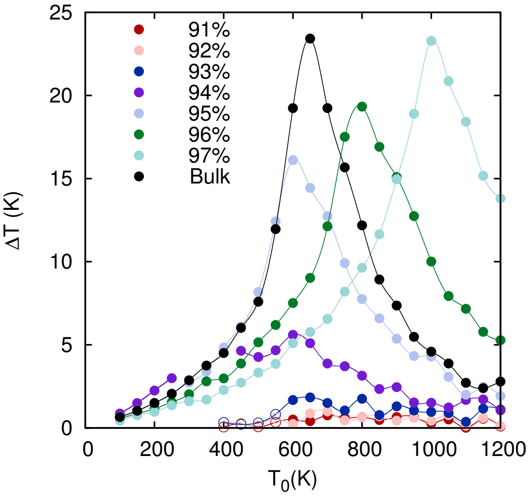

FIG. 2. The change in temperature in response to the electric field of 500 kV/cm as a function of initial temperature. Filled (open) symbols indicate data for the films which undergo transition into a single domain (nanostripe domains) state. Only reversible ΔT are reported

Acknowledgements: This work is supported by the National Science Foundation Grant, No DMR-1250492.

[1] A. S. Mischenko, Q. Zhang, J. F. Scott, R. W. Whatmore, and N. D. Mathur, Science **311**, 1270 (2006).
[2] B. Neese, B. Chu, S.-G. Lu, Y. Wang, E. Furman, and Q. M. Zhang, Science **321**, 821 (2008).
[3] J. F. Scott, Ann. Rev. Mat. Sci. **41**, 229 (2011).
[4] S.-G. Lu and Q. Zhang, Adv. Mater. **21**, 1983 (2009).
[5] M. Valant, Prog. Mater Sci. **57**, 980 (2012).
[6] E. Glazkova, C.-M. Chang, S. Lisenkov, B. K. Mani, and I. Ponomareva, Phys. Rev. B **92**, 064101 (2015).
[7] I. Ponomareva, I. I. Naumov, I. Kornev, H. Fu, and L. Bellaiche, Phys. Rev. B **72**, 140102 (2005).

First-principles re-investigation of bulk WO_3

Hanen Hamdi,[1] Philippe Ghosez,[1] Emilio Artacho,[2] Pablo Aguado Puente,[2] Ekhard Salje,[3] and Eric Bousquet[1]

[1] *Theoretical Materials Physics, University of Liege B-4000 Sart Tilman, Belgium*
[2] *CIC Nanogune, Tolosa Hiribidea 76, 20018 San Sebastián, Spain*
[3] *Department of Earth Sciences, University of Cambridge,*
Downing Street, Cambridge CB2 3EQ, United Kingdom

Tungsten trioxide WO_3 is a very unique transition-metal oxide because of its simple A-site vacant perovskite structure BO_3 that exhibits a wide diversity of behaviours. Piezoelectricity, superconductivity, electrochromicity or spin current transport are examples of the most common properties observed in WO_3. In spite of its simple structure, bulk WO_3 has a rich phase diagram going from a high symmetry tetragonal phase at 1000°C (space group $P4/nmm$) to a monoclinic ground state at -272.15°C (space group Pc) and thus through 6 successive structural phase transitions [1, 2]. Several first-principles studies have been performed in order to characterise the phases around room temperature where it appeared that none of them predicted the polar Pc phase [3].

Here, we present a density functional theory (DFT) re-investigation of the whole WO_3 phase diagram through the hybrid functional B1WC as implemented in the CRYSTAL code. We show that the B1WC is the most appropriate exchange-correlation functional to reproduce the structural and electronic properties of WO_3 when compared with LDA, GGA and LDA+U functionals. We start our study by analysing the phonon dispersions curves of WO_3 in its hypothetical cubic high symmetry reference structure. In Figure 1 we report these calculated phonon dispersion curves in which we can see a chain of instabilities (imaginary frequencies plotted as negative numbers in Figure 1) along various high symmetry directions in the Brillouin zone. The strongest unstable mode in the cubic phase is a polar mode at the Γ point (-373 cm^{-1}), which would led one to expect a ferroelectric ground state for WO_3. We also remark that the polar unstable branch propagates along the X and M point and strongly disperse when going toward the R point, a behaviour very similar to the one observed in cubic $BaTiO_3$.

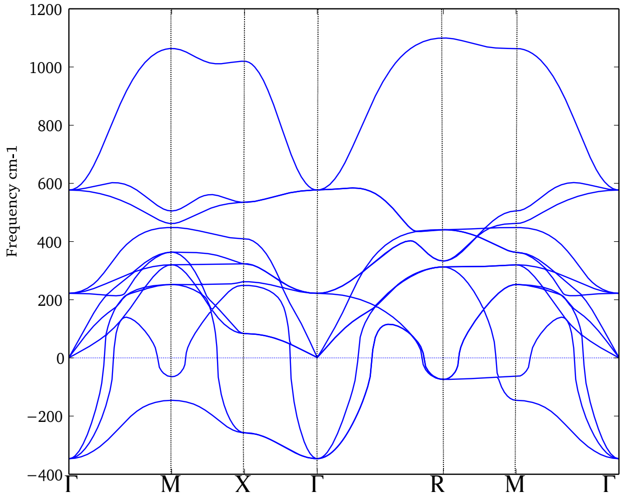

FIG. 1. Phonon dispersion curves of cubic WO_3. Unstable modes are plotted with negative frequencies. We see a very strong polar instability at the Γ point that propagates along the X ($\frac{1}{2}$, 0, 0) and M ($\frac{1}{2}$, $\frac{1}{2}$,0) zone boundary points and a smaller antiferrodistortive instability at the M and R ($\frac{1}{2}$, $\frac{1}{2}$, $\frac{1}{2}$) points.

At the M and R zone boundary points we also observe antiferrodistorte (AFD) unstable modes with octahedral tilting of the oxygen. Interestingly, when condensing these different modes we observe that the maximum gain of energy is given by the zone boundary modes and thus in agreement with the experimental measurements, which, beside the Pc phase, never observe a polar structure. We will show that WO_3 can be considered as an anti-ferroelectric crystal in the sense that (i) its structure is dominated by an anti-polar unstable mode from the M point and (ii) that a ferroelectric phase ($R3c$) is close in energy with the calculated ground phase ($P2_1/c$), such that it should be possible to switch from the $P2_1/c$ phase to the $R3c$ phase by applying an electric field. Our calculations do not reproduce the experimental ferroelectric Pc phase while all the other phases are well reproduced. The experimental Pc phase is related to the $P2_1/c$ phase by the condensation of a polar mode but our calculations do not show any unstable or even soft polar mode in the $P2_1/c$ phase. We conclude that another mechanism might be at the origin of the Pc phase.

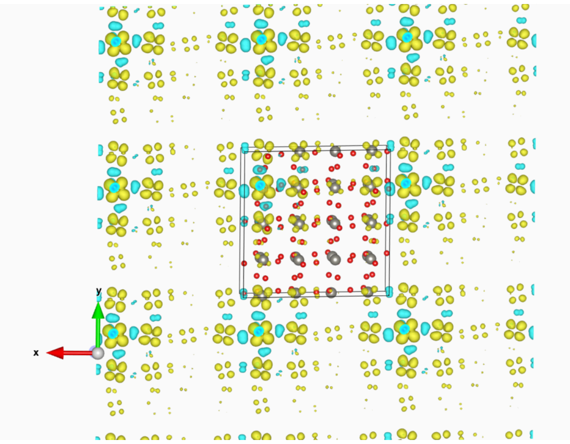

FIG. 2. Spin electron density in a 4 × 4 × 2 (128 atoms) supercell. Spin localization is observed, with the maximum density centered on one tungsten atom and shared with the first tungsten neighbors.

We remark that several physical properties of WO_3 are strongly driven by the presence of polarons. Indeed, stoichiometric WO_3 is difficult to achieve such as oxygen vacancies are easily formed and they are at the source of polarons and polaronic effects [4, 5]. As a second step, we also present DFT simulations of polarons in WO_3 in which we have injected an extra electron into the system with charge neutrality assured by a corresponding homogeneous positively charged background in the $P2_1/c$ phase. We will show that it is possible to localise a polaronic state in WO_3 through this procedure by playing with the exact exchange of the hybrid functional and the size of the cell (see Figure 2). We will discuss how the polaron affects the structure of WO_3 and how it might be responsible for the ferroelectric Pc phase.

BIBLIOGRAPHY

[1] C. J. Howard, V. Luca, and K. S. Knight, Journal of Physics: Condensed Matter **14**, 377 (2002).
[2] K. R. Locherer, I. P. Swainson, and E. K. H. Salje, Journal of Physics: Condensed Matter **11**, 6737 (1999).
[3] G. A. d. Wijs, P. K. d. Boer, R. A. d. Groot, and G. Kresse, Phys. Rev. B **59**, 2684 (1999).
[4] E. K. H. Salje, S. Rehmann, F. Pobell, D. Morris, K. S. Knight, T. Herrmannsdörfer, and M. T. Dove, Journal of Physics: Condensed Matter **9**, 6563 (1997).
[5] J. Ederth, A. Hoel, G. A. Niklasson, and C. G. Granqvist, Journal of Applied Physics **96**, 5722 (2004).

Mott-Hubbard gap in insulating phases of VO_2: ab initio calculations of the infrared and optical spectra

C. Hendriks, T. J. Huffman, E. J. Walter, M. M. Qazilbash, H. Krakauer
Department of Physics, College of William and Mary, Williamsburg, VA 23187, USA

The nature of the metal-insulator transition in VO_2, from the rutile R to the monoclinic M1, has so far proven elusive and continues to be a matter of debate to this day. Of the numerous theoretical and experimental studies conducted on the subject [1], some attribute the existence of the insulating M1 phase to a Peierls-like mechanism in which the V-V dimerization leads to the opening of an energy gap; others present evidence that the gap arises from Mott-Hubbard correlations. We have recently performed IR micro-spectroscopy and spectroscopic micro-ellipsometry on a single-crystal sample of VO_2. Analysis of phonon spectra revealed two distinct phases identified as triclinic T and monoclinic M2, further confirmed via x-ray spectroscopy, making our study the first of its kind on these VO_2 phases [2]. While measured IR phonon spectra differ significantly, the measured optical conductivities of the two phases were found to be nearly identical, in spite of the significant difference in the V-V arrangement of the two insulating phases. We then performed ab initio DFT+U calculations of the IR phonon and optical spectra. Figure 1a shows the theoretical IR spectra generated from calculated phonon frequencies and oscillator strengths, while Figure 1b shows the calculated optical conductivities. These calculations similarly demonstrate the insensitivity of the optical conductivity to the structural differences evident in the phonon spectra. Additionally, DFT+U finds both M1 and M2 to be insulating with indirect band gaps of ~0.7 eV and ~0.9 eV, respectively. These results support the Mott-Hubbard mechanism as responsible for the formation of the insulating gap in the M1, M2, and T phases, as opposed to the Peierls-type mechanism. [3, 4].

We will present first-principles calculations of infrared spectra and electronic response for the insulating monoclinic phases and compare these to available measurements for the insulating phases. All calculations were done with the Vienna Ab-initio Simulation Package (VASP) [5]. Phonon frequencies were obtained through computation of force constants via density functional perturbation theory and subsequent analysis using PHONOPY [6].

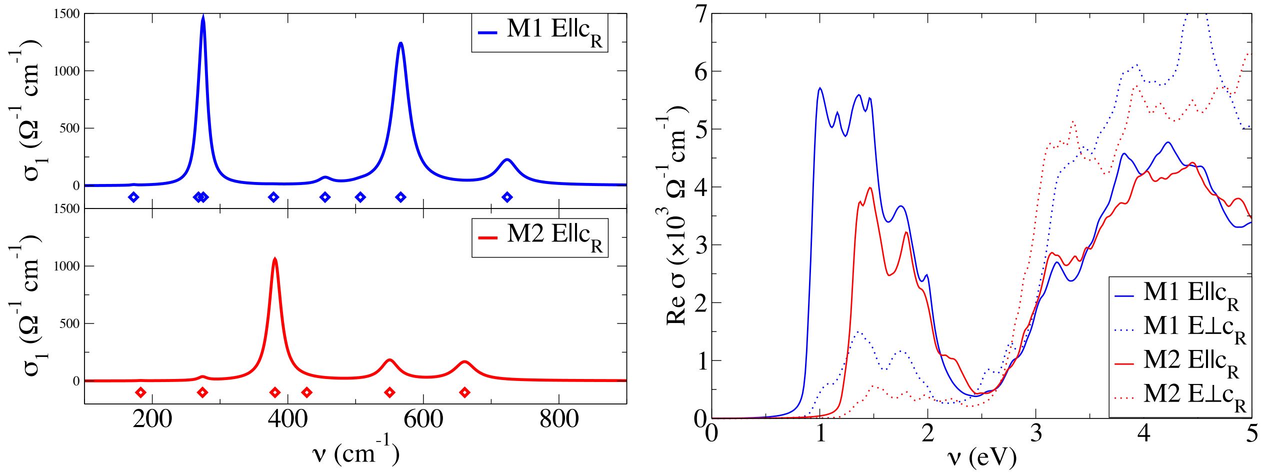

(a)

(b)

Figure 1: DFT+U calculated (a)infrared spectra and (b)optical conductivities for M1 and M2. Due to the weakness of some oscillator strengths, we indicate center frequencies with symbols. Despite the difference in structural and vibrational properties, the electronic response remains quite similar between the two phases.

To describe correlation effects within the V 3d bands, we used the DFT+U extension of standard DFT (= GGA). Calculated results can depend sensitively on the numerical value of the effective on-site electronic interaction parameter, the Hubbard U. A common approach is to tune the value of U in a semi-empirical way, seeking agreement with available experimental measurements of certain properties. Since the metalic R phase is the parent compound of the various insulating phases that we are interested in studying, we focus on its calculated phonon frequencies and structural instabilities, fitting the sensitive A2u Γ-mode to experimentally measured values, obtaining a value of $U = 5.7\,\mathrm{eV}$. Subsequent calculations used this value of U. Previously, IR phonon calculations in the M1 phase have been reported using a slightly different value of U [7]; the current work yields similarly good agreement with experiment[8, 9] for the M1 and M2 phases.

Previous studies have shown [3, 10] that, under doping or tensile strain and upon heating, the VO_2 transition from an insulating monoclinic M1 to a metallic R phase may progress through a triclinic T phase and a second monoclinic phase M2, both of which are insulating. Structurally, this progression from M1 to R through T and M2 can be characterized by the progressive breaking of the V dimers. As in the case of the present study, further examination of the structural, electronic and vibrational properties of these intermediate phases may help to shed more light on the nature of the metal-insulator transition in VO_2.

Acknowledgments: This work was supported by ONR grant N00014-12-1-1042. All calculations were performed on the High Performance Computing cluster at the College of William and Mary.

References

[1] V. Eyert, *Annalen der Physik (Leipzig)* **11**, 650-702 (2002) and references therein.

[2] T. J. Huffman, M. M. Qazilbash, C. Hendriks, E. J. Walter, H. Krakauer, Joonseok Yoon, Honglyoul Ju, R. Smith, G. L. Carr, to be published.

[3] J. P. Pouget, H. Launois, T. M. Rice, P. Dernier, A. Gossard, G. Villeneuve, and P. Hagenmuller, *Physical Review B* **10**, 1801 (1974).

[4] T. M. Rice, H. Launois, and J. P. Pouget, *Physical Review Letters* **73**, 3042 (1994).

[5] G. Kresse and J. Furthmuller, *Physical Review B* **54**, 11169 (1996).

[6] A. Togo, F. Oba, and I. Tanaka, *Physical Review B* **78**, 134106 (2008).

[7] T. J. Huffman, P. Xu, M.M. Qazilbash, E.J. Walter, H. Krakauer, J. Wei, D.H. Cobden, H.A. Becthel, M.C. Martin, G.L. Carr and D.N. Basov, *Physical Review B* **87**, 115121 (2013).

[8] P. Schilbe and D. Maurer, *Material Science and Engineering A* **370**, 449-452 (2004).

[9] C. Marini, E. Arcangeletti, D. Di Castro, L. Baldassare, A. Perucchi, S. Lupi, L. Malavasi, L. Boeri, E. Pomjakushina, K.Conder and P. Postorino, *Physical Review B* **77**, 235111 (2008).

[10] J. H. Park, J.M. Coy, T.S. Kasirga, C. Huang, Z. Fei, S. Hunter and D.H. Cobden, *Nature* **500**, 431 (2013).

Electrocaloric Effect in Ferroelectric Nanowires from Atomistic Simulations

Ryan Herchig, C.-M. Chang, B. K. Mani, and Inna Ponomareva
Department of Physics, University of South Florida, Tampa, Florida 33620, USA
e-mail: rch@mail.usf.edu

In recent years, ferroelectrics have received considerable interest as potential candidates for solid-state cooling applications [1]. These applications take advantage of the electrocaloric effect (ECE) which is defined as a reversible change in temperature under the adiabatic application of an electric field. Ferroelectric nanostructures could offer even better performance as they allow the application of much larger electric fields [1]. In fact, the majority of giant electrocaloric effects were reported for thin film samples [2]. The research on other low-dimensional ferroelectrics, such as nanowires and nanodots, is limited [3]. As a result, it is currently unclear what effect the reduced dimensionality has on the electrocaloric properties of ferroelectrics.

The aims of this study are: (i) to predict the intrinsic features of ECE in ferroelectric ultrathin nanowires; (ii) to understand the effect of reduced dimensionality and size on the electrocaloric properties of nanoscale ferroelectrics; (iii) to explore the potential of ferroelectric nanowires for nanoscale cooling applications.

We simulate three nanowires made of $PbTiO_3$, $BaTiO_3$, and $KNbO_3$ ferroelectric perovskites. These materials are chosen as representatives of ferroelectrics with single ($PbTiO_3$) and multiple ($BaTiO_3$, and $KNbO_3$) phase transitions. Here we model nanowires with a 12x12 unit cells square cross section grown along the <001> pseudocubic direction. Each nanowire is simulated using a 12x12x20 supercell which is periodic along the nanowire's axial direction ($z-$ Cartesian axis in our case). The energy of the supercell is given by the first-principles effective Hamiltonian [4]. The degrees of freedom for the Hamiltonian include local modes, $\mathbf{u}_i$, that are proportional to the dipole moment in the unit cell, and strain variables tensors η_i (in Voigt notations) that are responsible for mechanical deformations of a unit cell. Here we simulate a realistic situation of a partial surface charge compensation by a limited number of free carriers. Technically this is achieved by compensating only 10% of the surface charge (open-circuit electrical boundary conditions) using the approach of Ref.[5]. The energy given by the effective Hamiltonian is used in the framework of classical Monte Carlo (MC) and Molecular Dynamics (MD) to compute finite temperature properties of the nanowires.

We begin by investigating the sequence of phase transitions in nanowires using the simulated annealing approach. In such an approach, the simulations begin at a temperature much above the Curie point and proceeds in steps of 5 K decrements until the simulated temperature reaches 5 K. Figure 1(a) shows the data for $PbTiO_3$ nanowire and the bulk, where the bulk data is included for comparison. It demonstrates that the reduction in dimensionality leads to a decrease in transition temperature and a smearing of the phase transition [6]. For $BaTiO_3$ nanowire (see Fig.1(b)) we find very little change in the ferroelectric transition temperature as compared to the bulk. However, the phase transition sequence is drastically different from the one in the bulk. We do not find any polarization along the nanowire's truncated dimensions due to a prohibitively large depolarizing field associated with the chosen electrical boundary conditions. To gain further insight into the ferroelectric phases and phase transitions character we computed dielectric constant ε_{33} for all nanowires and their bulk counterparts using a direct simulation approach. Our computational data predict that ferroelectric nanowires with a poorly compensated surface charge develop ferroelectric phases with a polarization along the axial direction. Nanowires may develop polydomain phases with multiple order parameters. The common features are the smearing of the phase transition and the dielectric constant. They can be attributed to the decrease in the correlation length due to the reduced dimensionality.

Having established the equilibrium phases and electric properties of nanowires, we turn to the modeling of the ECE. To simulate the ECE we apply an electric field along the nanowire's axial direction under adiabatic conditions using the computational approach of Refs.[7, 8]. In bulk the electric field is applied along the polarization direction. The electrocaloric change in temperature as a function of the initial temperature is given in Fig.2 for a few different values of the applied electric field. We have also included data for the linear electrocaloric response, dT/dE, at low fields which were computed by taking the zero field slope of temperature versus electric field data. In all nanowires we found a reduction in the maximum electrocaloric effect which can be elucidated with the help of the Maxwell relation

$$\frac{dT}{dE} \approx -\frac{T}{C_E}\left[\left(\frac{\partial P_{spon}}{\partial T}\right)_{E=0} + \varepsilon_0\left(\frac{\partial \varepsilon}{\partial T}\right)_{E=0} E\right] \tag{1}$$

where P_{spon} is the spontaneous polarization and ε is the dielectric constant. Both the spontaneous polarization and the dielectric constant are reduced in the nanowire as evident from Fig.1 due to the reduced correlation length. This explains the observed decrease in the maximum ECE in the nanowire as compared to bulk.

In summary, we studied the ECE in poorly compensated ferroelectric ultrathin nanowires and compared the findings to the ECE in bulk ferroelectrics. The computational data demonstrate a reduction in the ECE in nanowires as compared to bulk which is attributed to the reduced correlation length. In nanowires with polydomains the ECE is nearly negligible.

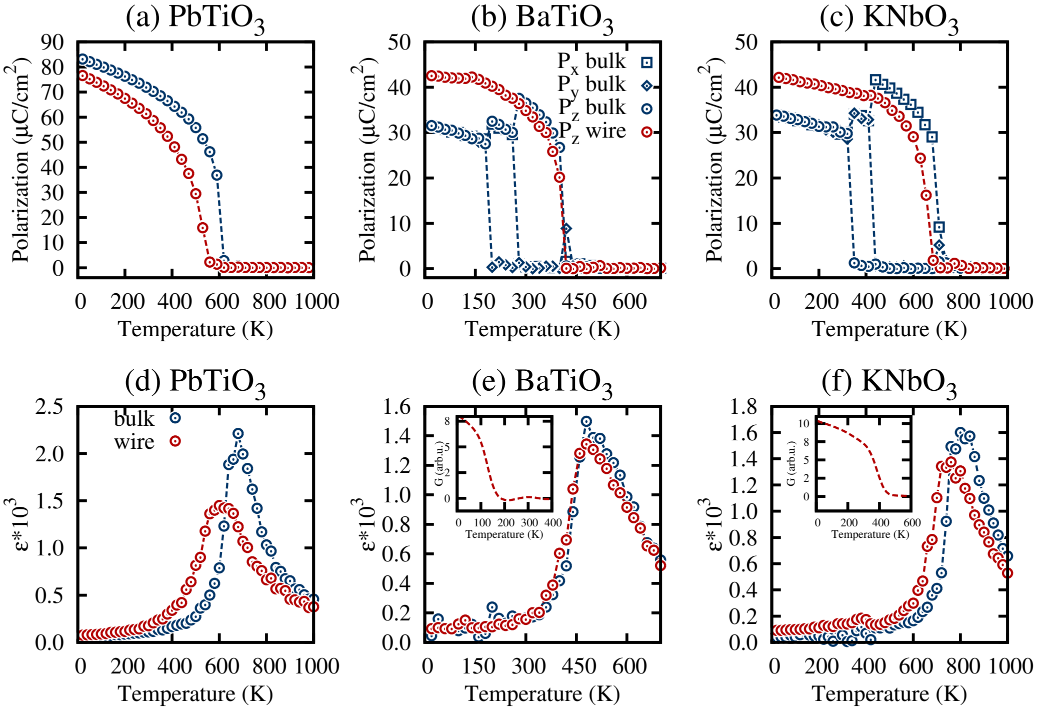

FIG. 1. Dependence of the polarization components on the temperature in bulk and nanowires (a-c). Dependence of the dielectric constant on the temperature in bulk and nanowire (d-f). The inset gives the toroidal moment of polarization.

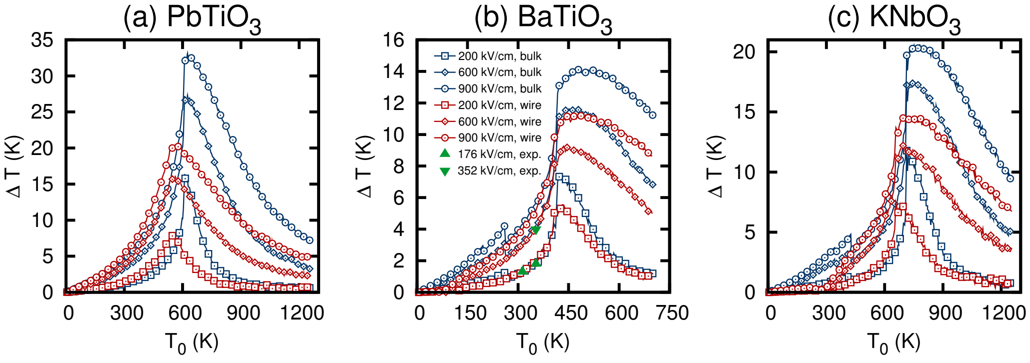

FIG. 2. The electrocaloric change in temperature as a function of the initial temperature for a few representative values of the electric field [(a)-(c)]. In (b) the triangles give the experimental data from the direct measurements on thick films. [9]

Acknowledgements: Financial support for this work provided by the National Science Foundation Grant, No DMR-1250492.

[1] J. F. Scott, Ann. Rev. Mater. Sci. **41**, 229 (2011)
[2] A. S. Mischenko, Q. Zhang, J. F. Scott, R. W. Whatmore, and N. D. Mathur, Science **311**, 1270 (2006)
[3] M. Liu and J. Wang, Sci. Rep. **5** (2015)
[4] W. Zhong, D. Vanderbilt, and K. Rabe, Phys. Rev. B **52**, 6301 (1995)
[5] I. Ponomareva, I. I. Naumov, I. Kornev, H. Fu, and L. Bellaiche, Phys. Rev. B **72**, 140102 (2005)
[6] A. M. Bratkovsky and A. P. Levanyuk, Phys. Rev. Lett. **94**, 107601 (2005)
[7] I. Ponomareva and S. Lisenkov, Phys. Rev. Lett. **108**, 167604 (2012)
[8] S. Lisenkov and I. Ponomareva, Phys. Rev. B **86**, 104103 (2012)
[9] Y. Bai, G. Zheng, and S. Shi, Appl. Phys. Lett. **96**, 192902 (2010)

Theoretical study for fundamental physics of low dielectric loss perovskite $Ba(Zn_{1/3}Ta_{2/3})O_3$

Atsushi Honda, Shin'ichi Higai, Keisuke Kageyama, Yukio Higuchi, and Kosuke Shiratsuyu
Murata Manufacturing Co., Ltd., Kyoto, Japan
e-mail: hnd@murata.com

Introduction

The downsizing of electric components has accelerated the portability of wireless mobile communication devices. The development of dielectric resonators, which cut noises off in the radio signal, reduced the volume and weight of cavity resonators remarkably. The dielectric materials suitable for dielectric resonators are required to have large relative dielectric constant ε_r and high quality factor Q (inverse of dielectric loss). The latter is more important, since it affects a loss of signal which passes through the resonator. The high Q characteristic is known to be hardly compatible with large ε_r, except for complex perovskite materials such as $Ba(Zn_{1/3}Ta_{2/3})O_3$ (BZT)1-4). The origin of high Q characteristic of BZT was found to relate to the ordering of Zn^{2+}/Ta^{5+} cations arrangement4). However, the atomistic mechanisms based on solid-state quantum physics have hardly been understood. We carried out first-principles theoretical calculations, not only to clarify the origin of high Q characteristic of BZT in detail, but also to understand fundamental physics behind complicated phenomena of dielectrics including ferroelectric materials5). In this presentation, we show the importance of theoretical designing of potential energy surfaces for development of novel dielectric materials and devices.

Methods

First-principles calculations based on density functional theory (DFT) were performed using Vienna *ab-initio* simulation package (VASP)6,7). The plane wave basis set was employed. The projector augmented wave (PAW) type was selected as the atomic potential. The generalized gradient approximation (GGA) was used to calculate the exchange-correlation energies of electrons. The density functional perturbation theory (DFPT) was applied to calculate phonon eigenfrequencies (ω_Γ) and eigenvectors at Γ point of the first Brillouin zone, as well as Born effective charges (Z^*) and ε_r. The phonopy code was used to calculate phonon band structures by analyzing the dynamical matrix from DFPT calculations8). The lattice parameter was fixed to the experimental value (a = 4.10 Å) for all calculation models with different Zn^{2+}/Ta^{5+} arrangements in BZT lattice, since it has been shown that Zn^{2+}/Ta^{5+} ordering/disordering hardly affects the lattice parameters4,9).

Results & Discussion

We first calculated ω_Γ of Zn^{2+}/Ta^{5+} ordered BZT, and found that BZT is paraelectric, namely, none of ω_Γ have the imaginary values. In addition, ε_r was calculated to be 32.4, which agrees well to the experimental value (ε_r = 29.5-30.2)4). Next, we calculated the phonon band structure of charge compensated $BaTaO_3$, as a model of the Ta segregated region in Zn^{2+}/Ta^{5+} disordered BZT. It was shown that the Slater mode vibration in TaO_6 octahedron with imaginary eigenfrequency was found at Γ, X, and M points in the first Brillouin zone. This means that $BaTaO_3$ has a ferroelectric nature with double-well potential. A high Q value is hardly expected from double-well potential, since its shape completely differs from parabolic and the oscillation is less harmonic. Therefore, Zn^{2+} in BZT was considered to suppress the ferroelectric nature that is originated from $BaTaO_3$. We examined a $Ba_8(Zn_1Ta_7)O_{24}$ model shown in Figure, to calculate the potential energy surface of Slater mode for each TaO_6 octahedron. Then, we found that TaO_6 octahedra next to and apart from ZnO_6 octahedron have single-well and double-well potentials, respectively. This shows that the intrinsic ferroelectricity of BZT originated from $BaTaO_3$ is partially suppressed by Zn^{2+}.

It was found that two changes are brought to TaO_6 octahedra by being adjacent to ZnO_6 octahedra. One

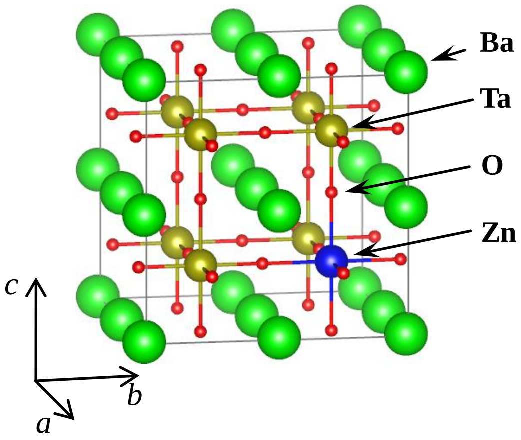

Figure Schematic crystal structure of $Ba_8(Zn_1Ta_7)O_{24}$.

is the decrease of Ta-O bond lengths. The ionic radius of six coordinated Zn^{2+} and Ta^{5+} are 0.74 Å and 0.64 Å, respectively[10)]. This resulted in compression of TaO_6 octahedra by adjacent ZnO_6 octahedra in BZT lattice. Then, two minima in double-well potential of Slater mode in TaO_6 octahedra were overlapped to be parabolic single-well. The other is the weakening of the covalent characteristic between Ta and O atoms. The Born effective charge of Ta^{5+} in charge compensated $BaTaO_3$ was calculated to be $Z^*[\mathrm{Ta}] = 8.63$, and it is much larger than formal valence state of Ta^{5+}. This shows that there are significant covalent characteristic between Ta and O. On the other hand, $Z^*[\mathrm{Ta}]$ decreased to 6.35 for TaO_6 octahedra which were adjacent to ZnO_6 octahedra. This means that Zn^{2+} partially weakens covalent characteristic between Ta and O. In addition, the weakening of covalency was also identified by calculating charge density distribution for Ta-5*d* orbitals that hybridize with O-2*p* orbitals.

It has been shown theoretically that one of the most important characteristics of ferroelectricity is the covalency between cation and anion in perovskite crystals[11)]. Thus, Zn^{2+} in BZT was found to have effects to suppress the intrinsic ferroelectric nature of $BaTaO_3$ in BZT lattice, and it results in high Q characteristics of BZT. Apparently, these effects are maximized when all of Ta^{5+} are adjacent to Zn^{2+}. It is identical to the ordering of Zn^{2+}/Ta^{5+} in BZT. Consequently, our findings can properly explain the experimental fact that the ordering of Zn^{2+}/Ta^{5+} by prolonged firing is effective to increase Q value significantly.

Conclusions

The origin of high Q characteristic of BZT was theoretically studied by first-principles calculations. We found that ZnO_6 octahedra which are adjacent to TaO_6 octahedra decrease bond length and weaken covalency between Ta and O in BZT lattice. These two effects suppress the intrinsic ferroelectricity of $BaTaO_3$, and then result in high Q characteristic of BZT. Our findings provide new understandings of complex perovskite materials not only with high Q value but also with large dielectric constant. We are now confident that the novel dielectric materials that are far superior to the existing ones must be developed by the theoretical approach via accurate artificial designing of potential energy surfaces.

References

1) K. Kageyama, J. Am. Ceram. Soc. **75**, 1767 (1992).
2) Y. Higuchi and H. Tamura, J. Eur. Ceram. Soc. **23**, 2683 (2003).
3) H. Tamura, T. Konoike, Y. Sakabe, and K. Wakino, J. Am. Ceram. Soc. **67**, c59 (1984).
4) S. Kawashima, M. Nishida, I. Ueda, and H. Ouchi, J. Am. Ceram. Soc. **66**, 421 (1983).
5) A. Honda, S. Higai, K. Kageyama, Y. Higuchi, and K. Shiratsuyu, Jpn. J. Appl. Phys. **54**, 10NE01 (2015).
6) G. Kresse and J. Furthmüller: Phys. Rev. B **54**, 11169 (1996).
7) G. Kresse and D. Joubert, Phys. Rev. B **59**, 1758 (1999).
8) A. Togo, F. Oba, and I. Tanaka, Phys. Rev. B **78**, 134106 (2008).
9) A.K. Ganguli, K.P. Jayadevan, G.N. Subbanna, and K.B.R. Varma, Solid State Commun. **94**, 13 (1995).
10) R. D. Shannon, Acta Crystallogr. A **32**, 751 (1976).
11) R. E. Cohen, Nature 358, **136** (1992).

Resonance Damping of the THz-frequency Transversal Acoustic Phonon in the Relaxor Ferroelectric $K(Ta_{1-x}Nb_x)O_3$

E.Iolin[1,2], J.Toulouse [1*], B.Hennion[3], D.Petitgrand[3], and R.Erwin[4]

[1]*Physics Department, Lehigh University, Bethlehem, PA, 18015, USA, *jt02@lehigh.edu*
[2]*Latvian Academy of Science, Riga, Latvia, eiolin@netzero.net*
[3]*Laboratoire Leon Brillouin, CEA, Saclay, France*
[4]*National Center for Neutron Research, NIST, Gaithersburg, MD, USA*

$K(Ta_{1-x}Nb_x)O_3$ (KTN) is a mixed perovskite characterized by the presence weak static compositional random electric field (REF). It can be considered as a useful model system for the study of relaxor ferroelectrics with homovalent cations ($(K_{1-x}Li_x)TiO_3$ (KLT), $Ba(Zr_{1-x}Ti_x)O_3$ (BZT), and $Ba(Sn_{1-x}Ti_x)O_3$ (BST). In KTN, the Ta^{5+} ion is replaced by the isovalent Nb^{5+} ion with almost the same ionic radius. Neutron diffuse scattering, DS, observed near (110) B.Z. point [1], and dielectric measurements data demonstrate that KTN could be labeled as "weak" relaxor. In KTN, the Nb^{5+} ions are displaced from their high symmetry site by ~0.145 Å in eight equivalent <111> directions. The collective reorientation of these dipoles give rise to the relaxor behavior (Fig.1). Because the width of the relaxation peak in KTN is only one tenth that in PMN or PZN, KTN can be regarded as a "weak" relaxor in comparison with PMN, PZN.[2].

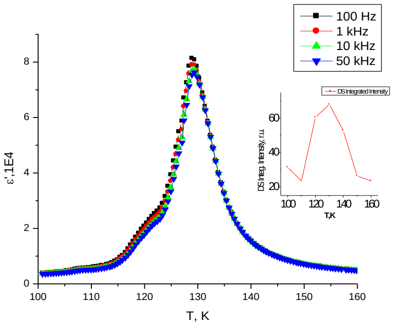

Fig.1 . Dielectric susceptibility of KTN15 vs temperature; inset: integral intensity of the DS as a function of temperature near (110) BZ point.

We have studied the transverse acoustic (TA) phonon in two KTN crystals with Nb concentration of 15% and 17% by means of inelastic neutron scattering near the (020) BZ point (see [1] for experimental details). The dispersion curves of the two phonons are presented at the Fig.2.

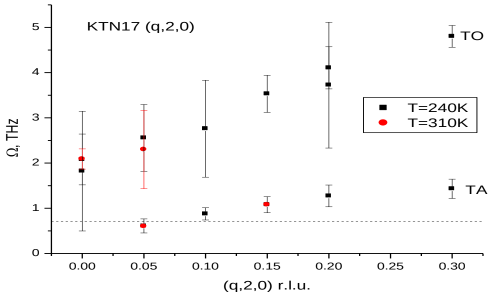

Fig.2. Dispersion of the transverse optic (TO) and transverse acoustic (TA) phonon in KTN17. The dash line at E=2.9 meV marks the value of energy of the dispersionless resonance mode (RM).

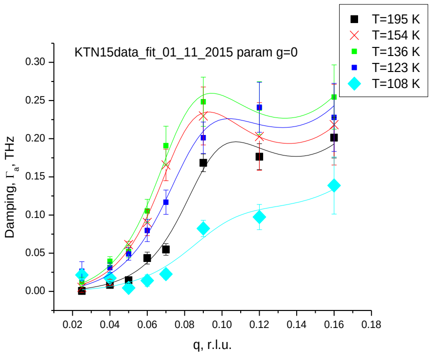

Fig.3. Damping ***Γ$_a$*** of the TA phonon vs wave vector ***q*** in KTN15 at different temperatures. Solid lines are fits to the data using eq. (1).

Although diffuse scattering isn't observed at that point (unlike near (110) as shown in Fig.1), the damping ***Γ$_a$*** of the TA phonon is nevertheless seen in Fig.3 to rise in a step like fashion near ***q***≈0.07. This rise can be attributed to scattering of the TA phonon by a dispersionless resonance mode (RM) with energy $\boldsymbol{\omega_R}$≈0.7 THz (see dashed line in Fig.2), damping $\boldsymbol{\Gamma_R}$, and oscillator strength M.

$$\Gamma_a(q) \approx \frac{M^2 q^2 \Gamma_R}{(\omega_a(q)^2 - \omega_R^2)^2 + \omega_a(q)^2 \Gamma_R{}^2} \quad (1)$$

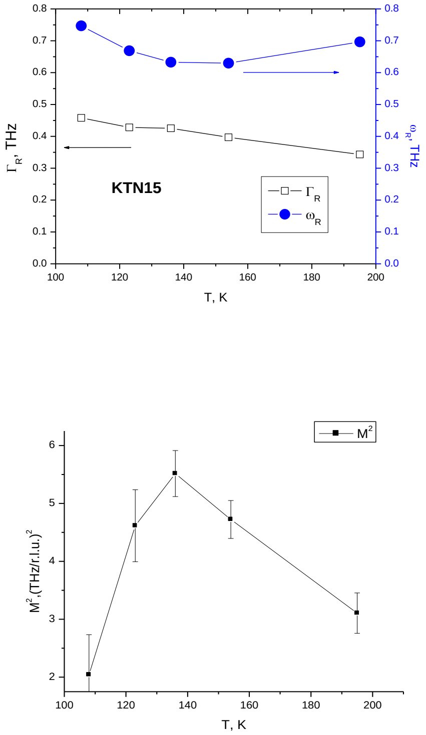

Fig.4. Frequency, width, and oscillator strength of the RM vs temperature. Value of $\boldsymbol{M^2}$ is strongly increased in the region of relaxation behavior.

Debye relaxation model is unable to reproduce TAW damping data in our case. The TA damping $\boldsymbol{\Gamma_a}$ vs $\boldsymbol{q}$ is *very well* fitted in the frame of Havriliak-Negami relaxation model [3] with exponent α≈3/2 contained resonance –like (transition) oscillation in the time domain representation:

$$f_{HN} = 1/(1+(i\omega\tau)^\alpha), \quad \alpha \approx 3/2,$$

$$\Gamma_a = qP\frac{(\omega\tau)^\alpha \sin(\pi\alpha/2)}{1+2(\omega\tau)^\alpha \cos(\pi\alpha/2)+(\omega\tau)^{2\alpha}} \quad (2)$$

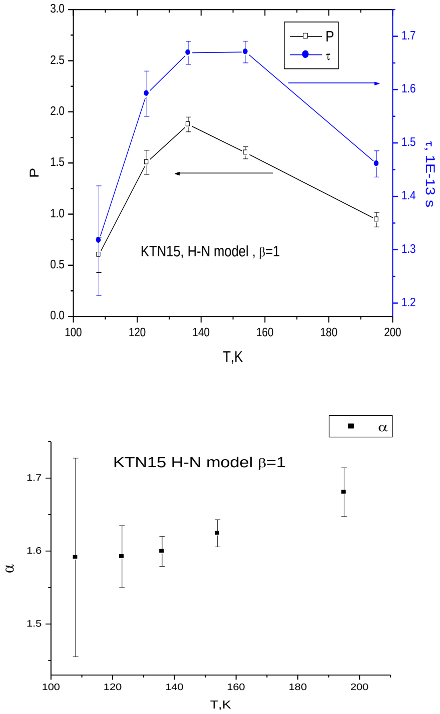

Fig. 5 Temperature dependence of the relaxation time $\boldsymbol{\tau}$, oscillator strength ***P,*** and exponent $\boldsymbol{\alpha}$ from the HN fit.

We explain that the resonance mode appears as result of the correlation motion of the off-center Nb^{5+} ions between eight equivalent <111> positions. The obtained frequency $\boldsymbol{\omega_R}$ of this RM mode is in fact found to be in agreement with the theoretical estimate previously obtained by Girshberg and Yacoby [4],[5]. The HN model with α≈3/2 corresponds to the non-local relaxation of the off-center Nb^{5+} ions in contrast to the Debye relaxation.

[1] J.Toulouse et al, arXiv:1001.4096. [2] D.Phelan et al, PNAS,v.111, no.5, 1754-59, (2014).[3]Havriliak, S., Negami,S., Polymer ***8***, 161-210 (1967).[4] Ya. Girshberg, Y.Yacoby, Solid State Commun., **103**, 425 (1997) ; [5] Y.Girshberg and Y.Yacoby, J. Phys.: Condens. Matter, **24**, 015901 (2012).

Special quasirandom structures for complex perovskite alloys

Zhijun Jiang,[1,2] Yousra Nahas,[2] Dawei Wang,[1] and L. Bellaiche[2]
[1]*Electronic Materials Research Laboratory–Key Laboratory of the*
Ministry of Education and International Center for Dielectric Research,
Xi'an Jiaotong University, Xi'an 710049, China
[2]*Physics Department and Institute for Nanoscience and Engineering,*
University of Arkansas, Fayetteville, Arkansas 72701, USA

A special quasirandom structure (SQS) [1] is typically designed by building and selectively populating a relatively small supercell such that the short-ranged, geometric correlations approximate that of the random alloy. This approach has been widely used to calculate the electronic structure and physical properties of semiconductor solid solutions and properties of metallic alloys, but (to our knowledge) very few studies about SQS have been carried out in disordered perovskite alloys [2, 3]. In particular, it is unclear if SQS can reproduce properties of complex ferroelectric systems, such as $Pb(Zr_{1-x}Ti_x)O_3$(PZT), that can possess subtle monoclinic phases as ground state, and $Pb(Sc_{0.5}Nb_{0.5})O_3$ (PSN), that exhibits strong random fields dramatically affecting its properties. To address these issues, we report here first-principles-based effective Hamiltonian simulations in both PZT and PSN.

Practically, the studied PZT material is made of 50% of Zr and Ti ions. Two different types of supercells are constructed: a large 12×12×12 supercell (8,640 atoms) inside which Ti and Zr are randomly distributed *versus* two SQS configurations, namely of 3×3×4 and 4×4×4 sizes, that are generated by imposing the so-called Cowley parameters of the first three neighboring cells are as close to zero as possible [4]. The effective Hamiltonian approach used to model properties of PZT is described in Ref. [5], and contains both the local modes (which are proportional to the electrical polarization) and the antiferrodistortive motions (AFD), which represents oxygen octahedral tiltings. Figure 1(a) shows the predicted supercell averaged local mode vectors as a function of temperature, for both the 12×12×12 random supercell and the 4×4×4 SQS configuration. One can see that this SQS configuration can reproduce rather well the polar properties of a large disordered $Pb(Zr_{0.5}Ti_{0.5})O_3$ system, for temperature below 300 K, including the transition from the tetragonal (for which only one component of the polarization is non-zero) to the monoclinic phase (that has two non-vanishing and equal Cartesian components that are smaller than the third one). Figure 1(a) further reveals that the SQS configuration can *not* be safely used above 300 K because of its small size. Figure 1(b) reports the same property as in Fig. 1(a), but adding here the results of the smaller 3×3×4 SQS supercell. This latter SQS structure is less accurate than the 4×4×4 SQS configuration for low temperatures and produces results that differs from those of the large 12×12×12 supercell at smaller temperature than for the 4×4×4 SQS structure. Such features therefore demonstrate that a minimal size is needed to reproduce subtle properties of PZT.

Moreover, Figure 2 displays the Cartesian components of the pseudo-vector characterizing the AFD motions, as

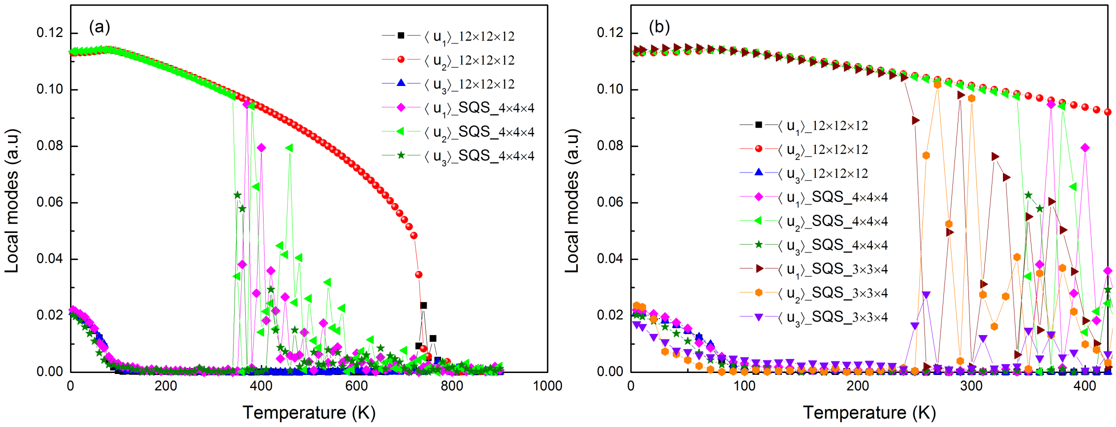

FIG. 1: The average Cartesian components of the local mode vectors as a function of temperature in $Pb(Zr_{0.5}Ti_{0.5})O_3$ [panels (a) and (b)]. The alloy configurations are randomly generated for 12×12×12 supercell, while 4×4×4 and 3×3×4 supercells correspond to the two studied SQS configurations.

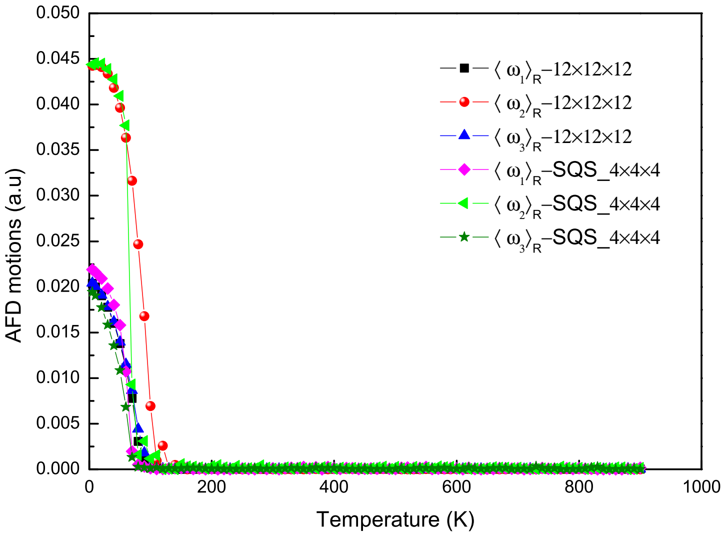

FIG. 2: The average Cartesian components of the AFD-related $\langle\omega\rangle_R$ pseudo vectors as a function of temperature in Pb(Zr$_{0.5}$Ti$_{0.5}$)O$_3$.

resulting from the use of the 12×12×12 random supercell and the 4×4×4 SQS supercell. This SQS structure is shown to reproduce the AFD phase transition demonstrated in the large disordered PZT alloy below room-temperature. Once again, the SQS structure can be used to investigate complex properties of perovskites.

In addition, we also mimicked the disordered heterovalent PSN perovskite alloy. The 4×4×4 SQS configuration was also found to yield properties that reproduce well those of larger disordered supercell, especially at low temperature. We therefore hope that SQS will be soon frequently used (especially by direct first-principles method) to investigate complex perovskite solid solutions.

This work is financially supported by the National Natural Science Foundation of China (NSFC), Grant No. 51390472, and National Basic Research Program of China, Grant No. 2015CB654903. Z.J. thanks the NSFC Grant No. 11574246, China Scholarship Council (CSC No. 201506280055). Y.N. thanks ARO grant W911NF-12-1-0085 and L.B. thanks ONR Grant N00014-12-1-1034. Some computations were also made possible thanks to the MRI grant 0722625 from NSF, the ONR grant N00014-15-1-2881 (DURIP) and a Challenge grant from the Department of Defense.

---

[1] A. Zunger, S. H. Wei, L. G. Ferreira, and J. E. Bernard, Phys. Rev. Lett. **65**, 353 (1990).
[2] A. I. Lebedev, Phys. Solid State **51**, 2324 (2009).
[3] B. K. Voas, T. M. Usher, X. Liu, S. Li, J. L. Jones, X. Tan, V. R. Cooper, and S. P. Beckman, Phys. Rev. B **90**, 024105 (2014).
[4] A. M. George, J. iguez, and L. Belleiche, Phys. Rev. Lett. **91**, 045504 (2003).
[5] I. A. Kornev, L. Bellaiche, P. E. Janolin, B. Dkhil, and E. Suard, Phys. Rev. Lett. **97**, 157601 (2006).

Investigation of Local Structure and Cation Ordering in Dielectric Oxide Microwave Ceramics Using ^{7}Li and ^{93}Nb Solid-state NMR Spectroscopy

R. Kalfarisi, G. Hoatson, and R. Vold
Physics Department, College of William and Mary, Williamsburg VA

Oxides perovskite, chemical formula ABO_3, are probably the most widely studied metal oxides. In part, this is because of their ability to accommodate extensive chemical substitution on both the A and B-sites. This results in a wide variety of interesting and useful physical and chemical properties. Microwave dielectric oxides applications are examples of such interesting materials. They have high dielectric permittivity and very low energy loss at microwave frequency (high quality factor). This combination makes these materials an excellent candidate for microwave wireless telecommunication applications. The continued development and improvement of wireless telecommunication technology will rely upon our fundamental understanding and potential manipulation of these systems. ^{7}Li and ^{93}Nb NMR spectroscopy measurements were done on five cation-ordered complex perovskite microwave ceramics powders, which can be grouped into two different categories, mixed A-site (group 1) and single A-site (group 2). The ordering adopts repeating layers of BO_6 octahedra in the <111> direction of simple cubic perovskite cell. Although the ordering in B-site cation has been confirmed, no ordering was observed for the A-site ions in group one [1].

Result of ^{7}Li MAS spectra of all samples show one strong and sharp central transition (or CT) and accompanied by the spinning side-band manifold, due to the $\pm 3/2 \leftrightarrow \pm 1/2$ satellite transition (or ST). No anisotropic second order quadrupolar broadening has been observed. Similar spectra were obtained for all samples, except for $(Ca_{2/3}La_{1/3})Li_{1/3}Nb_{2/3}O_3$ or CLLN which shows two peaks at central transition (Fig. 1). Simulation of the MAS NMR spectrum of the complete spinning sideband manifolds, used data from three different spinning speeds at two different magnetic field strengths. The simulations were used to extract the values of NMR parameter. The analysis is done with the program DMFIT [2]. The quadrupolar coupling constant and the asymmetry parameter (C_Q and η_Q), chemical shift anisotropy and asymmetry (δ_{CS} and η_{CS}), and Euler angles ($\propto, \beta, \gamma$) describing the relative orientation of quadrupolar and chemical shift tensor frames were taken into account.

There are only three samples containing niobium nucleus and their respective ^{93}Nb MAS NMR spectra are shown in Fig. 2. All of MAS spectra show partially averaged second-order quadrupolar powder pattern for the CT and an array of spinning sidebands due to ST, indicating very large C_Q values. The CT of SLLN and CLN spectra exhibit a low-frequency tail and could not be simulated with only one peak. It has been reported previously that when a MAS NMR central transition resonance of glasses and disordered materials shows a tail at low frequency, it indicates that a distribution of chemical shifts and quadrupole couplings are present in the system [3]. Further studies on 3QMAS experiment on the samples, revealed one single resonance which is broadened along the 'CS' and 'QIS', the axes giving the direction of, respectively, the isotropic chemical shifts and the quadrupole induced shifts confirming the presence of such distributions.

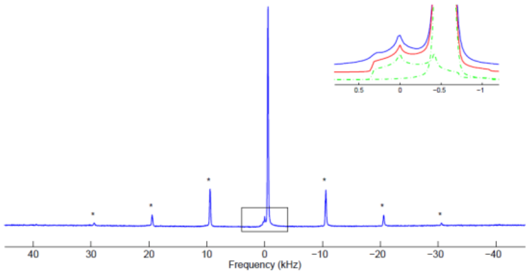

Figure 1: ^{7}Li MAS spectrum of CLLN spun at 10 kHz and spinning sideband manifold resulting from the satellite transition are indicated by stars. Inset figure shows two resolvable resonances at the central transition. The simulated spectrum (red) and individual line components (green) are shown below the experimental data.

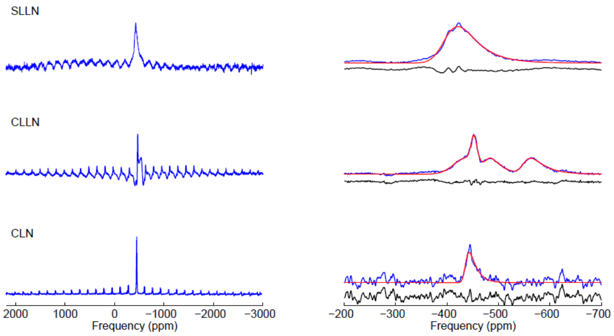

Figure 2: ^{93}Nb MAS NMR spectra of niobium-contained samples spun at 30 kHz. The left column show spectra with 1MHz spectral window while the right one show selective pulse excitation of the central transition. On the right column, the lower trace (black) represents the difference between the experimental (blue) and simulated (red) spectra.

Acknowledgement: This work was supported by NSF grant number CHE-1012344.

References

[1] P. K. Davies, H. Wu, A. Borisevich, I. E. Molodetsky, and L. Farber, Annu. Rev. Mater. Res. **38**, 369 (2008).

[2] D. Massiot, F. Franck, M. Capron, I. King, S. L. Calve, B. Alonso, J. O. Durand, B. Bujoli, Z. Gan, and G. Hoatson, magn. Reson. Chem. **40**, 70 (2002).

[3] C. Jager, G. Kunath, P. Losso, and G. Scheler, Solid state Nucl. Magn. Reson. **2**, 73 (1993).

Ultra-large-scale Hybrid Monte Carlo simulations of ferroelectric and relaxor materials

K. Kalke,* S. Prokhorenko,† and L. Bellaiche
Physics Department and Institute for Nanoscience and Engineering,
University of Arkansas, Fayetteville, Arkansas 72701, USA

Relaxor ferroelectrics display a high degree of system-wide interactions which give rise to macroscopic effects whose mechanisms are not yet fully understood [1]. Since these mechanisms arise at the nano-scale, atomic level simulations are of critical importance for study of relaxor physics. In this study we focus on the development of more powerful effective Hamiltonian simulations than previously available for the purpose of studying properties of relaxors that were before computationally infeasible. We do this by leveraging both the power of massively-parallel computations made possible by the use of Graphics Processing Units (GPUs) and simulation algorithms with better computational complexity than is used in current state-of-the-art simulations.

We chose to approach the developmental hurdle of designing a more powerful simulation code by making use of the parallelism offered by GPUs. Modern GPUs have thousands of processing cores and are therefore perfectly suited to tackle complexity related to the long-range nature of dipolar interactions in relaxor materials. From this a large speedup is gained before any algorithmic optimization of the simulation is done. Furthermore, modern GPU code libraries are well-optimized from a hardware perspective and now give significant advantages for large-scale simulation and calculations in comparison to simple CPU code as has been used until this point. The other main improvement this study employs is the use of the Hybrid Monte-Carlo (HMC) [2] algorithm in place of the commonly used Metropolis Monte-Carlo (MMC) or molecular dynamics (MD) simulations. Remarkably, HMC combines the advantages offered by both MMC and MD techniques by generating an ensemble of connected short-scale phase-space trajectories governed by true Hamiltonian dynamics. During the run, these trajectories are frequently filtered via the Metropolis acceptance criteria that forces the generated bundle of macroscopic states to comply with canonical ensemble distribution. Therefore, in contrast to MMC simulations, HMC algorithm provides access to the “real time” dynamics while still effectively probing a large volume of the phase space inaccessible within canonical MD. Moreover, the use of molecular dynamics within the simulation scheme provides a straightforward way to parallelize the algorithm by using recently developed speed-up strategies that have proved their efficiency for large-scale simulations of ferroelectric materials.

Here, we present a beta version of the code that employs the aforementioned simulations scheme. The implementation of the Hybrid Monte Carlo algorithm (HMC) [2] is based on the $O(NLog(N))$ scaling fast Fourier transform (FFT) based calculation of long-range dipolar [3] forces, that allows to avoid the $O(N^2)$ computational complexity of the commonly used Metropolis Monte Carlo algorithm, and to thoroughly study the statistical properties of the first-principles based ϕ^4 lattice models of relaxor compounds. The code benchmarks show that our code is able to perform effective Hamiltonian simulations with up to $N \sim 10^9$

---

*Electronic address: kruzkalke@gmail.com
†Electronic address: prokhorenko.s@gmail.com

local-mode lattice sites in contrast to the state-of-the-art Monte Carlo based code that are limited to system sizes of $N \sim 10^4$. In the second part of this study we plan to use the developed code to study critical properties of relaxor ferroelectrics. Specifically, we will focus on investigating the microscopic origin of dielectric relaxation exhibited by one of the prototypical examples of relaxor compounds - structurally disordered Ba(Zr,Ti)O3 (BZT) alloys using effective Hamiltonian model of Ref. [4].

In summary, this study presents a beta version of an ultra-large-scale effective Hamiltonian simulations code, that, as we hope, will significantly extend the horizon of first-principles based simulations of ferroelectric, relaxor and multiferroic materials. Upon progress the production version of this will be made available to the community under an open-source software license.

This work is financially supported by DARPA grant HR0011-15-2-0038 (under the MATRIX program) and by the Physics department of the University of Arkansas. K.P. also thanks the financial support of the Arkansas Department of Higher Education through the SURF grant.

---

[1] R. A. Cowleyab, S. N. Gvasaliyac, S. G. Lushnikovd, B. Roesslic, and G. M. Rotaru, "Relaxing with relaxors: a review of relaxor ferroelectrics." *Advances in Physics*, **60**, 229 (2011)

[2] S. Duane, A.D. Kennedy, B. J. Pendleton, D. Roweth, "Hybrid Monte Carlo." *Physics Letters B*, **195**, 216 (2011)

[3] T. Nishimatsu, U. V. Waghmare, Y. Kawazoe, and D. Vanderbilt, "Fast molecular-dynamics simulation for ferroelectric thin-film capacitors using a first-principles effective Hamiltonian." Phys. Rev. B, **78**, 104104(2008)

[4] A. R. Akbarzadeh, S. Prosandeev, E. J. Walter, A. Al-Barakaty, and L. Bellaiche, "Finite-Temperature Properties of Ba(Zr,Ti)O_3 Relaxors from First Principles." *Phys Rev Lett.*, **108**, 257601 (2012)

Exploring the Properties of [100]-, [110]- and [111]-oriented Vanadate Superlattices from First Principles

Karandeep, Julien Varignon, Eric Bousquet and Philippe Ghosez
Theoretical Materials Physics, University of Liege, B-4000 Sart Tilman Belgium
(Dated: December 3, 2015)

In today's world, the ferromagnetic and ferroelectric materials are of great scientific and technological importance. On the one hand, ferroelectric materials are mostly used in transducers, capacitors and memory devices because of their piezoelectric, dielectric and ferroelectric properties. On the other hand, ferromagnetic compounds are used in magnetic recording devices, read heads and memories based on giant magneto-resistance. Magneto-electric multiferroic materials are both ferroelectric and ferromagnetic. These materials are interesting not only for their individual ferroelectric and ferromagnetic properties but also for their ability to couple them, which could lead to a whole range of new applications. In past decade, a lot of research has been devoted in developing these materials. The family of ABO_3 perovskites is ideally suited for this purpose because they display a fascinating range of properties and structures depending upon the different size and type of A, B cations. Prototypical ferroelectric transition metal perovskites have the d_0 B-site cation or lone pair active A cation which show polarizations by second-order-Jahn-Teller effect. Whereas the ferromagnetic transition metal perovskites have partially filled d-orbital. Therefore at the bulk level the ferroelectric and ferromagnetic orders in perovskites are generally exclusive. Recent studies by Bousquet *et al* [1] have shown a new type of improper ferroelectricity originating from the trilinear coupling of two independent anti-ferrodistortive (AFD) motions and one ferroelectric distortion in the $PbTiO_3/SrTiO_3$ superlattices. As it was anticipated there, it was further showed that strong magneto-electric effect can be achieved by this type of coupling [2]. Vanadates (AVO_3) in there ground state have these AFD motions but also exhibit Jahn-Teller distorsions which where recently shown to also give rise to ferroelectricity in [001] AVO$_3$/A'VO$_3$ superlattices [3]. In present work, we investigate by first principles methods the behaviour of the vanadates superlattices($AA'V_2O_6$) having A and A' cations alternating along [001], [110] and [111] directions respectively (Fig:1).

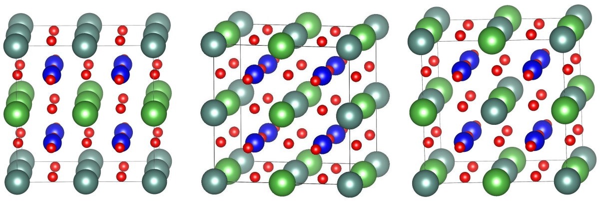
(a) Layered (001) (b) Columnar (110) (c) Rock-salt (111)

FIG. 1: Three type of A/A' cation ordered superlattices.

First-principles calculations have been performed by using density functional theory and projector augmented-wave potentials (PAW) as implemented in the Vienna ab initio simulation package (VASP) [4]. Convergence is achieved by using a planewave cutoff of 500 eV and 6 × 6 × 4 k-point mesh. To include the effect of strong corrections among Vanadium d-electrons electrons LDA+U approach with PBEsol exchange-correlation functional and U = 3.5 eV is used. This value of U have been used in earlier works [3]. The $\sqrt{2} \times \sqrt{2} \times 2$; 20-atom cells are used for the calculations. All structures are relaxed until the forces on the atoms are less than 10^{-5} eV/Å with energy convergence of 10^{-9} eV. The polarizations are calculated using berry phase approach. AMPLIMODES software is used for symmetry mode analysis [5].

ABO_3 perovskites have the same reference cubic $Pm\bar{3}m$ structure. But most of them usually have a lower symmetry structure at room temperature. These structures can even undergo further phase transitions if the temperature is lowered. Among the $A^{+3}V^{+3}O_3$ rare earth perovskites, the smallest A cations (A=Yb-Dy,Y) perovskites have orthorhombic $Pbnm$ ground state structure with AMFG anti-ferromagnetic ordering and large A cations (La,Ce Pr) have monoclinic $P2_1/b$ ground state structure with AMFC ordering. The medium size A cations (Tb-Nd) exhibit a mixed ordering (C+G)[6, 7]. The ideal undistorted structures of presently studied superlattices are: $P4/mmm$ for layered (001); $P4/mmm$ for columnar (110) and $Fm\bar{3}m$ for rock-salt (111) ordering respectively(see Fig 1). As the ground state in bulk perovskites is either orthorhorombic(AMFG) or monoclinic(AMFC), we have compared the energy of both arrangements to find ground states of superlattices . We have selected $(YLa)V_2O_6$, $(PrLa)V_2O_6$ superlattices for this purpose; the result are shown in the Table 1. We find that $(YLa)V_2O_6$ perovskite has a ground state with AMFG magnetic ordering for all three cation ordered structures. On the contrary in $(PrLa)V_2O_6$ perovskite rock-salt order have AMFG magnetic ordering, while the layered and columnar orders have AMFC magnetic ordering in their ground state respectively. In $(YLa)V_2O_6$ and $(PrLa)V_2O_6$ materials rock-salt and layered cation order have the lowest energy respectively.

Polarizations are also shown in the Table 1. To understand these energies trend and polarizations we have performed the symmetry mode analysis (see Table 2). As suggested by Young et al.[8], the Madelung energy of rock-salt order is lower than the layered and columnar orders, also the columnar order does not have any energy lowering polar displacement causing it to have more energy than layered order. Hence AMFG $(YLa)V_2O_6$ perovskites have ground state in rock-salt cation order. In layered and columnar $(PrLa)V_2O_6$ AMFC magnetic order introduces the R-type Jahn-Teller distortions represented by M_1^- and Z_3^+ modes in Table 2, this lowers the energy of these orders with respect to the AMFG rock-salt order. Hence the layered order has minimum energy in $(PrLa)V_2O_6$. The polarizations P_{xy}, P_z in layered structures are produced by the modes Γ_5^- and Γ_3^- respectively. These modes appears as a result of rotationally and Jahn-Teller (JT) distortions driven hybrid improper mechanism due to trilinear couplings $\Gamma_5^- M_5^- M_2^+$ and $\Gamma_3^- M_1^- M_3^+$ respectively[3]. Here M_5^-, M_2^+ can be represented by rotational modes ϕ_{xy}^-, ϕ_z^+ and M_3^+, M_1^- by JT modes M_{JT}, R_{JT} respectively. In rock-salt structures, the improper ferroelectric mechanism due to $\Gamma_4^-(\Gamma_5^-)^3$ coupling produce the polarization. Here Γ_5^- can be represented by rotational mode ϕ_{xy}^-. In addition to this coupling the trilinear couplings involving Jahn-Teller distortion $X_3^+(M_{JT})$ are also been seen: $\Gamma_4^- X_3^+ X_5^-$, $\Gamma_5^- X_3^+ X_5^-$ in rock salt structure. Since JT distortions are connected to orbital-ordering and hence to magnetic ordering, a strong coupling is expected between polarization and magnetism in these structures.

TABLE I: Summary of Calculated Ground State Properties of Ordered Perovskites $(AA')V_2O_6$.[a]

Material	Cation ordering	Magnetic ordering	Space Group	ΔE	P_{xy}	P_z
$(YLa)V_2O_6$	layered	AMFG	$Pmc2_1$	1.81	7.90	0
	columnar	AMFG	$P2_1/m$	2.83	0	0
	rock salt	AMFG	$Pmn2_1$	0	3.35	0
$(PrLa)V_2O_6$	layered	AMFC	Pb	0	2.95	0.37
	columnar	AMFC	$P\bar{1}$	1.35	0	0
	rock salt	AMFG	$Pmc2_1$	2.13	1.10	0

[a] ΔE is the energy difference between ground state structures of the given compound with respect to cation ordering (in meV/f.u). P_{xy} and P_z are polarizations in respective directions (in $\mu C/cm^2$)

TABLE II: Symmetry Mode Analysis.

Modes	$(YLa)V_2O_6$	$(PrLa)V_2O_6$
Γ_1^+	0.0896	0.0217
Γ_5^+	-	0.0022
Γ_3^-	-	0.0042
Γ_5^-	0.7564	0.5810
M_2^+	1.1142	0.9213
M_3^+	0.1203	0.0116
M_5^+	-	0.0012
M_1^-	-	0.0924
M_4^-	-	0.0100
M_5^-	1.6048	1.3561

(a) Layered (001)

Modes	$(YLa)V_2O_6$	$(PrLa)V_2O_6$
Γ_1^+	0.0687	0.1678
Γ_2^+	0.0120	0.0013
Γ_3^+	0.1345	0.0120
Γ_4^+	1.0929	0.9259
Γ_5^+	-	0.0087
Z_1^+	-	0.0116
Z_2^+	-	0.0012
Z_3^+	-	0.0924
Z_4^+	-	0.0100
Z_5^+	1.6048	1.3561

(b) Columnar (110)

Modes	$(YLa)V_2O_6$	$(PrLa)V_2O_6$
Γ_5^+	0.0236	0.0051
Γ_4^-	0.2165	0.1534
Γ_5^-	1.6316	1.3688
X_2^+	1.0478	0.9097
X_3^+	0.1291	0.1036
X_5^-	0.7398	0.5858
-	-	-
-	-	-
-	-	-
-	-	-

(c) Rock-Salt (111)

References

[1] E. Bousquet, M. Dawber, N. Stucki, C. Lichtensteiger, P. Hermet, S. Gariglio, J.-M. Triscone, and P. Ghosez, Nature **452**, 732 (2008).

[2] N. A. Benedek and C. J. Fennie, Physical review letters **106**, 107204 (2011).

[3] J. Varignon, N. C. Bristowe, E. Bousquet, and P. Ghosez, Scientific reports **5** (2015).

[4] G. Kresse and J. Furthmüller, Phys. Rev. B **54**, 169 (1996).

[5] D. Orobengoa, C. Capillas, M. I. Aroyo, and J. M. Perez-Mato, Journal of Applied Crystallography **42**, 820 (2009).

[6] S. Miyasaka, Y. Okimoto, M. Iwama, and Y. Tokura, Physical Review B **68**, 100406 (2003).

[7] I. D. Prodan, G. E. Scuseria, and R. L. Martin, Physical Review B **76**, 033101 (2007).

[8] J. Young and J. M. Rondinelli, Chemistry of Materials **25**, 4545 (2013).

First principles calculations of oxygen vacancies in the bulk and on surface of complex perovskites for solid oxide fuel cell cathodes

E. A. Kotomin[1,2], Yu. A. Mastrikov[2], R. Merkle[1], M. M. Kuklja[3], and J. Maier[1]

[1]Max Planck Institute for Solid State Research, Heisenbergstr.1, Stuttgart, Germany
[2]Institute for Solid State Physics, University of Latvia, Kengaraga str. 8, Riga, Latvia
[3] Materials Science and Engineering Dept., University of Maryland, College Park, USA

ABO_3-type perovskite solid solutions with a large oxygen deficiency δ exhibit a perceptible ionic conductivity, leading to their use as electrolytes ((La,Sr)(Ga,Mg)$O_{3-\delta}$ or materials for oxygen permeation membranes and solid oxide fuel cell cathodes ((La,Sr,Ba)(Mn,Fe,Co)$O_{3-\delta}$) [1,2]. The oxygen migration in perovskites occurs by the vacancy mechanism with the migration through the "critical triangle" of one *B* site cation and two *A* cations as the bottleneck [3] (Fig. 1).

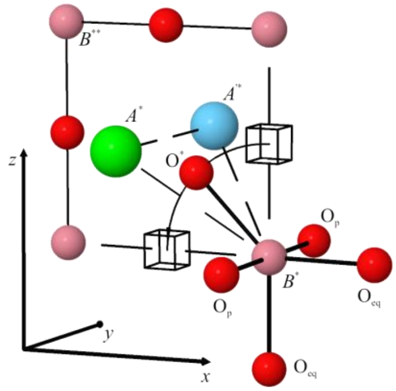

Fig. 1. The transition state of an oxygen vacancy migration through the "critical triangle" in ABO_3 perovskite structure

As it is established now, the formation and migration energies of oxygen vacancies are two major factors determining oxygen reduction rate [2,4]. Based on first principles DFT calculations for supercells containing 40 up to 320 atoms, we analyze these two quantities for the bulk and surface for a series of complex (La,Sr)(Co,Fe)$O_{3-\delta}$ (LSCF) perovskites [5]. The atomic relaxation, charge redistribution and energies of the transition states for oxygen ion migration are obtained and differences with $Ba_{1-x}Sr_xCo_{1-y}Fe_yO_{3-\delta}$ (BSCF) perovskites [2,4] (which exhibit considerably lower migration barriers) are discussed in detail. It is demonstrated, in particular, that the main reason for a considerably reduced vacancy migration energy in BSCF compared to LSCF (and many other perovskites) is due to the charge transfer from an oxygen ion in its transition state towards nearest B-type cation which results in a smaller oxygen size and thus a smaller lattice distortion. It is shown also that the two major factors determining the vacancy migration energy in BSCF are geometric factors (Fig. 1, distance of migrating O* and A-type cation in transition state) and vacancy formation energy (i.e. the electronic structure) (Fig.2).

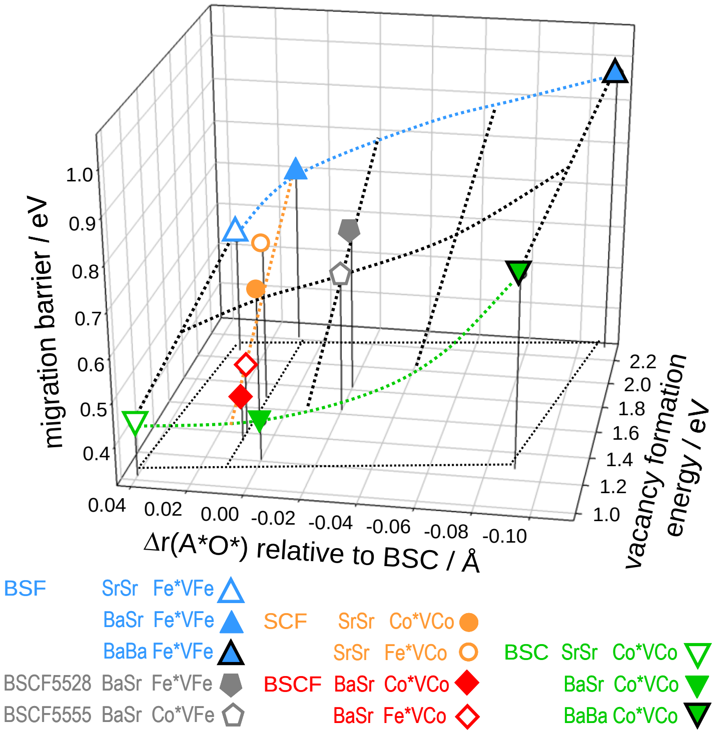

Fig. 2. Oxygen vacancy migration barriers E_m in $Ba_{1-x}Sr_xCo_{1-y}Fe_yO_{2.875}$ as a function of the geometric factor (deviation from (Ba,Sr)*-O* distance (Fig. 1) from the BSC values used as a reference) and the electronic factor (vacancy formation enthalpy). The black dotted lines are a guide to the eye only.

In contrast to BSCF, the perovskites from the (La,Sr)(Fe,Co,Mn)$O_{3-\delta}$ family have higher migration barriers, typically ~ 0.8 eV, and do not depend much on the nature of the *B* cation. The geometrical criteria do not vary much between LSCF and BSCF (the larger average *A* cation ion radius in BSCF is balanced by the larger lattice parameter). On the other hand, the generally larger vacancy formation energies for LSCF, reflecting that electron transfer from removed O atom to the *B* cation is less favorable, also makes the partial electron transfer from the migrating O* in the transition state less favorable, resulting in much smaller charge transfers. As this charge transfer is the main reason for the low barriers in BSCF, it is not surprising that with smaller charge transfers the O migration barrier is higher in LSCF and less dependent on the vacancy formation energy.

[1]. E.A. Kotomin, R. Merkle, Yu.A. Mastrikov, M.M. Kuklja, and J. Maier. Chapter 6 in a book: *Computational Approaches to Energy Materials* (eds. A.Walsch, A.Sokol, C.R.A. Catlow, Wiley), 2013, p. 149-186.
[2] M. Kuklja, E. Kotomin, R. Merkle, Yu. Mastrikov, J. Maier, PCCP **15**, 5443 (2013).
[3] J. Kilner, R. Brook. Solid State Ionics, 6, 237 (1982).
[4] R. Merkle, Yu.A. Mastrikov, E.A. Kotomin, M.M. Kuklja, J. Maier. J Electrochem. Soc. **159**, B 219 (2012).
[5] Yu.A. Mastrikov, R. Merkle, E.A. Kotomin, M.M. Kuklja, J. Maier, Phys. Chem. Chem. Phys. **15,** 911 (2013).

Single Crystal Diffuse Scattering Study of Relaxor $(1\text{-}x)\text{PbMg}_{1/3}\text{Nb}_{2/3}\text{O}_3\text{-}x\text{PbTiO}_3$

Matthew Krogstad[1,2], Peter Gehring[3], Jacob Ruff[4], Feng Ye[5], Stephan Rosenkranz[2], Raymond Osborn[2], Justin Wozniak[6], Wenzhi Chen[7], Zuo-Guang Ye[7], and Daniel Phelan[2]

[1]Department of Physics, Northern Illinois University, DeKalb, IL
[2]Materials Science Division, Argonne National Laboratory, Argonne, IL
[3]NIST Center for Neutron Research, Nat'l Inst. of Standards and Technology, Gaithersburg, MD
[4]Cornell High Energy Synchotron Source, Cornell University, Ithaca, NY
[5]Spallation Neutron Source, Oak Ridge National Laboratory, Oak Ridge, TN
[6]Mathematics and Computing Sciences Division, Argonne National Laboratory, Argonne, IL
[7]Department of Chemistry and 4D LABS, Simon Fraser University, Burnaby, BC, Canada

Relaxor ferroelectrics possess intriguing electromechanical and dielectric properties which are widely regarded to be related to local, correlated atomic displacements from long-range symmetry [1]. However, the details of how short range correlations and disorder are related to relaxor behavior remain unresolved, and there remains no consensus on a real-space model for the ground state of these materials. Single crystal diffuse scattering provides a powerful probe of such deviations from an average structure correlated over varying length scales, and over the last few years, techniques and instruments for measuring diffuse scattering with both x-rays and neutrons have seen a dramatic improvement, allowing for large volumes of reciprocal space to be measured in little time. We have applied these complementary methods to solid solutions of PMN-xPT, revealing new structure to the diffuse scattering of relaxors at low temperatures.

Figure 1: Neutron diffuse scattering taken in the H-K plane for PMN-*x*PT.

a) Pure PMN

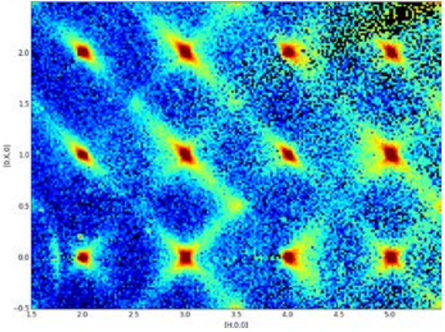

b) PMN-30PT

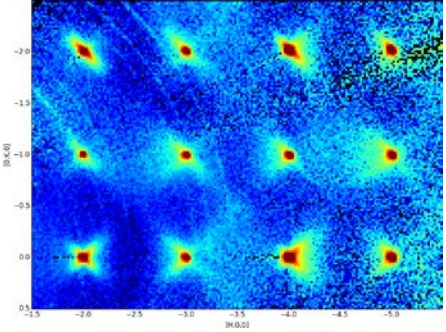

c) PMN-50PT

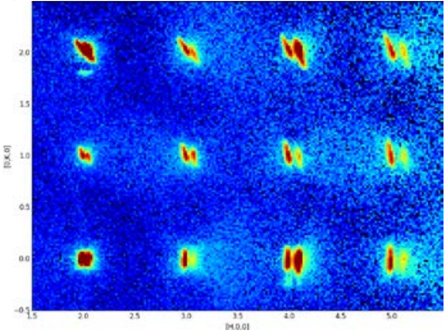

Single crystals of PMN-xPT, with x ranging from 0% to 50%, were studied at the Spallation Neutron Source using CORELLI, an instrument designed to measure elastic diffuse scattering while filtering out inelastic contributions from phonons. For samples on the Ti-poor side of the morphotropic phase boundary, although many previously observed features in the diffuse scattering around individual peaks were reproduced [2, 3, 4], an additional zone-to-zone modulation pattern was apparent, where diffuse scattering was asymmetric between the higher- and lower-*q* regions surrounding many Bragg peaks. This diffuse scattering indicates some correlation between chemical order and displacement order. Even as other diffuse scattering features vary with concentration of titanium, the parity rules governing these modulations appear to be the same for all measured samples. Other features, including diffuse peaks at the **R** and **M** points and diffuse rods in low-titanium samples as well as splitting of Bragg reflections due to tetragonal domains in high-titanium samples are also seen, offering insight into the kinds of local distortions present in these samples and how these distortions are correlated. The temperature dependence of these elastic phenomena is also investigated, with many features diminishing as the sample temperature is increased and largely disappearing above T_C.

X-ray diffuse scattering measurements on two of these samples were also taken at the Cornell High Energy Synchotron Source (CHESS). Small pieces were taken from the original crystals measured using CORELLI and etched in a hot HCl bath. Using continuous rotation in shutterless mode and a large area detector, data were collected over a range of reciprocal space similar to that taken at CHESS. While there are some major differences between the neutron and x-ray data, many features are found to be in common. Most significantly, the zone-to-zone modulation of diffuse scattering observed with neutrons for PMN-30PT is also seen with x-rays.

Acknowledgments:

Work at the Materials Science Division at Argonne National Laboratory (M.K.,S.R.,R.O.,D.P.) was supported by the US Department of Energy, Office of Science, Materials Sciences and Engineering Division. Part of the research conducted at ORNL's Spallation Neutron Source was sponsored by the Scientific User Facilities Division, Office of Basic Energy Sciences, US Department of Energy.

References:

[1] D. Phelan *et al. Proc. Nat. Acad. Sci.* **111**, 1754 (2014)
[2] A. Bosak *et al., Acta Cryst. A* **A68**, 117 (2012)
[3] G. Xu *et al., Physics Review B* **70**, 174109 (2004)
[4] G. Xu *et al., Physics Review B* **69**, 064112 (2004)

NMR study of Ti- or Fe-doped $LiNbO_3$:Mg single crystals

Ae Ran Lim,[a*] **Tae Ho Yeom**,[b] **Jin-Hae Chang**[c]
[a]*Department of Science Education, Jeonju University, Jeonju 560-759, Korea*
[b]*Department of Laser and Optical Information Engineering, Cheongju University, Cheongju 360-764, Korea*
[c]*Department of Polymer Science and Engineering, Kumoh National Institute of Technology, Gumi 730-701, Korea*

$LiNbO_3$ single crystal is a ferroelectric material, and pure $LiNbO_3$ crystals, as well as $LiNbO_3$ crystals Co-doped with Mg and other transition-metal ions, are very important for technological applications, such as acoustic wave transducers, acoustic delay lines, the optical storage of holograms, electro-optic modulation, optical rectification, second harmonic generation, Q-switches, and memory elements, because of their excellent electro-optic, nonlinear, and laser-host properties [1-3].

Here, the spin-lattice relaxation times, T_1, of the ^{7}Li and ^{93}Nb nuclei in Ti- or Fe-doped $LiNbO_3$:Mg single crystals were investigated with a Fourier transform NMR spectrometer. The effects of paramagnetic impurities (Fe^{3+} or Ti^{3+}) on the dynamics of $LiNbO_3$:Mg crystals were investigated in five single-crystal systems: pure $LiNbO_3$, $LiNbO_3$:Mg (5 mol%), $LiNbO_3$:Mg (5 mol%)/Ti (0.05 wt.%), $LiNbO_3$:Mg (5 mol%)/Fe (0.05 wt.%), and $LiNbO_3$:Mg (5 mol%)/Fe (0.05 wt.%; thermally treated at 500°C). The effects of the impurities were determined by measuring the T_1 of the ^{7}Li and ^{93}Nb nuclei. The atomic-site distributions of the $LiNbO_3$:Mg single crystals doped with Fe^{3+} or Ti^{3+} were examined based on the parameters of the ^{7}Li and ^{93}Nb nuclei.

The T_1 values of ^{7}Li nuclei in the $LiNbO_3$:Mg/Fe and $LiNbO_3$:Mg/Fe (500°C) crystals, which contained paramagnetic Fe^{3+} ions, were shorter than that in the pure $LiNbO_3$, $LiNbO_3$:Mg, and $LiNbO_3$:Mg/Ti crystals (Fig. 1). The T_1 values of the $LiNbO_3$:Mg/Fe and $LiNbO_3$:Mg/Fe (500°C) crystals are shorter than that of the pure $LiNbO_3$ and $LiNbO_3$:Mg crystals because of the presence of paramagnetic ions. In addition, the T_1 values of the ^{7}Li and ^{93}Nb nuclei in the $LiNbO_3$:Mg/Fe (500°C) crystal are longer than those in the $LiNbO_3$:Mg/Fe crystal because the thermally treated $LiNbO_3$:Mg/Fe (500°C) crystal has more O vacancies than the $LiNbO_3$:Mg/Fe crystal.

The T_1 values of the ^{7}Li nuclei in the $LiNbO_3$:Mg/Fe crystal decrease with increasing temperature, whereas that in the $LiNbO_3$:Mg/Fe (500°C) crystal increase with increasing temperature. The results of the $LiNbO_3$:Mg/Fe (500°C) crystal are very abnormal when considering the lattice vibrations as a function of the temperature. According to the literature [3-7], Fe^{3+} ions can enter the Li^+ and/or Nb^{5+} sites depending on the crystal-growth conditions. The abnormality of the T_1 values in the $LiNbO_3$:Mg/Fe (500°C) crystal may be caused by the migration of Fe^{3+} ions during the thermal treatment. As the temperature increases, the Nb ions move in the direction of the center of inversion to occupy positions

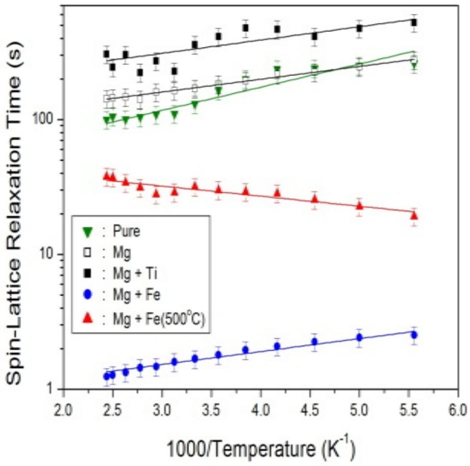

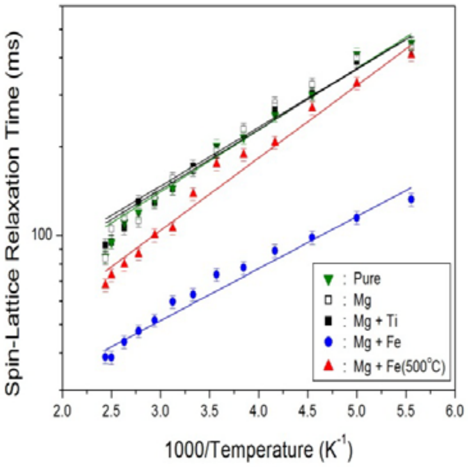

Fig. 1. T_1 for ^{7}Li nuclei in several $LiNbO_3$ crystals as a function of inverse temperature.
Fig. 2. T_1 for ^{93}Nb nuclei in several $LiNbO_3$ crystals as a function of inverse temperature.

between the O layers. On the other hand, the Li ions move away from the center of inversion to occupy positions in the same planes as the O layers. Fig. 2 shows that the relaxation times of the ^{93}Nb nuclei decrease with increasing temperature for all of the single-crystal systems. It is reasonable believe that the lattice vibrations of all of the nuclei in the host materials become active when the crystal temperature increases. That is, the relaxation times of the ^{93}Nb nuclei decrease as the temperature increases because of the quadrupole relaxation induced by the thermally activated phonons. The difference between the relaxation times for the ^{7}Li nuclei in the pure $LiNbO_3$ and $LiNbO_3$:Mg/Fe crystals is approximately two orders of magnitude, whereas that for the ^{93}Nb nuclei is approximately one order of magnitude. From the results of the present study, the Fe ions in the $LiNbO_3$:Mg, $LiNbO_3$:Mg/Ti, $LiNbO_3$:Mg/Fe crystals replace the Li sites of the pure $LiNbO_3$ crystal structure.

References

[1] A. Räuber, in Current Topics in Material Science, Edited by E. Kaldis, Vol. 1, North-Holland, Amsterdam, 1987, pp 481-601.
[2] F. Agulló-López, J.M. Cabrera, Properties of Lithium Niobate, EMIS Data Reviews Series No. 5, INSPEC, London, 1989, pp 8-17.
[3] R.S. Weis, T.K. Gaylord, Appl. Phys. A37 (1985) 191.
[4] C.R.A. Catlow, A.V. Chadwick, M. Cole, S.M. Tomlinson, Radiat. Eff. Defects Solids 119 (1991) 565.
[5] C. Prieto, C. Zaldo, Solid State Commun. 83 (1992) 819.
[6] H. Söthe, J.M. Spaeth, J. Phys.: Condens. Matter 4 (1992) 9901.
[7] M.D. Glinchuk, G.I. Malovichko, I.P. Bykov, V.G. Grachev, Ferroelectrics 92 (1989) 477.

Preferred: poster

Chemical phase-separation in ferroelectric layered transition metal thiophosphates

Michael A. Susner[1], Alex Belianinov[2], Marius Chyasnavichus[2], Albina Y. Borisevich[1], Qian He[1], Panchapakesan Ganesh[2], Hakan Demir[4], David S. Sholl[4], Douglas L. Abernathy[3], Michael A. McGuire[1], and Petro Maksymovych[2]

Transition metal thio- and selenophosphates comprise a honeycomb sub-lattice of metal ions immersed into a cage of thiophosphate $(P_2S_6)^{4-}$ or selenophosphate $(P_2Se_6)^{4-}$ ions[1]. Owing to strongly ionic bonding, the electronic band-gaps are fairly large, from 2 to 3.5 eV. Furthermore, a small subset of the known ionic compositions, mostly involving Cu^{+1} ions, is known to have ferroelectric, antiferroelectric and mutliferroic ground states.[2,3] Such properties are rarely found among covalently bonded layered chalcogenides, such as MoS_2. The details of ferroelectric ordering in thiophosphates are not well understood at present. Among approximately 230 known compositions of thiophosphates, only one material – $CuInP_2S_6$ [4]- has a Curie temperature slightly above room temperature. So far, the attempts to increase this value by chemical substitution (e.g. Se for S) have always led to suppression of the ordering temperature.

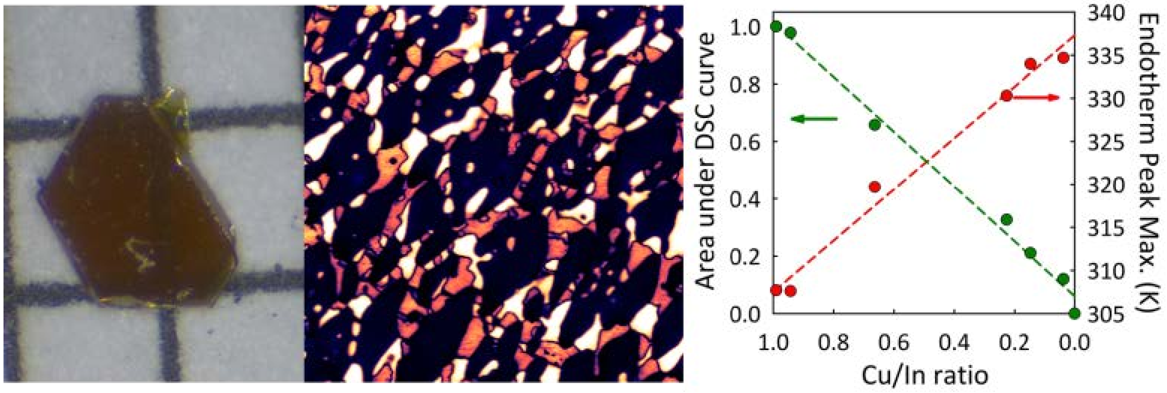

Figure 1. Left – a typical single crystal of Cu-deficient copper-indium thiophosphate, with a general stoichiometry of Cu_xIn_yP2S6. Middle – PFM image (amplitude) showing non-piezoelectric inclusions of In4/3P2S6 (black) coexisting with ferroelectric CuInP2S6 (white/brown) within each layer of a layered crystal. White and brown colors correspond to up and down polarized domains, separated by domain walls. Right: ferroelectric Tc as a function of average Cu/In ratio. The maximum Tc is achieved in a crystal with the lowest volume fraction of the ferroelectric CuIn phase.

Motivated by finite ionic conductivity in these materials, we have investigated them experimentally and theoretically from the perspective of solid solutions.[5] In particular, depleting $CuInP_2S_6$ of electroactive Cu^{+1} ions creates a unique layered structure – which has all the signatures of coherent spinodal decomposition into stoichiometric $CuInP_2S_6$ and $In_2P_3S_9$ phases. When probed on the nanoscale, the materials reveal a rich and self-organized texture of ferroelectric and non-ferroelectric domains (Fig. 1 middle) with nearly nanoscale-sharp boundaries. Spinodal decomposition occurs without any significant perturbation of the basic layered structure – producing cleavable and air-stable surfaces and quasi-2D sheets. Perhaps most strikingly, we found that chemical phase-separation *increases* the Curie temperature for ferroelectric ordering by up to 40K (Fig. 1 right) – which we surmise to be the chemical pressure effect. From the analysis of the pressure-dependent T_c,[6] we also inferred about 10-fold larger entropy of the ferroelectric phase transition in $CuInP_2S_6$, compared to $BaTiO_3$, most likely due to combined effect of the layered structure and the order-disorder type of the phase transition. This large entropy allows Tc to be meaningfully tuned by alloying. The rich dielectric functionality offered by this underexplored class of compounds may give rise to unique layered and 2D materials, as well as new physics at van-der-Waals interfaces to known families of 2D compounds.

This research was sponsored by the Laboratory Directed Research and Development fund at the Oak Ridge National Laboratory. Probe microscopy was carried out at the Center for Nanophase Materials Sciences, sponsored at the Oak Ridge National Laboratory by the Division of User Facilities, Basic Energy Sciences, US Department of Energy.

1. Evain, M., Brec, R. & Whangbo, M.-H. Structural and electronic properties of transition metal thiophosphates. *J. Solid State Chem.* **71,** 244–262 (1987).
2. Simon, A., Ravez, J., Maisonneuve, V., Payen, C. & Cajipe, V. B. Paraelectric-Ferroelectric Transition in the Lamellar Thiophosphate $CuInP_2S_6$. *Chem. Mater.* **6,** 1575–1580 (1994).
3. Macutkevic, J., Banys, J., Grigalaitis, R. & Vysochanskii, Y. Asymmetric phase diagram of mixed $CuInP_2(S/Se)_6$ crystals. *Phys. Rev. B* **78,** 064101 (2008).
4. Belianinov, A. *et al.* $CuInP_2S_6$ Room Temperature Layered Ferroelectric. *Nano Lett.* **15,** 3808–3814 (2015).
5. Susner, M. A. *et al.* High-Tc Layered Ferrielectric Crystals by Coherent Spinodal Decomposition. *ACS Nano* (2015). doi:10.1021/acsnano.5b05682
6. Grzechnik, A., Cajipe, V. B., Payen, C. & McMillan, P. F. Pressure-induced phase transition in ferrielectric $CuInP_2S_6$. *Solid State Commun.* **108,** 43–47 (1998).

First-Principles Calculations of Rare Earth Iron Garnets

Ryan Nakamoto[1], Bin Xu[1], Laurent Bellaiche[1]

[1]Physics Department and Institute for Nanoscience and Engineering, University of Arkansas, Fayetteville, Arkansas 72701, USA

Rare earth iron garnets encapsulate an array of ferrimagnetic materials, with a composition of $R_3Fe_5O_{12}$ where R is an element in the lanthanide series or Yttrium. The physical properties of rare earth iron garnets have been studied experimentally, however due to the large size of the unit cell (160 atoms, space group Ia3d) its first principles calculations are computationally expensive [1]. These calculations may serve as reference point and/or provide a microscopic insight into these complex systems.

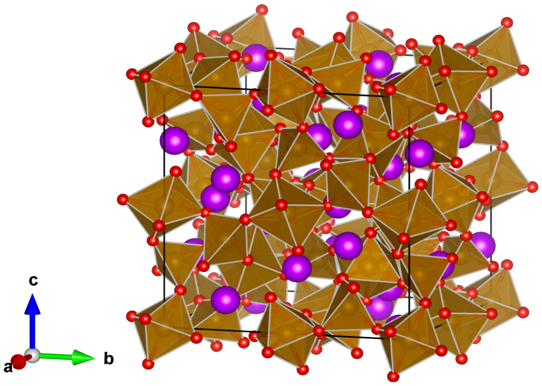

Figure 1, Unit cell of rare earth iron garnet

The magnetic moment of the rare earth is antiparallel with the total magnetic moment of the octahedral and tetrahedral iron elements as shown in Figure 2. The ordering temperature of the rare earth causes the moment of the garnet to invert as it approaches room temperature as its contribution to the overall magnetic moment decreases as shown in Figure 3. In addition, its Faraday rotation is known to be dependent on its magnetic moment allowing it to be used in a variety of uses in magneto-optical, microwave, acoustic, and optical applications [2].

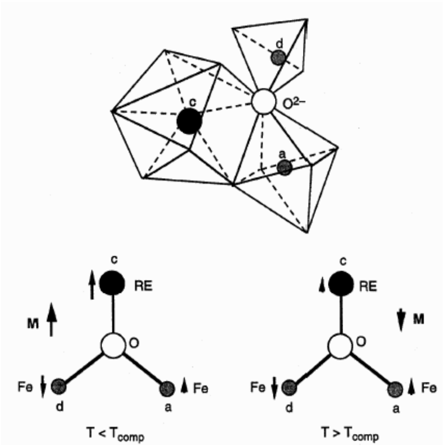

Figure 2, Structure of rare earth iron garnet with magnetic moment [3]

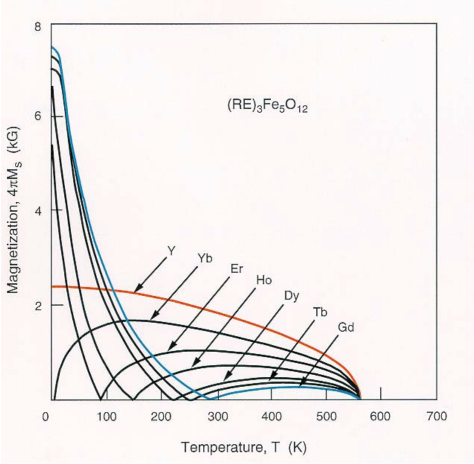

Figure 3, Absolute value of the magnetic moment of rare earth elements [3]

Some work has already been done on select iron garnets, e.g. YIG [4]. Here, we computed the lattice constants, magnetic moments, and density of states of several of the rare earth iron garnets, by using the Vienna Ab-initio Simulation Package [5]. Calculations were done by using pseudopotentials without and with f-electrons to understand the effect of these localized electrons on structural and magnetic properties of garnets.

The first principles calculations of the lattice constants with and without f-electrons are both found to be within 2% of experimental results by Espinosa [6], with the calculation for $Gd_3Fe_5O_{12}$ even coming in below 1% error of the experimental results by Geller [7].

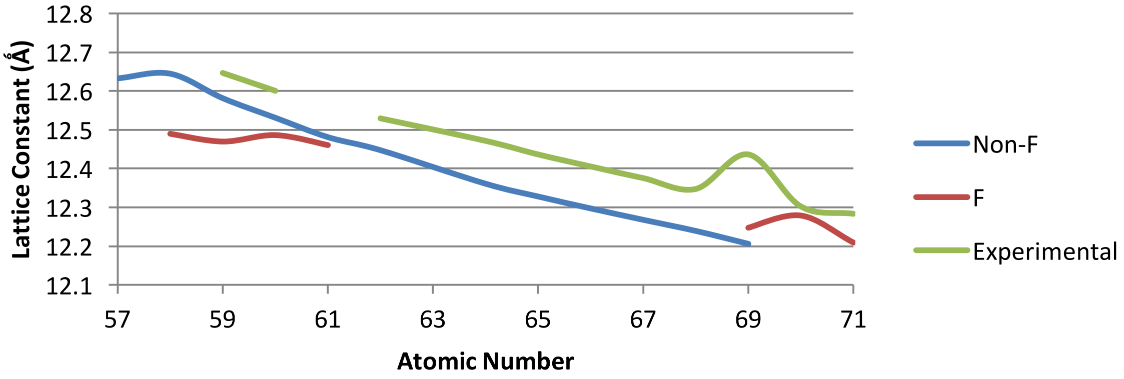

Figure 4, First principles lattice constants of rare earth iron garnets vs measured lattice constants.

If time allows, first principles calculations on electronic band structure, phonons, and spin orbit coupling will also be reported.

Acknowledgements This work is financially supported by the Arkansas Department of Higher Education through the SURF grant (R.N.). B.X. thanks the Department of Energy, Office of Basic Energy Sciences, under contract ER-46612 and L.B. acknowledges NSF grant DMR-1066158.

References

[1] S. Geller and M.A. Gilleo, Acta Crytallographica 239 (1957)

[2] W. A. Crossley, R. W. Cooper, J. L. Page, and R. P. van Stapele, J. Appl. Phys. Journal Of Applied Physics 1497 (1969).

[3] M. Viret, International School Of Oxide Electronics 2015 (2015).

[4] Y.-N. Xu, Z.-Q. Gu, and W. Y. Ching, J. Appl. Phys. Journal Of Applied Physics 4867 (2000).

[5] J. Hafner and G. Kresse, Properties Of Complex Inorganic Solids 69 (n.d.).

[6] G. P. Espinosa, The Journal Of Chemical Physics J. Chem. Phys. 2344 (1962).

[7] S. Geller, J. P. Remeika, R. C. Sherwood, H. J. Williams, and G. P. Espinosa, Phys. Rev. Physical Review (1965).

Heterophase Polydomain Nanostructure in Epitaxial Ferroelectric Films

Alexander Roytburd,[1,2] Jun Ouyang[1,2,3]

[1.] Materials Measurement Lab, National Institute of Standards and Technology, Gaithersburg, MD, 20899

[2.] Dept. of Materials Science and Engineering, University of Maryland, College Park, MD, 20740, USA

[3.] Key Laboratory for Liquid–Solid Structural Evolution and Processing of Materials, Dept. of Materials Science and Engineering, Shandong University, Jinan, Shandong 250061, China

Starting with [1], temperature-misfit diagrams have become important tools for investigation, design and engineering of ferroelectric and ferroelastic films in different phase states. Most of existing theoretical works do not consider possibility of formation of heterophase state. Therefore, they are correct only for very thin films where the effect of interface energies between phases forbids the formation of multi-phase structures. However, this effect becomes relatively small if the film is thicker than ~100nm where its elastic interaction with the substrate drives formation of heterophase structures. These structures can contain co-existing stable and metastable phases with the latter being stabilized by an epitaxial constraint. We present theoretical analysis and experimental results on the engineering of polydomain heterophase nanostructures in epitaxial films. These structures can demonstrate substantial extrinsic responses to external electrical and mechanical forces due to the evolution of domains under the field.

References:

[1] N. A. Pertsev, A. G. Zembilgotov, and A. K. Tagantsev, "Effect of Mechanical Boundary Conditions on Phase Diagrams of Epitaxial Ferroelectric Thin Films", *Phys. Rev. Lett.*, **80**(9), 1998.
[2] A. L. Roytburd, Jun Ouyang, Brad M. Boyerinas, Hugh A. Bruck, "Stability of Heterophase Nanostructure and Field Induced Response of Epitaxial Ferroelectric Films", *Appl. Phys. Lett.*, **99**, 172902, 2011.
[3] J. Ouyang, W. Zhang, X. Huang, A. Roytburd, "Thermodynamics of formation of tetragonal and rhombohedral heterophase polydomains in epitaxial ferroelectric thin films", *Acta Mater.*, **59**, 3779, 2011.

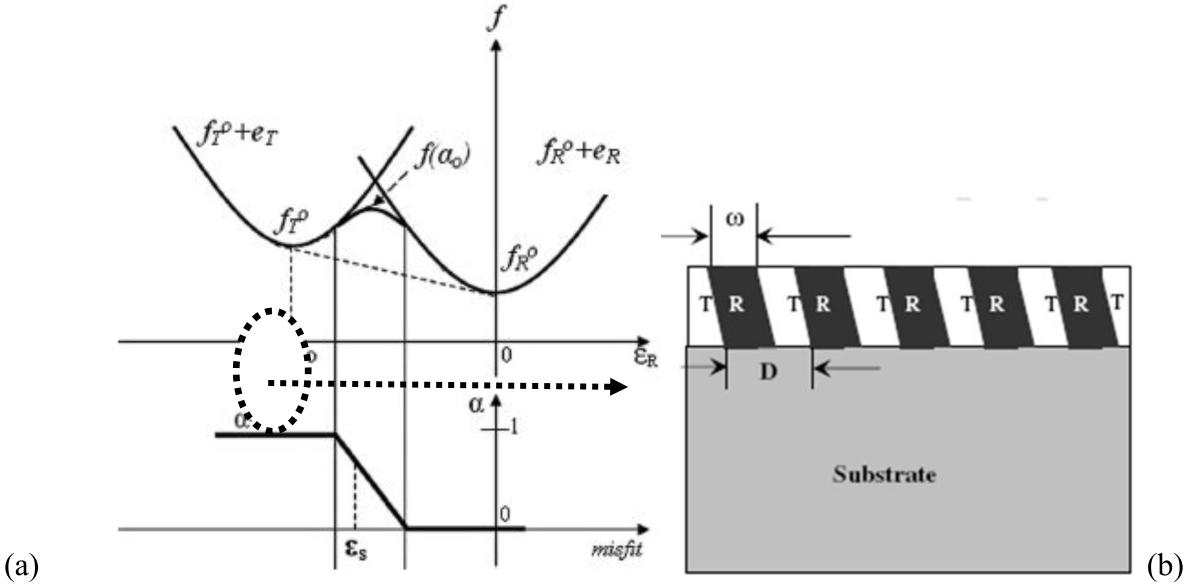

Fig. 1. (a) Free energies of the single phases and heterophase consisting with one tetragonal –T phase and one rhombohedral –R phase, as a function of substrate misfit in an epitaxial film and dependence of domain fraction on misfit (adapted from Ref 2); (b) schematic of the heterophase structure in the epitaxial film (adapted from Ref 3).

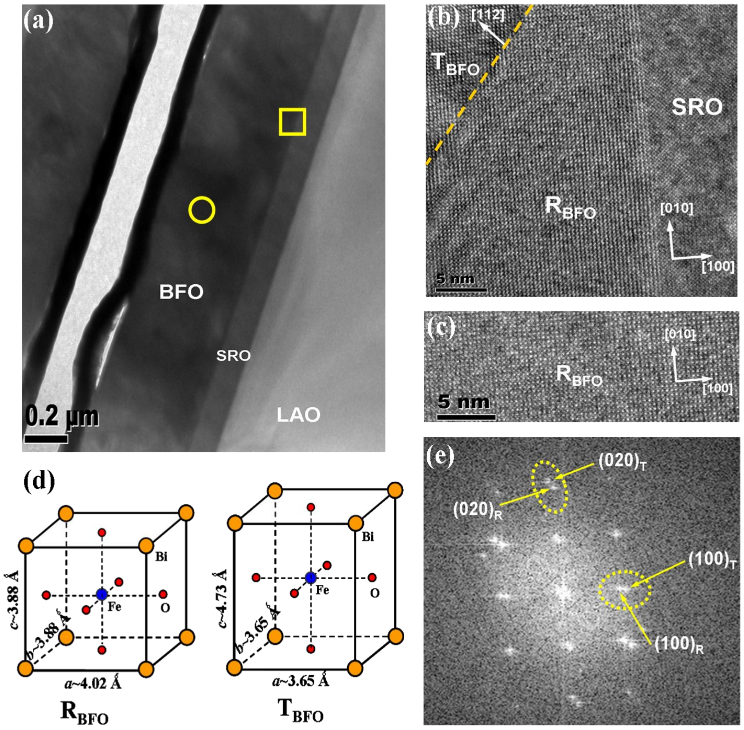

Figure 2. (a) Cross-sectional TEM image of a BFO/SRO/LAO heterostructure. (b) High-resolution TEM image of the BFO/SRO interface corresponding to the region marked by a yellow box in (a), the nanoscale domain interface between the R and T phases in the BFO film is denoted by an orange dashed line. (c) High-resolution TEM image of the BFO film bulk corresponding to the region marked by a yellow circle in (a). (d) Schematic illustration of the R_{BFO} and T_{BFO} unit cells, and (e) Fast Fourier Transformed (FFT) electron diffraction pattern of the two-phase region. (Jun Ouyang et al., unpublished results)

Photostriction in $BiFeO_3$ from first-principles

Charles Paillard[1,2], Bin Xu[2,3], Brahim Dkhil[1], Gregory Geneste[4] & L. Bellaiche[2,3]
[1] Laboratoire SPMS, CentraleSupélec/CNRS, Grande Voie des Vignes, 92 295 Châtenay-Malabry, France
[2] Physics Department, University of Arkansas, Fayetteville, Arkansas 72701, USA
[3] Institute for Nanoscience and Engineering, University of Arkansas, Fayetteville, Arkansas 72701, USA
[4] CEA, DAM, DIF, F-91297 Arpajon, France

E-mail adress : charles.paillard@centralesupelec.fr

Since 2009, the investigation of the coupling of multiferroic materials with light has experienced a renewed interest, as above-bandgap photovoltages were found to occur in BiFeO3 thin films[1]. The so-called Bulk Photovoltaic Effect (BPVE)[2,3], occurring in any material lacking inversion symmetry, has therefore attracted interest for the design of new efficient and cheap solar cells. Therefore, the lack of inversion symmetry of ferroelectrics makes them natural candidates to the design of tnew kinds of solar cells, and also provides them with interesting piezoelectric properties. The lack of inversion symmetry of ferroelectrics is also fundamental to their so-called piezoelectric properties, i.e. the coupling of their electric polarization to strain. Therefore, ferroelectrics offer a natural route towards the realization of light-induced actuators among the so-called class of photostrictive materials[4]. Experimental evidences towards this goal have appeared in the last five years, with intense studies of the so-called photostriction in bismuth ferrite[5,6]. Besides this steady state response of ferroelectrics to excitation by light, a giant shear strain induced by femtoseconds laser pulses has been detected in bismuth ferrite, and attributed to the conjunction of the BPVE and the piezoelectric effect in BFO[7,8]. In addition, time-resolved synchrotron diffraction showed that shifting of Bragg peaks on a picosecond time scale occurs in both bismuth ferrite[9] and a more conventional ferroelectric, lead titanate[10].
However, until now, theory has not investigated the coupling of light with the electromechanical properties of ferroelectrics on a microscopic scale. To tackle this problem, we employ a Δ-SCF scheme[11] in which the occupation numbers of the Kohn-Sham orbitals are constrained. According to our results, BFO should shrink along its pseudo-cubic and the polarization axes, with the pseudo-cubic angle getting closer to 90°. On the other hand, the directions perpendicular to the polarization, such as $[1\text{-}10]_{pc}$ stretches under excitation of electrons in the conduction band. Looking at the character of the states of the conduction band, which are mainly 3*d*-states from iron, we interpret the photostriction as the result of the screening of the polarization by excited electrons localized on iron ions.

This work is mostly supported by the Department of Energy, Office of Basic Energy Sciences, under contract ER-46612. L.B. also thanks the support from the Air Force Office of Scientific Research Under Grant FA9550-16-1-0065. C. P. thanks acknowledges support from a public grant overseen by the French National Research Agency (ANR) as part of the “Investissements d’Avenir” program (reference: ANR-10-LABX-0035, Labex NanoSaclay).

References

[1] S. Y. Yang, J. Seidel, S. J. Byrnes, P. Shafer, C.-H. Yang, M. D. Rossell, P. Yu, Y.-H. Chu, J. F. Scott, J. W. Ager, L. W. Martin, and R. Ramesh, *Nature Nanotechnology* **5**, 143 (2010).
[2] B. I. Sturman and V. M. Fridkin, *The Photovoltaic and Photorefractive Effects in Noncentrosymmetric Materials*, Gordon and Breach Science Publishers (1992).
[3] V. M. Fridkin, *Crystallography Reports* **46**, 654 (2001).

[4] B. Kundys, *Applied Physics Review* **2**, 011301 (2015).
[5] B. Kundys, M. Viret, D. Colson, and D. O. Kundys, *Nature Materials* **9**, 803 (2010).
[6] B. Kundys, M. Viret, C. Meny, V. Da Costa, D. Colson, and B. Doudin, *Physical Review B* **85**, 092301 (2012).
[7] P. Ruello, T. Pezeril, S. Avanesyan, G. Vaudel, V. Gusev, I. C. Infante, and B. Dkhil, *Applied Physics Letters* **100**, 212906 (2012).
[8] M. Lejman, G. Vaudel, I. C. Infante, P. Gemeiner, V. E. Gusev, B. Dkhil, and P. Ruello, *Nature Communications* **5**, 4301 (2014).
[9] D. Schick, M. Herzog, H. Wen, P. Chen, C. Adamo, P. Gaal, D. G. Schlom, P. G. Evans, Y. Li, and M. Bargheer, *Physical Review Letters* **112**, 097602 (2014).
[10] D. Daranciang, M. J. Highland, H. Wen, S. M. Young, N. C. Brandt, H. Y. Hwang, M. Vattilana, M. Nicoul, F. Quirin, J. Goodfellow, T. Qi, I. Grinberg, D. M. Fritz, M. Cammarata, D. Zhu, H. T. Lemke, D. Walko, E. M. Dufresne, Y. Li, J. Larsson, D. A. Reis, K. Sokolowski-Tinten, K. A. Nelson, A. M. Rappe, P. H. Fuoss, G. B. Stephenson, and A. M. Lindenberg, *Physical Review Letters* **108**, 087601 (2012).
[11] R. M. Martin, *Electronic Structure: Basic Theory and Practical Methods*, Cambridge University Press (2008).

Charge-order-induced ferroelectricity in $LaVO_3/SrVO_3$ superlattices

Se Young Park,[1] Anil Kumar,[2] and Karin M. Rabe[1]

[1]*Department of Physics & Astronomy, Rutgers University, Piscataway, NJ, USA*
[2]*Materials Science and Technology Division,*
Los Alamos National Laboratory, Los Alamos, NM, USA

Ferroelectric polarization induced by charge order has been reported in transition-metal compounds in which the symmetry breaking by charge order is crucial to the ferroelectricity[1]. However in many cubic perovskite transition metal oxides, the charge-ordered ferroelectricity is prohibited by high point group symmetry. Forming superlattices composed of two (or more) transition metal oxides is an effective way to induce the ferroelectricity by charge order since the superlattice lowers the point-group symmetry and allows to control the *d*-orbital occupancy to have a fractional value, leading to charge ordered phases[2]. If the charge ordering breaks the symmetry prohibiting the ferroelectricity, the ferroelectric polarization will emerge with the formation of the charge order.

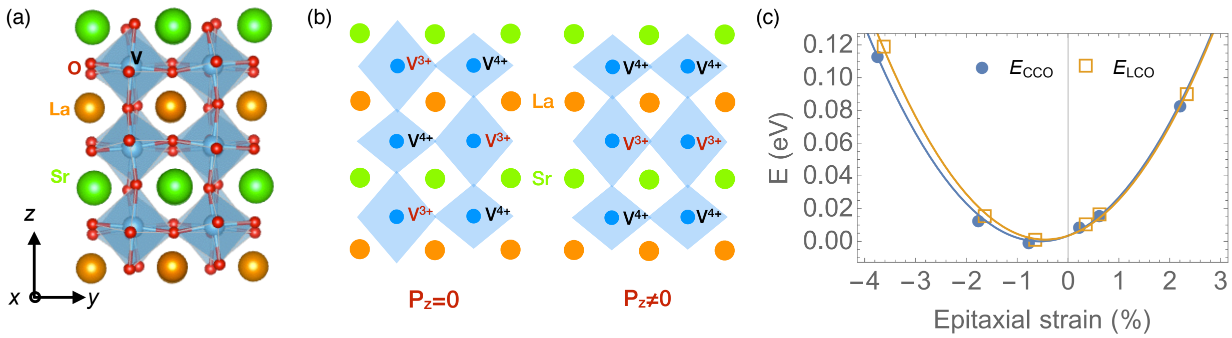

FIG. 1. (a) Atomic structure of $(LaVO_3)_1/(SrVO_3)_1$ superlattice. (b) Schematics of two charge order patterns. Left: checkerboard-type charge order where all the nearest neighbors of V^{4+} cation are in V^{3+} and vice versa. Right: layered charge order where the valence of V cations are uniform within the xy plane and have alternating valence configuration of V^{4+} and V^{3+} along the z-direction. (c) Total energy in CCO (blue circle) and LCO (brown square) phases as a function of the epitaxial strain relative to the bulk $LaVO_3$ lattice constant.

The 1:1 superlattice composed of $LaVO_3$ and $SrVO_3$ is investigated as a candidate material for the charge-order-induced ferroelectricity using density functional theory plus U (DFT+U) method. The atomic structure of the superlattice is presented in Fig. 1 (a). The low temperature phase of orthorhombic $LaVO_3$ and cubic $SrVO_3$ are antiferromagnetic Mott-insulating and correlated metallic phase, respectively[2–4]. When they form the 1:1 superlattice, the average valence of the Vanadium has a fractional value of $\mathrm{V}^{3.5+}$. Due to the strong on-site Coulomb interaction, the Mott-insulating state with charge, orbital, and magnetic order would be preferred where the half of the Vanadium cations have the nominal valence of V^{3+} and the other half of V^{4+}. We investigate low-energy charge-ordered phases and identify the ferroelectric phase driven by charge ordering.

We calculate the low-energy phases of the superlattice using GGA+U method (U= 4 eV, J= 0.6 eV) and find the Mott-insulating antiferromagnetic phases with two distinct charge ordering patterns as illustrated in Fig. 1 (b). Both checkerboard charge-order (CCO) and layered charge-order (LCO) phases have a ferroelectric polarization in the xy plane due to the octahedral rotation and tilt[5]. In contrast, we find that the out-of-plane polarization is non-zero in the LCO phase, whereas the corresponding polarization for the CCO phase vanishes by symmetry, showing charge-ordered-induced ferroelectricity in the LCO phase. The out-of-plane polarization calculated by the Berry phase method[6] is 32 $\mu\mathrm{C/cm}^2$ where we have identified a possible switching path on which the system remains insulating. When the structures are fully relaxed, the energy of this polar (LCO) state relative to the lower-energy nonpolar (CCO) state is found to be only 3 meV/5 atom unit cell. The epitaxial strain dependence of the energy difference between the two phases is calculated as in Fig. 1 (c) and we find that the energy difference can be reduced to zero by tensile strain. This suggests that the polar state could be induced by applied electric field, and, depending on the switching process, a ferroelectric hysteresis loop could be observed.

[1] J. van den Brink and D. I. Khomskii, Journal of Physics: Condensed Matter **20**, 434217 (2008).

[2] M. Imada, A. Fujimori, and Y. Tokura, Reviews of Modern Physics **70**, 1039 (1998).

[3] P. Bordet, C. Chaillout, M. Marezio, Q. Huang, A. Santoro, S.-W. Cheong, H. Takagi, C. Oglesby, and B. Batlogg, Journal of Solid State Chemistry **106**, 253 (1993).

[4] T. Yoshida, K. Tanaka, H. Yagi, A. Ino, H. Eisaki, A. Fujimori, and Z.-X. Shen, Phys. Rev. Lett. **95**, 146404 (2005).

[5] N. A. Benedek, A. T. Mulder, and C. J. Fennie, Journal of Solid State Chemistry **195**, 11 (2012).

[6] R. D. King-Smith and D. Vanderbilt, Phys. Rev. B **47**, 1651 (1993).

Abstract –ferro 2016

Universal energetic coupling in complex antiferroelectric and incommensurate perovskites

Kinnary Patel[1], Sergey Prosandeev[1,2], Yurong Yang[1], Bin Xu[1], Jorge Íñiguez[3], and L. Bellaiche[1]

[1]Physics Department and Institute for Nanoscience and Engineering, University of Arkansas, Fayetteville, Arkansas 72701, USA

[2]Institute of Physics and Physics Department of Southern
Federal University, Rostov-na-Donu 344090, Russia

[3]Materials Research and Technology Department, Luxembourg Institute of Science and Technology (LIST), 5 avenue des Hauts-Fourneaux, L-4362 Esch/Alzette, Luxembourg

Antiferroelectrics form a class of important materials that are currently receiving a lot of attention, mainly because they are promising candidates for delivering high-energy storage density[1-5]. They are also fundamentally interesting, as, e.g., demonstrated by the recent activities aimed at understanding the unusual ground state of the prototype of antiferroelectrics, that is $PbZrO_3$ (PZO) [6-12]. Such ground state is of *Pbam* symmetry, and possesses three significant phonon modes. One of these modes is denoted as R^+_4 and is rather simple, in the sense that it corresponds to typical antiphase oxygen tilting. The other two modes are much more complex, as evidenced by their atypical pattern of lead and oxygen displacements shown in Fig. 1. They are the so-called Σ_2 and S_4 modes. Some recent works suggested that the formation of *Pbam* as the ground state of PZO originates from a trilinear energy that couples R^+_4, Σ_2 and S_4 [6-8]. However, this trilinear energy only amounts to 27 meV out of the 392 meV gain of the *Pbam* state with respect to the cubic paraelectric phase, according to first-principles calculations[6], and does not explain why the unusual Σ_2 and S_4 modes are strongly unstable by themselves in PZO[6]. One may therefore wonder if another energy plays a crucial role in PZO, and what is the analytical form of such energy in terms of elemental interatomic couplings (if any).

It is also legitimate to determine if such hypothetical energy can further describe other complex antipolar states that many materials are known to exhibit and may also be of relevance to the formation of incommensurate phases in perovskites.

Here, we report the discovery of a novel atomistic energy that bi-linearly couples the A-cation displacements and oxygen octahedral tilting in ABO_3 perovskites. Analytical derivations starting from this atomistic energy result in macroscopic energies that not only explain why the Σ_2 and S_4 antipolar modes of PZO are unstable but also yield the unusual atomic patterns of these modes. This atomistic energy is further demonstrated to (i) be applicable to k-points that are neither at the zone-center nor at the zone-borders of the cubic first Brillouin zone; (ii) describe other complex antipolar states and other antiferroelectrics; and (iii) can also explain why some perovskites adopt incommensurate structures.

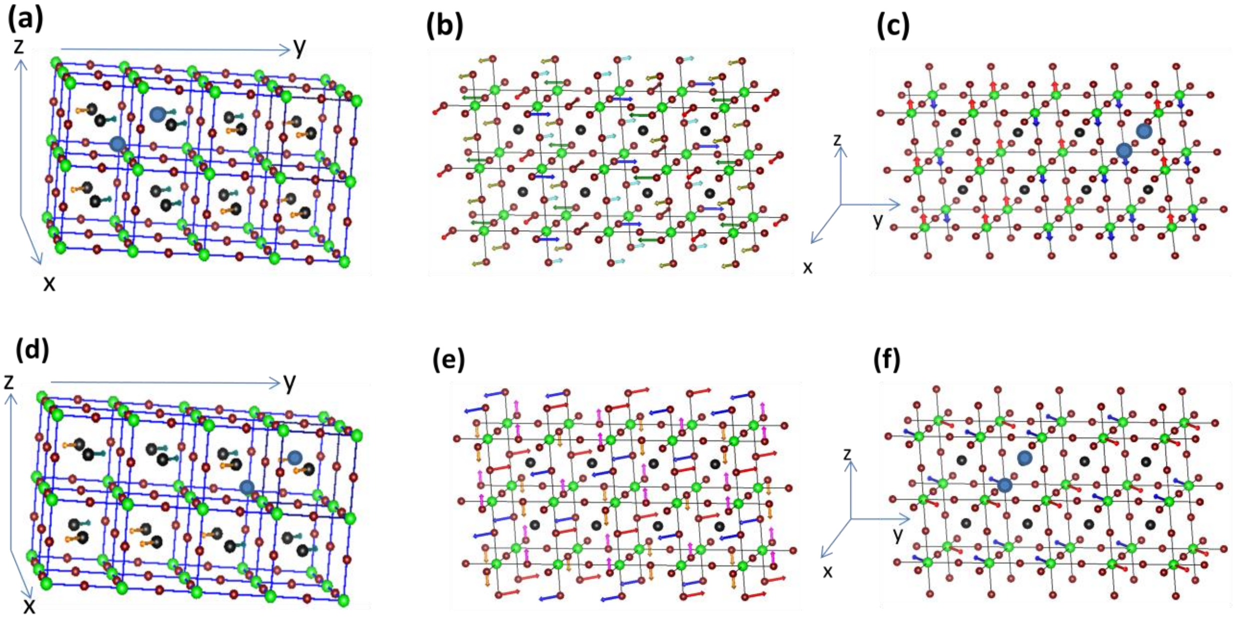

Figure 1: Panel (a) shows the pattern of Pb displacements in the Σ_2 mode of the Pbam ground state of $PbZrO_3$. Panel (b) displays the oxygen motions associated with the tilting of the oxygen octahedral in this Σ_2 mode, and Panel (c) depicts the resulting pattern of the ω_i pseudo-vector (representing oxygen octahedral tilting) in this Σ_2 mode. Panels (d), (e), and (f) show similar information but for the S_4 mode.

Acknowledgments. This work is supported by the ARO Grant W911NF-12-1-0085 (K.P. and L.B.), the ONR Grant N00014-12-1-1034 (S.P., Y.Y. and L.B.), FNR Luxembourg Grants FNR/P12/4853155/Kreisel (J.I.), INTER/MOBILITY/15/9890527 GREENOX (L.B. and J.I.), and MINECO-Spain Grant MAT2013-40581-P (J.I.).

References

1. X. Hao, J. Adv. Dielectr. 3, 1330001 (2013).

2. B. Ma, D.-K. Kwon, M. Narayanan and U. Balachandran, J. Mater. Res. 24, 2993 (2009).

3. B. Ma, M. Narayanan and U. Balachandran, Mater. Lett. 63, 1353 (2009).

4. X. Hao, Y. Wang, L. Zhang, L. Zhang and S. An, Appl. Phys. Lett. 102, 163903 (2013).

5. B. Peng, Q. Zhang, X. Li, T. Sun, H. Fan, S. Ke, M. Ye, Y. Wang, W. Lu, H. Niu, J. F. Scott, X. Zeng and H. Huang, Adv. Electron. Mater. (2015); DOI: 10.1002/aelm.201500052.

6, J. Íñiguez, Massimiliano Stengel, Sergey Prosandeev and L. Bellaiche, Phys. Rev. B 90, 220103(R) (2014).

7. S. Prosandeev, Changsong Xu, R. Faye, Wenhui Duan, H. Liu, B. Dkhil, P.-E Janolin, J. Íñiguez and L. Bellaiche, Phys. Rev. B 89, 214111 (2014).

8. J. Hlinka, T. Ostapchuk, E. Buixaderas, C. Kadlec, P. Kuzel, I. Gregora, J. Kroupa, M. Savinov, A. Klic, J. Drahokoupil, I. Etxebarria, and J. Dec, Phys. Rev. Lett. 112, 197601 (2014).

9. E. Cockayne and K. M. Rabe, J. Phys. Chem. Solids 61, 305 (2000).

10. A.K.Tagantsev, K.Vaideeswaran, S.B.Vakhrushev, A.V.Filimonov, R.G.Burkovsky, A.Shaganov, D. Andronikova, A. I. Rudskoy, A. Q. R. Baron, H. Uchiyama, D. Chernyshov, A. Bosak, Z. Ujma, K. Roleder, A. Majchrowski, J.-H. Ko and N. Setter, Nature Communications 4, 2229 (2013).

11. J.-H. Ko, M. Gorny, A. Majchrowski, K. Roleder, and A. Bussmann-Holder, Phys. Rev. B 87, 184110 (2013).

12. B. K. Mani, S. Lisenkov, and I. Ponomareva, Phys. Rev. B 91, 134112 (2015).

Symmetry vs topology and dipolar fluctuations in proper ferroelectrics

S. Prokhorenko,[1, 2, *] Y. Nahas,[1] and L. Bellaiche[1]
[1] *Physics Department and Institute for Nanoscience and Engineering,*
University of Arkansas, Fayetteville, Arkansas 72701, USA
[2] *Physique Théorique des Matériaux, Université de Liège, B-4000 Sart Tilman, Belgium*

Strong crystalline *anisotropy* is one of the signature features of proper ferroelectrics. It forces local electric dipoles to orient along specific lattice directions and therefore limits the underlying rotational symmetries to a finite set of point group operations. In turn, such symmetry reduction has a significant impact on the physics of ferroelectric phase transitions, drawing a line between proper ferroelectrics and systems described by underlying continuous symmetries.

However this borderline, being sharp at a first glance, smears out under careful investigation. For instance, spin-orbit coupling in "real-life" magnetic systems gives rise to antisymmetric superexchange and magnetocrystalline anisotropy that, albeit weak, break continuous rotational symmetry. Improper ferroelectrics stand as another example, where continuous symmetry can only be seen as "*approximate*". Nonetheless, both magnetic materials and improper ferroelectrics carry an imprint of an *exact* continuous symmetry. Namely, both can exhibit non-trivial linear or point topological defects. This raises an interesting question of when the symmetry can be considered "continuous enough" so as to allow existence of such defects. Moreover, if the continuous symmetry is not a necessary condition, can proper ferroelectrics exhibit such defects? If so, what would be the mechanism of topological protection?

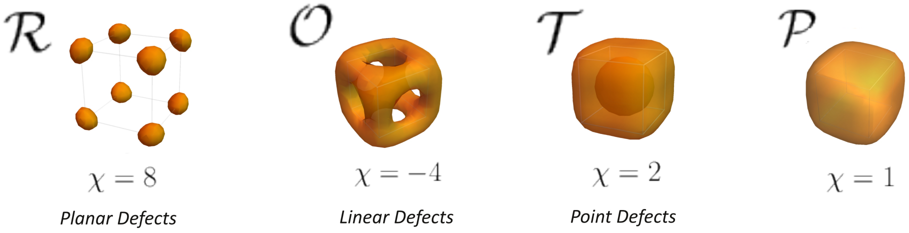

FIG. 1: Internal space manifolds for paraelectric ($\mathcal{P}$), tetragonal ($\mathcal{T}$) and orthorhombic ($\mathcal{O}$) phases of bulk $BaTiO_3$. For each case, all possible values of local electric dipoles, $\vec{d}$, fall within the filled regions constituting the manifolds. In the paraelectric phase, the internal states manifold corresponds to a volume bounded by a cube with rounded edges and centered at $\vec{d} = 0$. The edges of the bounding cube are perpendicular to d_x, d_y and d_z coordinate axes. At each ferroelectric phase transition the topology of the manifold changes — it is ruptured at points corresponding to possible macroscopic polarization value in the high symmetry phase. This change, reflected in varying values of the Euler characteristic χ, stabilizes point topological defects in the tetragonal phase, linear defects in orthorhombic phase and planar defects (domain walls) in the rhombohedral phase.

In this study, taking $BaTiO_3$ as a model example, we attempt to clarify these questions. For this, we step away from the commonly used notion of an order parameter space and, instead, consider the topology of the so-called internal states manifolds. Internal states manifolds, introduced by G. Toulouse and W. Kléman at the dawn of the topological defects theory, can be defined as sets of all possible values of the local order parameter [1]. Such sets have a lot of common with order parameter spaces, and often both definitions can be even equivalent. However, unlike the notion of an order parameter spaces, the concept of an internal space manifold does not rely on the symmetry of the system. Therefore, internal space manifolds generally contain much more

---

[*] Electronic address: prokhorenko.s@gmail.com

information about finite-temperature fluctuations of the local order parameter. In order to examine this subtle difference, we have computed (see Fig. 1) the internal states manifolds for all phases of bulk $BaTiO_3$ using Monte Carlo simulations and the effective Hamiltonian model of Ref. [2].

From Fig.1, one can see, that at each ferroelectric phase transition, the topology of the internal states manifold changes — it is ruptured at points corresponding to possible macroscopic polarization values in the higher symmetry phase. Moreover, Fig. 1 shows that the $\mathcal{T}$ and $\mathcal{O}$ phases are stabilized by strong dipolar fluctuations, in accordance with the Comes-Guinier-Lambert model [3], perturbative fluctuation theory of Ref. [4] and recent molecular dynamics simulations [5]. Finally, the obtained results show that in the $\mathcal{O}$ and $\mathcal{T}$ phases, the topology of the internal states manifolds is different from that of the corresponding order parameter spaces. For instance, in the $\mathcal{T}$ phase, the order parameter space consists only of six disconnected points (equivalent values of macroscopic polarization), while the internal states manifold constitutes a continuous set that is topologically equivalent to a sphere. In another words, the internal states manifold in the $\mathcal{T}$ phase is, in fact, equivalent to the order parameter space of a spherically-symmetric Heisenberg model! Therefore, analyzing the topology of internal states manifolds we are led to conclude that despite a strong crystalline anisotropy and unambiguously discrete symmetry, tetragonal and orthorhombic phases of $BaTiO_3$ can host point and linear topological defects, that are essentially protected by finite-temperature fluctuations.

Pursuing the topological analysis of dipolar configurations in bulk $BaTiO_3$ we further inquire on whether linear and point topological defects can be stable even in the case when finite-temperature fluctuations seize to provide necessary protection. Such situation is realized in the $\mathcal{R}$ phase of $BaTiO_3$, where the “true” topological defects correspond to domain walls. In this case, one can expect formation of linear “defects” corresponding to junctions of domain walls or even contact points of ferroelectric domains as a result of large-scale continuity of the domain network. Casting this continuity requirement in the form of a conservation law relating numbers of defects of different dimensionality, we reveal the topological nature of domain wall junctions and explore possible elementary processes leading to elimination of these linear defects from a domain network. As a result, we find that three-fold junctions can be locked within a domain pattern, and in this sense can be seen as topological defects, protected by the geometry of the domain network.

In summary, the results of our study shake the common belief that continuous symmetry is a prerequisite for stability of linear and point topological defects. This conclusion not only allows us to suggest that overlooked topological structures can exist in proper bulk ferroelectrics, but also provides a leeway to generalize a plethora of “continuous-symmetry” theorems and theoretical arguments to systems with strong anisotropy.

This work is financially supported by DARPA grant HR0011-15-2-0038 (under the MATRIX program) and by the Physics department of the University of Arkansas. Y.N. and L.B. also acknowledge the ARO grant W911NF-12-1-0085. S.P. acknowledges the support of Marie Curie COFUND fellowship.

---

[1] G. Toulouse and M. Kléman, J. Physique Lett. **37**, 149 (1976).

[2] L. Walizer, S. Lisenkov, and L. Bellaiche, Phys. Rev. B **73**, 144105 (2006).

[3] R. Comes, M. Lambert, and A. Guinier, Solid State Commun. **6**, 715 (1968)

[4] A. I. Sokolov, and A. K. Tagantsev, JETP Lett. **75**, 483 (2002).

[5] J. Hlinka, T. Ostapchuk, D. Nuzhnyy, J. Petzelt, P. Kuzel, C. Kadlec, P. Vanek, I. Ponomareva, and L. Bellaiche, Phys. Rev. Lett. **101**, 167402 (2008).

Temperature–Driven Phase Transitions in $BaTiO_3$: an Atomic Scale Description

Y. Qi, S. Liu, I. Grinberg and A. M. Rappe
The Makineni Theoretical Laboratories,
Department of Chemistry,
University of Pennsylvania,
Philadelphia, PA 19104–6323 USA

Barium titanate ($BaTiO_3$) is a ferroelectric oxide which undergoes four phase transitions (rhombohedral–orthorhombic–tetragonal–cubic) as the temperature increases. In this study, a classical interatomic potential for $BaTiO_3$ based on the bond–valence theory was developed. This atomistic potential was parameterized from density functional calculation results, and enables accurate large–scale molecular dynamics (MD) simulations at finite temperatures. Our model potential for $BaTiO_3$ can not only reproduces the temperature–driven phase transitions well, but also allows the atomic scale analysis of $BaTiO_3$ structures. By carrying out MD simulations, we demonstrate that the phase transitions of $BaTiO_3$ have a mix of displacive and order–disorder characters. Besides, our calculation also provides insight in structural dynamics during phase transition: we discovered that the global phase transition of $BaTiO_3$ is associated with transitions of every component, including the ones already averaging to zero. Besides, during the orthorhombic to tetragonal transition, the x component exhibits a bond–hardening character, which is opposite to the conventional understanding that temperature increase generally causes bond–softening.

$BaTiO_3$ possesses promising applications in electronic devices, such as high–κ dielectrics, non–volatile memory, and piezoelectric sensors [1–4]. Therefore, developing an atomistic potential which enables large scale and fast molecular dynamics (MD) simulations is of great importance. However, because of the small energy differences among the four phases (rhombohedral, orthorhombic, tetragonal and cubic) [5–7], the development of an accurate classical potential for $BaTiO_3$ has proven to be not straightforward, In this work, we apply the bond–valence model to $BaTiO_3$ and parameterize an all–atom interatomic potential. This potential is able to reproduce the rhombohedral–orthorhombic–tetragonal–cubic (R-O-T-C) phase transition in isobaric–isothermal ensemble (NPT) MD simulations well. The phase transition temperatures agree with previous theoretical results perfectly [8].

To examine the performance of the recently obtained force field, we studied the temperature dependence of lattice constants (a, b and c), local displacements of Ti atoms (d_x, d_y, and d_z), and polarization (P_x, P_y, and P_z). NPT MD simulations were carried out with a $10\times10\times10$ supercell (5000 atoms), and the temperature was controlled via the Nóse–Hoover thermostat. The pressure was maintained at 1 atm via the Parrinello–Rahman barostat [9]. The MD simulation results are shown in FIG. 1, the simulations clearly reveal the R-O-T-C four phases in different temperature ranges and all the phase transitions are first order. Below 100 K, the polarization lies along [111] direction ($P_x = P_y = P_z$), which is the character of the rhombohedral phase. As temperature increases above 100 K, the z component of polarization, P_z, becomes zero, indicating that the phase transits from rhombohedral to orthorhombic ($P_x = P_y > 0$, $P_z = 0$). Above 110 K, the polarization aligns preferentially along (100) direction ($P_x > 0$, $P_y = P_z = 0$) and the phase is tetragonal. Around 160 K, the ferroelectric-paraelectric phase transition occurs and this temperature is the Curie temperature acquired from our MD simulation. The Curie temperature is underestimated in MD simulations and the underestimation is attributed to the systematic error of density functional used for force field optimization [10, 11].

It is worth mentioning that the phase transition temperatures given by our bond–valence model match well with those predicted by the shell model [8]. The averaged lattice constants at the four phases from MD simulations are also in good agreement (error less than 1%) with the PBEsol values. All these results demonstrate the robustness of this interatomic potential.

We also conducted MD simulations with varying temperatures, in order to investigate the features of structural dynamics during phase transitions. The temperatures were controlled by the Nóse–Hoover thermostat with a thermal inertia parameter M_s=10 and increased from 100 K to 110 K (R to O), 110 K to 120 K (O to T) and 155 K to 165 K (T to C) respectively in three different sets of simulations. The Ti displacement distributions changing with temperature along three axes were analyzed and plotted in FIG. 2.

The changes of Ti displacement distributions during the rhombohedral to orthorhombic phase transition is shown in the first column (from 100 K to 110 K). In the x and y direction, the centers of the Ti distributions shift up, indicating the transitions are displacive. However, in the z direction, both the average and the standard deviation change a lot, demonstrating that the transition involves a mix of displacive and bond–softening characters [12]. The second column shows the orthorhombic to tetragonal transition, the transition of the y component includes both displacive and bond–softening features, same as the z one in the rhombohedral to or-

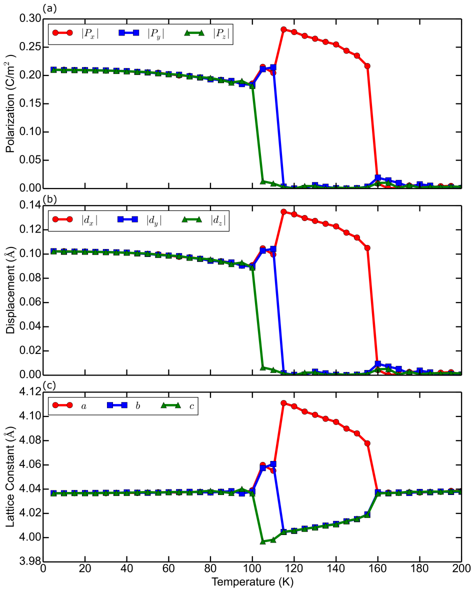

FIG. 1. The polarization, Ti displacement, and lattice constants of BaTiO$_3$ at different temperatures. The phase transition temperatures are 105 K, 115 K and 160 K.

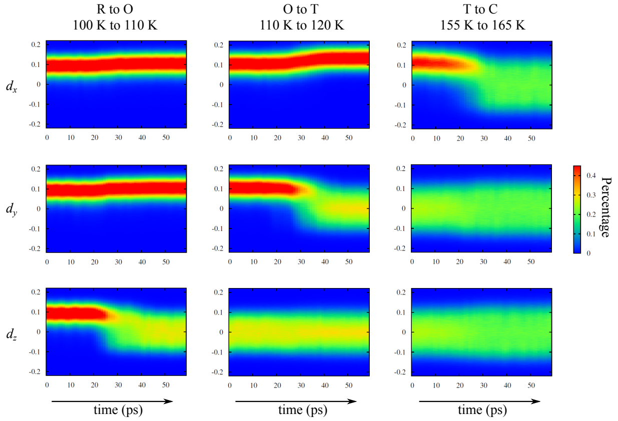

FIG. 2. Dynamics of Ti displacement distributions during phase transitions. The horizontal axis represents the time, the vertical axis represents the fraction of the Ti displacements and the color scale represents the percentages of Ti displacement.

thorhombic transition. However, the z component exhibits a novel transition feature: after the transition, the Ti displacements are located closer to 0, indicating bond hardening. The bond–hardness–changing transition can also be observed for the y and z components in the tetragonal to cubic transition.

Based on the features of the Ti displacement distributions at different phases, the characteristics of BaTiO$_3$ phase transition can be summarized as: (1) Opposite to the conventional sense that thermal excitation usually causes bond–softening, increasing temperature can also induce bond hardening. The dynamics of x component polarization during the orthorhombic to tetragonal transition is an example. (2) For BaTiO$_3$, all the phase transitions possess both bond–hardness–changing and displacive characters; (3) When the global phase transition occurs, each component undergoes phase transition, even for the non–polar ones;

---

[1] W. S. Yun, J. J. Urban, Q. Gu, and H. Park, Nano Lett. **2**, 447 (2002).

[2] K.-H. Chen, Y.-C. Chen, Z.-S. Chen, C.-F. Yang, and T.-C. Chang, Appl. Phys. A Mater. Sci. **89**, 533 (2007).

[3] W. Buessem, L. Cross, and A. Goswami, J. Am. Ceram. Soc. **49**, 33 (1966).

[4] T. Karaki, K. Yan, and M. Adachi, Jpn. J. of Appl. Phys. **46**, 7035 (2007).

[5] G. Kwei, A. Lawson, S. Billinge, and S. Cheong, J. Phys. Chem. **97**, 2368 (1993).

[6] O. Diéguez, S. Tinte, A. Antons, C. Bungaro, J. B. Neaton, K. M. Rabe, and D. Vanderbilt, Phys. Rev. B **69**, 212101 1 (2004).

[7] A. Von Hippel, Rev. Mod. Phys. **22**, 221 (1950).

[8] S. Tinte, M. G. Stachiotti, M. Sepliarsky, R. L. Migoni, and C. O. Rodriquez, J. Phys.: Condens. Matter **11**, 9679 (1999).

[9] M. Parrinello and A. Rahman, Phys. Rev. Lett. **45**, 1196 (1980).

[10] S. Liu, I. Grinberg, and A. M. Rappe, J. Physics.: Condens. Matter **25**, 102202 (2013).

[11] M. Sepliarsky, M. G. Stachiotti, and R. L. Migoni, Phys. Rev. B **72**, 014110 (2005).

[12] K. Gaffney and H. Chapman, Science **316**, 1444 (2007).

Ferroelectric instability in nanotubes and spherical nanoshells

R. Qiu[1,2*], E. Bousquet[2] and A. Cano[1]
[1]CNRS, Université de Bordeaux - ICMCB, UPR 9048, F-33600 Pessac, France
[2]Physique Théorique des Matériaux (B5a), Université de Liège,
B-4000 Liège, Belgium
*qiuruihao@gmail.com

Ferroelectric nanoparticles receive a considerable research attention [1, 2] and novel fabrication methods are being developed [3]. These particles can be embedded in another medium, with which the corresponding heterostructure can be supplied with novel topologies and additional functionalities [1, 2]. However, one of the critical factors determining the use of these systems is the ferroelectric instability itself.

We study theoretically the ferroelectric instability in nanotubes and spherical nanoshells by following a Ginzburg-Landau-like approach. In addition to the overall size effect, we analyze the impact of the thickness, relative permittivities, and boundary conditions on the transition temperatures corresponding to both irrotational and vortex-like distributions of polarization.

We have found an intriguing topological finite-size effect that can promote the competition between different types of ferroelectricity in the ultra-thin limit. Figure 1 plots the transition temperature T_c for vortex-like polarization state in a ferroelectric nanotube. T_c as a function of R_1 and R_2 can show rather different behaviors when these parameters are varied separately. This is eventually determined by the extrapolation length λ. Specifically, the “topography" of the $T_c(R_1,R_2)$ map changes in such a way that its maximum gradient rotates by 45° as λ goes from 0 to ∞. This unequivalence in the finite-size effect is related to the specific topology of the systems under consideration [4].

Our results are expected to provide useful insights for the engineering of the ferroelectric properties at the nanoscale.

References

[1] F. D. Morrison et al. Rev. Ad. Mat. Sci. 4, 114, (2003), J. Scott, science 315, 954 (2007).

[2] A.Gruverman and A. Kholkin, Reports on Progress in Physics 69, 2443 (2006).

[3] G. Philippot, C. Elissalde, M. Maglione, and C. Aymonier, Advanced Powder Technology 25, 1415 (2014).

[4] R. Qiu, E. Bousquet and A. Cano, EPL (Europhysics Letters), in press (2015).

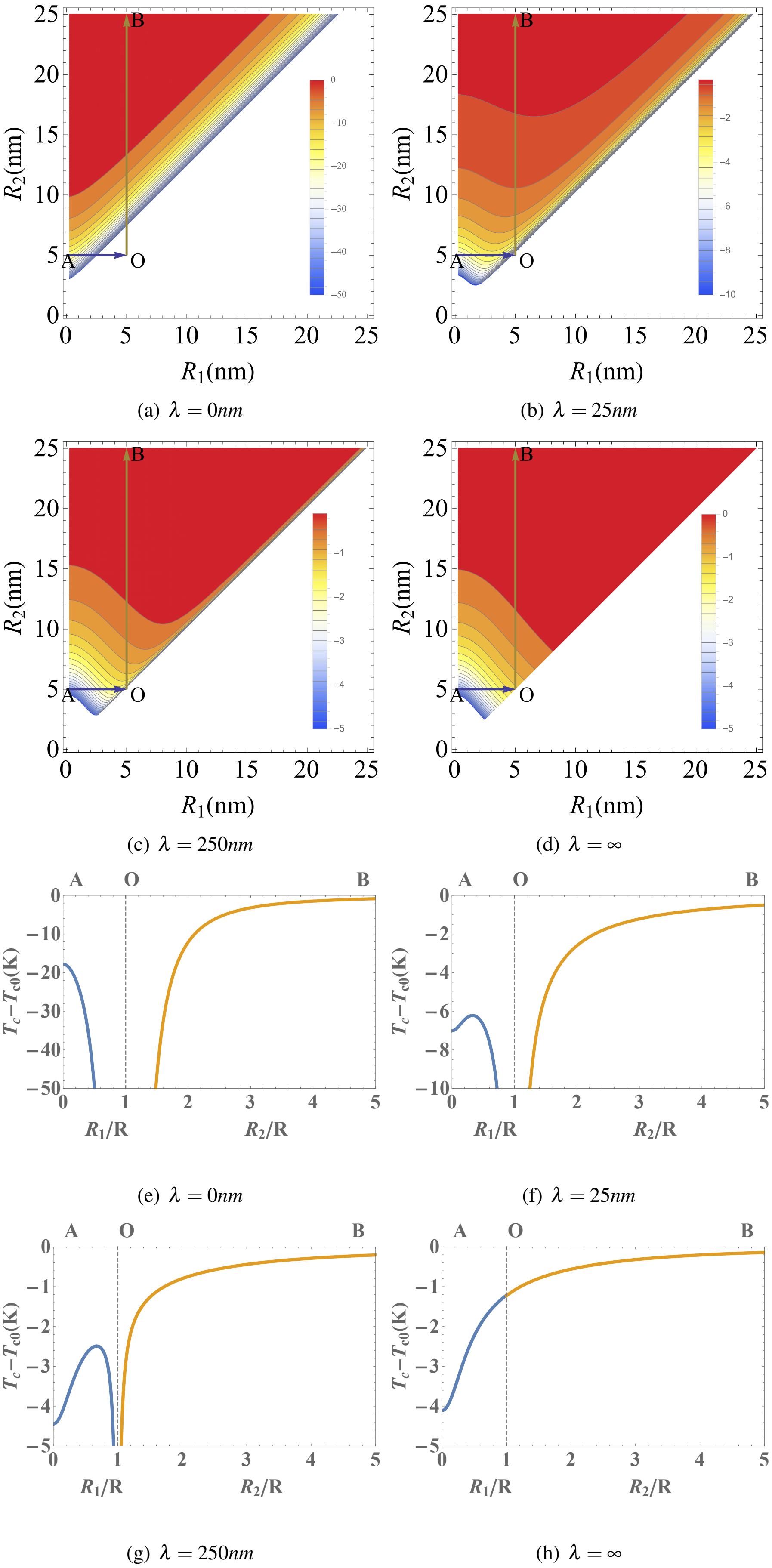

(a) $\lambda = 0nm$
(b) $\lambda = 25nm$
(c) $\lambda = 250nm$
(d) $\lambda = \infty$
(e) $\lambda = 0nm$
(f) $\lambda = 25nm$
(g) $\lambda = 250nm$
(h) $\lambda = \infty$

Figure 1: Transition temperature for vortex-like polarization state in a ferroelectric nanotube. Figures (a) - (d) plot the $T_c - T_{c0}$ as a function of internal (R_1) and external (R_2) radii of the nanotube. Figures (e) - (h) plot $T_c - T_{c0}$ along the paths A-O (blue) and B-O (orange).

Effect of hydrostatic strain in the photocatalytic properties of $BiVO_4$ from first principles

Sebastian E. Reyes-Lillo$^{(1,2)}$ and Jeffrey B. Neaton$^{(1,2,3)}$
(1) Molecular Foundry, Lawrence Berkeley National Laboratory, Berkeley, California 94720, USA
(2) Department of Physics, University of California, Berkeley, California 94720 USA
(3) Kavli Energy NanoSciences Institute at Berkeley, Berkeley, California, 94720 USA
(Dated: December 3, 2015)

Bismuth vanadate ($BiVO_4$), a well known photocatalytic material [1, 2], has a ferroelastic tetragonal to monoclinic transition at $T_c = 528$ K [3, 4]. While the high temperature tetragonal phase has negligible photocatalytic activity, the room temperature monoclinic phase has shown promising water splitting properties due to both a low optical band gap (~2.4 eV) and a proper band edge alignment to water redox potentials.

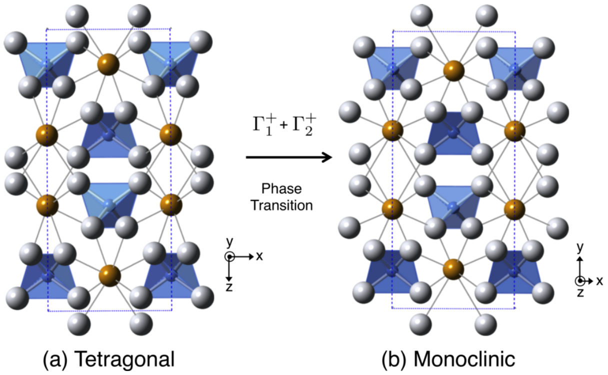

(a) Tetragonal (b) Monoclinic

FIG. 1. Tetragonal to monoclinic phase transition.

The high temperature phase of $BiVO_4$ has a $I4_1/a$ (#88) tetragonal structure [5]. The low temperature monoclinic $C2/c$ (#15) phase corresponds to a small centrosymmetric distortion of the tetragonal phase. As shown in Fig 1, both tetragonal and monoclinic structures are composed of VO_4 tetrahedra connected to Bi oxygen cages. The monoclinic phase arises through an antiparallel off centering of the Bi atoms, and is characterized by a large difference between largest and smallest Bi-O bond length $\delta \sim 0.275$Å.

Previous first principles studies on $BiVO_4$ has focused on the structural and electronic properties of the tetragonal and monoclinic phases, and the stereochemical activity of the Bi lone-pair [6–10]. However, a clear understanding of the role of the ferroelastic transition in the photocatalytic properties of $BiVO_4$ remains elusive. Remarkably, the experimental local geometry of the monoclinic structure is not reproduced by standard first principles methods [6].

In this work, we use first principles calculations to investigate the effect of hydrostatic strain in the structural and optoelectronic properties of $BiVO_4$. We find that, above a certain critical strain ($\eta > 1.5\%$), the tetragonal structure develops an instability and distort into the monoclinic phase. The experimental structure of the monoclinic phase is recovered at $\eta \sim 1.75\%$ strain.

As a function of strain, the electronic band gap of the monoclinic phase increases and switches from *quasi*-direct to indirect. The band structure and density of states (DOS) are modified with increasing strain. This effect is originated by the increase of local distortions around the Bi atom and the contribution of Bi 6*s* states in the upper portion of the valence bands.

In addition, we construct an effective energy expansion to describe the ferroelastic phase transition as a function of strain. The monoclinic phase is stabilized at large strain due to a linear coupling term between strain and Bi displacements. We study the dependence of the model on exchange correlation functionals.

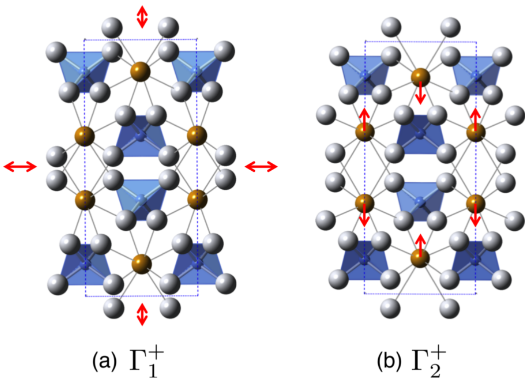

(a) Γ_1^+ (b) Γ_2^+

FIG. 2. (a-b) Structural modes relating the tetragonal and monoclinic structures.

The reference tetragonal structure is related to the lower symmetry monoclinic structure by the combined distortions of two zone-center ($q = 0$) modes: Γ_1^+ and Γ_2^+, depicted in Fig 2. The Γ_1^+ acoustic mode corresponds to a uniform compression/expansion of the unit cell. The Γ_2^+ optical mode corresponds to an antiparallel displacement of the Bi atoms, and originates the characteristic asymmetry of the Bi-O bond lengths in the monoclinic phase.

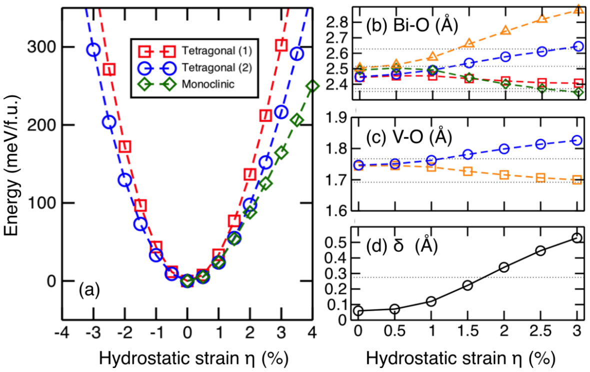

FIG. 3. (a) Energy of the tetragonal and monoclinic phases as a function of hydrostatic strain. Monoclinic (a) Bi-O bond lengths, (b) V-O bond lengths, and (c) δ as a function of hydrostatic strain. Experimental values are represented by a dash line [5].

Fig. 3 (a) shows the energy of the tetragonal and monoclinic structure as a function of strain $\eta = Q_{\Gamma_1^+}$. Tetragonal (1) shows the effect of uniform strain in the tetragonal structure. Tetragonal (2) represents the structure obtained by relaxing the internal atomic positions of Tetragonal (1). For small strain ($-1\% < \eta < 1\%$), the energy difference between tetragonal and monoclinic is less than 1 meV per formula unit (f.u.). For compressive strain ($\eta < -1\%$), the monoclinic structure converge to the tetragonal structure. For tensile strain ($\eta > 1\%$), the monoclinic structure is increasingly favored over the tetragonal phase.

Fig. 3 (b-d) shows the magnitude of the Bi-O and V-O bond lengths, and δ as a function of strain. Tensile strain splits the Bi-O bonds in the tetragonal structure and increases the asymmetry δ, stabilizing the monoclinic phase. The best approximation of the experimental local geometry, represented with a dash line, is recovered for $\eta \sim 1.75\%$.

In order to understand the coupling mechanism between the structural modes, we expand the energy of the monoclinic phase as a function of strain $\eta = \Gamma_1^+$ and Γ_2^+ [11]:

$$E = a_1\eta + a_2\eta^2 + a_3 Q^2_{\Gamma_2^+} + a_4\eta^3 + a_5 Q^2_{\Gamma_2^+}\eta + ...$$
$$..a_6 Q^2_{\Gamma_2^+}\eta^2 + a_7\eta^4 + a_8 Q^4_{\Gamma_2^+}$$

Using first principles calculations we compute the value of the coefficients in front of the expansion and reproduce the essential features of the phase transition. The coupling term $Q^2_{\Gamma_2^+}\eta$ is responsible for the stabilization of the monoclinic phase at large strain.

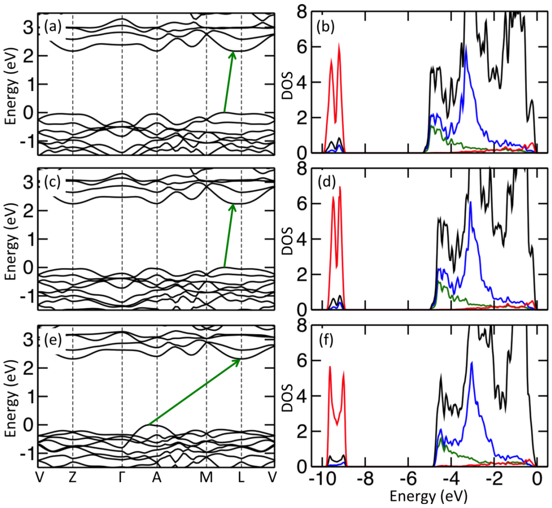

FIG. 4. Band structure and density of states (DOS) for the monoclinic phase at (a-b) $\eta = 0\%$, (c-d) $\eta = 1.5\%$ and (e-f) $\eta = 3\%$ strain.

Finally, Fig. 4 (a-f) show the effect of strain in the electronic and optical properties of the monoclinic structure. We find that with increasing strain, the band gap increases and switches from *quasi*-direct to indirect. The large modification of band structure and density of states is explained by the large distortion of the Bi-O cage, associated to the increase of $Q_{\Gamma_2^+}$. We further explore the effect of strain in the photocatalytic properties of the material.

[1] A. Kudo, K. Omori and H. Kato, J. Am. Chem. Soc. 121, 11459 (2001).
[2] S. Tokunaga, H. Kato and A. Kudo, Chem. Mater. 13, 4624 (2001).
[3] J. D. Bierlein and A. W. Sleight, Sol. State. Comm. 16 69 (1975).
[4] I. Tomeno *et al.*, Phys. Rev. B 84, 014302 (2011).
[5] A. W. Sleight *et al.*, Mater. Res. Bull. 14, 1571 (1979).
[6] J. Ma and L.-W. Wang, Appl. Phys. Lett. 105 172102 (2014).
[7] Z. Zhao, Z. Li, and Z. Zou, Phys. Chem. Chem. Phys. 13, 4746 (2011).
[8] K. Ding *et al.*, Theor. Chem. Acc. 132, 1352 (2013).
[9] A. Walsh *et al.*, Chem. Mater. 21, 547 (2009).
[10] J. K. Cooper *et al.*, Chem. Mater. 26, 5365 (2014).
[11] J. Feng *et al.*, Phys. Rev. B 90, 094102 (2014).

ONR's Research Program on Acoustic Transduction Materials and Devices

Harold C. Robinson, Wallace A. Smith and Carl C.M. Wu
Office of Naval Research
Materials Division, ONR 332
875 North Randolph Street
Arlington, Virginia 22203-1995

Research on innovative materials and device structures is sought that enhances the performance of electro-mechanical transducers used by the Department of Navy to generate, detect and suppress undersea sound waves. The present Office of Naval Research program has two thrusts. The first aims to devise and validate first-principles quantum-mechanical methods to evaluate the properties of materials with structural phase transitions; this will enable the exploration of the properties of new materials in advance of their synthesis. The second focuses on the new high coupling, high-strain relaxor piezoelectric single crystals. Efforts underway aim to produce and characterize these piezocrystals and to design, fabricate and test innovative transducers from them for Navy SONAR systems.

Improper magnetic ferroelectricity of nearly pure electronic nature in cycloidal spiral $CaMn_7O_{12}$

Diomedes Saldana-Greco, Jin Soo Lim, and Andrew M. Rappe

The Makineni Theoretical Laboratories, Department of Chemistry,
University of Pennsylvania, Philadelphia, PA 19104-6323, USA

Materials exhibiting ferroelectricity induced by noncentrosymmetric spiral magnetism have received much attention due to their strong magnetoelectric effect and the potential applications in spin-driven electronics. In charge-ordered quadruple perovskite system $CaMn_7O_{12}$, noncollinear cycloidal magnetic order breaks the inversion symmetry [Fig. 1], generating a very large magnetically coupled ferroelectric polarization experimentally measured to be 2870 $\mu C/m^2$ [1]. In this work, we use first-principles calculations to study the microscopic origin of the polarization. Our Berry phase computed polarization exhibits almost pure electronic behavior, as the Mn displacements are negligible, ≈ 0.7 mÅ. The polarization magnitude and direction are both determined by the Mn spin current, where the p-d orbital mixing is driven by the inequivalent exchange interactions within the charge-ordered B-site Mn^{3+}-Mn^{4+} cycloidal spiral chains along each Cartesian [100], [010], and [001] direction [Fig. 1]. The existing mechanisms of ferroelectricity in $CaMn_7O_{12}$ have not provided a unified explanation for both the nearly nonionic nature of the polarization and its direction perpendicular to the spin rotation plane. We employ the generalized spin-current model [2] with a Heinsenberg-exchange Dzyaloshinskii-Moriya interaction model to resolve these issues. Ultimately, our results suggest that persistent electronic polarization activated solely by helical spin order in inversion-symmetric ionic crystal lattices suggests ultrafast magnetoelectric response in a single ferroelectric-magnetic domain.

This work was supported by the US Office of Naval Research under Grant No. N00014-11-1-0664. Computational support was provided by the High Performance Computing Modernization Office of the US Department of Defense, and the National Energy Research Scientific Computing Center of the US Department of Energy.

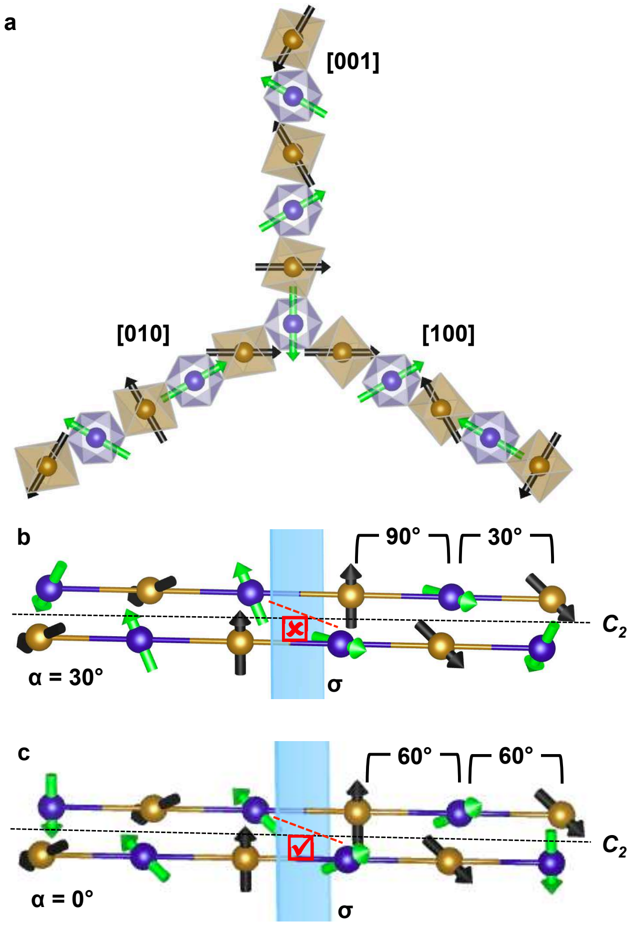

FIG. 1. (a) B-site Mn^{3+}(gold)-Mn^{4+}(blue) chains along the Cartesian directions [100], [010], and [001] with Mn^{3+} spins (black arrows) and Mn^{4+} spins (green arrows) at $\alpha = 30°$. The spins form cycloidal spiral chains along the three cubic axes. Two pairs of inversion-related cycloidal spiral chains for (b) $\alpha = 30°$ and (c) $\alpha = 0°$. The mirror plane is perpendicular to the C_2 axis, which is set parallel to the chain direction. Upon magnetic inversion operation, the $\alpha = 30°$ configuration breaks the inversion symmetry as indicated by the dashed red line, whereas the $\alpha = 0°$ configuration retains the inversion symmetry.

---

[1] R. D. Johnson, L. C. Chapon, D. D. Khalyavin, P. Manuel, P. G. Radaelli, and C. Martin, Phys. Rev. Lett. **108**, 067201 (2012).

[2] H. J. Xiang, E. J. Kan, Y. Zhang, M.-H. Whangbo, and X. G. Gong, Phys. Rev. Lett. **107**, 157202 (2011).

Spin-driven polarization in Bi*M*O_3 (*M*=3*d* transition metals) multiferroics: From first-principles

Santosh KC*, Jun Hee Lee, and Valentino R. Cooper

Materials Science and Technology Division, Oak Ridge National Laboratory, Oak Ridge, Tennessee 37831, USA

*E-mail: kcs1@ornl.gov

Since, the discovery of the giant magnetoelectric effect (ME) in $TbMnO_3$ by Kimura and coworkers [1], spin-driven ferroelectric polarization has emerged as an important research field for multiferroic systems. Here, the spin-driven ferroelectric (FE) polarization arises from the breaking of space inversion symmetry by magnetic ordering in the crystal. The ability to control magnetism using an electric field has potential in applications such as magnetic data storage, spintronics, logic, and memory devices [2, 3]. As such, ferroelectricity induced by spin ordering may have significant consequences for creating novel ME phenomena in these materials.

Bismuth ferrite ($BiFeO_3$) which exhibits coupling between ferroelectricity and (anti)ferromagnetism [4] is regarded as one of the most promising multiferroics. It stabilizes in a perovskite type rhombohedral crystal structure (space group *R*3c) at room temperature and has recently been reported to possess a giant spin-driven polarization [5] even higher (~3.0 $\mu C/cm^2$) than any other reported materials.

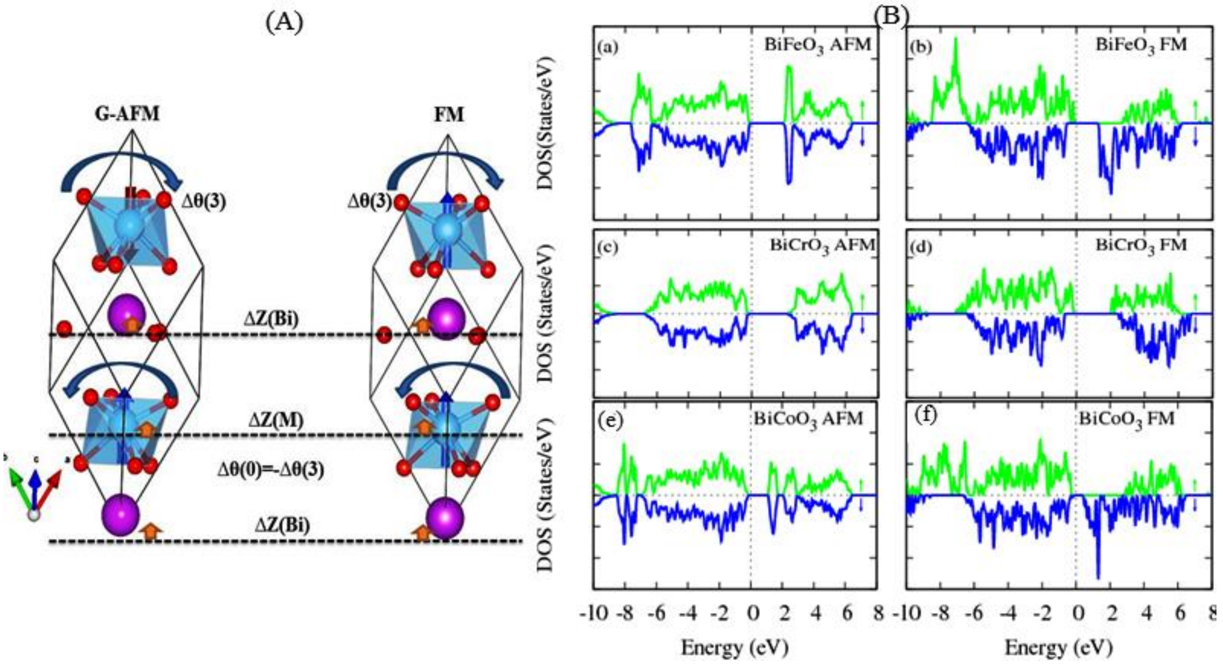

Figure 1 (A) DFT optimized atomic structure of Bi*M*O_3 for (left) G-AFM and (right) FM magnetic orderings. FE distortions of *M* (ΔZ (M)) and Bi (ΔZ (Bi)) along [111] and AFD R^{+4} rotations perpendicular to [111] are indicated. (0) and (3) are indices of hexagonal layers (x + y + z = n). (B) Spin resolved density of states (DOS) for $BiFeO_3$, $BiCrO_3$ and $BiCoO_3$ in the rhombohedral crystal structure for both AFM and FM spin orderings.

To probe the underlying mechanism of the large spin-phonon response observed in $BiFeO_3$, we examine these couplings within other Bi based 3*d* transition metal oxides $BiMO_3$ (M= Ti, V, Cr, Mn, Fe, Co, Ni) using density functional theory (DFT). Figure 1 (A) depicts the DFT optimized atomic structure of $BiMO_3$ for AFM and FM magnetic orderings with the atomic displacements and the corresponding DOS for $BiFeO_3$, $BiCrO_3$ and $BiCoO_3$ are displayed in Fig.1 (B). Our results indicate that only $BiCrO_3$, $BiCoO_3$ and $BiFeO_3$ are found to be insulating for both types of spin arrangements (see Fig. 1(B)) in the rhombohedral crystal structure and are thereby suitable materials for the investigation of spin-driven polarization. However, for $BiCrO_3$ and $BiCoO_3$ the rhombohedral phase is not the ground state. Thus, the materials challenge may be to crystallize or epitaxially grow these materials in the desired phase.

Nevertheless, our results demonstrate that rhombohedral $BiCoO_3$ has the largest spin-driven polarization which is a consequence of symmetry breaking due to the competition between ferroelectric distortions and anti-ferrodistortive (AFD) octahedral rotations. Furthermore, we find a strong dependence of these enhanced spin-driven polarizations on the crystal structure; with the rhombohedral phase having the largest spin-induced atomic distortions along [111]. These results give us significant insights into the magneto-electric coupling in these materials which are essential for the magnetic and electric field control of polarization and magnetization in multiferroic based devices.

This research was supported by the US Department of Energy, Office of Science, Basic Energy Sciences, Materials Sciences and Engineering Division and the Office of Science Early Career Research Program and used computational resources at NERSC.

References:

[1] T. Kimura *et.* al; *Nature* 426, 55 (2003).

[2] D. Sando *et.* al.; *Nature materials* **12**, 641-646 (2013).

[3] S. Neusser and D. Grundler; *Advanced Materials* **21**, 2927-2932 (2009).

[4] C.Weingart, N. Spaldin; E. Bousquet; *Physical Review* B **86,** 094413 (2012).

[5] J. H. Lee, and R. S. Fishman; *Physical Review Letters* **115** (20), 207203 (2015).

Controlling Phase Coexistence in Mixed Phase $BiFeO_3$

Omid Sayedaghaee[1,2], David Edwards[3], Niall Browne[3], Marty Gregg[3], Amit Kumar[3],

Bin Xu[2], Dawei Wang[2], Sergey Prosandeev[2] ,Laurent Bellaiche[1,2,4],

Sergei V. Kalinin[5], Stephen Jesse[5], Dipanjan Mazumdar[6], Arun Gupta[6]

[1]Microelectronics-Photonics Program, University of Arkansas, Fayetteville, AR 72701, USA
[2]Physics Department, University of Arkansas, Fayetteville, AR 72701, USA
[3]Queen's University Belfast, UK
[4]Institute for Nano Science and Engineering, University of Arkansas, Fayetteville, AR, 702701, USA
[5]Oak Ridge National Laboratory, USA [6]University of Alabama, USA

Ferroelectrics with morphotropic phase boundaries (MPBs) are currently capturing more and more attention due to their multifunctional properties. These materials, owing to their large piezoelectric response, are widely used in variety of technological applications such as micropositioners, acoustic sensors in sonar, and actuators [1],[2]. $Pb(Zr_xTi_{1-x})O_3$ (PZT), $Pb(Mg_{0.33}Nb_{0.67})O_3$-$PbTiO_3$ (PMN-PT), and $Pb(Zn_{0.33}Nb_{0.67})O_3$-$PbTiO_3$ (PZN-PT) are reported to have giant piezoelectric responses [2]. $BiFeO_3$ (BFO) is a promising alternative to these lead-based perovskites. BFO is one of the few lead-free multiferroics which are magnetic and ferroelectric at room temperature [3],[4]. In fact, BFO shows antiferromagnetism which is coupled with ferroelectric order [5]. The current work is an effort to control the properties of BFO by means of electric field and pressure which is useful in technological applications such as data storage as well as understanding the evolution of phase in strained MPB systems. The properties of BFO within different physical configurations are theoretically studied and predictions made according to computer simulations. The same configurations are investigated experimentally as well.

As consistent with literature, epitaxial strain can be used to form a MPB with giant piezoelectric responses. Growing $BiFeO_3$ on $LaAlO_3$ as substrate will form a rhombohedral-like phase (R) as well as a tetragonal-like phase (T) (Figures 1-2) [6]. These two phases can coexist in the scale of tens of nanometers and the piezoelectric response for such a system is large. By controlling phase competition between T phase and R phase, we can control the properties of the material [2].

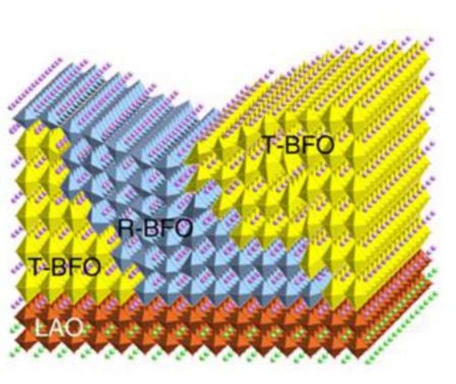

Figure 1 - Co-existence of phases in strained $BiFeO_3$ [6]

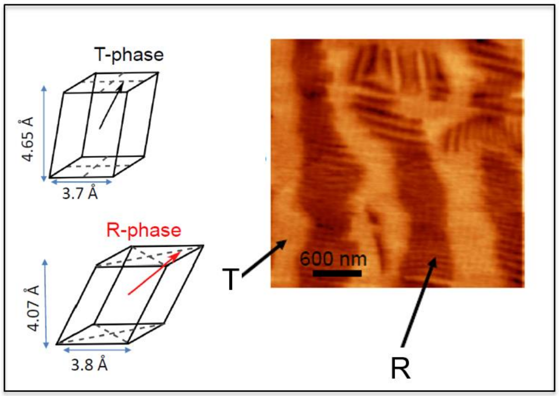

Figure 2 – Left: T and R phase structures, Right: The combination of T phase (light region) and R phase (dark region) in experiment

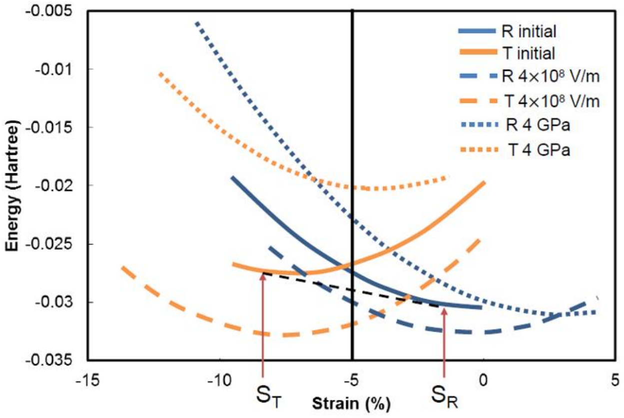

Figure 3 – R and T phase at initial state (solid lines) and under electric field (dashed lines) and pressure (dotted lines) based on Monte Carlo simulations and effective Hamiltonian method

Here, we want to control this competition via an interplay between an applied electric field and uniaxial pressure. Theoretically, Monte Carlo and Effective Hamiltonian Methods were used to calculate the total energy of the system under different electric fields and pressures [7] (Figure 3). The ratio between T and R phases at each electric field or pressure was calculated using the interception of a common tangent with each phase (Lever rule). Using the obtained free energy diagrams of each phase as a function of strain, we can generate a scatter plot of the percentage of that phase in terms of different values of electric field and pressure. The results exhibit a soft variation of R phase by changing pressure, electric field, and strain. The computer simulation results show that by means of electric field and pressure a tetragonal-like phase (T) can be converted into a rhombohedral-like phase (R) reversibly.

The same results were observed in experiment as well. Applying electric field results in the conversion of R phase (dark region in Figure 2) to T phase (light region in Figure 2) and applying pressure reverses the changes back and more R phase is generated. This means that we can have a dual control over the phases with electric field and pressure, experimentally. The acquired results enable us to generate a ternary phase diagram (epitaxial strain, uniaxial pressure and electric field) for BiFeO3.

Comparing the theoretical and experimental results shows that there is a good correlation between theoretical predictions by thermodynamics and experimental results. The predictions as well as the computational, and experimental methods of this work can be applied to other material systems.

Acknowledgements

This work is financially supported by the ARO Grant W911NF-12-1-0085, the ONR Grant No. N00014-12-1-1034, the Air Force Office of Scientific Research under Grant FA9550-16-1-0065 and the Department of Energy, Office of Basic Energy Sciences, under contract ER-46612.

References:

[1] K. Uchino, *Ferroelectric devices*. New York: Marcel Dekker, 2000.
[2] R. J. Zeches, M. D. Rossell, J. X. Zhang, A. J. Hatt, Q. He, C.-H. Yang, A. Kumar, C. H. Wang, A. Melville, C. Adamo, G. Sheng, Y.-H. Chu, J. F. Ihlefeld, R. Erni, C. Ederer, V. Gopalan, L. Q. Chen, D. G. Schlom, N. A. Spaldin, L. W. Martin, and R. Ramesh, “A Strain-Driven Morphotropic Phase Boundary in BiFeO3,” *Science*, vol. 326, no. 5955, pp. 977–980, Nov. 2009.
[3] G. Catalan and J. F. Scott, “Physics and Applications of Bismuth Ferrite,” *Adv. Mater.*, vol. 21, no. 24, pp. 2463–2485, Jun. 2009.
[4] R. Ramesh and N. A. Spaldin, “Multiferroics: progress and prospects in thin films,” *Nat. Mater.*, vol. 6, no. 1, pp. 21–29, Jan. 2007.
[5] W. Eerenstein, N. D. Mathur, and J. F. Scott, “Multiferroic and magnetoelectric materials,” *Nature*, vol. 442, no. 7104, pp. 759–765, Aug. 2006.
[6] Q. He, Y.-H. Chu, J. T. Heron, S. Y. Yang, W. I. Liang, C. Y. Kuo, H. J. Lin, P. Yu, C. W. Liang, R. J. Zeches, W. C. Kuo, J. Y. Juang, C. T. Chen, E. Arenholz, A. Scholl, and R. Ramesh, “Electrically controllable spontaneous magnetism in nanoscale mixed phase multiferroics,” *Nat. Commun.*, vol. 2, p. 225, Mar. 2011.
[7] S. Prosandeev, D. Wang, W. Ren, J. Íñiguez, and L. Bellaiche, “Novel Nanoscale Twinned Phases in Perovskite Oxides,” *Adv. Funct. Mater.*, vol. 23, no. 2, pp. 234–240, Jan. 2013.

Emergence of long-range order in $BaTiO_3$ from local symmetry-breaking distortions

M. S. Senn,[1,*] D. A. Keen,[2] T. C. A. Lucas,[3] J. A. Hriljac,[3] and A. L. Goodwin[1]

[1]Department of Chemistry, Inorganic Chemistry Laboratory,
University of Oxford, South Parks Road, Oxford OX1 3QR, United Kingdom
[2]ISIS, Rutherford Appleton Laboratory, Harwell Oxford, Didcot OX11 0QX, United Kingdom
[3]School of Chemistry, University of Birmingham,
Edgbaston, Birmingham, B15 2TT, United Kingdom

arXiv:1512.03643

The study of displacive phase transitions has been exceptional fruitful. Both Landau-Ginzburg theory and the theory of soft-mode phase transitions frequently provide a very good description for many phase transitions in perovskites and related materials. The study of the microscopic structure of these materials and the relationship to the macroscopic observable property has been greatly aided by two factors. 1) Crystallography is now a mature field, allowing for the precise determination of the microscopic distortions arising as a result of subtle displacive phase transitions. 2) The studies of global lattice and electronic instabilities benefits from the fact that global symmetry breaking (an order parameter) has been well classified in terms of irreducible representations of the parent symmetry space, which themselves have a correspondence with the eigenvectors (harmonic phonons) of the system under study.

However, many macroscopic observables are a result of emergent phenomena driven by local ordering which combine in often counter-intuitive ways to produce the global symmetry of the structure and hence the local symmetry effectively controls the physical property. Here the global symmetry is at odds with the local symmetry and a phenomenological model based around a macroscopic (or crystallographic) parameter will not lead to a valid physical insight into the phase transition. Hence, microscopic studies of local symmetry-breaking are vitally important if physical understanding is to be gained into these “order-disorder” phase transitions. The lack of sensitivity of conventional crystallographic methods to local order, and their correlated disorder, presents a bottle neck to the study of such systems.

Here I will demonstrate that, by using a symmetry motivated basis to evaluate local distortions against pair distribution function data (PDF), we can gain new insight into the archetypal ferroelectric $BaTiO_3$ in which the existence of order-disorder phase transitions has been widely debated. I will show without prior bias, that the off-centre Ti displacements in $BaTiO_3$ are zone centred and rhombohedral-like in nature across all of its known ferroelectric and paraelectric phases, contrary to the macroscopic polarisation direction in all but its lowest temperature phase.

With this newly-gained insight I will show how a simple Monte Carlo (MC) model, capturing our main experimental findings, can reproduce the rich crystallographic phase diagram of $BaTiO_3$ (see Figure 1). The results demonstrate how this complex phase diagram may emerge from correlations of local symmetry-breaking distortions alone. The MC model, which reproduce the experimentally observed diffuse scattering, strongly support the order-disorder picture for these phase transitions, but can also be reconciled with the soft-mode theory of $BaTiO_3$ that is supported by some spectroscopic techniques.

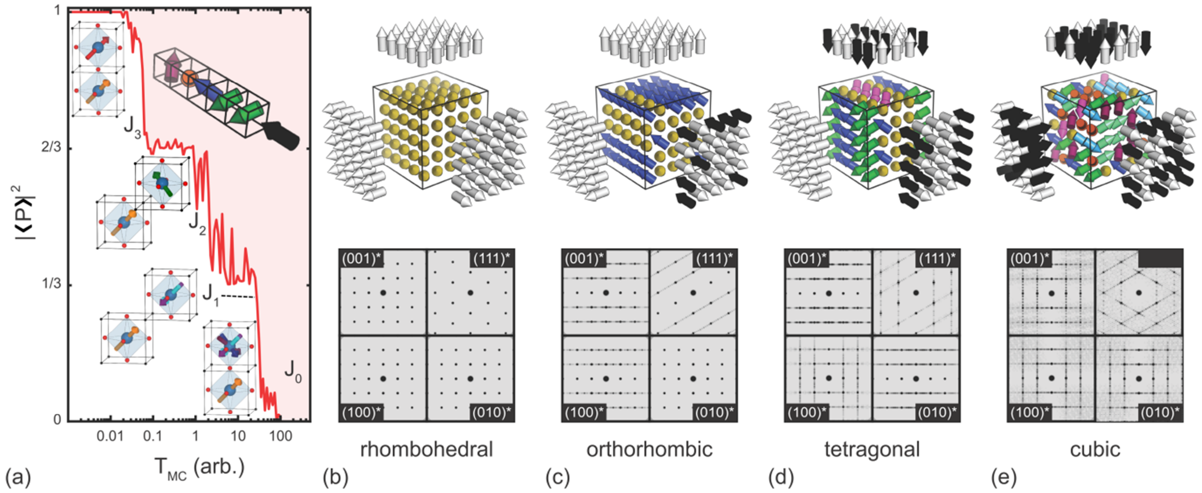

Figure 1. a) MC simulation reproducing the tetragonal, orthorhombic and rhombohedral phase transitions, with the square of the average polarization serving as an order parameter. Insets below the polarization line show a graphical visualization for the relevant interactions penalized by our Hamiltonian, shown at the temperatures their energy scales become important in the MC simulation, and above the line, a representation of the chain like correlations present in the cubic phase (J_0, hardwired into our simulations) showing how the projection of the polarization along the direction of a chain is always preserved (black arrow). b)-e) a portion of an MC configuration for each phase, along with their polar vector projections along <1 0 0> directions, and their calculated diffuse scattering in the planes indicated. The polar vector projections (white and black arrows) represent columns of Ti displacements all with a common component along the chain, and it is this inter-chain disorder which gives rise to diffuse planes of scattering in reciprocal space. Inter-chain disorder in the cubic phase in all three <1 0 0> directions, leads to three sets of intersecting orthogonal diffuse scattering planes in reciprocal space, and each successive phase transition represent inter-chain orderings occurring along successive <1 0 0> directions.

The fundamental insight gain in this study into $BaTiO_3$ highlights the importance of this methodology for determining local symmetry in order-disorder phase transitions, and demonstrates its power when coupled to MC simulations.

Ferroelectric-like poling in paraelectric system

Stella Skiadopoulou[1], *Stanislav Kamba*[1], *Jan Drahokoupil*[1], *Jan Kroupa*[1], *Nitin Deepak*[2], *Martyn E. Pemble*[2,3] *and Roger W. Whatmore*[3,4]

[1]Institute of Physics, Czech Academy of Sciences, Prague, Czech Republic
[2]Tyndall National Institute, University College Cork, Cork, Ireland
[3]Department of Chemistry, University College Cork, Cork, Ireland
[4]Department of Materials, Imperial College, London, UK
E-mail: stella@fzu.cz

Very recently there was a report of switchable ferroelectric polarization in 1.6 % tensile-strained TiO_2 thin film with anatase crystal structure (a-TiO_2) using piezoresponse force microscopy (PFM).[1] The polarization disappeared only above 450 K, which was assigned as a Curie temperature, T_C. We performed X-ray diffraction, second-harmonic generation (SHG) and infrared investigations of the same films. None of the above studies revealed any hint of ferroelectric phase transition in strained a-TiO_2 film.[2] We claim that previously reported polarization is defect and/or electrochemically induced, in spite of the fact that it was stable with time at elevated temperatures. Our results can be generalized also on other dielectric systems: Observation of poling and ferroelectric hysteresis loop cannot be taken as conclusive evidence of presence of ferroelectricity. Other experiments like X-ray diffraction, SHG and lattice dynamic studies are always necessary.

A polar piezoelectric domain structure and electrically switchable polarization (hysteresis loops) were observed by the use of piezoresponse force microscopy by Deepak *et al.*,[1] for film thicknesses varying from 20 to 100 nm and reported as possible evidence for ferroelectric behavior. The induced tensile strains from $NdGaO_3$ (NGO) substrate were approximately 1.67%, 1.44% and compressive -1.57 % for the *a*-, *b*- and *c*-axis respectively for the case of 20 nm – thick films. The ferroelectric polarization was observed out-of-plane, i.e. along *c*-axis, and was stable against prolonged exposure to elevated temperature, implying a non-electrochemical origin for the effects observed, but disappeared on heating above 450 to 460 K, implying the possible existence of a Curie point, T_C (Fig. 1).

Our infrared reflectance studies show no shifts of E_u phonon frequencies with strain and heating, as can be seen in Fig. 2(a) in the temperature dependence of dielectric loss spectra of 20 nm thin film with approximately 1.6 % tensile strain. For that reason the hypothetical phase transition cannot be a displacive ferroelectric one, even if we cannot directly measure the A_{2u} symmetry soft phonon polarized along expected ferroelectric axis. If the material is ferroelectric, its phase transition can only be of order-disorder type, where the structural change is driven by a soft dielectric relaxation with relaxation frequency below optical phonon frequencies.

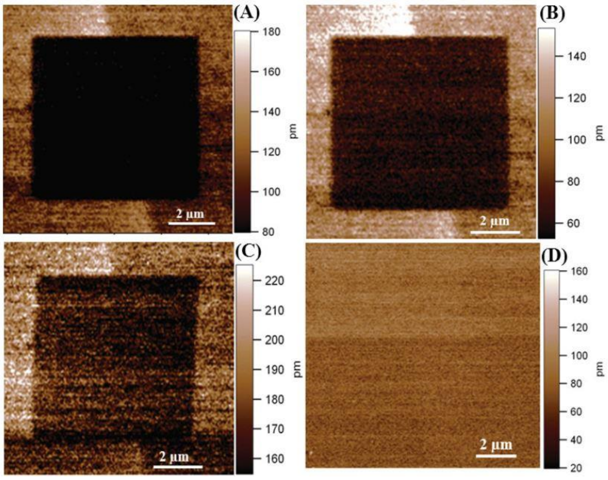

Figure 1 PFM amplitude images of a poled region (10 µm × 10 µm; +30 V DC bias) of 20 nm a-TiO_2/$NdGaO_3$ at: A) 370 K, B) 420 K, C) 450 K and 470 K. The amplitude of the poled region vanishes on heating to temperatures higher than 450 K. This observation points towards the Curie temperature for ferroelectric a-TiO_2 lying between 450 and 470 K.

X-ray diffraction measurements of the *c*-lattice parameter did not reveal any anomaly up to 620 K, typical for a structural phase transition (Fig. 2(b)). Moreover, room-temperature SHG measurements did not reveal any signal typical for broken inversion symmetry in ferroelectric phase, although the SHG method is in principle sensitive on a small inversion-symmetry breaking in spin-induced ferroelectrics.

Our results do not support, within the accuracy of our measurements, the existence of ferroelectric phase transition in tensile-strained a-TiO_2 thin films. One can speculate that the switchable ferroelectric response can be caused by electric-field induced migration of various defects (oxygen or Ti vacancies, Ti in interstitial positions etc. – see e.g. review of Szot et al.[3]). It was demonstrated e.g. in non-ferroelectric $SrTiO_3$ that bias-induced defect migration can give rise to an apparent polarization or piezoelectric hysteresis loops, which are difficult to distinguish from true ferroelectric hysteresis loops.[3–5] Nevertheless, in this case the polarization should decay with time, but as reported in Ref. [1] the poled domains in a-TiO_2 were stable for more than 48 h at 300 K. The lack of decay of polarization with time observed at elevated temperatures did not support the idea of defect migration in electric field.

One can claim that ferroelectric polarization is very small in a-TiO_2 films and therefore the expected SHG signal is too weak to be detected in the thin films. Here we can argue that the polarization in a-TiO_2 should be robust according to Ref. [1], because there is no report of piezoelectric hysteresis loops observed by the use of PFM in weak ferroelectrics.

We can summarize that our SHG, XRD and lattice dynamics studies do not support a ferroelectric phase transition in tensile-strained a-TiO2 film. There are two possible explanations: the ferroelectric distortion is too small (less than 0.05 μC/cm^2) and cannot be detected by the SHG and XRD techniques used, or the piezoelectric response reported in Ref. [1] is defect and/or electric field induced, in spite of the fact that it was stable with time at elevated temperatures.

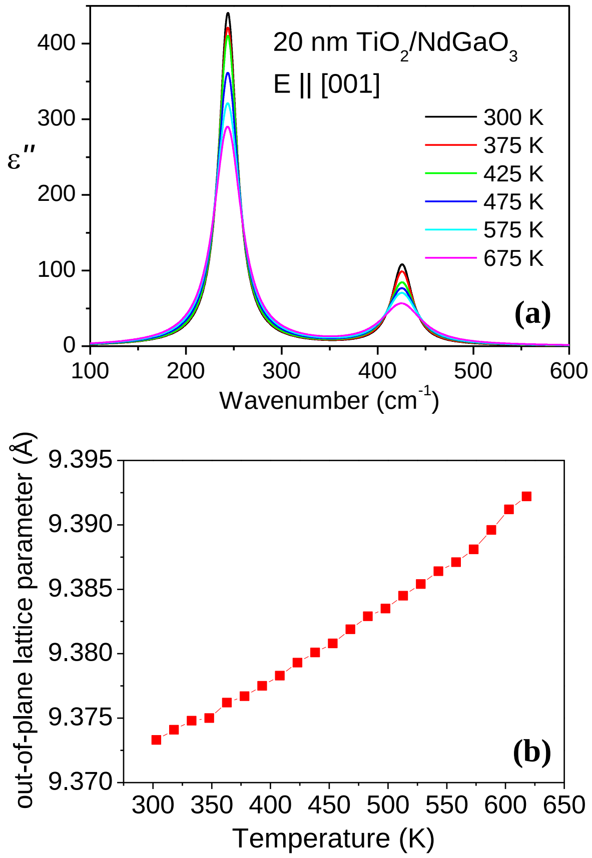

Figure 2 **(a)** Dielectric loss spectra calculated from temperature-dependent reflectance spectra of 20 nm thin film of a-TiO_2. **(b)** Out-of-plane lattice parameter of a-TiO_2/NGO as a function of temperature, as measured by X-ray diffraction, from room temperature up to 618 K. Error bars have the same size as the symbols. No anomaly near expected $T_C = 450$ K is seen.

[1] N. Deepak, M.A. Caro, L. Keeney, M.E. Pemble, and R.W. Whatmore, Adv. Funct. Mater. **24**, 2844 (2014).

[2] S. Skiadopoulou, S. Kamba, J. Drahokoupil, J. Kroupa, N. Deepak, M.E. Pemble, and R.W. Whatmore, Adv. Funct. Mater. (2015). DOI: 10.1002/adfm.201502441

[3] K. Szot, G. Bihlmayer, and W. Speier, in *Solid State Phys.* (2014), pp. 353–559.

[4] S. Jyotsna, A. Arora, J.S. Sekhon, and G. Sheet, J. Appl. Phys. **116**, (2014).

[5] N. Balke, P. Maksymovych, S. Jesse, A. Herklotz, A. Tselev, C.-B. Eom, I.I. Kravchenko, P. Yu, and S. V Kalinin, ACS Nano **9**, 6484 (2015).

Structure of color centers in $BaTiO_3$ and $SrTiO_3$ doped with cobalt

A. I. Lebedev and I. A. Sluchinskaya

Physics Department, Moscow State University, Moscow, 119991, Russia

Ferroelectric perovskites have recently attracted much attention because of their possible use in solar energy converters based on the bulk photovoltaic effect. Since the perovskite oxides have a relatively large band gap (~3 eV), to tailor their absorption spectra to the spectrum of solar radiation they can be doped with 3*d* elements which create so-called color centers [1]. Recently [2] it was experimentally shown that doping $SrTiO_3$ with 3*d* elements results in a strong absorption in the visible region of the spectrum. Unfortunately, $SrTiO_3$ is an incipient ferroelectric and its doping with cobalt does not result in ferroelectricity. That is why it is more interesting to study the properties of ferroelectric $BaTiO_3$ doped with cobalt in the hope that its absorption spectra can be fitted to the spectrum of the sunlight. In this case, new material suitable for solar energy converters based on the bulk photovoltaic effect will be proposed.

Since the electronic transitions in impurity color centers are determined by the oxidation state of an impurity and the microscopic structure of these centers, in this work we use the XAFS-spectroscopy technique to determine the oxidation state of the Co impurity in $BaTiO_3$ and $SrTiO_3$. These results are used to propose a model of the impurity color centers, and the calculations of their electronic structure are used to explain the observed optical properties.

Dark-brown samples of $SrTiO_3$, $BaTiO_3$, and $Ba_{0.8}Sr_{0.2}TiO_3$ doped with 0.5–3% Co were prepared by the solid state reaction method at 1100–1500°C. The composition of samples was deliberately shifted from stoichiometry toward excess Ba(Sr) in order to incorporate the impurity into the *B* site. Since the structure of $BaTiO_3$ may change from cubic to hexagonal upon doping with 3*d* elements, 20% of $SrTiO_3$ were added to $BaTiO_3$ to retain the cubic structure. According to X-ray diffraction, all studied samples had a cubic ($SrTiO_3$, $Ba_{0.8}Sr_{0.2}TiO_3$) or hexagonal ($BaTiO_3$) perovskite structure at 300 K. $SrTiO_3$ and $BaTiO_3$ samples doped with Co were single-phase; in the sample $Ba_{0.8}Sr_{0.2}TiO_3$(3%Co) contained a small amount of the Ba_2TiO_4 second phase.

X-ray absorption spectra in the EXAFS and XANES regions were recorded in fluorescence mode in the vicinity of the Co *K* edge (7.709 keV) at 300 K on the KMC-2 station of the BESSY synchrotron radiation source. Isolation of the oscillatory EXAFS function $\chi(k)$ from the fluorescence excitation spectra was performed in a traditional way. For each sample 3–4 spectra were recorded, they were then independently processed, and the resulting $\chi(k)$ curves were averaged.

To determine the oxidation state of cobalt in $SrTiO_3$, $Ba_{0.8}Sr_{0.2}TiO_3$, and $BaTiO_3$, the position of the absorption edge in XANES spectra of these samples was compared with the edge positions in the $LaCoO_3$ and $Co(NO_3)_2 \cdot 6H_2O$ reference compounds (Fig. 1). An analysis of these spectra shows that the oxidation state of Co in $SrTiO_3$ is 3+, whereas in $BaTiO_3$ and $Ba_{0.8}Sr_{0.2}TiO_3$ cobalt is in a state intermediate between 2+ and 3+. The impurity concentration has little effect on its oxidation state, as well as the addition of 20% of strontium to barium titanate.

To determine the structural position and local environment of Co in $SrTiO_3$, $Ba_{0.8}Sr_{0.2}TiO_3$, and $BaTiO_3$, their EXAFS spectra were analyzed. The best agreement between the calculated and experimental spectra was obtained in a model in which Co replace Ti^{4+} ions. The Co-O distance to the nearest oxygen atoms is 1.92 Å in $SrTiO_3$ and ~2.06 Å in $Ba_{0.8}Sr_{0.2}TiO_3$. Comparison of the obtained interatomic distances with known values of ionic radii suggests that in $SrTiO_3$ cobalt is predominantly in the low-spin 3+ oxidation state, whereas in hexagonal $BaTiO_3$ and cubic $Ba_{0.8}Sr_{0.2}TiO_3$ it is simultaneously in 2+ and 3+ oxidation states, predominantly in high-spin configuration. This conclusion is consistent with the XANES data.

The first-principles calculations were performed on 80-atom FCC supercells, in which one of the Ti atoms was substituted by the Co atom. The calculations were performed using the ABINIT program and PAW pseudopotentials within the LDA+U approximation for Co^{3+} and Co^{2+} ions in both high-spin and low-spin configurations. The parameters describing the Coulomb and exchange interaction inside the d shell were $U = 5$ eV and $J = 0.9$ eV.

The calculations showed that for both oxidation states, the low-spin configuration is energetically more favorable compared to the high-spin one. For the Co^{3+} ion in the low-spin configuration, the predicted interatomic Co-O distances are 1.920 Å for $SrTiO_3$ and 1.985 Å for $BaTiO_3$. A good agreement with the results of the EXAFS data is observed only for strontium titanate. However, if one looks at the results of calculations for a high-spin cobalt configuration in $BaTiO_3$(Co), the predicted Co-O distances of 2.047 Å for Co^{3+} and 2.096 Å for Co^{2+} are much closer to the distance observed in experiment.

The calculations of site-projected partial density of states (DOS) show that cobalt creates a narrow (~0.2 eV) impurity band in the forbidden gap of $SrTiO_3$ and $BaTiO_3$. For the low-spin (diamagnetic) Co^{3+} configuration, this impurity band is located near the valence band and is separated from it by a narrow gap (in $SrTiO_3$) or is merged with it (in $BaTiO_3$). For this configuration, the Fermi level is located near the middle of the forbidden gap. Adding of one more electron to the system in order to obtain Co^{2+} configuration moves the Fermi level into the conduction band without noticeable changes of the DOS. Despite the odd number of electrons, this configuration remains diamagnetic. It is seen that this low-spin configuration cannot explain the changes in color of doped samples. For the high-spin (paramagnetic) Co^{3+} and Co^{2+} configurations, the DOS is significantly changed, and a narrow impurity band for spin-down states which are partially occupied by electrons appears slightly below the middle of the forbidden gap (Fig. 2). The optical transitions between this impurity band (in which Co 3d and O 2p states are strongly hybridized) and the band edges are allowed by selection rules and can be responsible for the intense light absorption observed in doped samples at the energies well below the band gap. So we can conclude that intense light absorption in Co-doped samples is associated with the existence of high-spin Co^{3+} or Co^{2+} states; the appearance of the high-spin configurations is possible at 300 K because of the low energy difference between the low-spin and high-spin states.

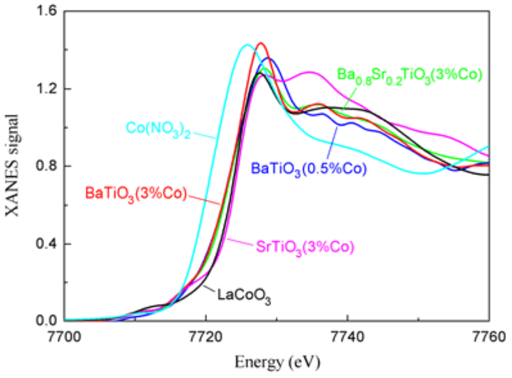

Fig. 1. XANES spectra for four investigated samples and two reference compounds.

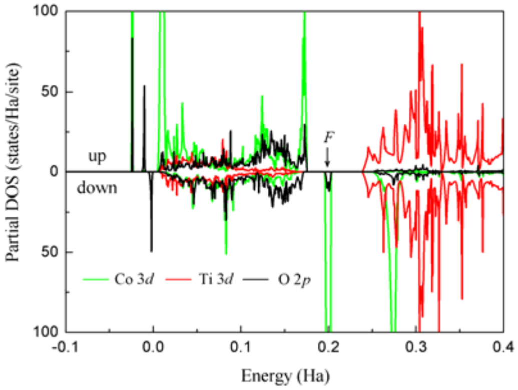

Fig. 2. Site-projected density-of-states for Co^{3+}-doped $BaTiO_3$ in the high-spin configuration.

Acknowledgment. This work was supported by RFBR Grant No. 13-02-00724. The authors are grateful to the BESSY staff for fruitful collaboration.

References

[1] G. Blasse, P. H. M.de Korte, A. Mackor. *J. Inorg. Nucl. Chem.* **43**, 1499 (1981).
[2] I. A. Sluchinskaya, A. I. Lebedev, A. Erko. *Phys. Solid State* **56**, 449 (2014).

Dielectric, IR and Raman spectroscopic studies of NBT based solid solutions

Š. Svirskas[1], J. Banys[1], A. Kežionis[1], M. Dunce[2], E. Birks[2], T. Ostapchuk[3], J. Pokorný[3], S. Kamba[3]

[1]*Faculty of Physics, Vilnius University, Sauletekio av. 9/3b., Vilnius, LT-10222, Lithuania*
[2]*Institute of Solid State Physics, University of Latvia, Kengaraga 8, Riga, Latvia, LV-1063*
[3]*Institute of Physics, Czech Academy of Sciences, Na Slovance 2, 182 21 Prague 8, Czech Republic*

email: sarunas.svirskas@ff.vu.lt

Sodium bismuth titanate ($Na_{0.5}Bi_{0.5}TiO_3$ - NBT) is well renowned perovskite which is extensively studied due to its promising piezoelectric properties [1]. It is believed that NBT along with KNN are piezo-materials which are capable to match the properties of PZT.

The pure NBT undergoes a fascinating sequence of phase transitions which is thoroughly studied by various techniques. Furthermore, NBT has dispersion at room temperature which resembles the dispersion in canonical relaxors like PMN [2]. But the main difference is that in NBT the dispersion extends in rather narrow frequency range. It lies in the frequency region below 1 MHz which is not the same as in canonical relaxors where the dispersion lies in very broad frequency range (i. e. 12 orders of magnitude).

One of the attractive features of sodium bismuth titanate is that it can form solid solutions quite easily with other compounds. This allows one to tune the properties of NBT and diminish its unwelcomed properties for piezoelectric applications. This route was applied to reduce the conductivity of pure NBT.

Usually, the solid solutions of NBT exhibit relaxor behaviour with broad dispersion. However, it has some different features compared to canonical relaxors. It is not always possible to induce ferroelectric phase transition with electric field in such solid solutions (this is observed in some of the NBT solid solutions with strontium titanate [3]).

This contribution is dedicated to the study of NBT-based solid solutions with A site disorder. The two systems under investigation are $(0.4\text{-}y)Na_{0.5}Bi_{0.5}TiO_3\text{-}0.6SrTiO_3\text{-}yPbTiO_3$ (NBT-ST-PT) and $xNa_{0.5}Bi_{0.5}TiO_3\text{-}(1\text{-}x)Sr_{0.7}Bi_{0.2}TiO_3$ (NBT-SBT). The work is concentrated on several experimental techniques: broadband dielectric spectroscopy, Raman Spectroscopy, FT Infrared spectroscopy and also ferroelectric hysteresis. The experiments were performed in 30 – 500 K temperature interval.

The features and peculiarities of relaxor behaviour in investigated compounds will be discussed. NBT-ST-PT system shows crossover from relaxor/glassy state to the ferroelectric state which is followed by the 1st order phase transition to relaxor phase. Temperature dependencies of large signal d_{33} and pyrocoefficient shows maximal values in the concentration region where pure relaxor state is observed (but not far from the concentrations where 1st order PT appears).

Temperature dependencies of large signal d_{33} and pyro-coefficient will be presented as well. Figure 1 represents temperature dependences of pyro coefficient which indicates that the sample for which it is possible to induce ferroelectric phase transition has the largest anomaly. Similar result is reflected in large signal d_{33} measurements (largest relative displacement in relaxor sample). Figure 2 represents temperature dependence of dielectric permittivity for the sample which has largest anomaly of pyro coefficient (i. e. 0.3NBT-0.6ST-0.1PT). Relaxor-like dispersion is observed in the sample from low frequencies up to 300 GHz frequency.

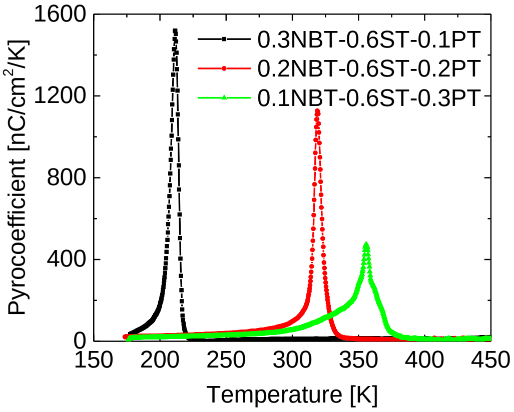

Figure 1 Temperature dependence of pyro coefficient in (0.4-y)NBT-0.6ST-yPT system

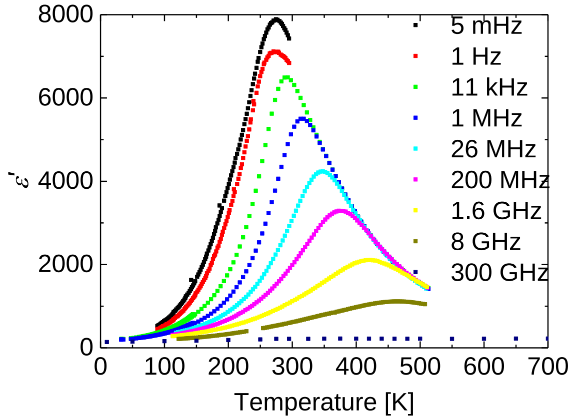

Figure 2 Temperature dependence of dielectric constant ε' at different frequencies for sample 0.3NBT-0.6ST-0.1PT

Finally, NBT-SBT system shows interesting relaxation behaviour. Two relaxation components exist in all compositions and they are well observed in the experimental spectra. Apparently, these two relaxations are coupled and their concentration dependence of activation energy and freezing temperature obtained from Vogel-Fulcher law shows peculiar behaviour. Earlier microwave and THz data on pure NBT showed evidence of two relaxations as well [4].

References

1. Roedel et al. *J. Amerc Ceram. Soc.*, vol. 92(6) 1153-1177 (2009);
2. Bokov, Ye *J. Mat. Sci.*, vol. 41(1), 31-52 (2006);
3. Krauss et al. *J. Eur. Ceram. Soc.*, vol. 30(8), 1827-1832 (2010);
4. Petzelt et al. *Phase transitions*, vol. 87(10-11), 953-965 (2014);

First-principles Studies of Effects of Defects on Reversible Electro-Strain Coupling in $BaTiO_3$

H. Takenaka[1], S. Liu[1] and R. E. Cohen[1,2]
[1] *Extreme Materials Initiative, Carnegie Institution for Science, Washington D.C. 20015, USA*
[2] *Department für Geo-und Umweltwissenchaften, Ludwig-Maximilians-Universitaet, Munich, Germany*

(Dated: December 3, 2015)

Ferroelectric materials possessing switchable spontaneous polarization have a wide range of applications. The strain of a ferroelectric crystal will change during a non-180° switching due to the exchange of nonequal crystallographic axes. However, the electric field-induced large strain change accompanied by non-180° switching is usually an one-time effect as the switching is not reversible once the field is removed.

The properties of ferroelectrics can be engineered by simple doping in a controllable way. Previous experimental studies demonstrated that doping perovskite ferroelectrics with Mn could significantly improve their electromechanical properties [1–4]. Furthermore, Ren [5] and his co-worker [6] showed that a reversible giant electron-strain coupling can be realized in alkaline-metal and transition-metal doped $BaTiO_3$ (BTO) through a defect-dipole-assisted reversible domain switching. It is proposed that the built-in electric field arising from dopant-vacancy pairs can serve as the driving force for recovering the initial strain state when the external electric field is turned off (FiG. 1).

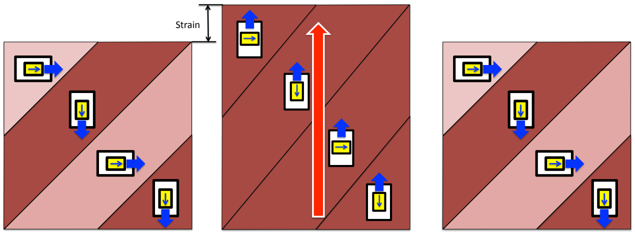

FIG. 1. Schematic illustration of defect-dipole-assisted reversible domain switching [5]. The left panel is the structure with 90° domains before electric field is applied. Thin blue and thick blue arrows denote the defect dipoles and bulk spontaneous polarization, respectively. The middle panel shows domain switching under electric field (red arrow). The defect dipoles do not change directions due to slow vacancy migrations. The 90° domain switching gives large strain change. When the electric field is turned off, the domains switch back to their initial states, shown in the right panel.

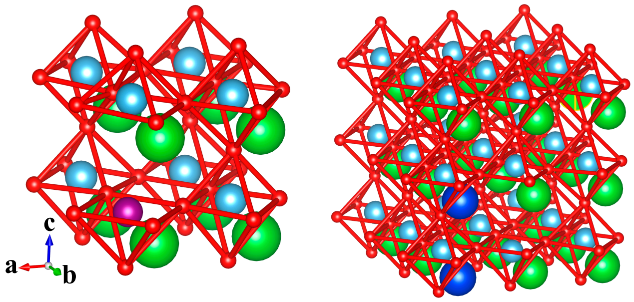

FIG. 2. The structures of Mn-doped and K-doped BTO in left panel and right panel, respectively. The left panel is for Mn-doped BTO. Green, purple, blue, cyan, and red balls denote Ba, Mn, K, Ti, and O atoms, respectively.

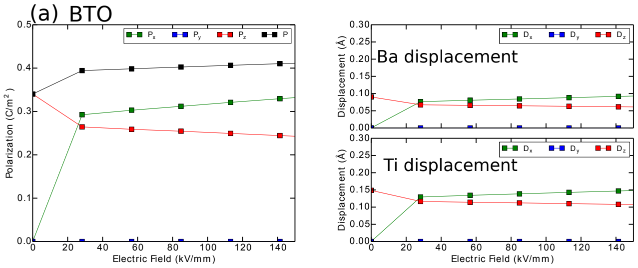
(a) BTO

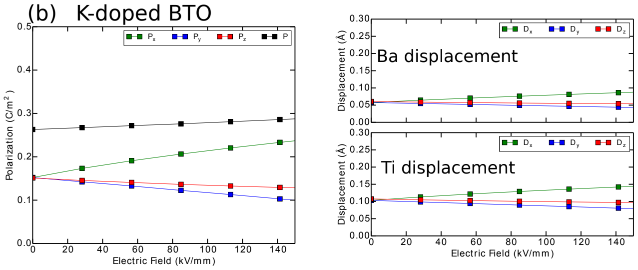
(b) K-doped BTO

FIG. 3. Evolution of polarization and atomic displacements under an electric field along x axis for (a) pure tetragonal BTO and (b) K-doped BTO.

Despite active experimental studies, there is still a lack of first-principles-supported microscopic understanding of the roles of defect dipoles in reversible domain switching. In our earlier work [7], we find that Mn ions in BTO can exist in oxidation states of Mn^{2+} and Mn^{4+} depending on the environment, with the charge compensated by an oxygen vacancy which favorably occupies the nearest apical site of the oxygen octahedral cage, as shown in FIG. 2. This results in a defect dipole aligned along with the spontaneous bulk polarization, in a good agreement with Ren's proposal. In this work, we explore the intrinsic effects of dopant-vacancy pairs on the 90° switching process in both Mn-doped (B-site doped) and K-doped (A-site doped) $BaTiO_3$ with first-principles density functional theory (DFT). The $U = 4.6$ and $J = 1.0$ eV [8] are used for the strongly correlated electrons of Mn^{2+}. The effect of electric field

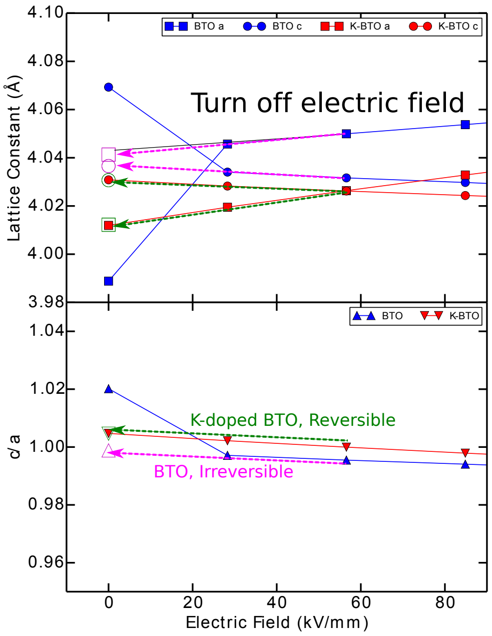

FIG. 4. The change of lattice constants (Top) and c/a (Bottom) as a function of electric field along x. Open symbols show the lattice constants and c/a value after the electric field is turned off.

(E) is modeled in DFT by adding extra force $f_{atom,i}$ on each atom, $f_{atom,i} = Z^*_{atom,i} \times E$, with values of the effective charges Z^* calculated from first-principles perturbation theory [9].

Figure 3 shows the change of polarization and atomic displacements during the 90° switching process for pure tetragonal BTO and K-doped BTO. We find that the tetragonal BTO evolve into an orthorhombic phase under an electric applied along the x axis. This is also found for Mn-doped BTO. The switching is characterized with a sharp change in polarization. It is noted that at 0 K, the tetragonal BTO is at a saddle point of the potential energy surface, with the rhombohedra and orthorhombic phases lower in energy. Further investigations are required to relate this 0 K switching process to the switching mechanism occurred at room temperature under which BTO adopts a tetragonal structure. The K-doped BTO exhibits decisively different local structures and switching behavior. We find that the optimized ground state for K-doped BTO is better categorized as a rhombohedra phase based on the polarization and atomic displacements, despite the lattice constants still possess tetragonal crystal symmetry. The presence of an electric field along x rotates the polarization, with the magnitude changing smoothly.

We further examine the strain change induced by the electric field. As shown in Figure 4, both pure BTO and K-doped BTO exhibit large electro-strain coupling. However, for pure BTO, once the field is turned off, the c/a ratio is not recovered, and the structure is trapped at an orthorhombic phase at 0 K. We also found similar trapping in Mn-BTO. The observed irreversible strain change for tetragonal BTO and Mn-doped BTO at 0 K via DFT again needs further investigation due to the saddle point issue discussed above. To the contrary, K-doped BTO shows reversible electro-strain coupling even at 0 K.

In summary, our first-principles studies suggest that it is possible to achieve giant reversible electro-strain coupling via doping. The dopants could strongly modulate the local structures and the energetics of different phases, which underlies the origin of recoverable strain change after non-180° switching.

Acknowledgement This work was supported by the Office of Naval Research under grant number N00014-14-1-0561, and we acknowledge support of the Carnegie Institution and the European Research Council Advanced Grant ToMCaT. Computational support was provided by the HPCMO of the U.S. Department of Defence.

[1] P. Lambeck and G. Jonker, Ferroelectrics **22**, 729 (1978).
[2] T. Kamiya, T. Suzuki, T. Tsurumi, and M. Daimon, Japanese Journal of Applied Physics **31**, 3058 (1992).
[3] S. Wu, S. Wang, L. Chen, and X. Wang, Journal of Materials Science: Materials in Electronics **19**, 505 (2008).
[4] E. Perez-Delfin *et al.*, Journal of Applied Physics **110**, 034106 (2011).
[5] X. Ren, Nature materials **3**, 91 (2004).
[6] L. X. Zhang and X. Ren, Phys. Rev. B **71**, 174108 (2005).
[7] J. F. Nossa, I. I. Naumov, and R. E. Cohen, Phys. Rev. B **91**, 214105 (2015).
[8] D. Kasinathan, K. Koepernik, and W. E. Pickett, New Journal of Physics **9**, 235 (2007).
[9] P. Ghosez, J.-P. Michenaud, and X. Gonze, Physical Review B **58**, 6224 (1998).

Ab Initio Modelling of the Magnetoelectric Response in Cr_2O_3

Natalie Tillack[*] and Jonathan R. Yates
Department of Materials, University of Oxford, Oxford, OX1 3PH, United Kingdom

Paolo G. Radaelli
Department of Physics, University of Oxford, Oxford, OX1 3PU, United Kingdom

The appearance of toroidal moments in the spinflop case of Cr_2O_3, the influence of pressure on the magnetoelectric response, and the numerical dependence of different exchange-correlation functionals on the coupling tensor.

The search for magnetoelectric (ME) materials, i.e. materials that respond with a polarisation upon application of an external magnetic field and vice versa, has received a lot of attention in recent years [1–4] - both as a standalone property [5–7] and as part of the cross-coupling in modern multiferroics [8]. The linear ME coupling can be described by an axial rank-two tensor:

$$\alpha_{ij} = \left(\frac{\partial P_i}{\partial H_j}\right) = \mu_0 \left(\frac{\partial M_j}{\partial \epsilon_i}\right) \tag{1}$$

with $\mathbf{P}$ ($\mathbf{M}$) being the induced polarisation (magnetisation), $\mathbf{H}$ ($\boldsymbol{\epsilon}$) the external magnetic (electric) field, and μ_0 as the magnetic permittivity. Cr_2O_3 was the first material to be predicted – solely on the grounds of symmetry considerations [9, 10] – and later demonstrated experimentally [11, 12]. Even though its coupling is comparatively weak, it is a useful material to study. Firstly, it is the subject of many experimental studies, so that data is plentiful. Secondly, it is the ideal prototype to study the fundamental mechanisms behind magnetoelectricity: it is not multiferroic, and – because of its magnetic point group – exhibits neither higher-order ME coupling nor piezomagnetic interactions. The magnetic ground state structure of Cr_2O_3 is shown in the left panel of Fig. 1. Below the Nèel temperature of $T_N = 308\,\mathrm{K}$ it orders in the G-type AFM magnetic structure with the spins aligned along the rhombohedral z-axis. Group-theoretical analyses find that its magnetic point group $\bar{3}'m'$ allows for the ME coupling tensor shown in the left panel of table I.

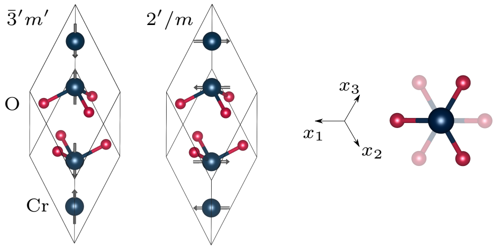

FIG. 1: Structures of Cr_2O_3. Left panel: Rhombohedral primitive cell of Cr_2O_3 with arrows indicating the AFM coupled Cr magnetic moments along z. The magnetic point group is $\bar{3}'m'$. Two 180° domains are possible, linked via time reversal. Middle panel: The $2'/m$ spinflop state, with spins aligned in the basal plane, thus breaking the threefold symmetry. Right panel: View along the z-axis (the half-transparent O atoms belong to the "lower" structural unit). 3 inequivalent coordinate systems can be defined with the x_i pointing along each of the O atoms and the orthogonal y_i accordingly. Figures plotted with VESTA [13].

TABLE I: Tensor forms of the Cr_2O_3 ground state magnetic structure (left) and the two spinflop cases (right).

$\bar{3}'m'$	$2'/m$	$2/m'$
$\begin{pmatrix} \alpha_{11} & 0 & 0 \\ 0 & \alpha_{11} & 0 \\ 0 & 0 & \alpha_{33} \end{pmatrix}$	$\begin{pmatrix} 0 & \alpha_{12} & \alpha_{13} \\ \alpha_{21} & 0 & 0 \\ \alpha_{33} & 0 & 0 \end{pmatrix}$	$\begin{pmatrix} \alpha_{11} & 0 & 0 \\ 0 & \alpha_{22} & \alpha_{23} \\ 0 & \alpha_{32} & \alpha_{33} \end{pmatrix}$

From a modelling standpoint, the ME response can be split into four parts: the lattice and the electronic part (representing the mechanism that makes the external field couple to the system), and the spin and orbital part (distinguishing between the characteristics of the magnetic properties). The spin-lattice contribution of the ME coupling in Cr_2O_3, $\boldsymbol{\alpha}^{\mathrm{latt}}$, has been shown to be the most significant [14]. In this work, $\boldsymbol{\alpha}^{\mathrm{latt}}$ is determined by expanding the macroscopic response into microscopic quantities according to Ref. [15]:

$$\alpha^{\mathrm{latt}}_{kl} = \frac{\partial P_k}{\partial H_l} = \left(\frac{\partial P_k}{\partial u_i}\right)\left(\frac{\partial u_i \partial u_j}{\partial E}\right)\left(\frac{\partial F_j}{\partial H_l}\right) \tag{2}$$

with the indices $k, l = 1, 2, 3$ and the composite indices (accounting for three directional dimensions and the number of atoms in the unit cell N) $i, j = 1, \ldots, 3N$. Here, the lattice response depends linearly on the force-constant matrix inverse $K^{-1}_{ij} = \frac{\partial u_i \partial u_j}{\partial E}$, the Born effective charges (BEC) Z^{e}_{ki}, and the dynamical magnetic charges. The latter can be understood as the magnetic analogue of the BEC and are defined as the derivative of the ionic forces with respect to a magnetic field, $Z^{\mathrm{mag}}_{il} = \frac{\partial F_i}{\partial B_l}$. A Zeeman field was implemented in the Density Functional Theory (DFT) codes used.

On this basis, we conducted a thorough first-principles study of Cr_2O_3, expressing the contributions to eq. 2 in the basis of its IR active modes. Close attention was paid to the numerics; the influence of different exchange-correlation functionals has been studied, shedding light on the quantities that have the most impact on the overall tensor. Secondly, trends were derived for the size of the ME response under pressure.

The present work's main focus however was the fundamental understanding on how the appearance of a toroidal moment influences the magnetoelectric response. Under strong magnetic fields along the rhombohedral z-axis, Cr_2O_3 undergoes a first-order phase transition into its so-called *spinflop* case, with spins still aligned in the G-type AFM state, but directed in the basal plane [16]. The spinflop (SF) phase also exhibits the magnetoelectric effect and the motivation to apply the recently developed *ab initio* methods to model it is threefold; it clarifies the directions of the Cr magnetic moments, provides the ideal example to interpret the recently introduced dynamical magnetic charges with respect to its symmetry requirements, and allows for a fundamental study of the toroidal moments in ME materials.

The actual direction of the magnetic moments is still unclear: along the binary axes (i.e. along one of the O atoms, lowering the symmetry to the magnetic point group $2'/m$ as illustrated in the right panel of Fig. 1), along the glide planes (i.e. perpendicular to the binary axes, leading to the point group $2/m'$), or along a random position in between (lowering the symmetry to $\bar{1}'$). In early studies, the form of the magnetoelectric coupling tensor had been used to determine its magnetic point group [17]. The experimental approach proves however difficult; because the threefold symmetry of the $\bar{3}'m'$ phase is lost, the three coordinate systems along the different oxygen atoms are no longer equivalent. Each of those configurations provide two 180° domains (linked by time reversal). Every measurement of the ME effect, even for single crystals, therefore has to take into account the presence of six domains. In addition, this setting assumes that the anisotropy is large enough to prevent a random orientation within the basal plane. In the present work, we determine the ME coupling tensor for the two distinct SF cases and show that some of the elements are in fact negligible, yet allowed by symmetry.

We show that the BEC and force-constant matrix of all considered magnetic structures are similar. Therefore, we demonstrate how the overall form of the ME coupling tensor is determined by the on-site symmetry of the dynamical magnetic charges. The results were also analysed with respect to the toroidal moment. Defined in Ref. [18], the toroidal moment reads as

$$\mathbf{t} = \frac{1}{2}\sum_N \mathbf{r}_N \times \mathbf{m}_N, \tag{3}$$

where $\mathbf{r}_N$ defines the position and $\mathbf{m}_N$ the magnetic moment of ion N. We show that the Cr_2O_3 spinflop phases indeed show a toroidal moment, which follows in a nonzero ME tensor, as observed experimentally in Ref. [19]. We argue however that the description is inadequate, as it does not predict the longitudinal susceptibility to be small – in the same way that the pseudo-scalar description for the symmetric response in the $\bar{3}'m'$ phase is inadequate. An analysis following the spin-orbit polarisation approach by Mostovoy [20] is performed and an in-depth discussion of the applicability of the toroidal description according to Ref. [21] follows.

---

[*] natalie.tillack@materials.ox.ac.uk

[1] H. Schmid, Ferroelectrics **162**, 317 (1994).
[2] M. Fiebig, Journal of Physics D: Applied Physics **38**, R123 (2005).
[3] S.-W. Cheong and M. Mostovoy, Nature materials **6**, 13 (2007).
[4] J. F. Scott, Journal of Materials Chemistry **22**, 4567 (2012).
[5] M. Fiebig and N. A. Spaldin, The European Physical Journal B **71**, 293 (2009).
[6] P. Borisov, A. Hochstrat, X. Chen, W. Kleemann, and C. Binek, Physical Review Letters **94**, 117203 (2005).
[7] P. Borisov, a. Hochstrat, V. V. Shvartsman, and W. Kleemann, The Review of scientific instruments **78**, 106105 (2007).
[8] W. Eerenstein, N. D. Mathur, and J. F. Scott, Nature **442**, 759 (2006).
[9] I. Dzyaloshinsky, Journal of Physics and Chemistry of Solids **4**, 241 (1958).
[10] I. E. Dzyaloshinskii, Sov. Phys. JETP **10**, 628 (1960).
[11] D. N. Astrov, Sov. Phys. JETP **11**, 708 (1960).
[12] V. J. Folen, G. T. Rado, and E. W. Stalder, Physical review letters **6**, 607 (1961).
[13] K. Momma and F. Izumi, Journal of Applied Crystallography **44**, 1272 (2011).
[14] A. Malashevich, S. Coh, I. Souza, and D. Vanderbilt, Physical Review B **86**, 1 (2012).
[15] M. Ye and D. Vanderbilt, Physical Review B **89**, 064301 (2014).
[16] J. Ohtani and K. Kohn, J. Phys. Soc. Jpn. **53**, 3744 (1984).
[17] H. Wiegelmann, a. G. M. Jansen, P. Wyder, J.-P. Rivera, and H. Schmid, Ferroelectrics **162**, 141 (1994).
[18] C. Ederer and N. A. Spaldin, Physical Review B **76**, 214404 (2007).
[19] Y. F. Popov, A. M. Kadomtseva, D. V. Belov, and G. P. Vorob, Journal of Experimental and Theoretical Physics Letters **69**, 330 (1999).
[20] M. Mostovoy, Physical Review Letters **96**, 067601 (2006).
[21] N. a. Spaldin, M. Fiebig, and M. Mostovoy, Journal of Physics: Condensed Matter **20**, 434203 (2008).

Effect of manganese substitution in barium titanate and PIN-PMN-PT

Rajasekarakumar Vadapoo, [1] Muhtar Ahart, [1] and R. E. Cohen [1,2]

[1]Extreme Materials Initiative, Geophysical Laboratory, Carnegie Institution for Science, Washington, DC 20015 USA

[2]Department of Earth and Environmental Sciences, Ludwig Maximilians University, Munich, Germany.

Barium titanate ($BaTiO_3$) single crystals exhibit a very large recoverable nonlinear strain with aging, which is an order higher than $Pb(Zn_{1/3}Nb_{2/3})O_3$-$PbTiO_3$ (PZN-PT) single crystals.[1,2] Multivalent transition metal dopants improve the electromechanical properties of these classic ferroelectrics and third generation relaxor ferroelectrics.[3] To understand the source of these effects, we systematically investigate the effect of Manganese substitution in the classic ferroelectric $BaTiO_3$ (Mn-BTO) and relaxor PIN-PMN-PT. Recent work shows that the environment of defect-vacancy complex plays a crucial role in Mn defect's valence and magnetic moment in BTO.[4]

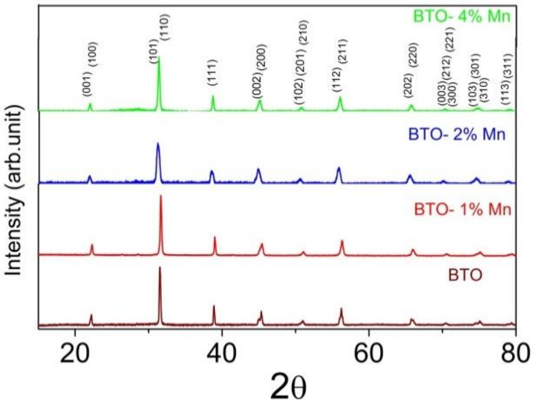

Figure 1. X-Ray diffraction with Mn doping in $BaTiO_3$ (BTO).

We synthesized Mn substituted $BaTiO_3$ ceramics by solid state reaction. We found that $BaTiO_3$ accommodates up to 4 atomic % of Mn in the tetragonal phase (Fig. 1). Further increase in Mn substitution leads to the formation of a hexagonal phase. Raman spectra shows that, with increasing Mn substitution reduces the intensity of A_1(TO) and B_1, E(TO+LO) modes and broadens the E(TO), A_1(TO) modes (Fig. 2). We observed a new peak at ~ 629 cm^{-1}, which find to increase in intensity with increase of Mn doping.

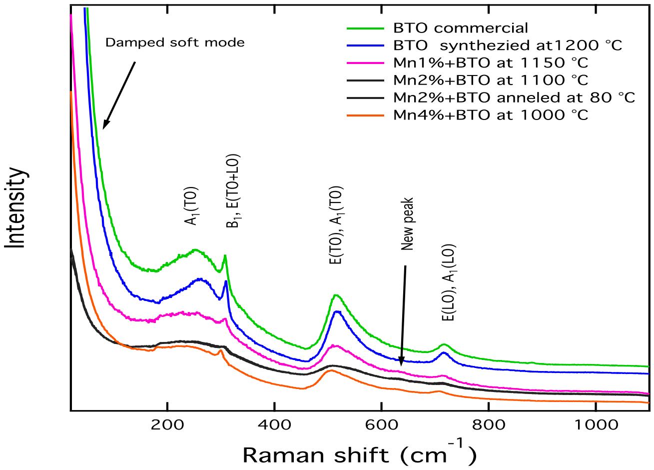

Figure 2. Raman spectra with Mn doping in BTO.

We find that Mn substitution induces enhanced strain behavior with electric field (Fig. 3). We observed cohesive field of 0.367 kV/ mm in grown BTO ceramic (Fig. 4) which agree with reported results.[5] We also observed the effect of aging and Mn substitution on the relaxor ferroelectric PIN-PMN-PT single crystals. We found improved electromechanical properties on Mn substitution and aging (Fig. 5). The improved electromechanical properties in these ferroelectric systems will be discussed in-line with Mn substitution and aging.

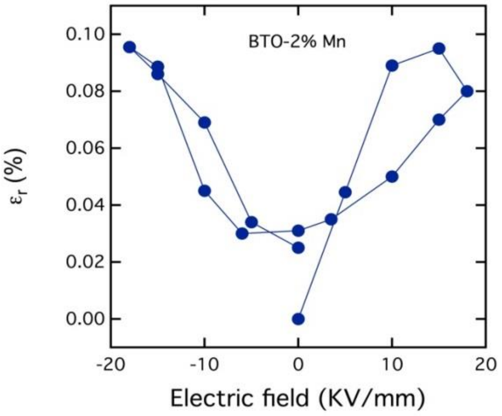

Figure 3. Electric field induced strain (ε) dependence of 2 % Mn substituted BTO. Where, $\varepsilon = (c/a) - 1$ and $\varepsilon_r = \varepsilon_0 - \varepsilon_E$ (at corresponding field with reference to absence of field.)

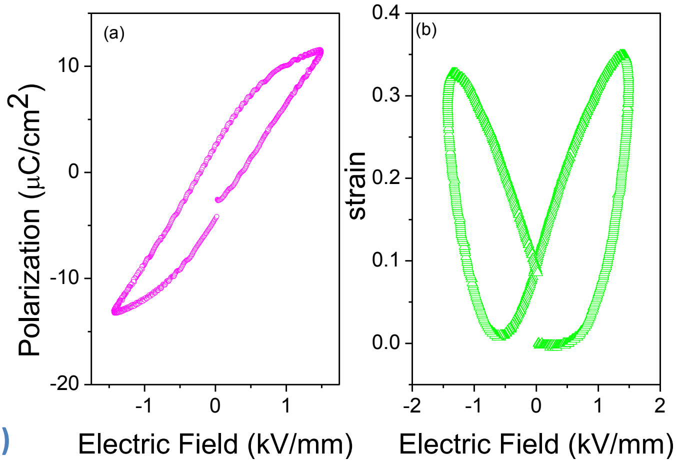

Figure 4. (a) Polarization and (b) strain behavior on BTO ceramics.

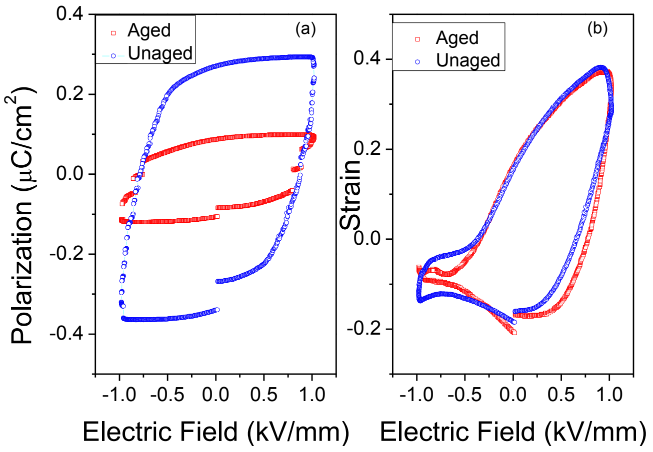

Figure 5. Effect of aging on (a) Polarization and (b) strain in Mn-PIN-PMN-PT single crystal.

Acknowledgement: This work is supported by ONR.

References:

[1] X. Ren, Nat Mater, 3, 91 (2004).

[2] L. Zhang, and X. Ren, Phys. Rev. B **73**, 094121 (2006).

[3] Zhang et al., IEEE Trans. Ultrason., Ferroelect., Freq. Control **60**, 1572 (2013).

[4] J. F. Nossa, I. I. Naumov, and R. E. Cohen, Phys. Rev. B **91**, 214105 (2015).

[5] T. Yongqiang et al., Scientific Reports **5**, 9953 (2015).

Electrical Control of Chiral Phases in Electrotoroidic Nanocomposites

R. Walter[1,2], S. Prokhorenko[1], Z. Gui[3], Y. Nahas[1], L. Bellaiche[1]
[1]Physics Department and Institute for Nanoscience and Engineering, University of Arkansas, Fayetteville, Arkansas 72701
[2]Department of Mathematical Sciences, University of Arkansas, Fayetteville, Arkansas 72701
[3]Department of Materials Science and Engineering, University of Delaware, Newark, Delaware 19716

This work discusses the electrical control of chiral phases and their optical properties in electrotoroidic nanocomposites, which exhibit topological defects in the electrical polarization field (specifically, electrical vortices having order parameter of electrical toroidal moment). Electrical vortices were first theoretically predicted about a decade ago [1] and were found experimentally a few years later [2-8], but they have received less attention than vortices in magnetic and other systems. However, their smaller scale and THz rather than GHz dynamics relative to magnetic vortices better suits electrical vortices for ultrafast, high-density memory [9]. Moreover, they have potential applications in nanoscale optical circulators, since systems with parallel electrical polarization and toroidal moment can be chiral and thus exhibit optical activity [10], or the rotation of the plane of linearly polarized light by a fixed amount per unit length characterized by the gyrotropy tensor g_{mk} [11]. Molecular dynamics (MD) and Monte Carlo (MC) simulations in a first-principles-based effective Hamiltonian are used to better realize these optical applications, and find optical rotation is maximized at room temperature for some applied DC electric field in a ferroelectric nanocomposite [12].

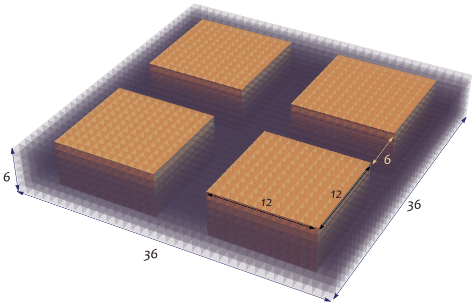

Figure 1: Schematic for 36x36x6 supercell (38 880 atoms) used in our simulations

Specifically, we consider a nanocomposite consisting of a periodic square array of $BaTiO_3$ nanowires embedded in a $SrTiO_3$ medium, each wire oriented along the pseudocubic [001] direction (z) with cross-section 4.8x4.8 nm^2 in the (x, y)-plane ([100] the x-direction and [010] the y-direction) and adjacent wires separated by 2.4 nm. The supercell used is represented in Figure 1. This system was introduced in [13], where under heating from an appropriately prepared ground state it was found to exhibit a series of phase transitions with order parameters of electrical polarization and electrical toroidal moment along the wire axis (P_z and G_z) accompanied by complex phenomena novel to ferroelectrics, including a vortex core transition at 75 K. Most important here is the Curie temperature of T_C=240 K and the temperature at which toroidal moment vanishes T_G=330 K.

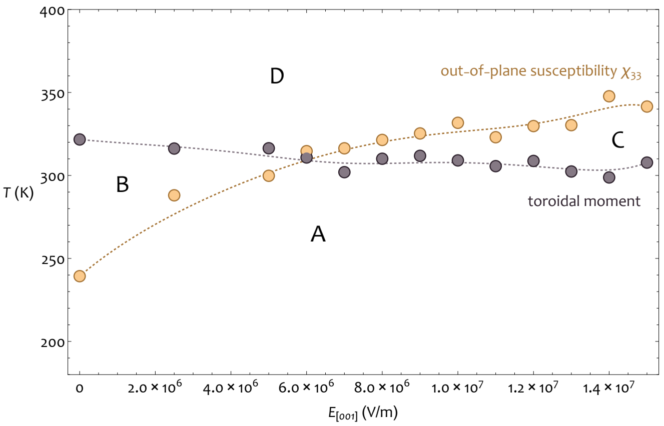

Figure 2: Temperature–electric field phase diagram showing transition temperatures for overall polarization and toroidal moment in the wires; note crossing around 6×10^6 V/m at 312 K

In [10] it is proved that electrotoroidic or ferrotoroidic materials are gyrotropic if the toroidal moment **G** has nonzero first derivatives with respect to an applied electric field **E**: with Einstein summation, for angular frequency of applied field ω and speed of light *c*,

$$g_{mk} = \frac{4\pi\omega}{c}\left[\frac{dG_m}{d\mathcal{E}_k} - \frac{dG_l}{d\mathcal{E}_l}\delta_{mk}\right].$$

Such nonzero derivatives exist if the material exhibits spontaneous polarization or piezoelectricity, where either this polarization has a biquadratic coupling with the electrical toroidal moment or the toroidal moment couples with strain. The former applies for our system. Indeed, using MD with a $(Ba,Sr)TiO_3$ first-principles-based effective Hamiltonian, at 15 K by applying a sinusoidal AC electric field along the z-direction of amplitude 10^9 V/m with frequency ranging between 1 and 100 GHz, for the first quarter-cycle it was found $g_{11}/\omega=0.94\times10^{-16}$ Hz^{-1}, giving optical rotation as much as 0.62 radians/meter at 100 GHz. Moreover, the sign of g_{11} can be reversed using such an AC electric field. It was found that, consistent with typical Landau phenomenological theory, the gyrotropic coefficient varies with temperature T as $g_{11}=A[(T_C-T)(T_G-T)]^{-1/2}$ for some constant A. One way to enhance the gyrotropic coefficient and hence optical rotation, then, is to make $T_C=T_G$ and let T approach this common temperature. We accomplish this [12] by applying a DC electric field in addition to an AC electric field: enhancement not only occurs, g_{11} is maximized (doubled) at room temperature!

We begin with MC simulations, by heating the supercell from its ground state at 5 K through 565 K while applying a fixed DC electric field along [001] ranging between 0 and 1.5x10^7 V/m. Equilibration occurs over 10^5 sweeps and averages are taken over another 10^5 sweeps. For particular temperatures and DC electric fields, final configurations are used as input for MD simulations as in [10], but with the DC field added to the AC field. Transition sequences of polarization, out-of-plane dielectric susceptibility, and toroidal moment are determined by MC. Applying a DC electric field enhances P_z and increases T_C, while by weakening the depolarization field this slightly decreases G_z and decreases T_G. This is accounted for by a simple Landau phenomenological model with a constant strength repulsive biquadratic coupling of P_z and G_z under the DC electric field. Also dielectric susceptibility "flattens out," and the usual statements about phase transition under field apply. Based on the transition temperatures, a temperature-electric field phase diagram is constructed in Figure 2. We expect our maximal optical rotation at the crossing point: room temperature around 6x10^6 V/m applied DC electric field.

For a few selected applied DC electric fields approaching the critical field over the temperature range considered, the gyrotropic response is calculated. Values are reported in Figure 3 at the highest temperatures for which the response could be calculated, which match the lowest transition temperatures well: T_C =285 K (T_G =315 K), T_C =305 K (T_G =315 K), and T_C =T_G =312 K. The last of these is approximated by $g_{11}=A/(T_0-T)$, T_0=320 K, almost matching the temperature dependence in [10] and possibly accounted for by MC/MD differences; but at lower finite fields deviations occur as expected. Nonetheless, at the critical field and room temperature, gyrotropic response is double the largest value attained for no DC electric field. Realizing enhanced optical rotation at room temperature means novel nanoscale optical devices based on electrical vortices might indeed be possible.

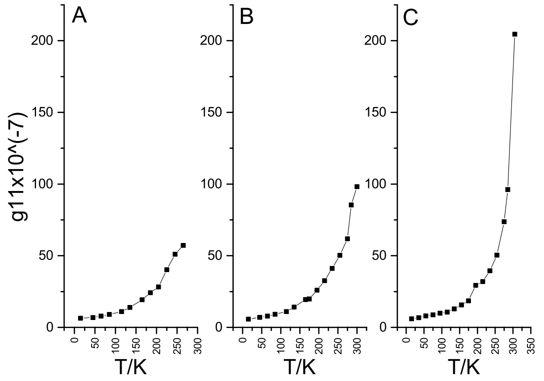

Figure 3: Temperature evolution of the gyrotropic coefficient after heating the system while applying fixed DC electric fields (A) 2.5x10^6 V/m, (B) 5.0x10^6 V/m, (C) 6.0x10^6 V/m

We thank Sergey Prosandeev for indicating references and providing useful suggestions on critical phenomena and phase transitions. R.W. acknowledges that this material is based upon work supported by the National Science Foundation Graduate Research Fellowship Program under Grant No. DGE-0957325 and the University of Arkansas Graduate School Distinguished Doctoral Fellowship. Y.N., Z.G., and L.B. acknowledge the support of the ARO grant W911NF-12-10085. S.P. and L.B. thank the financial support of the DARPA grant HR0011-15-2-0038 and the Physics Department of the University of Arkansas.

References

[1] I. Naumov, L. Bellaiche, H. Fu, *Nature* **2004**, 432, 737.

[2] N. Balke, B. Winchester, Y.-H. Chu, A. Morozovska, E. Eliseev, M. Huijben, R. Vasudevan, P. Maksymovych, J. Britson, S. Jesse, I. Kornev, R. Ramesh, L. Bellaiche, L.-Q. Chen, S. Kalinin, *Nat. Phys.* **2012**, *8*, 81.

[3] A. Gruverman, D. Wu, H.-J. Fan, I. Vrejoiu, M. Alexe, R. Harrison, J. Scott, *J. Phys.: Condens. Matter* **2008**, *20*, 342201.

[4] L. McGilly, A. Schilling, J. Gregg, *Nano Lett.* **2010**, *10*, 4200.

[5] R. McQuaid, L. McGilly, P. Sharma, A. Gruverman, J. Gregg, *Nat. Commun.* **2011**, *2*, 404.

[6] Y. Ivry, D. Chu, J. Scott, C. Durkan, *Phys. Rev. Lett.* **2010**, *104*, 207602.

[7] N. Balke, S. Choudhury, S. Jesse, M. Huijben, Y.-H. Chu, A. Baddorf, L.-Q. Chen, R. Ramesh, S. Kalinin, *Nat. Nanotechnol.* **2009**, *4*, 868.

[8] C. Jia, K. Urban, M. Alexe, D. Hesse, I. Vrejoiu, Science 2011, 331, 1420.

[9] Z. Gui, L. Bellaiche, *Phys. Rev. B* **2014**, 89, 064303.

[10] S. Prosandeev, A. Malashevich, Z. Gui, L. Louis, R. Walter, I. Souza, L. Bellaiche, *Phys. Rev. B* **2013**, 87, 195111.

[11] L. D. Landau, E. M. Lifshitz, L. P. Pitaevskii, *Electrodynamics of Continuous Media*, 2nd edn, Vol. 8 (Course of Theoretical Physics), Elsevier, New York **1984**.

[12] R. Walter, S. Prokhorenko, Z. Gui, Y. Nahas, L. Bellaiche, *Advanced Electronic Materials*, accepted.

[13] L. Louis, I. Kornev, G. Geneste, B. Dkhil, L. Bellaiche, *J. Phys.: Condens. Matter* **2012**, 24, 402201.

Polarization in Ferroelectrics

C L Wang

School of Physics, State Key Laboratory of Crystal Materials,

Shandong University, Jinan 250100, P R China

Since the observation of dielectric anomalous in Rochelle salt by J. Valasek in 1921, many efforts have been devoted to understand this unusual physical behavior. From its early stage, concepts from linear or traditional dielectrics, including polarization, electric displacement and dielectric constant etc., have been used, and are still used in understanding the ferroelectricity nowadays. These concepts seem not well-defined for ferroelectricity, as it is a nonlinear phenomenon. With analog of ferromagnetism, its name as well as concepts and theories have been adopted, parallel between these two phenomena are emphasis. Current theories, such as Landau-type thermodynamic theory, lattice dynamic theory for soft mode and DFT calculations etc., always focus on the polarization, which is still defined as the dipole per unit volume.

Dipole array model is frequently used to explain ferroelectricity phenomenon, such as hysteresis loop and domains structures etc. This model is simple and easy for understanding with its counterpart of ferromagnetism. The alignment of dipoles in the direction of the polar direction is energy favorable. But the alignment of dipoles perpendicular the polar direction is not energy favorable. Simple dipole array model cannot fully explain ferroelectricity. This implies that there might exist other interactions, apart from dipole-dipole interactions.

Normally it is believed that the electric filed in ferroelectric materials is different from the electric field applied externally. The electric field inside the material is called internal field, or effective field. Effective field in a dielectric can be expressed as $E_{eff} = E + \beta P$, with β as materials parameter. A statistical method based upon the effective field, which is an analog of Weiss theory for ferromagnetism either, has been used to study the ferroelectric phase transition property extensively. It is found that quantitative agreement with experimental data cannot be achieved when Lorentz type effective field is adopted, unless high order terms have been included. These work implies that the contribution of higher order electric moments play a crucial role in the formation of ferroelectric stability.

To fully understand of the polarization measured in ferroelectric materials, hysteresis loop together with Sawyer-Tower circuit is re-visited in a more careful way in the following, since a material is called as ferroelectric only it can display hysteresis loop.

As can be seen in the Figure 1, the hysteresis loop displays actually two voltages cross the standard capacitor C_0 and capacitor C_X made of ferroelectric materials. The voltage cross C_X display as electric field, and the voltage cross C_0 denoted as the so-called polarization. We believe that the standard capacitor is made from liner dielectrics, i.e., the charge on its plate is proportional to the crossed voltage. Since the two capacitors is connected in series, the charge on C_X is proportional to the voltage cross C_0. At the remnant polarization point *Pr* in the hysteresis loop as shown in Figure 1, the voltage cross C_X is zero, but with charge $Q=C_0V_0$ on the C_X plates. That means that there is an effective field inside C_X to compensate the voltage built by charge Q, as shown in Figure 2 schematically. The remnant polarization in the hysteresis loop is proportional to this amount of charge Q. The field E displaying in hysteresis loop, effective field E_{eff} and electric field E_Q formed by charge Q are shown schematically in Figure 2. The remnant polarization in the hysteresis loop is proportional to the effective field of the ferroelectrics.

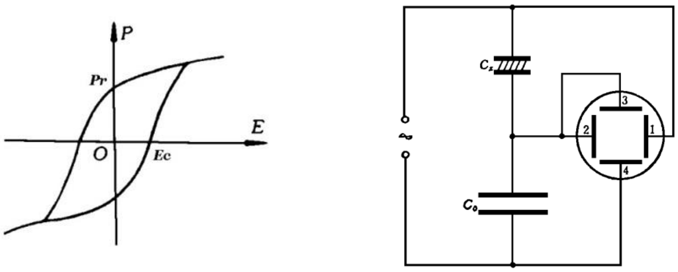

Figure 1 Hysteresis loop and Sawyer-Tower circuit

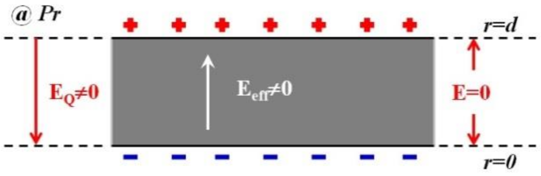

Figure 2 Field E in hysteresis loop, effective field E_{eff} and electric field E_Q formed by charge Q

Precisely calculation of the effective electric field is a tough task. However what we need for the remnant polarization is the potential difference across the capacitor. The potential due to a continuous charges distribution can be expressed as

$$\Phi(r)=\frac{1}{4\pi\varepsilon_0}\int_v \frac{n(r')d^3r'}{|r-r'|}=\frac{1}{4\pi\varepsilon_0}\frac{q}{r}-\frac{1}{4\pi\varepsilon_0}p\cdot\nabla\frac{1}{r}+\frac{1}{4\pi\varepsilon_0}\left(\frac{1}{6}Q\cdot\nabla\nabla\frac{1}{r}\right)+\dots$$

The first term on the right hand-side is zero as ferroelectric is charge neutral system. The second term is the dipolar contribution, and is used for explain the formation of ferroelectricity. The third and other higher order terms should be very important for the ferroelectricity, but usually ignored. The potential difference of the two surfaces $\Delta\Phi=\Phi(r=d)-\Phi(r=0)=E_{eff}\cdot d$. Then the polarization of ferroelectricity is $Pr=\varepsilon_0\cdot\Delta\Phi/d$. The key issue is still the determination of the potential from a given constitution, i.e., structure and composition.

Overall, I have to say that the contribution to polarization of ferroelectric material is not only dipole moment, higher order polar moments do not play negligible roles. More effects have to do to have more concise expressions regarding the polarization.

Effects of Oxide on the Detonation Initiation of Energetic Materials from First Principles

Fenggong Wang, Roman V. Tsyshevsky, and Maija M. Kuklja
Department of Materials Science and Engineering,
University of Maryland, College Park, MD 20742, USA

Energetic materials have a variety of civilian and military applications, ranging from medicine to rocket engine fuels and propellants, construction, planetary and environmental sciences.[1, 2] Understanding the energy absorption and release processes in energetic materials, in particular, how the detonation of explosives can be controllably initiated by laser light, is of great significance for safe handling and applications of these materials. In this aspect, one of the grand challenges is to establish how the detonation of wide band gap explosives is able to be initiated and controlled by laser light with a modest amount of optical energy when energetic materials are mixed with oxides. Recent experiments found that PETN (pentaerythritol tetranitrate), when mixed with an additive oxide MgO, prompts its light absorption and triggers denotation initiated by laser light.[3–6] Finding out the underlying mechanism responsible for this process, elucidating the dictating physical and chemical properties, rationalizing design principles for relevant oxide and explosive systems, selectively designing some specific detonation system combinations with optimal performances, and achieving controllable practical applications are among the cutting-edge directions in this area. The interface between the inorganic oxide and the organic molecule provides both intrigues and opportunities for designing systems that possess properties and functionalities inaccessible by the individual component. In particular, the electronic, polarization induced, chemical, and defect related properties of inorganic surfaces can significantly affect and alter the adsorption, chemical stability, decomposition/degradation, light absorption, and photo-responsive properties of organic molecules.

Here, we choose the highly catalytic oxide TiO_2 and explosive TNT (trinitrotoluene, $C_7H_5N_3O$) as a prototypical example to explore the role of the oxide surface on the detonation initiation chemistry of explosives from first principles. We mimic the interface between the TiO_2 oxide and TNT organic crystals by modeling the system with a TNT molecule adsorbed on the TiO_2 surface. TiO_2 is well-known for its good catalytic properties with its band gap at the visible-light edge. It has several different stable phases, a vast possibility of surface terminations and reconstructions, very rich defect configurations, and great tunability. These features make it serve as a good platform for studying the interplay between explosives and additives and exploring the change of their structural, electronic, and optical properties upon light absorption. Additionally, its much lower band gap (3.0 eV) differs it from MgO, and hence allows us to discern the role of the light responsive additives with different electronic properties on enhancing (or suppressing) light absorption, chemical degradation (or stability), and detonation initiation (or termination of chemical reaction) of high explosives. We show that the TNT-TiO_2 (110) interface induces optical transitions between TiO_2 and TNT, shifting the light absorption edge to lower energy. This helps to control the detonation initiation by laser light with a modest optical energy. In addition, the presence of surface oxygen vacancies leads to electron transfer from surface to molecule, facilitating the decomposition of TNT. Our results not only provide guidelines for designing a controllable oxide-explosive formulation that can be initiated by available lasers, but also are helpful for understanding the role of molecule-surface interactions on interfaces with target properties and functionalities. In particular, it will be of great

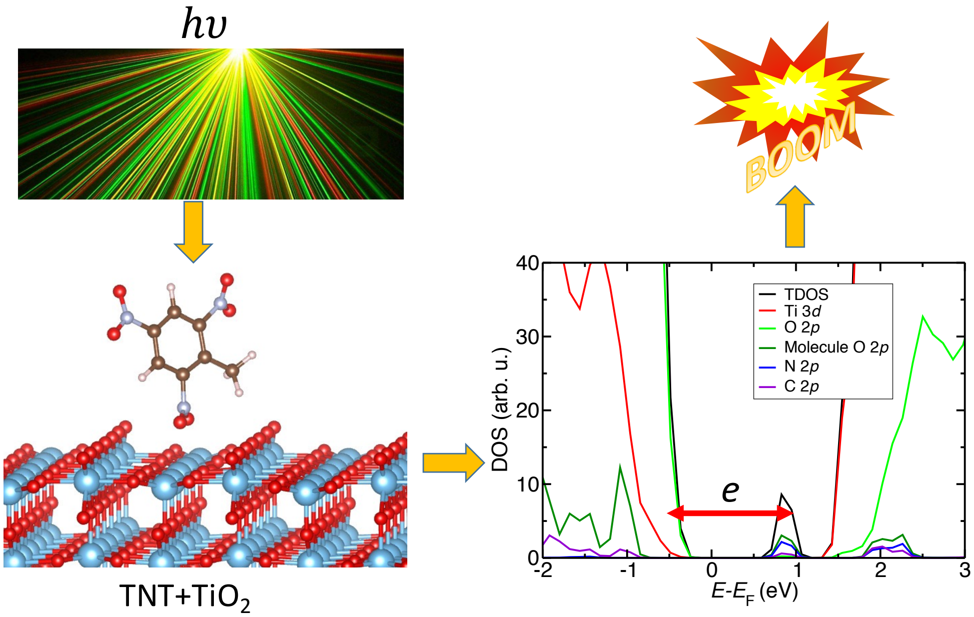

FIG. 1: The detonation initiation mechanism by laser light in TNT when mixed with TiO$_2$. The interplay between TNT and TiO$_2$ induces electronic gap states, prompting light absorption and optical transition and initiating the decomposition of TNT molecule and the then detonation process.

interest to explore the role of ferroelectric oxide on initiating the detonation of explosives.

[1] Y. Bhattacharjee, Science **320**, 1416 (2008).

[2] E. L. Rylott, R. G. Jackson, J. Edwards, G. L. Womack, H. M. B. Seth-Smith, D. A. Rathbone, S. E. Strand, N. C. Bruce, Nat. Biotechnol. **24**, 216 (2006).

[3] E. D. Aluker, A. G. Krechetov, A. Y. Mitrofanov, D. R. Nurmukhametov, M. M. Kuklja, J. Phys. Chem. C **115**, 6893 (2011).

[4] E. D. Aluker, A. G. Krechetov, A. Y. Mitrofanov, A. S. Zverev, M. M. Kuklja, J. Phys. Chem. C **116**, 24482 (2012).

[5] E. D. Aluker, A. G. Krechetov, A. Y. Mitrofanov, A. S. Zverev, M. M. Kuklja, Molecules **18**, 14148 (2013).

[6] R. V. Tsyshevsky, S. N. Rashkeev, M. M. Kuklja, Surf. Sci. **637**, 19 (2015).

Large elasto-optic effect in epitaxial $PbTiO_3$ films

Yurong Yang,[1] L. Chen[2], Z. Gui,[1] D. Sando[3], M. Bibes[4], X. K. Meng,[2] L. Bellaiche[1]

[1]*Department of Physics and Institute for Nanoscience and Engineering, University of Arkansas, Fayetteville, Arkansas 72701, USA*

[2]*Institute of Materials Engineering, National Laboratory of Solid State Microstructures, College of Engineering and Applied Sciences, Nanjing University, Jiangsu, China*

[3]*School of Materials Science and Engineering, University of New South Wales, Kensington, New South Wales 2052, Australia*

[4]*Unité Mixte de Physique CNRS/Thales, 1 Avenue A. Fresnel 91767 Palaiseau, France and Université Paris-Sud, 91405 Orsay, France*

Ferroelectric materials have been known for several decades to exhibit large piezoelectric and dielectric responses. Some of their other cross-coupling properties have also received considerable attention, resulting in new perspectives of using ferroelectrics in photovoltaic applications and the discovery of, e.g., strong electro-optic effects [1], giant photo-induced strain, and coupling between optical fields and ferroelectric order. One particular conversion between properties of different nature, which has only been studied in a few ferroelectrics (or perovskites), is the effect of strain on the refractive index, which is described by the so-called elasto-optic coefficients [2]. It is thus timely to ascertain whether some ferroelectrics can also exhibit large elasto-optic coefficients, an endeavor which would open up new possibilities towards applications aimed at controlling optical fields and mechano-optical transduction. Here we investigate elasto-optic effects in epitaxial films made of the prototypical ferroelectric $PbTiO_3$ (PTO) system by first-principles.

Practically, the elasto-optic coefficient, p_{ij}, is computed via the equality $\Delta\left(\frac{1}{n^2}\right)_i = \sum_j p_{ij}\,\eta_j$, where η_j are components of the strain tensor and $\Delta\left(\frac{1}{n^2}\right)_i$ is the resulting strain-induced change in the inverse of the square of the refractive index. We only consider here the ‘1’ and ‘2’ components of the strain tensor (with the ‘1’, ‘2’ and ‘3’ axes being along the pseudo-cubic [100], [010] and [001] directions, respectively) in this formula, with $\eta_1 = \eta_2$, to reflect epitaxial growth of the film.

Figure 1a show the energies of the tetragonal (*T*), orthorhombic (*O*) and monoclinic phases (possessing *Cm* and *Pm* space groups) for PTO films being under tensile strain. The *T* and *O* phases are the ground state at small and large tensile strain, respectively. The *Cm* and *Pm* phases are low-energy phases or even ground state in the intermediate strain range. Figure 2a presents the predicted ordinary and extraordinary refractive indices, n_o and n_e, respectively, of the *T*, *O* and *Cm* phases as a function of epitaxial strain, for an $\hbar\omega$ energy being 0.3 eV smaller than the computed band gap of bulk PTO. Figure 2a also reports the in-plane n_1 and n_2 refractive indices of the *Pm* phase as well as its out-of-plane n_3 index at this energy. One can see that n_o is larger than n_e for the *T* phase for the range of strain explored here, while the reverse situation holds for the *O* phase. On the other hand, the hierarchy between n_o and n_e is found to be dependent on the strain range in *Cm*. This leads to large strain variation of n_e in Cm and n_3 in Pm, resulting in large elasto-optic coefficients of p_{31} and p_{32}: as shown in Table I, the effective elasto-optic coefficient $\frac{1}{2}(p_{31}+p_{32})$ of *Cm* and *Pm* is twice the magnitude of that of the *T* phase and four times larger than that of the *O* phase. In fact, to the best of our knowledge, these $\frac{1}{2}(p_{31}+p_{32})$ parameters are the largest elasto-optic coefficients found in any material. For instance, they are about twice as large as the elasto-optic coefficient of lithium niobate, for which p_{31} = 0.18, and 30-60% bigger than that of quartz (p_{31}= 0.29) [2].

Figure 1: Total energy and refractive indices of the four studied phases of epitaxial (001) PTO films as a function of tensile strain.

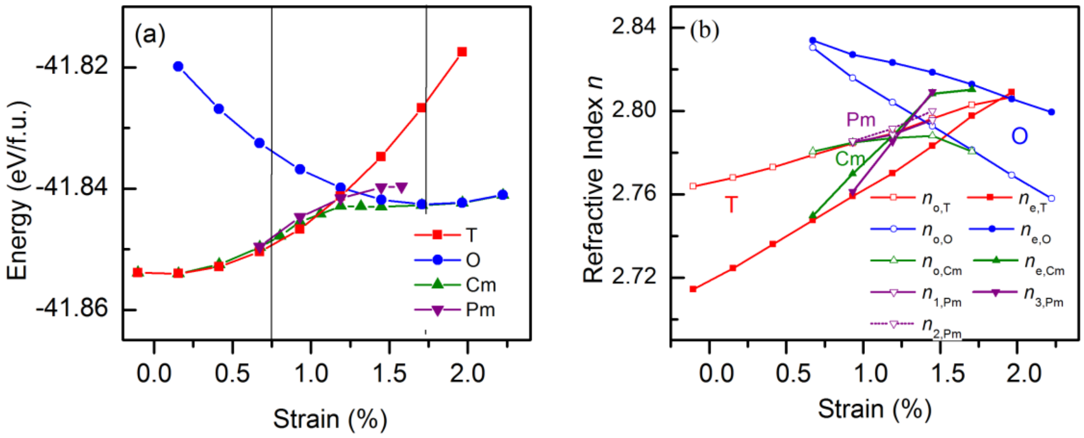

Table I: Elasto-optic coefficients for the studied phases of epitaxial (001) PTO films under a tensile strain of 1.2%. The number in parentheses corresponds to $(p_{21}+\ p_{22})/2$ of *Pm*, which, due to symmetry and unlike in the *T*, *O* and *Cm* phases, differs from $(p_{11}+p_{12})/2$. Note that $p_{31}=p_{32}$ in the *T*, *O* and *Cm* states, therefore making $(p_{31}+p_{32})/2=\ p_{31}$ in these phases.

Phase	*T*	*O*	*Pm*	*Cm*
$(p_{11}+p_{12})/2$	-0.10	0.20	-0.09 (-0.13)	-0.04
$(p_{31}+p_{32})/2$	-0.22	0.10	-0.43	-0.35

This work is supported by ONR Grant N00014-12-1-1034. We also acknowledge a challenge grant from DoD allowing us the access of supercomputers.

References:

[1] D. Sando, P. Hermet, J. Allibe, J. Bourderionnet, S. Fusil, C. Carrétéro, E. Jacquet, J. C. Mage, D. Dolfi, A. Barthélémy, et al., Phys. Rev. B **89**, 195106 (2014).

[2] D. Royer and E. Dieulesaint, *Elastic waves in solids II: generation, acousto-optic interaction, applications*. Vol. 2. 2000: Springer Science & Business Media.

Partial Glass Isosymmetry Transition in Multiferroic Hexagonal ErMnO$_3$

A. Barbour[1], A. Alatas[2], X. Wang,[3] S.-W. Cheong[3], and H. You[1*]

[1]Materials Science Division, Argonne National Laboratory, IL 60439
[2]Advanced Photon Source, Argonne National Laboratory, IL 60439
[3]Department of Physics and Astronomy, Rutgers University, Piscataway, New Jersey 08854

At high temperatures, hexagonal multiferroics such as YMnO$_3$ forms a simple hexagonal para phase with $P6_3/mcm$ symmetry. Below T_c (1195ºC), one of three Y atoms buckles out of the plane forming an antiferroelectric $\left(\sqrt{3}\times\sqrt{3}\right)R30^\circ$ superlattice with concomitant titling of MnO$_5$ bipyramids (trimerization) lowering the symmetry to $P6_3cm$.[1] This transition has been a controversy over many years, especially, whether the transition occurs in *two* steps, and if so, what the nature of the second transition is. Recently, it was suggested that there is an intermediate isosymmetry transition hundreds of degree below T_c.[2] In our study of ErMnO$_3$, we studied the nature of the isosymmetry transition by x-ray techniques including quasi-elastic lines of non-resonant high-energy-resolution inelastic x-ray scattering (HERIX) and high-momentum-resolution diffraction measurements. We show that the isosymmetry transition accompanies a rapid change in the dynamic property, much like a glass transition while maintaining the overall symmetry of the system unchanged. The coherent x-ray scattering measurements also identify the transition and provide behavior of domain dynamics.

We find that the (1 0 4) intensity near T_c between 900°C and 1195°C fits very well with $\propto (T-1195)^{2\beta}$ with β=0.25(1) (black solid line). However, the (1 0 4) intensity deviates significantly from the solid line below 900°C. Henceforth, we denote this intermediate isosymmetry transition[2] at 880ºC as T^*. Below T^* transition, the quasi-elastic line intensity *increases* as temperature *decreases*. Selected HERIX scans at (1.05 0 4) and (0.75 0 2.95) are shown in Figure 1 (a) and (b), respectively. In both cases, there are unusually large central quasi-elastic peaks, albeit truncated to show the transition better. The quasi-elastic peak appears at T^* and its intensity increases as T decreases. The quasi-elastic peak intensity is expected to be zero or weak away from Γ (Bragg) points for ideal lattices. The strong quasi-elastic peak indicates that there are static, frozen, over-damped, or sluggish modes. We find at room temperature that the quasi-elastic intensity of (1±η 0 4) drops rapidly as η (η≪1) increases, indicating that the frozen or sluggish modes are due to imperfect $\left(\sqrt{3}\times\sqrt{3}\right)R30^\circ$ ordering. The amplitudes of frozen or sluggish modes are large at low temperature and gradually unfreezes at T^* as T increases much like a behavior of a glass. This behavior is also similar to the behavior of PbMnO$_3$,[3] a prototypical relaxor. The frozen imperfections most likely suppress Γ_2^- mode, which is a primary ferroelectric mode along c-axis.[2] In Figure 1(b) of the energy scans at (0.75 0 2.95), independent of the ordering for its odd L values, the quasi-elastic peaks are weak. The glassy behavior disappears above T^*. The glassy behavior is further evidenced in high-momentum-resolution diffraction experiments to be presented in my talk.

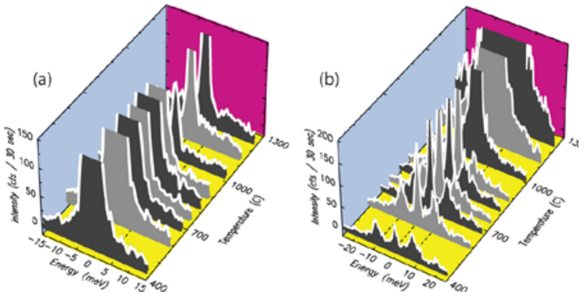

Figure 1. HERIX scans at (1.05 0 4) (a) and (0.75 0 2.95) (b). The dashed lines are 0 and ±8 meV. The intensities are truncated at 150 and 200 for clarity.

While the above quasielastic scattering measurements are *in*sensitive to domain boundaries, coherent x-rays are sensitive to the domain boundaries and their fluctuations, which are accessible with x-ray photon correlation spectroscopy (XPCS).[4] The surface-sensitive speckle patterns on a crystal truncation rod (CTR)[5,6] arise from interferences between structure factors of up (+) and down (−) ferroelectric domains. The CTR structure factor for a fixed l from mixed + and – domains is

$$S_{CTR}\left(l,p,q\right)=\frac{f^{+}e^{i\Delta\phi}}{1-e^{-i2\pi l}}\iint_{S^{+}} e^{-i\left(px+qy\right)}dxdy$$

where f^{+} and $\Delta\phi$ are the amplitude of + domain and the phase difference between + and − domains, p and q momentum transfers of a given pixel and S^+ represents the fragmented area of the + domains. The calculated phase difference is almost π near (004) and S_{CTR} is proportional to $2f^{+}/2\pi\Delta l$ times the integral. Note that the speckle pattern changes when domain boundaries meander or reshape. (0,0,4.125) was chosen for to satisfy strong intensity for XPCS analysis and sufficient sensitivity for near surface domains.

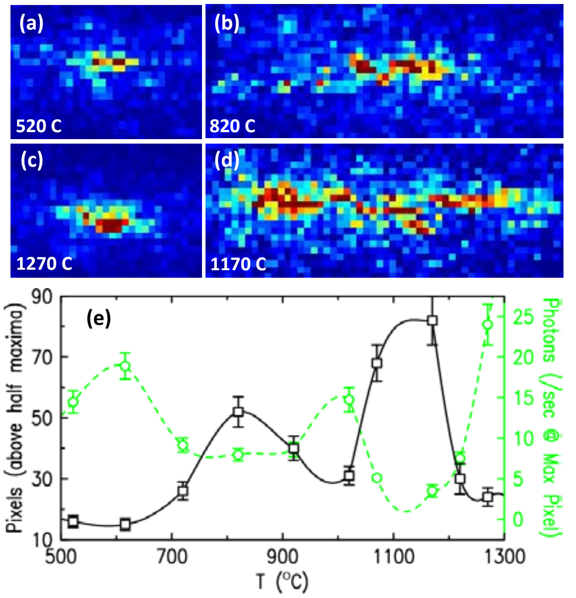

Figure 3. (a)-(d) Speckles measured at the respective temperatures. (e) Squares are numbers of the pixels above the half maxima and the circles are peak intensities per pixel averaged from 4 pixels of highest intensities. The lines are guides to eyes.

The two-step transitions are evident in domain dynamics shown in Figure 2(a)-(d). In (e), while the integrated intensity (peak intensity times the FAHM) shows no significant change over the temperature range, FAHM increases drastically near both T^* and T_c and drops down between them. This can also be seen from the images in (b) at 820ºC and (d) at 1170ºC where speckles spread, indicating that domain sizes are smaller below both transitions. The domains are much smaller near the ferroic transition as expected.

The temporal behavior of the domain boundary motions can be characterized by a parameter τ, correlation time, using XPCS autocorrelation analysis. We plot τ vs. temperature in Figure 3. The value of τ changes more than an order of magnitude from ~20000 sec at 720ºC to <2000 sec at 1270ºC. The two-time correlation maps are also shown as insets where we can clearly compare two temperatures. For a domain boundary to meander, of course, Er atom must overcome the activation potential (see the lower inset) between the up and down domains with appropriate adjustment of the MnO_3 polyhedron. This is the essentially equivalent to K_3 phonon activation energy per unit cell. τ follows a simple Arrhenius form[6,7] with the activation energy of 0.54(5) eV. The domain boundary energy decreases (smaller domain sizes) at the phase transitions while the activation energy of the moving the domain boundaries remain constant over the entire temperature ranges of the two transitions. It is also remarkable to see that the activation energy agree well with the *ab initio* calculation where the energy barrier of K_3 mode between the amplitudes of 0 Å and 0.85 Å (energy minimum) is ~0.5 eV when the energies are renormalized by the ratio of T_c's for $ErMnO_3$ and $YMnO_3$.

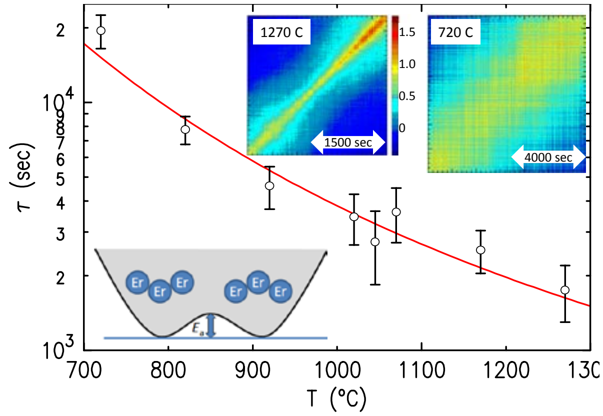

Figure 2. Correlation time of domain boundary dynamics is plotted against temperature. The solid line is the fit with the activation energy of 0.54(5) eV. The upper insets are two-time correlations for 1270 K and 720 K and the lower inset shows schematically configurations of Er positions and the activation energy.

In summary, we will report in my talk evidences for partial glassy behavior of the isosymmetry dynamic phase transition of $ErMnO_3$ and discuss the coherent x-ray measurements of domain dynamics in detail. We believe that similar partial glass transitions exist likely in other multiferroics, and probably in other complex materials such as relaxor ferroelectrics.[8,9] We also propose that the coherent x-ray techniques shown here can be widely used for details of domain dynamics studies in various ferroic materials.

*hyou@anl.gov

[1] B.B. Van Aken, A. Meetsma, T.T.M. Palstra, Acta Crystallographica E57, i38-i40 (2001)
[2] A.S. Gibbs, et al., Phys. Rev. B 83 094111 (2011).
[3] H. You and Q.M. Zhang, Phys. Rev. Lett., 79, 3950 (1997).
[4] D. Lumma, et. al., *Rev. Sci. Inst.* 71, 3274 (2000).
[5] I. K. Robinson, Phys. Rev. B 33, 3830 (1986).
[6] M. S. Pierce, et al., Phys. Rew. Lett. 103, 165501 (2009).
[7] M. S. Pierce, et al., Appl. Phys. Lett. 99, 121910 (2011).
[8] V. Westphal, et al., Phys. Rev. Lett. 68, 847 (1992)
[9] I. P. Swainson, et al., Phys. Rev. B 79, 224301 (2009).

A first-principles study of ferroelectric $PbTiO_3$, $BaTiO_3$ and $KNbO_3$: exchange and correlation effects

Simuck F. Yuk* and Valentino R. Cooper

Materials Science and Technology Division, Oak Ridge National Laboratory, Oak Ridge, TN 37831, USA

*Email Address: yuksf@ornl.gov

Understanding phase transitions in ferroelectric oxides requires the ability to accurately predict the structure and relative stability of crystal phases from first-principles calculations. Such information can readily be used to parameterize empirical models such as effective Hamiltonians to exploring/predict the relevant phase diagrams. However, standard density functionals often lead to inaccuracies in predicted structures, with LDA underestimating the lattice parameters, while PBE overestimating them. These inaccuracies may have significant effects when predicting phase transition temperatures and pressures.

In this study, density functional theory was used to investigate the relative energetics of various phases in $PbTiO_3$, $BaTiO_3$, and $KNbO_3$ perovskites. We examined how the choice of exchange-correlation functionals, including one that incorporates dispersion interactions (i.e. the van der Waals density functional), affects our predictions of the oxide structures of different crystal phases. The optimized lattice parameters and spontaneous polarization of

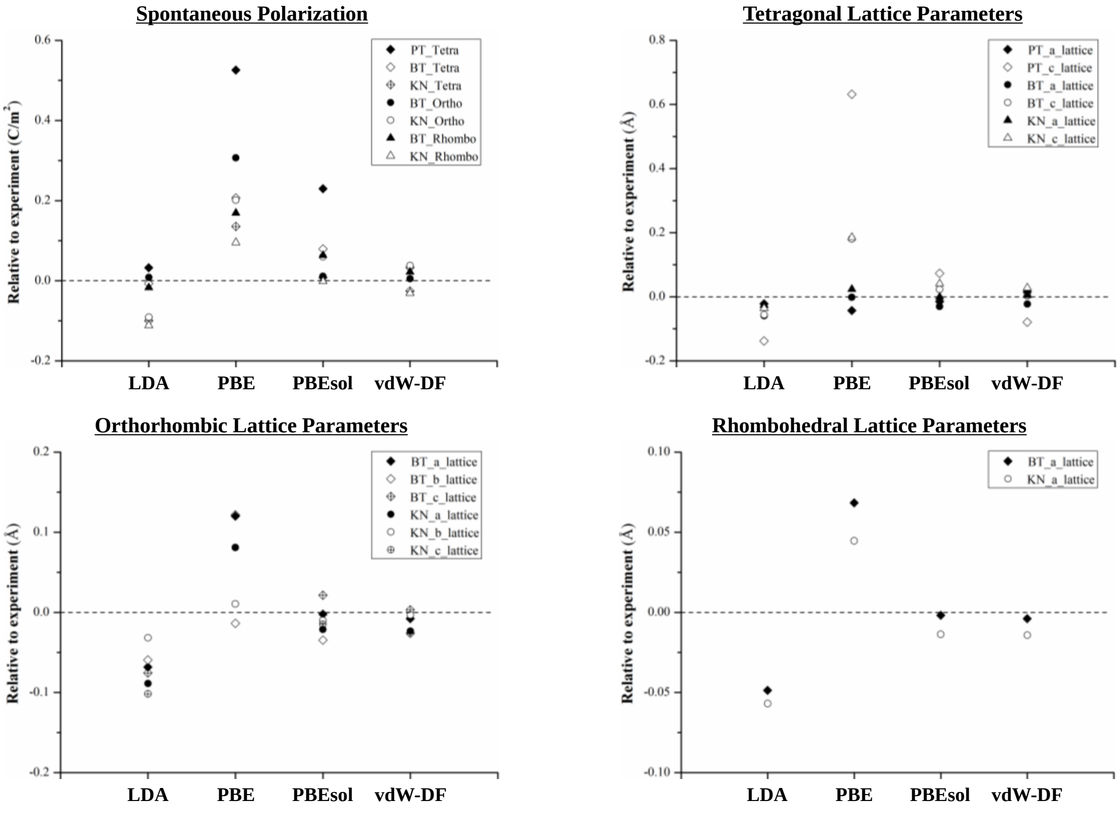

Figure 1. Optimized lattice parameters and spontaneous polarization of $PbTiO_3$, $BaTiO_3$, and $KNbO_3$ at the tetragonal, orthorhombic, and rhombohedral phases. The experimental lattice parameters and spontaneous polarization are from [1-3] and [1, 4-7], respectively.

three *AB*O_3 perovskites for the relevant phases were calculated and compared against available experimental values as shown in Figure 1.

As expected, the LDA functional underestimates both the lattice parameters and spontaneous polarizations. The PBE functional overestimates them and the PBEsol gives a reasonable agreement with the experiments. Surprisingly, we found that the vdW-DF functional with C09x exchange [8] yields the best agreement with the experimental values. Such results suggest that vdW-DF-C09x may be a general-purpose functional suitable for accurately treating densely- and sparsely-packed systems. Also, this study is a good starting point for further investigation in using effective Hamiltonians to simulate temperature- and pressure-dependent phase transitions of ferroelectric oxides. As a next step, the nudged elastic band method will be employed to measure the energy barrier between each crystal phase and identify any local minimum that is energetically lower than the ideal crystal structures.

Research supported by the U.S. Department of Energy, Office of Science, Basic Energy Sciences, Materials Sciences and Engineering Division and the Office of Science Early Career Research Program and used resources at NERSC and OLCF.

References:

[1] A. Hewat, J. Phys. C. **6**, 2559 (1973).
[2] J. Wang, F. Meng, X. Ma, M. Xu, and L. Chen, J. Appl. Phys. **108**, 034107 (2010).
[3] H. Sharma, J. Kreisel, and P. Ghosez, Phys. Rev. B **90**, 214102 (2014).
[4] H. Wieder, Phys. Rev. **99**, 1161 (1955).
[5] F. Michel-Calendini, M. Peltier, and F. Micheron, Solid State Commun. **33**, 145 (1980).
[6] W. Kleemann, F. Schäfer, and M. Fontana, Phys. Rev. B **30**, 1148 (1984).
[7] M.J. Haun, E. Furman, S. Jang, H. McKinstry, and L. Cross, J. Appl. Phys. **62**, 3331 (1987).
[8] V.R. Cooper, Phys. Rev. B **81**, 161104 (2010).

Rashba Spin-Orbit Coupling Enhanced Carrier Lifetime in $CH_3NH_3PbI_3$

Fan Zheng, Liang Z. Tan, Shi Liu, and Andrew M. Rappe

The Makineni Theoretical Laboratories, Department of Chemistry, University of Pennsylvania,
Philadelphia, Pennsylvania 19104-6323, USA

Organometal halide perovskites are promising solar-cell materials for next-generation photovoltaic applications. The long carrier lifetime and diffusion length of these materials make them very attractive for use in light absorbers and carrier transporters. Previous studies reported a relatively low defect concentration in MAPbI3, which reduces the scattering centers for nonradiative charge carrier recombination. Recently, it has been suggested that the spatial carrier segregation caused by disorder-induced localization or domains acting as internal p-n junctions may reduce the recombination rate. In addition, the dynamic motion of the molecules will result in fluctuating indirect band gap, which can further enhance its lifetime.

While these aspects of organometal halide perovskites have attracted the most attention, the consequences of the Rashba effect, driven by strong spin-orbit coupling [1], on the photovoltaic properties of these materials are largely unexplored. In this work, taking the electronic structure of methylammonium lead iodide as an example, we propose an intrinsic mechanism for enhanced carrier lifetime in 3D Rashba materials. After photo-excitations, the phonon modes originating mainly from the molecules will relax the excited carriers to the band edges quickly before they can recombine. With ferroelectric distortions, the strong spin-orbit coupling and the broken inversion symmetry drives the Rashba splitting of different spins. Under some distortions, the band edge spins will be anti-aligned, leading to the spin-forbidden transitions for the recombination. Furthermore, the different wavevectors of the conduction and valence band edges reduces the recombination rate. Based on first-principles calculations, we demonstrate the fast phonon-assisted relaxation by calculating the electron-phonon coupling. With a Rashba spin-orbit model, the distortions that giving rise to spin-forbidden transitions are also identified.

This mechanism is not limited to $CH_3NH_3PbI_3$ but applied to other organometal halide perovskites. Such mechanism can be realized by the joint action of molecules (ferroelectric distortion and phonon-assisted transition) and PbI3- sublattice (strong spin-orbit coupling). These results are important for understanding the fundamental physics of organometal halide perovskites and for optimizing and designing the materials with better performance. The proposed mechanism including spin degrees of freedom offers a new paradigm of using 3D Rashba materials for photovoltaic applications.

[1] M. Kim, J. Im, A. J. Freeman, J. Ihm, and H. Jin, Switchable S = 1/2 and J = 1/2 Rashba bands in ferroelectric halide perovskites, *Proc. Natl. Acad. Sci.* 111, 6900 (2014).

[2] F. Zheng, L. Z. Tan, S. Liu, and A. M. Rappe, Rashba Spin–Orbit Coupling Enhanced Carrier Lifetime in CH3NH3PbI3, *Nano Letters*, (2015).